Development of Membrane-based Calorimeters to Measure Phase Transitions at the Nanoscale

Thesis Submitted by
Aitor Fernández Lopeandía
to apply for the degree of Doctor in Materials Science.

Thesis supervisor: Dr. Javier Rodriguez Viejo.

Grup de Nanomaterials i Microsistemes.
Departament de Física.
Universitat Autònoma de Barcelona.
Bellaterra, May 2007

Dr. Javier Rodríguez Viejo, profesor titular de Física Aplicada en la Facultad de Ciencias de la Universidad Autónoma de Barcelona.

CERTIFICA:

Que Aitor Fernández Lopeandía, Licenciado en Ciencias Físicas por la Universidad Autónoma de Barcelona, ha realizado bajo su dirección el trabajo que lleva por título "Development of Membrane-based Calorimeters to Measure Phase Transitions at the Nanoscale", el cual se recoge en esta memoria para optar al grado de Doctor en el programa de Ciencia de Materiales por la Universidad Autónoma de Barcelona.

Dr. Javier Rodríguez Viejo
Bellaterra, Mayo 2007

Dedicada

a mi familia
y
a Libertad

Development of Membrane-based Calorimeters to Measure Phase Transitions at the Nanoscale.

Aitor Fernández Lopeandía

Submitted for the degree
of Doctor in Materials Sciences
on May 2007

Supervisor

Dr. Javier Rodríguez Viejo

Agradecimientos

"Si he visto más lejos ha sido porque he subido a hombros de gigantes".

— Sir Isaac Newtow

Durante estos años de tesis doctoral he tenido el honor y la suerte de disfrutar de la ayuda y el apoyo de mucha gente, a todos muchas gracias.

En primer lugar quisiera agradecer tanto al Dr. Javier Rodríguez-Viejo como a la Prof. Maria Teresa Mora Aznar por haberme acogido en el Grupo de Física de Materiales I de la UAB, y siempre haberme respaldado. Al Ministerio de Educación por la beca de colaboración de último curso de licenciatura, y al entonces Ministerio de Ciencia y Tecnología por la posterior beca predoctoral FPI.

De forma especial quisiera agradecer a mi director de tesis, el Dr. Javier Rodríguez Viejo, por su paciencia y estímulo continuo, por su constante interés y enorme capacidad de trabajo, pero sobretodo por el aprecio y la confianza que en todo momento ha depositado en mí.

A la Prof. Maria Teresa Mora Aznar y al Dr. Narcís Clavaguera Plaja, por el interés demostrado, las fructíferas discusiones y por concederme siempre un comentario agradable.

A los compañeros de GNAM y del departamento de Física, a todos gracias, por que de todos aprendí algo. Quisiera destacar especialmente a los que de una forma más directa han tenido mucho que ver con este trabajo:

Al Dr. Manuel Chacón, profesor de la Universidad de Cali (Colombia), por ayudarme a dar los primeros pasos, e impresionarme día tras día con sus montajes experimentales.

A Lluís Cerdó que me introdujo en el fascinante y complicado mundo del control. Gracias por tu ayuda en el desarrollo del controlador de compensación de potencia, por tu amistad y por esas charlas tan fructíferas en el Rinky.

A la Dra. Gemma García por las múltiples horas de despacho compartidas, por su continuo apoyo y por siempre tener un momento para resolver mis infinitas dudas. También

quisiera agradecerle su importante contribución en el trabajo sobre la cristalización del a-Ge.

Al Dr. Francesc Xavier Muñoz y a su equipo de investigación del IMB-CNM (Barcelona) por la colaboración en los procesos tecnológicos de microfabricación en los dispositivos finales. De forma especial, quisiera agradecer tanto a Roser Mas como a la Dra. Marta Duch. Al Dr. Eduardo Romero por sus clases de elementos finitos que me fueron de gran ayuda en los posteriores trabajos de simulación.

Al Dr. Francesc Pi por permitirme adaptar su evaporador para realizar medidas in-situ, y por su disponibilidad a la hora de trabajar día y noche. A Edgar León por su ayuda en el día a día experimental y su capacidad de trabajo. Al Dr. Sridharan por las horas de trabajo compartidas e introducirme en la gastronomía de la India. A Roger Doménech por estar siempre dispuesto a ayudarme y demostrar una motivación envidiable. A José Valenzuela por el trabajo realizado durante este último año en el desarrollo del sistema de compensación de potencia basado en FPGAs. Tampoco quisiera olvidarme del importante papel de los trabajadores tanto del Taller mecánico de la UAB, Luis y Francesc, como del Departamento de Física, Manel, Jordi y Rafa. Sin su ayuda el trabajo experimental sería aún más difícil.

Al doctorando Alessandro Bernardi, al Dr. Alejandro Goñi, a la Dra. Isabel Alonso y al Dr. Miquel Garriga del ICMAB-CSIC (Barcelona) por las caracterizaciones de espectroscopía Raman, elipsometría y las fructíferas discusiones. Al Dr. Angel Pérez del ICMAB por las caracterizaciones con AFM.

Al Dr. Leonel Arana y al Prof. Klavs Jensen del MIT (Cambridge, USA) por la colaboración en el diseño y microfabricación de los dispositivos iniciales.

A la Dra. M. Ángeles Benítez y a Raquel Palencia del Laboratori d'Ambient Controlat de la UAB por los consejos y ayudas prestadas. Al Prof. Philippe Godignon del IMB-CNM por los procesos de RTA y a Carles Mateu por el asesoramiento en los procesos de RIE.

Al Dr. Kontantinos Zekentes del FORTH (Heraklion, Grecia) por recibirme en su laboratorio e introducirme en el mundo del Ge durante la estancia breve disfrutada en Creta. No quisiera olvidarme de la gente que más me ayudó en el día a día experimental, el Dr. Nicolás Camara, Dr. Muchang y Anne.

Al Prof. Philippe Godignon del IMB-CNM por los procesos de RTA.

A los técnicos de Servicio de microscopía de la UAB por las imágenes de SEM y TEM en planar view.

Al Prof. Janos Lábár del RITPMS (Budapest, Hungría) por la preparación de muestras

para TEM en cross-section y su posterior observación.

A la Prof. Claire Bergman por recibirme en su laboratorio, el L2MP-CNRS (Marseille, Francia). Durante esta estancia breve se inició una colaboración para el estudio nanocalorimértrico de la formación NiSi, que hoy en día está en desarrollo. De este periodo me gustaría agradecer también tanto al Dr. Dominique Mangelinck como al doctorando Loeizig Ehouarne por todo lo que me enseñaron.

Y a los compañeros y amigos del ICMAB (Adrián, Bernat, Oscar, Andrea, Nico,... y otros muchos) gracias por las ayudas brindadas y las dudas resueltas. Muchos sabéis seguramente más de lo que hubieseis deseado de nanocalorimetría a raiz de las meriendas en la terraza. Un abrazo del eterno visitante.

Y por supuesto a mi familia. A mis padres, a mi hermana y a Libertad, la doctora de la casa, por estar siempre a mi lado y ayudarme en todo para que pudiera llegar hasta aquí.

GRACIAS A TODOS!!!

Summary

Thin film calorimetry opens the possibility to perform calorimetric measurements on ultra-thin or thin films due to the substantial increase in sensitivity compared to commercial systems. Based on this premise the present research work deals with the development of membrane-based nanocalorimeters incorporating thin film heaters and thermometers which can work with high sensitivity because of their very low thermal mass.

In the first part we describe semiconductor processing techniques that are used to fabricate the microdevices with a special care devoted to their high temperature thermo-mechanical stability. It is shown that alumina coated Pt/Ti resistive elements can be reproducibly used for heating/sensing up to temperatures around 1200 K.

Quasi-adiabatic nanocalorimetry is presented in Chapter 4. The technique works at heating rates above 10^4 K/s. At these rates phase transitions in ultra-thin films can be measured with energy sensitivity in the nJ range. The associated noise in heat capacity is around 20 pJ/K, for reversible transitions. The size-dependent melting point and enthalpy of ultra-thin films of In is analyzed as a case study. A new methodology to account for power losses at high temperatures is presented in this chapter. By employing this methodology the heat capacity of very thin films of Ni at the Curie transition is determined. It is shown that size effects also play a key role in this transition. The last part of this chapter is devoted to the analysis of ultra-thin films of Ge embedded within SiO_2 layers during ultrafast heating up to 1200K. The melting of the amorphous phase along with the size-dependent melting and supercooling of Ge nanocrystals is also described.

In Chapter 5 we present a new digital-based control system which has been developed to work in power compensation mode at heating rates spanning from 0.1 to 10^3 K/s. It permits to analyze samples in the microgram range with an energy sensitivity around the μJ. This new development opens the possibility to study kinetically limited transformations that typically need for lower rates or to mimic real conditions similar to those achieved in rapid thermal processing in the microelectronic industry.

Finally, several appendix dealing with control theory, calorimetry and the crystallization of Ge films of different thickness are also presented.

Contents

Chapter 1

Introduction

In this short introduction we provide with the general background concerning Materials Science at the nanoscale and the general tendency towards miniaturization of devices to measure it. In chapters 4 and 5 a more specific and detailed introduction including the state-of-the-art and references of relevant works is written for every type of material and device.

This century, Material Science will be deeply marked by the growing interest in the fabrication of systems with nanometric dimensions. During last years improvements in the tailoring of nano-scale materials, such as thin films, nanowires or isolated nanocrystals, have been driven by both a scientific and a technological-based development. In these materials, the physical properties are influenced by their size, with behaviours dominated by quantum and surface effects, which are clearly different from the bulk samples. For instance, in semiconductors when the size in any of the three dimensions is reduced below the exciton Bohr radius, the electron wave-function is confined with a change in the optical and electrical properties. One of the most exciting examples of the quantum size effect corresponds to the CdSe quantum dots (QD) where it is possible to tune the band gad of the material across the visible spectrum only by changing their size [1]. Concerning surface effects, it is well known that surface atoms, in any material, make a distinct contribution to the free energy due to the presence of dangling bonds. In nanosized materials the number of surface and interface atoms is a large fraction of the total, producing significant changes in the thermodynamic properties. Phenomena like the melting point depression [2], or the change in pressure needed to induce solid-to-solid transformations [3, 4], can be explained by the contribution of surface atoms. The study of these size effects is interesting not only in fundamental physics, allowing the understanding of the underlying molecular processes,

but also for the technological community, showing the potential use of these nanometric materials in technological applications[1]. The advance in materials processing requires the refinement of the usual characterization techniques that traditionally have been helping the scientific community to gain a deep understanding on the different material properties.

Nanocalorimetry.

A suitable technique to characterize kinetic and thermodynamic properties of materials is calorimetry which is based in the measurements of the heat, released or absorbed by a material during any process. The most established method in calorimetry of inorganic materials is Differential Scanning Calorimetry (DSC), a powerful tool to analyze phase transitions over a large range of temperatures (See append A about DSC). The use of the DSC technique is typically performed in bulk samples, in the range of mg. When the aim is to measure transformations or phase transitions in ultra thin films or nanoscopic samples, the calorimetric measurements are troublesome [5], since the amount of energy released by a given reaction is too small to be measured and analyzed with accuracy using conventional calorimeters. This problem is sometimes overcome by increasing the calorimetric signal with multilayer structures [6, 7], but it is not suited for all types of samples, i.e. coalescence in quantum dots.

The need to measure new phenomena related to nanoscale behaviour has driven, in the last years, a significant effort towards the development of more sensitive calorimeters, capable to efficiently measure small samples [8]. The fundamental problem on measuring small samples is related to the ratio between the heat capacity of the calorimetric cell and the heat capacity of the sample, since the calorimetric signal is proportional to the total addenda[2], but the transformation signal is only proportional to the sample. Therefore, it is necessary to reduce the heat capacity of the calorimetric cell to increase the signal-to-noise ratio during the transformation. This concept has been guiding all the advances in the designs of new calorimeters, but it is not the only requirement. The difficulty to reduce the thermal link with the environment low enough to permit adiabatic measurements of the heat capacity, is another problem that should be considered [5].

The development of micromachining techniques associated to the Silicon technology [9, 10] has enabled the scaling down of several types of devices. One example showing

[1] The microelectronic industry is working, nowadays, with nanometer scales in the transistor technologies.

[2] total addenda is referred to the addition of the sample heat capacity plus the cell heat capacity.

the recent evolution in the actuators field is the membrane-based chemical microreactor developed at MIT [11]. These membrane-based devices[3], have become one of the most promising designs for new calorimeters. Using the thin membrane as substrate or sample support, the fundamental problems with the calorimetric cell addenda and the thermal link are reduced, increasing drastically the sensitivity.

Several groups have been adapting established calorimetric techniques to be used with these MEMS-based devices. Two examples are the AC calorimetry and adiabatic calorimetry.

An AC membrane-based calorimeter was developed by Denlinger et al. [12], where oscillating the temperature of a sample around one temperature value the heat capacity of the sample is obtained with high precision at temperatures above liquid He. Recently, O. Bourgeois et al. [13] have shown that energy resolutions of attojoules can be achieved, permitting to measure magnetic flux quanta in mesoscopic superconducting loops of Al. However, the technique is not useful to calculate enthalpy values of phase transformations. Adiabatic calorimetry with membrane-based calorimeters[4], also called thin-film differential scanning calorimetry (TDSC) has been developed by Allen's group at University of Illinois. In this mode, high heating rates ($> 10^4\, K/s$) are applied to a sample and the heat capacities and the amounts of heat during phase transformation can be measured [14]. The TDSC method allows the study of samples in the order of a few nanograms [15] with a high energy resolution (better than 1 nJ), but it has an important limitation in the dynamic range of operation, due to adiabatic requirement. Shick's group developed a non-adiabatic variant of the TDSC technique[16], working in low pressure gas environments and with a more linear scanning rates (around $10^3\, K/s$) permits to analyze thin film samples both during heating and cooling. With this improvement, they study materials in far from equilibrium conditions [17].

This fast scanning techniques are not suitable when the aim is to measure phase tranformations in kinetically limited phenomena. With commercial power compensation DSC calorimeters and heat flow DSC calorimeters slower heating (scanning) rates (<500 K/min) are used to study time dependent transitions[5]. These type of calorimeters, provide the pos-

[3]These type of microreactors are based on a free-standing silicon nitride (Si_xN_y) thin film membrane held over a silicon frame. A metallic elements is patterned on the top of the membrane, that is used as a resistive heater/sensors to control the temperature. The metallic heater/sensor are acceded through electrical contact pads patterned with the same metallization over the Si frame, allowing an easier connectivity using gold pogo-pin probes, see chapter 2.

[4]see in appendix A, classical adiabatic calorimeters for bulk samples are described.

[5]see in appendix about DSC, power compensation and heat flow operation mode.

sibility to measure the differential heat flux introduced into a twin system of calorimetric cells, one with sample and another as reference, in isothermal or isoperibolic mode. For small samples some approximations have been developed in heat flow DSC, where chip calorimeters based on heat flow thermopiles [8] are able to measure with high power resolution. However, the necessity of sample masses in the order of hundreds of micrograms is a major limitation to the study of some specific systems. Another interesting development is the cantilever calorimeter, based on a cantilever for atomic force microscopy and the principle of bimetallic bending [18]. This technique has a resolution of 0.5 nJ [8], but at the expense of a severe limitation on the types of samples to be analyzed and difficulties in sample location.

Differential scanning calorimetry in power compensation mode is typically limited to heating rates ranging from 1 to 160 K/min. In commercial devices, this is a good compromise between accuracy, resolution, sensitivity and measuring time. Measurements at higher heating rates present some advantages and limitations. One of the main problems to be solved in commercial systems is that high heating rates increases the thermal lag between sample and heater. In the membrane-based calorimeters the thermal lag is negligible even at heating rates close to 10^5 K/s. Another limitation, in commercial systems, comes from the high thermal mass of the addenda which precludes or difficults application of high heating rates. Recently, Perkin Elmer has commercialized a system, sold as capable to reach a high heating rate, with a limit of 1000 K/min. Besides the two above mentioned, the main limitations when raising the scanning rate could be that: i) High heating rates typically induce transformations at high temperatures and therefore higher ranges of temperatures are required. These may represents a problem for systems where the risk of decomposition is high, such as, polymers, ii) High sampling rates and faster electronics, iii) Lack of suitable standards in many cases and iv) Analysis of kinetically limited transformations (metallic glasses and diffusion limited processes). However high heating rates may introduce some advantages that could be summarized as follows: i) Shorting of measuring time, ii) Higher throughput, iii) Signal amplification for small samples and iv) Suppression of kinetically controlled effects (eg. prevent crystallization of a-Ge [19], Cold crystallization in polymers [20])

The aim of this work.

In this work we present our efforts to develop a microfabricated membrane-based calorimeter, suitable to work in both adiabatic (high heating rates and high sensitivity) and power

compensation mode (from high to slow heating rates) for sub-microgram or nanogram samples. We started from the MIT chemical microreactor, initially developed in 1997 to work in quasi-stationary conditions [11, 21], adapting many characteristics to our needs.

In a general perspective, this work is driven by the possibility to measure the heat capacity and phase transitions in unexplored systems such as ultra-thin film or new nanostructures, opening interesting new phenomena to be investigated. As a first step towards this goal, in this memory we mainly present the development of the microsystems and implementation of the two calorimetric methods providing some examples of application.

Overview of this thesis.

This thesis is divided in four main chapters, the conclusions, and appendixes as follows:

Chapter 2 Presents the microfabrication processes associated to the calorimeter and the design considerations of the several elements that make up the microdevices.

Chapter 3 Description of the vacuum setup used to perform the calorimetric measurements and grow the samples.

Chapter 4 The quasi-adiabatic nanocalorimetry technique is described. Tests over ultra-thin film samples are presented to show its potentiality. At low temperature, we present the calorimetric study on ultra-thin films of In (a well studied material in nanocalorimetry) to optimize both experimental setups and heater designs. At intermediate temperatures, we show preliminar results on the size dependence of the Curie transition in Ni films. Finally at high temperatures, we present the study of the first-order transition of nanometric films of amorphous Ge and the formation of Ge nanocrystals.

Chapter 5 This chapter deals with the development of digital controllers, to use the nanocalorimeter as a power compensation calorimeter. We present the two controllers developed and the final tests over small samples.

Chapter 6 Conclusions.

Appendix A A brief description of Differential Scanning and Adiabatic Calorimeters.

Appendix B Study of crystallization of amorphous Ge thin films.

Appendix C Feedback controller selection and tuning.

Chapter 2

Nanocalorimeters fabrication and characteristics.

Advanced micromachining techniques associated to the Silicon technology [9] have driven the scaling down of several types of devices, creating a new area of microelectromechanical systems (MEMS)[10]. In this chapter, we describe the technical details of the fabrication steps of a membrane-based nanocalorimeter, as well as the strategies employed to create the two devices currently in use. Several test prototypes were designed and tested before reaching a final version. Figure 2.1 shows the schematics of the procedure by which the final characteristics of the nanocalorimeter are based on the knowledge produced by the previous designs through experimental tests and thermal modeling.

From the initial MIT prototype, a microreactor with a long channel and several heaters and sensors originally designed to promote chemical reactions with hazardous gases in a safer scale [21], to the current designs some fundamental parts have been redesigned, in an attempt to fulfill the following fundamental rules:

- The need to control heat losses. This is a critical point to work in adiabatic mode, but even in power compensation it is necessary to increase the sensitivity. Placing the devices in a HV chamber, the convection losses can be controlled by adjusting the working pressures, see chapter 3. The thin silicon nitride membrane provides a good thermal conductive insulation if the sample is conveniently located in the center of the membrane beneath the heater to avoid new thermal pathways to the silicon frame.

- The temperature profile should be uniform in the sensing area to increase the sensi-

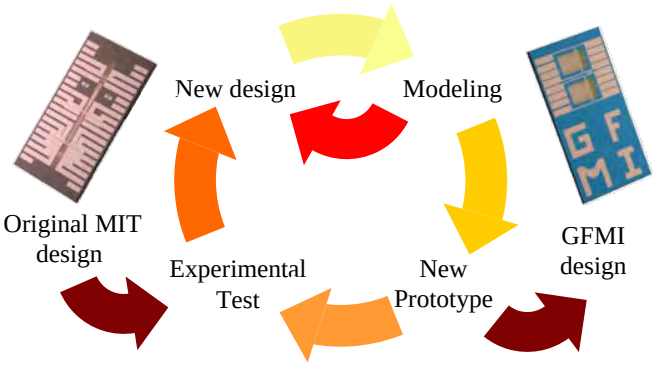

Figure 2.1: Design flow diagram.

tivity and get accurate temperature measurements. Thermal modeling both in the transient and in the steady state should guide the design process, through an a priori evaluation of the temperature profiles.

- The total addenda should be as small as possible to increase the signal to noise ratio and the resolution. In the nanocalorimeters the most important characteristic is the Si_xN_y thin film membrane that provides a holder with a very low heat capacity. Values around hundreds of nJ/K (or even lower depending on designs), at room temperature, are easily achieved.

- Increase the area of analysis. The analysis area should be as large as possible to increase the signal.

- Thermo-electrical stability of the devices. The heater/sensor materials must be electrically stable in the working temperatures range, to guarantee the reproducibility and repeatability of the measurements. The membrane should electrically insulate the heater/sensor elements from the rest of the device at the operation temperature, in order to prevent current shunting through the Si frame or in the presence of a conductive sample.

- Thermomechanical stability. The membrane has to be deposited in a slightly tensile state to minimize the risk of deformation during the temperature ramps. This fundamental requirement affects the minimum thickness of the Si_xN_y membrane and its shape and window size. It will also prevent cross sensitivity effects like buckling, that may occur upon high heating rates at high temperatures due to the presence of non-isotropic thermomechanical stresses.

- Material selection. All materials selected to conform the nanocalorimeter should have a close to linear dependence of its physical magnitudes (such as heat capacity, resistance, thermal conductance, emissivity) with temperature, and of course be stable without phase transitions in the temperature domain of interest.

2.1 Microfabrication process.

The first prototypes of nanocalorimeters were fabricated in the clean rooms at MIT's Microsystems Technology Laboratory and the actual microsystems are fabricated in the clean rooms at IMB-CNM and LAC-UAB, using standard micromachining technology [22, 23]. Figure 2.2 schematically shows the microfabrication process. The starting material for the nanocalorimeter fabrication has been a double-sided polished p-silicon wafer (4 inches - diameter, 520 μm - thick, 40 Ohms·cm - resistivity). The wafer is thermally oxidized at 1273 K to grow a 50 nm thick silicon oxide film. This electrical insulating layer is introduced to avoid electrical shunting problems that may appear in this type of devices at high temperatures [24]. As a second step, a 180 nm thick low-stress Si_xN_y is grown by low pressure chemical vapor deposition (LPCVD). The nitride deposition on the frontside of the wafer will eventually form the membrane of the nanocalorimeter. The Si_xN_y on the backside of the wafer, which will be used as a mask for the bulk etching, is patterned through photolithography[1] with positive photoresist and plasma etch in SF_6 to expose the underlying silicon in the channel regions and the alignment marks, see figure 2.2. The frontside of the wafer is coated with positive photoresist and patterned with the metallic structures, after an alignment with the bottom channel on the back side. The alignment through the Si wafer is achieved using infrared light. Subsequently, the thin film of the heater/sensor material (10nm Ti/100nm Pt) is electron beam evaporated over the frontside, the composition depends on the application of these devices, see section 2.3. The lift-off process defines the metallic heaters and temperature sensors. In a second photolithographic process in the front side the heater/sensor elements are capped with a 150nm Al_2O_3, deposited by e-beam evaporation. After this second lift-off, the wafer is annealed in a furnace for several hours at high temperatures (currently 925-975 K), in order to thermally stabilize the metallic elements. The annealing temperature depends on the metallic heater; being smaller for thinner layers of Pt.

[1]The chromium mask was fabricated in Photronics, with e-beam lithography. The design of these masks is made with a CAD program.

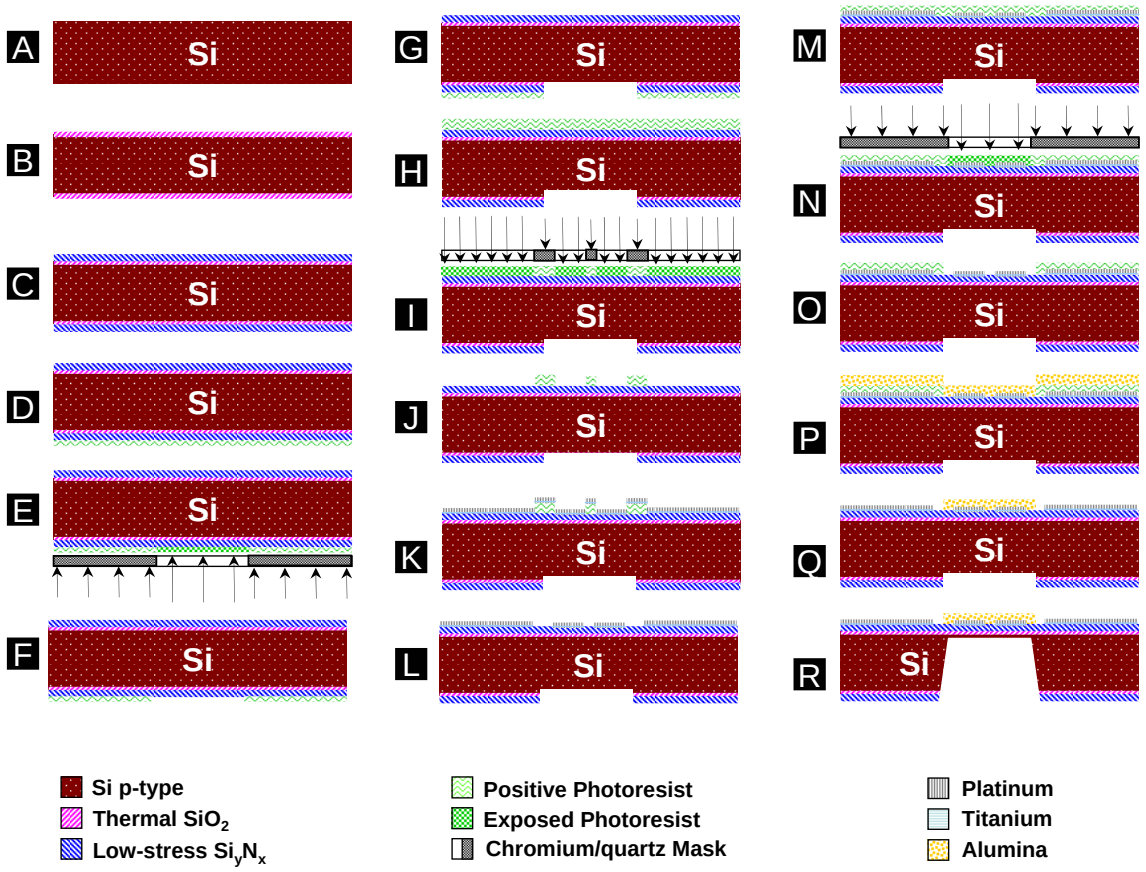

Figure 2.2: Nanocalorimeters microfabrication process.
A: Original Si p-type wafer; B: Oxidation forming 50nm SiO_2; C: Coating with 180nm of Si_xN_y by LPCVD; D: Photolithography preparation, coating the backside with positive photoresist; E: Exposure to UV light with a chromium/quartz mask; F: Exposed photoresist removed with developer; G: Plasma etch in SF_6 of the backside to exposure the underlying silicon; H: Photolithography preparation, coating the frontside with positive photoresist; I: Exposure to UV light with a chromium/quartz mask, the alignment with backside achieved using IR light; J: Exposed photoresist removed with developer ; K: E-beam evaporation of the metallic film in the frontside; L: A lift-off process patterns the metal elements that conforms the heater/sensor; M: Photolithography preparation, coating the frontside with positive photoresist; N: Exposure to UV light with a chromium/quartz mask, frontside alignment; O: Exposed photoresist removed with developer; P: Electron beam evaporation of the alumina layer in the frontside; Q: A lift-off process patterns the alumina capping layer; R: The KOH attack opens the channel leaving a 5 μm Si layer beneath the free-standing membrane of Si_xN_y;

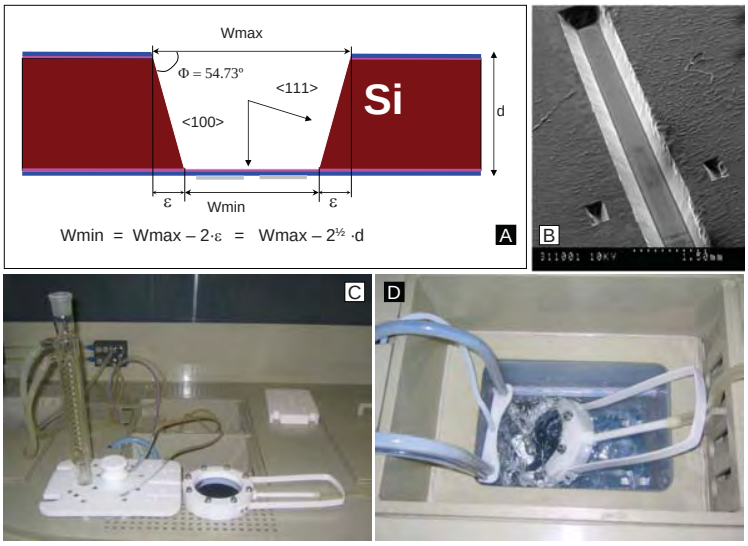

Figure 2.3: The KOH etching process.
A: Schematic showing the KOH anisotropic etch, where the anisotropy ratio between etching rates of planes ⟨100⟩or⟨110⟩and planes⟨111⟩is around 400, showing the trapezoidal profiles of the channels; B: SEM detail of the channel; C: View of the chemical bench and the custom-built chamber to protect the frontside of the wafer during the KOH attack; D: Vertical view of the chamber with a wafer inside a hot bath of KOH. (CNM)

Using a special wax and a Teflon custom-built chamber to protect the metallic elements in the frontside, the wafer is dipped in the KOH solution (30% by weight in water at 353 K), see images C and D in figure 2.3. The KOH etches anisotropically the Si, with slower etching rates along the ⟨111⟩ planes, thus forming a trapezoidal cross section terminating on the SiO_2, (images A and B in figure 2.3), since the SiO_2, etching rate is much slower than the Si rate.

However, the wafer is controlled and removed from the etching bath when still remains a 5 microns Si layer below the membrane. This layer is removed in every calorimeter one by one in a later process, section 2.2.2, to avoid damaging the Pt heaters on the front side if an accidental rupture of a membrane occurs while in the KOH bath. Afterwards, the wafer is diced to obtain the individual nanocalorimeter. The wax is maintained during the dicing process to prevent the adhesion of pollution of the free-standing membrane with fragments of Si. The protective wax is then cleaned by dipping in toluene and isopropyl alcohol. Finally, the nanocalorimeters are cleaned carefully with a dipping sequence in acetone, isopropyl alcohol and DI water, drying with a nitrogen flow at low angles to avoid the breaking of the membrane.

2.2 The Membrane.

The main factor that makes these MEMS a suitable device for calorimetric purposes is the possibility to use the extremely thin free-standing membrane as a calorimetric holder. The thinner the membrane, the smaller will be the total addenda and the conduction losses through it. Although the membrane can be made of different materials, i.e: Si_3N_4, SiC, single-crystalline Si, Si_xN_y, in this research work we have mainly used amorphous Si_xN_y, due to its outstanding mechanical and thermal stability. With a proper control of the KOH etching, it is possible to make Si_xN_y membranes about 30 nm thick, although they are quite fragile and manipulation is often a limiting step. However, there are some drawbacks that do not make advisable to use these very thin membranes. The thinner is the membrane the lower is the electrical insulation that prevents the shunting of electrical current from the heater to the Si frame. Moreover, extremely thin membranes easily break due to the build up of compressive stresses during heating. Besides the thickness, the shape also contributes to strength the mechanical stability of the membrane in the range of temperatures and heating rates employed in the calorimetric measurements. As an excellent compromise, we find that a 180 nm Si_xN_y membrane assures the operability of our device up to 1250 K at ultra fast heating rates up to 10^5 K/s.

2.2.1 Thermomechanical inestabilities.

The original MIT long channel devices showed a cross sensitive effect, the membrane buckling, which adversely affects the measurement of resistance. The problem was first evidenced during an adiabatic measurement (see chapter 4) at high temperatures where we detected a sudden increase in the voltage output that could not be due to a real transformation. The large temperature gradient between the center of the membrane and the silicon frame induces considerable stresses because of the differences in thermal expansion between the membrane and heater, and may induce buckling and eventually the rupture of the membrane, as can be observed in figure 2.4.

The resistive heaters bonded to a substrate or to a membrane are very sensitive to strain, i.e. a small deformation will induce a change in the resistance. To measure the temperatures we use a Pt resistance deposited over the membrane, as a thermometer. Therefore if the membrane buckles a change in resistance will not be associated only to a temperature change:

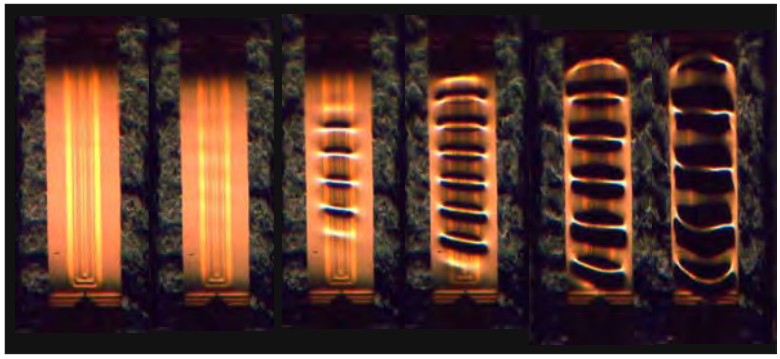

Figure 2.4: Sequence of caption of a buckled membrane.
Sequence of captions of the buckled membrane of the original MIT long channel devices for different input currents values feeding the U shape heater (increasing the current and therefore the temperature from left to right picture). The deformation of the membrane above 575 K was evidenced both under high heating rates and in steady state conditions. The membrane was illuminated from the back and the dark and bright colors correspond to different reflection shadows, giving idea of the membrane deformation. The captions shows how the thermal buckling increases for higher temperature values which resulted from the existence of high compressive stresses along the longitudinal direction.

$$R\left(T\right) = R_0\left(1 + \alpha \cdot \left(T - T_0\right)\right) + R(\varepsilon) \tag{2.1}$$

where $R\left(T\right)$ and $R_0\left(T\right)$ are the resistances at temperatures T and T_0, respectively, and α is the temperature coefficient of resistance (TRC). The $R\left(\varepsilon\right)$ is the contribution to the resistance of the deformation and will be dependent on each tensile state of the membranes. The deformation component will disturb the measurement and should be avoided, allowing a proper calibration of the resistance with temperature. Therefore, a constraint to fabricate a highly sensitive and reproducible nanocalorimeter is to ensure an excellent mechanical stability during heating.

Figure 2.5 shows the resistance change as a function of time when a constant pulse of current is injected into the heater. The dashed line corresponds to a long-channel microreactor, original MIT design (membrane dimension: 14 mm-length, 0.7 mm-width and 1 μm-membrane thickness). The highly nonlinear behavior is due to the deformation of the membrane/heater and illustrates the influence of the design on the mechanical response of the membrane. Obviously, as has been presented above, the deformation largely modifies the close to linear RTD characteristics of the Pt/Ti resistor and renders impossible the effective use of the microreactor as a high sensitive nanocalorimeter. To avoid mechanical

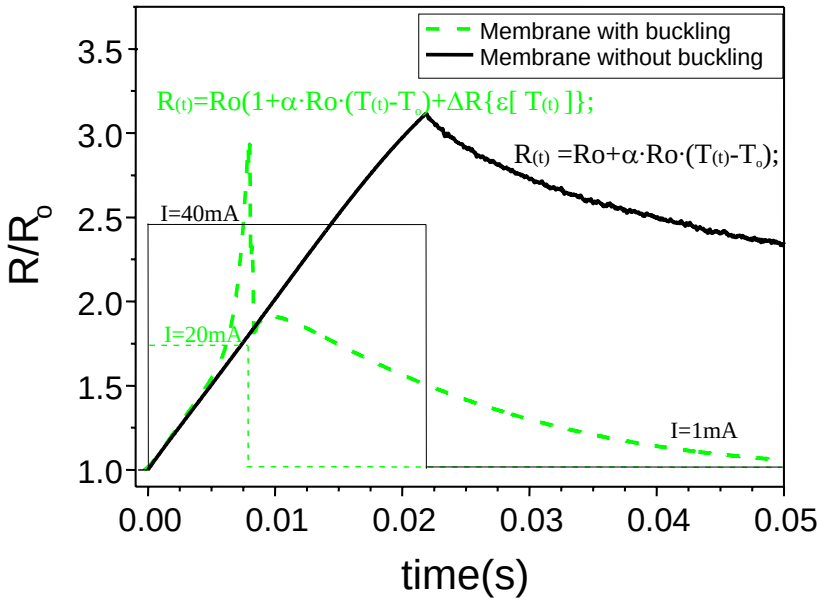

Figure 2.5: The buckling problem.
Relative resistance change as a function of time after injection of a current pulse. The dashed and continuous lines correspond to different membrane shapes designs. The dashed curve corresponds to the response of a nanocalorimeter with buckling effect. The sensing resistance binded to the membrane changes its shape modifying the effective resistance in a value $R(\varepsilon)$, disturbing its use as RTD. The black line corresponds to the optimized design, were this effect is suppressed.

problems, the geometry of the membrane was redesigned reducing the channel length and increasing the width with respect to former designs[25]. The continuous line is obtained from the final design of the nanocalorimeters. The monotonic and reproducible increase of R vs. t makes these microdevices better suited to perform calorimetric measurements. The redesign of the membrane dimensions (rectangular shape with 2.5 x 3.5mm) significantly increase the critical stress load to induce buckling to higher values. However, to preserve a good mechanical stability it is also necessary to: i) have a slightly tensile stressed membrane, which is obtained through suitable deposition conditions. (The LPCVD Si_xN_y grown at 1125 K from dichlorosilane and ammonia has a value of 250 MPa.). ii) keep a large ratio between the sensing and the total membrane area, to prevent built up of stress due to the anisotropy induced by local heating. Moreover, in the new microdevices the addition of the alumina layer on top of the heater slightly modifies the pre-stress. Up to temperatures around 1200 K we have not observed mechanical inestabilities which means

the thermo-mechanical induced stresses are far below the yield stress for Si_xN_y. On the contrary above 1250 K we have evidenced a quick rupture of the membrane.

2.2.2 Membrane thinning.

Although we always start with the 180 nm thick Si_xN_y membrane, occasionally we have reached thicknesses around 30 to 50 nm. These thin membranes are quite fragile, and try to free all of them simultaneously in the wafer (it means remove all the Si beneath in the initial KOH attack) resulted in a non-successful process, since some of the membranes break and the KOH (30% wt at 353 K) squeeze through holes and destroy the frontside elements of the wafer. As was mentioned in section 2.1 to prevent this limiting step, during the wafer microfabrication we stop the KOH attack leaving a 5 μm Si layer. The surface roughness of the Si layer is typically high. Under the typical conditions of concentration and temperature, the KOH chemical etch is quite vigorous and creates hydrogen bubbles (Seidel's model [22]), which hinder the transport of the fresh solution to the silicon surface, causing a sort of micromasking and hillock formation.

The optimum selected process to remove the 5μm Si layer was found to be an attack at room temperature with KOH solution at 60% wt. To etch the individual nanocalorimeters a microdrop is leaved, with a micropipette, in the hole or channel defined in the silicon by the previous KOH attack. This attack typically lasts around 6-8 hours (the typical etching rate under these conditions for Si(100) is close to 0.5 μm/hr), and highly improves the smoothness of the final surface while not significantly affecting the SiO_2 layer beneath the Si since the etching rate of SiO_2 is smaller than 0.81 nm/hr [22]. The resulting surface after the attack is very flat, as can be observed in the AFM image, in figure 2.7. The level of stress depends on the membrane thickness and influences the resistance value of the heater. Therefore, a suitable control of the etch process is critical a point to obtain identical calorimetric cells with the aim to measure in differential mode.

From time to time after etching some Si pyramids remained at the bottom of the SiO_2 layer, see figure 2.6. Then we use a 48% HNO_3 + 50% H_2O + 2% HF solution to further etch these small Si pyramids leaving the surface membrane clean. To further reduce the heat capacity, the thin SiO_2 layer can be removed from the centre of the membrane by diluted HF etching, leaving a bare Si_xN_y surface. If some particular application demands increased sensitivity at low temperature it is also possible to reduce the Si_xN_y layer without perturbing the mechanical stability. This is achieved with a highly diluted dissolution of HNO_3 with a very slow etching rate to avoid increasing the fragility of the membrane. The

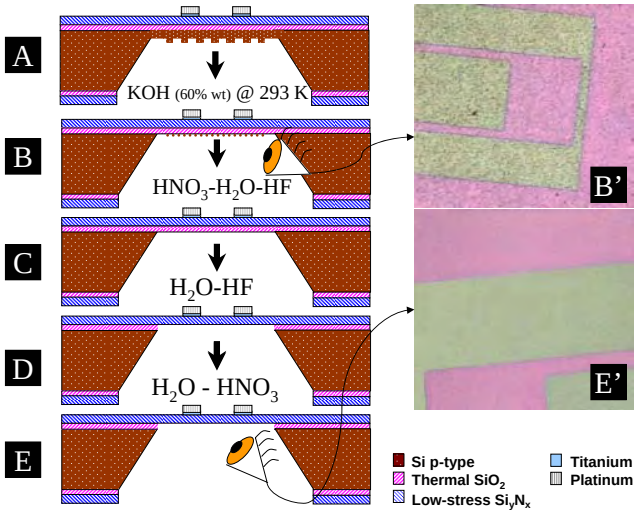

Figure 2.6: Schematics of the different chemical etching processes used to clean the membrane. At the top caption B' an optical microscopy image shows the Si pyramids on the membrane and at the bottom caption E' an image of the same membrane after the etching/cleaning.

initial heat capacity value at 323 K, obviously also depends on the heater design. The heat capacities before the SiO_2 layer is removed for both designs, the U-shape and serpentine-shape, are around 150 nJ/K and 1.1 μJ/K, respectively. After removing this layer Cp is typically reduced up to 130 nJ/K and 990 nJ/K, preserving the mechanical stability. Figure 2.6 shows an schematic drawing of the membrane thinning process. Exceptionally, the Si_xN_y of a couple of U-shape nanocalorimeters was reduced to reach a heat capacity of only 60 nJ/K at room temperature, which represents a 40% reduction with respect the initial heat capacity value. In the present work we have mainly focused on nanocalorimetric measurements at high temperatures, therefore no continued attempts to thin the membrane were explored.

The sensitivity of the quasi-adiabatic measurements largely depends on the differential signal between the sample and reference calorimeter, so the closer the heat capacity of both calorimetric cells[2] the better the energy resolution, see chapter 4. Inhomogeneities arising during the microfabrication process are the origin of small differences in heat capacities between the different devices in a wafer. One way to improve the similarity is by individual etching of the membranes, to realize an almost perfect twin calorimetric system. Figure

[2]The calorimetric cell is referred to the sum of the membrane in the sensing area plus the metallic elements plus the sample if it is present.

2.7, shows how by an appropriate etching procedure it is possible to exactly match the heat capacity of both calorimetric cells, the sample and reference. The red curve shows the heat capacity of the reference calorimetric cell (RCC) after a full etching treatment. In black, we see the as-built sample calorimetric cell (SCC), after the silicon pyramids cleaning. With the first etch the SiO_2 is removed, obtaining the green curve, and finally the Si_x N_y membrane is partially etch to equalize the sample calorimetric Cp value to the reference value.

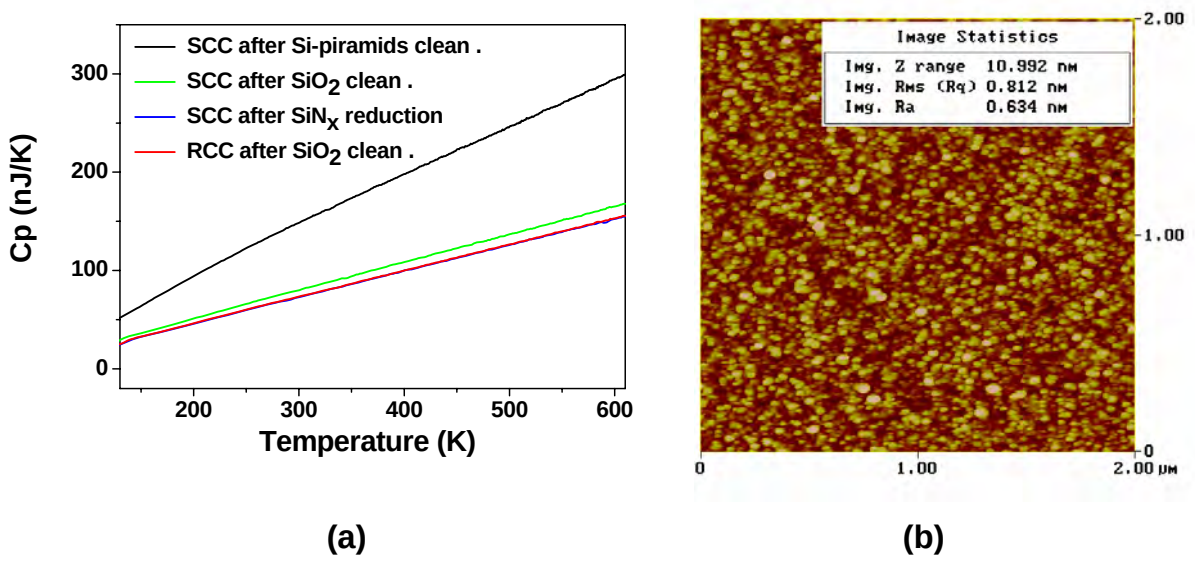

Figure 2.7: (a) The sample calorimetric cell heat capacity is matched to the reference calorimetric cell. Heat capacity vs. temperature curve obtained from quasi-adiabatic measurements for different membrane characteristics. (b) AFM image of the membrane after thinning process.

2.3 Heating/sensing elements.

The device operates like a bolometer. A pulse of current is introduced through the metallic heater, patterned on top of the membrane and the heat released by joule effect heats the calorimetric cell. The geometry of the patterned metallic elements, that dictates how the power is released, along with the thermal losses determine the map of temperatures in the calorimetric cell during a temperature scan. In the design of the heater/sensor we consider a correct choice of materials to ensure the thermoelectrical stability and sensibility in the measure, since this actuator is also used as a thermometer. There are several groups working on nanocalorimetry at low and moderate temperatures [16, 15, 13, 26], but extension to higher temperatures is a difficult task and remains to be fully explored. In this section, we review the important facts to be considered in order to obtain a proper high temperature thin film heater/sensor. In the literature it is possible to find high temperature ceramic heaters used in I.R. emitters MEMS, with a high thermal stability and long lifetime [27]. However, they are not suitable for calorimetry due to nonlinearities of the resistance with temperature and the small and negative TCR. By this reason, we focus our choice of materials in metallic heaters, and particularly in Pt based heaters, since they show a high TCR, linearity and the working range spans from 30 K to relatively high temperatures.

2.3.1 Materials.

The metallic element is used as a resistance thermal detector (RTD), using its resistivity dependence with temperature. The selection of the material should include several considerations but mainly regarding sensitivity and thermal stability that are summarized straight after:

In order to improve sensitivity, it is better to use a metal with high temperature coefficient of resistance (TCR) and low resistivity [28, 29]. Ferromagnetic materials like Ni and Co have high TCR, increasing the sensitivity, but the T(R) is less linear than other materials like Au or Pt, [30], furthermore they are not appropriate at high temperatures. Any unknown non-linearity in the resistivity or in the heat capacity variation with temperature in any of the microsystem physical properties renders difficult a correct interpretation of the calorimetric data. It is important to notice that in thin films the TCR decreases when decreasing the thickness. This behaviour marks a limit since a smaller Pt thickness reduces the heat capacity of the addenda but at the expense of reducing also the sensitivity of the device. In the low-to-medium temperature range a value of 50 nm has been found to be

the optimum [24, 25]. However, at higher temperatures the operation limit of thin metal lines is affected by the formation of pinholes and aggregation of Pt. These degradation processes are mainly driven by the high surface-to-volume ratio inherent to thin films and by electromigration at high current densities.

Another critical point is the thermal stability of the heater/sensor in the working temperature range. The electrical properties should also be stable to ensure a good reproducibility. Therefore, electromigration effects should be minimized. With high current densities the ions in the metallic net area have two forces (the electron wind and the electrical force over the ion) that increase their mobility in addition to the vibrational mobility due to temperature. This combination tends to degrade the metallic strips (see figure 2.8), and should be avoided, for a proper RTD use. Electromigration can be reduced, increasing the thickness of the heater to limit the current density, although at the expense of increasing the heat capacity of the calorimetric cell, decreasing the signal-to-noise ratio. Depending on the operative temperature range the heater material may change, to find a good trade-off between the above mentioned points.

Previous works [11, 31] have shown that a platinum deposition of 100 nm with a 10 nm thick Ti adhesion layer, is a good option that provides adequate thermal stability for prolonged expositions to high temperatures and a constant temperature coefficient of resistance. This combination works well until 1070K, where a 3% variation of the resistance at room temperature is observed after 200 minutes of hold test [31]. The degradation can be estimated through the change on the resistance at room temperature. For thinner films the limits of the temperature range decrease with the thickness. From the point of view of TCR, for a 100 nm Pt/ 10 nm Ti layer, the electrical dependence of the resistance with temperature is linear up to temperatures around 900K, following equation 2.5, with a TRC of $2.86 \cdot 10^{-3} K^{-1}$, slightly slower than the typical value for bulk Pt, $3.85 \cdot 10^{-3} K^{-1}$[11]. The difference can be explained due to thin film effects [32], the polycrystalline structure of the metal deposition and the possible intermetallic formation with the Ti adhesion layer. Several combinations using Pt as a heater element and Ti as adhesion layer were tested, i.e. 50nm Pt/20nm Ti, 75nm Pt/10nm Ti, 100nm Pt/10nm Ti and 150nm Al_2O_3/100nm Pt/10nm Ti. The combination with the minimum contribution to the heat capacity of the calorimetric cell was 50 nm Pt with 20 nm Ti as adhesion layer. The measured TRC was $2.0 \cdot 10^{-3} K^{-1}$ and the useful operation temperature in adiabatic mode spans from 77 up to 700 K. At higher temperatures this heater combination degrades dramatically, see figure 2.8. In power compensation mode the maximum working temperature is lower, since

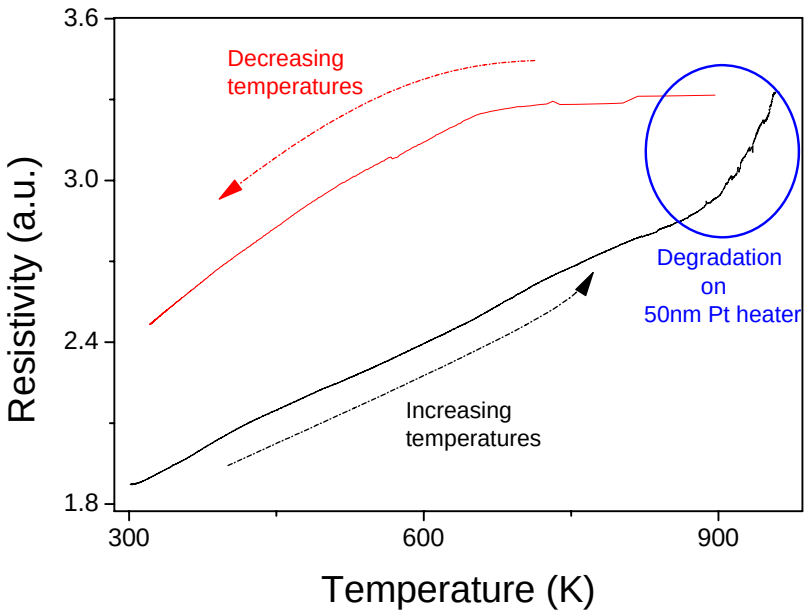

Figure 2.8: Degradation of the Heater material.
Resistivity measurement in a 50nm Pt + 20nm Ti thin film as function of the temperature. The degradation of the film heater, doubles the resistance at room temperature. The measurement was performed with a custom four probe instrument that uses a holder of a Perkin Elmer DSC to heat, controlling the temperature with a computer through a PI controller via GPIB.

a constant current is hold to heat the calorimetric cell during longer periods, therefore increasing the degradation through electromigration and agglomeration. With a thickness of 75nm Pt and using a 10nm of Ti as an adhesion layer, the operative range increased up to 850 K with a TRC of $2.4 \cdot 10^{-3} K^{-1}$.

Work performed by Jensen's group et al at MIT [31] have shown that growing a 150nm Al_2O_3 capping layer on top of the 100 nm Pt/10 nm Ti heater spans the working range towards higher temperatures. By using this approach in our devices reproducible scans could be performed in quasi-adiabatic or pulse-heating mode up to 1250 K [25], 250 K higher than without the capping, and up to 950 K in the power compensated or continuous mode. This improvement shows that the alumina prevents the agglomeration of Pt since one of the driving forces is the oxidation of the Ti layer beneath Pt, loosing the property of adhesion layer. E-beam evaporated Pt layers typically show a high granularity and therefore the grain boundaries are preferential paths for oxygen diffusion into the Ti layer. The alumina

layer not only prevents the oxygen diffusion through the platinum but also serves as a physical structure that prevents the platinum drift by electromigration. Electromigration is a concern since to attain the high heating rates in adiabatic measurement high current densities of the order of $2 \cdot 10^5 \mathrm{A}/cm^2$ are required.

Other materials have been tested in order to increase the operative range to upper temperatures. Tungsten with a chromium binding has been probed, but the TRC was too small decreasing the sensitivity due to its oxygen affinity at high temperatures.

Most of the results presented in this thesis have been carried out with the 100 nm Pt/10 nm Ti heater with the 150 nm of Al_2O_3 as a capping layer. This heater/sensor increases significantly the average lifetime operating under the fast heating/cooling cycles (heating: 40 ms, cooling: 200 ms) to 1200 K. Hundred of cycles could be run without change in the heater resistance, with an excellent reproducibility between them.

In the following table, we summarize the main characteristics of the different heater combinations, with average values.

Heater combination	50nm Pt + 20nm Ti	75nm Pt + 10nm Ti	100nm Pt + 10nm Ti	150nm Al_2O_3 + 100nm Pt + 10nm Ti
Operational temperature	77-700 K	77-850 K	77-1077 K	77-1300 K
RTC at 293K	0.0020 K^{-1}	0.00245 K^{-1}	0.00286 K^{-1}	0.0023-0.0024 K^{-1}

2.3.2 Heater Design.

A correct design of the heater is a key factor to obtain a flat temperature profile in the sensing area. A uniform temperature distribution across the membrane is required to simultaneously ensure the phase transition in the whole sensing area, improving the signal to noise ratio. Complex deconvolution procedures should be used if the difference in temperature within the sample area is large. Strip type heaters, like those used by Allen's group, give a suitable profile at fast heating rates, but an isotropic introduction of heat in the sensing area and the thermal link of the wide platinum wire with the Si frame tends to produce marked parabolic profiles in steady state preventing those devices to be used at lower heating rates. An U-shape design of the heater [33] gives a M shape profile in the sensing areas, but with the presence of a thermal layer, the temperatures gradient can be drastically reduced.

Several designs have been studied and experimentally tested. Here we present the two designs with the better performances. The first design is based on the U-shape geometry of the original MIT microreactor. The serpentine-type heater design is introduced to improve the temperature profiles during transient without the necessity to include a thermal layer and to guarantee a constant sensing area independently of the heating rate.

2.3.2.1 U-shape heater.

First, following the original design of MIT microreactors we worked with an U-shape heater due to its versatility to perform both adiabatic and power compensation measurements. The design of the U-shape heater consists basically on two symmetric strips (1.20mm long, 0.05mm wide) introducing power in the calorimetric cell. Through the heater lines, see b in figure 2.9, a pulse of current is applied (with values in the mA range). By means of the two voltage probes, see a in figure 2.9, the voltage drop in the sensing area is measured in a four-point mode. Following the same structure in order to measure over spatial isotherms, a sensor is placed between these strips. To use the sensor a bias current is introduced through d, and c is used to measure the voltage. A typical value of this current is around 250 μA, a compromise between the maximum that prevents self-heating and the minimum value that allows a low noise electrical measurement. Along this research work the sensor is only used to check the temperature profiles, providing with crucial information to model the temperature distribution within the nanocalorimeter membrane.

The shape of the heater, specially the width of the metallic strips, is critically linked with the thickness and the resistivity of the heater material. The initial transient in adia-

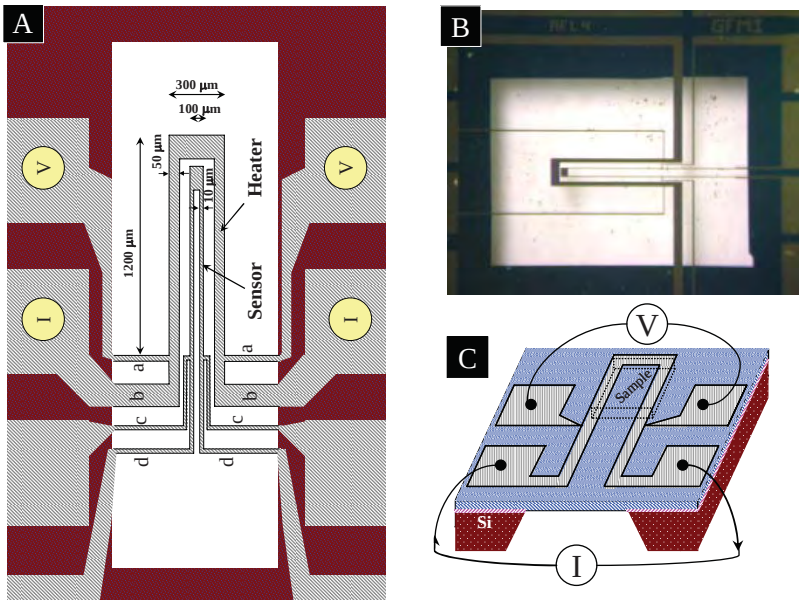

Figure 2.9: U-shape heater.
(A) U-shape design layout. (B) Photograph of the final device with U-shape heater. (C) 3D view of the nanocalorimeter.

batic measurement depends on the impedance accommodations [14]. In the MIT original design non desirable overshoots were recorded. To avoid the presence of spikes in the data, a correct value of the heater resistance is around 100 Ω.

Temperature modeling (U-shape heater).[3]

One essential step in the design process in order to improve the heater/sensor characteristics is to model the thermal behavior of the device during the heating ramps. Due to the high heating rates used in adiabatic conditions a two dimensional modeling in the plane perpendicular to the membrane was initially conducted to determine the temperature gradient across the thickness of the amorphous Si_xN_y membrane. The results indicate that because of the small thickness (180 nm) of the membrane the temperature difference between heater and sample is lower than 0.02K at heating rates closed to 10^5K/s. Therefore, we assume the temperature does not depend on the vertical coordinate and that the system can be treated as 2D in the plane of the membrane. To carry out the difference-finite model the device was divided into discrete volume elements (265x86) and an energy balance across each element was applied to define the equation of state for each one. Only

[3]Part of this section appears in [34]

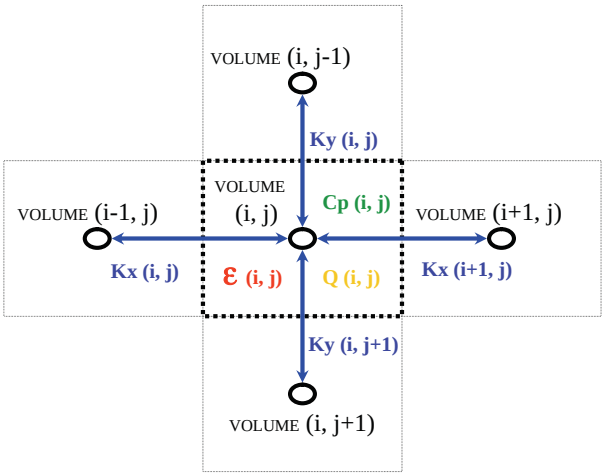

Figure 2.10: Mesh schematics.

conduction and radiation have been included since the experiments are typically carried out in high vacuum. Under this assumption the equation of state has the form:

$$\rho \cdot C_P \cdot \frac{\partial T}{\partial t} = Q_{Pt} + \nabla \cdot (K \cdot \nabla T) - \varepsilon \cdot \left(T^4 - T_0^4\right) \tag{2.2}$$

where T is the temperature, T_o the room temperature, t the time, ρ is the density, C_p the heat capacity, Q_{PT} the power introduced by the Pt heaters, K the thermal conductivity, ε the constant for the thermal radiation , for each one of the volumes in the mesh.

The differential equation 2.2 is rewritten in the centered finite difference approximation for the second order spatial and temporal derivative. Due to the discretization in the solution method, we only consider the four closest neighbours of a given volume element, in the matrix array ij, using the five point formula [35, 36]. The formula is directly extracted from the Taylor expansions around $T^n_{i,j}$, where n is the time index and i and j are the spatial indexes.

$$\begin{gathered}\rho_{(i,j)} \cdot C^t_{P(i,j)} \cdot \left(T^{t+\tau}_{(i,j)} - T^t_{(i,j)}\right) = \\ Q^t_{(i,j)} \cdot \tau - \left\{K_{X(i,j)} \cdot \frac{\left(T^t_{(i-1,j)} - T^t_{(i,j)}\right)}{\triangle x^2} + K_{X(i+1,j)} \cdot \frac{\left(T^t_{(i+1,j)} - T^t_{(i,j)}\right)}{\triangle x^2}\right\} \cdot \tau - \\ - \left\{K_{Y(i,j)} \cdot \frac{\left(T^t_{(i,j-1)} - T^t_{(i,j)}\right)}{\triangle y^2} + K_{Y(i,j+1)} \cdot \frac{\left(T^t_{(i,j+1)} - T^t_{(i,j)}\right)}{\triangle y^2}\right\} \cdot \tau - \varepsilon_{(i,j)} \cdot \sigma_{SB} \cdot \left(T^{t\,4}_{ij} - T_0^4\right) \cdot \tau\end{gathered} \tag{2.3}$$

Electrical heating is introduced by a power matrix $Q^t_{(i,j)}$that considers the contribution

of each volume element and is calculated from the input current density, J, which takes into account the specific heater design.

$$Q^t_{(i,j)} = \rho_{r^o(i,j)} \cdot J^2_{(i,j)} \cdot \left(1 + \alpha \cdot \left(T^t_{(i,j)} - T_O\right)\right) \tag{2.4}$$

where $\rho_{r^o(i,j)}$ is the resistivity matrix at T_O. The resistivity of the Pt film was experimentally determined from previous calibration measurements finding a value of $2.54 \cdot 10^{-7}$ Ω·m.

Bulk silicon frame is an efficient heat sink, due to its high thermal mass, and therefore we fixed the temperature of the frame to room temperature during simulations. It can be considered as a Dirichlet constriction over the value of the function temperature in the boundary volumes. This system of differential equations is solved from all the elements for a series of time increments that provides the temperature profile distribution throughout the device as a function of time. Although subject to stability considerations (Courant stability conditions) [37] the explicit approach was chosen over the implicit scheme to attain a fine resolution in the time step to analyze transient effects. This way, the need for matrix inversion at each step is eliminated. A constant time step of 1 ns was chosen to ensure stability for the volume elements used. It depends strongly on the spatial mesh resolution selected.

When different layers (Pt heater, Si_xN_y membrane, thermal plate and/or sample) are aligned in the same volume element, effective parameters (specific heat, resistivity, emissivity and thermal conductivities) are calculated assuming a linear independent contribution from each layer. The effective values are expressed as $(k_T, C_T) = (\sum_i (k_i, C_i) \cdot e_i) \diagup \sum_i e_i$; where e_i is the thickness of the different layers. The individual parameters were initially taken from the literature data [11, 38, 39, 40, 41, 42]; however as the thermal conductivity of the silicon nitride membrane is uncertain and highly dependent in processing conditions [43], they were subsequently refined during modeling to achieve a good fitting between experimental and calculated data. Values used in the modeling are shown in the table 2.1. Subsequent measurements of thermal conductivity of silicon nitride by using the 3ω techniques have reached similar values to the we reported in this work [44].

	k ($\frac{W}{m \cdot K}$)	C_p ($\frac{J}{g \cdot K}$)	Reference
Pt	73	0.132	[42, 39]
a-Si_xN_y	2.6 3.2	0.7	this work [40]
SiO_2	1.5	0.87	[39]
Ag	420	0.237	[39]
Al_2O_3	8	∼1	[39], this work.

Table 2.1: Thermal conductivities and heat capacities at room temperature of the several materials forming part of the nanocalorimeter.

The temperature profile across the channel was measured at the heater location and at the sensor placed 100 μm inside the heater loop. To compare with the measured values the average temperature from simulations along the longitudinal direction of the heater and sensor was extracted. We first compute the thermal profile in steady state for different constant input powers and fit them to the heater and sensor temperatures to obtain the effective thermal conductivities and emissivities. Figure 2.11 (a) shows the steady-state profile in the microreactor channel for 4 different heating powers. As has been already shown for the 1 μm thick Si_xN_y membrane [33], the parallel heater configuration shows an almost flat temperature profile in the temperature range up to 550 K. Our data shows that for a 180 nm thick membrane the temperature variation is around 10 K at 550K.

Decreasing the thickness of the membrane will reduce the heat capacity of the addenda but simultaneously will slightly increase the thermal gradient, since reducing the membrane thickness to a half is approximately equivalent to reducing the membrane thermal conductivity by a factor 2. The thermal conductivity value of the 180 nm amorphous silicon nitride membrane obtained from appropriate fitting of the experimental data is 2.6 W/m·K. The influence of radiation losses in the temperature range analyzed did not contribute significantly to the thermal profile.

In the symmetric heater design, the heat is delivered only at the edges of the sample region with no heat supplied at the center. Therefore, since conduction is the main mechanism of heat transfer, if the heating rate is fast a temperature minimum will be present in the center of the membrane between heaters, inducing a significant temperature difference. With increasing heating rate the temperature difference between heater and sensor increases as represented in figure 2.11 (b) for three different current pulses. The continuous lines in the figure account for the simulated values using the parameters obtained from the

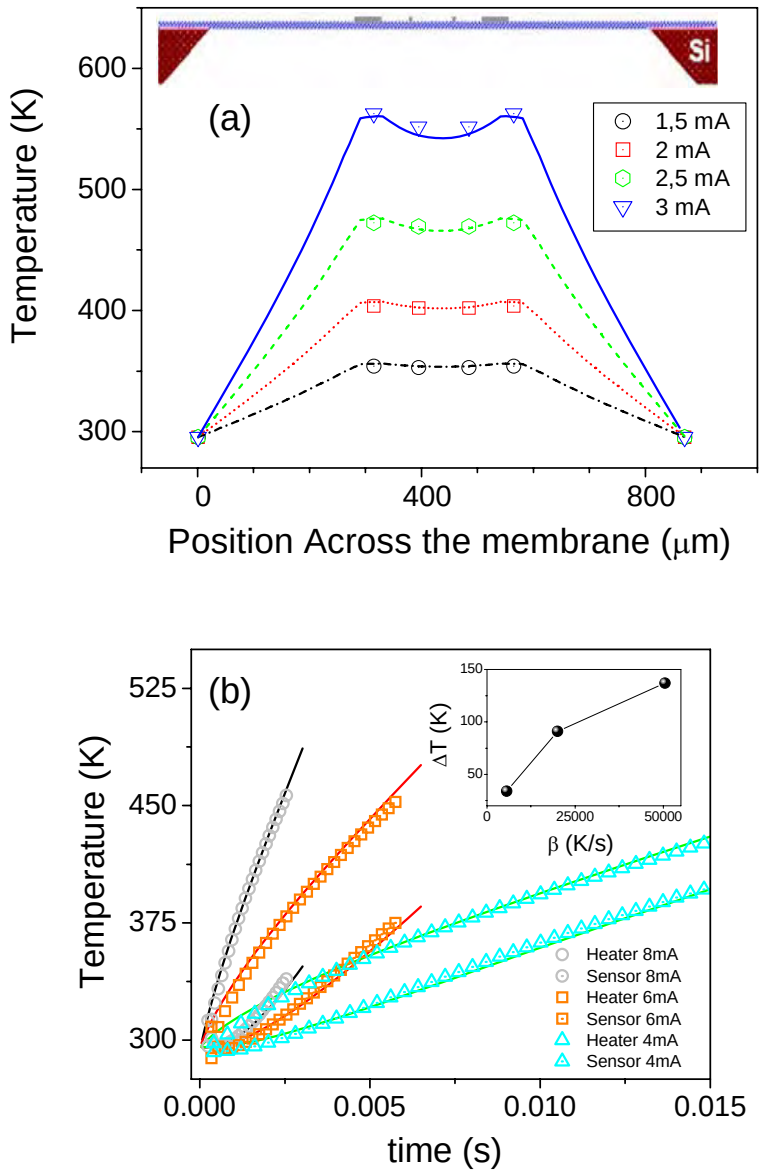

Figure 2.11: (a) Steady-state temperature profile at different input powers as a function of the position across the membrane. The symbols correspond to experimental data obtained at the heater and sensor locations. The continuous lines represent the simulation results. (b) Heat and sensor temperatures at three input currents i: 8mA; ii: 6 mA; iii: 4 mA. The symbols represent data at different input current, continuous line is the simulated data with the parameters obtained from steady-state. Inset: Maximum temperature difference between heater and sensor as a function of heating rate. The line is only a guide to the eye.

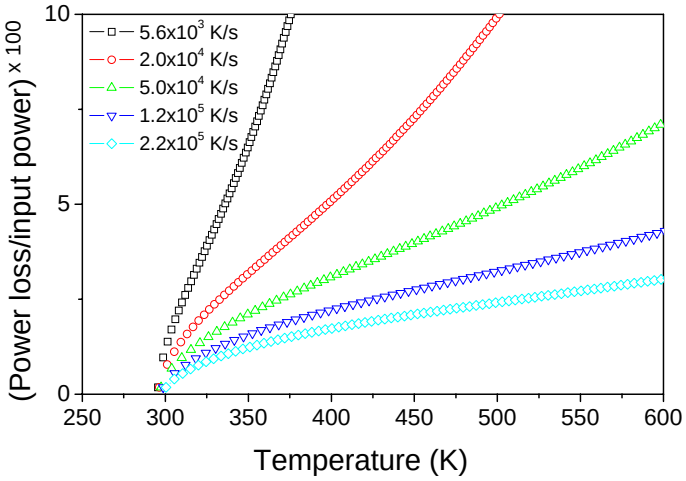

Figure 2.12: Power loss percentage as a function of temperature at different heating rates.

steady-state solution and the effective heat capacity. The inset shows the temperature difference as a function of heating rate. A substantial improvement in the temperature uniformity can be attained at slow heating rates. However, the high gradient observed at high heating rate shows that the isothermal area in the sensor, i.e. the sensing area, is drastically reduced to the area beneath the heater, as will be shown in section 4.2 . The reduction of the effective sample area was the driving force towards a new heater/sensor implementation.

As shown in figure 2.12, due to the specific design of the nanocalorimeter heat losses through conduction to the frame and radiation represent a small fraction of the total input power and only become significant for slow heating rates. At heating rates of $5{\cdot}10^4$ K/s power losses are around 6% at 600K, (figure 2.12). This behavior allows the nanocalorimetric measurements to be considered quasi-adiabatic in this temperature range. Small heat capacity corrections can be applied to account for these losses as we will present in the chapter 4.

As will be explained in detail in chapter 5, when a thick film sample is placed on the membrane the temperature profile may improve depending on the thermal conductivity of the sample. This fact promotes a variation in the conductive losses through the membrane with a corresponding change in the thermal resistance of the sample calorimetric cell, and complicates accurate differential measurements. This problem and simultaneously the temperature difference across the membrane can be significantly reduced by incorporating a thermal conducting layer at the center of the membrane on the channel side. The thermal

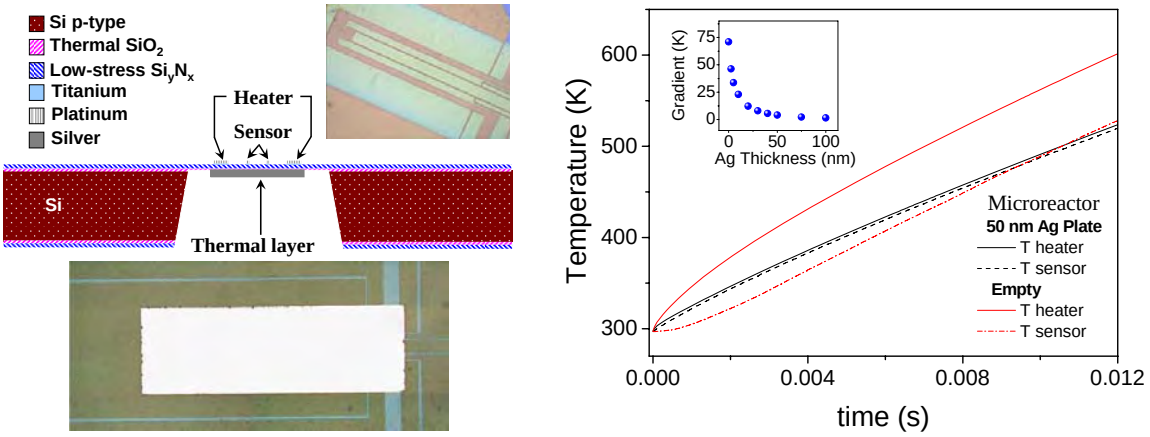

Figure 2.13: Thermal gradient reduction with deposition of a thermal plate.
A schematic figure in cross section of the thermal plate and the photography shows the correct location of this layer in the center of the membrane. The plate makes a contribution to the transversal conductivity in the sensing area assuring a flat profile, with an small contribution to the conduction losses through the Si frame. The graph shows experimental data of temperature vs. time at the heater and sensor location for the bare membrane (red) and with 50 nm Ag plate (black). The inset shows simulated values for the variation of the temperature gradient with the thickness of the Ag plate at a heating rate of $2{\cdot}10^4$K/s. (see section 2.3.2.1)

layer serves to conduct heat more evenly and faster across the surface. This effect can be evaluated by checking the improvement of the temperature difference between heater and sensor at fast heating rates. Figure 2.13 shows the effect of adding a 50 nm thermal Ag plate on the heater and sensor temperature measured for a current pulse of 8 mA. The inset of figure 2.13 shows simulated values of the temperature gradient as a function of Ag thickness at a heating rate of $2{\cdot}10^4$K/s.

As the addition of the conducting layer increases the heat capacity of the nanocalorimeter we reduce the membrane thickness by etching with a chemical etch diluted dissolution of HNO_3 (see section 2.2.2) to partially compensate this effect and improve the sensitivity. A typical value of heat capacity at room temperature of an empty nanocalorimeters is 100 nJ/K. This value is reduced to 60 nJ/K after etching for 30 min at a rate of 1 nm/min. After deposition of the 50 nm Ag plate in the central part of the channel the heat capacity at room temperature rises to 200 nJ/K.

Figure 2.14 shows the steady state temperature profile of a bare membrane and a membrane with 150 nm of Ag as thermal plate, after injection of a 2.5 mA current pulse. The

profile is drastically improved, although the thermal resistance increases sligthly, requiring higher power to reach the same average temperature. Then if a sample is placed inside the area covered by the thermal layer, it will not change the thermal resistance since the thermal profiles outside the sensing area will remain constant.

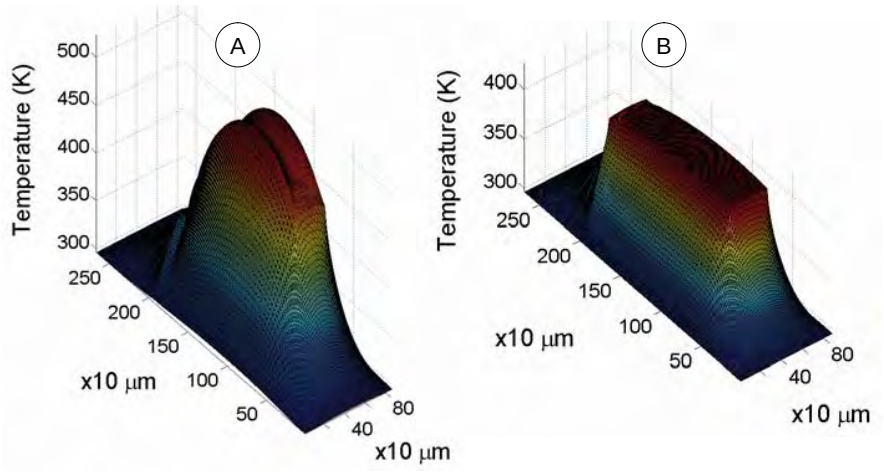

Figure 2.14: 3D surface plot of temperatures map over the membranes as a result of an input current of 2.5 mA. (A) a bare membrane. (B) membrane with 150nm Ag plate.

The transient evolution of temperature profiles in the membrane can be observed through a series of surface plots of these temperatures at different times. In figure 2.15, the influence of the heating rate, is evidenced through the surface plots at a given measured temperature for different heating rates. We can observe that the reduced sensing area is limited to the area beneath the two strips. Adiabatic measurements are possible since the temperature differences in the sensing area are less than 20K at high heating rates, but the amount of sample analized is small, decreasing significantly the thickness sensitivity.

With the addition of a 150nm Ag thermal plate we can recalculate the same curves, see figure 2.16. The map of temperatures clearly changes with an increase of the sensing area at high heating rates, but unfortunately this occurs at the expense of an increase in the temperatures differences in this region. This inhomogeneity will produce an artificial widening of the experimental peaks. This behaviour will be further explained in section 4.2, for the case of the melting transition in ultra-thin films of In.

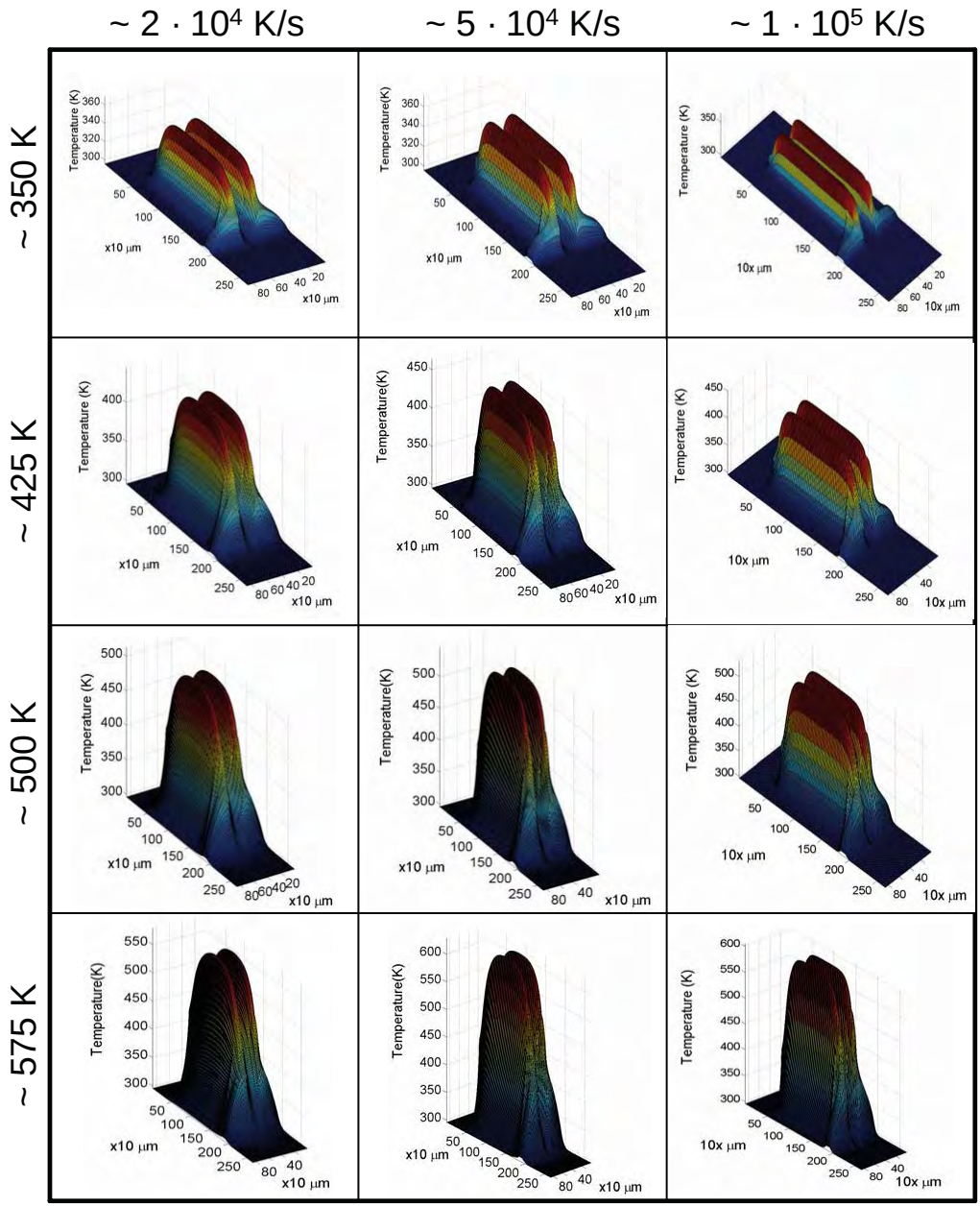

Figure 2.15: Transient temperature maps of bare membrane.

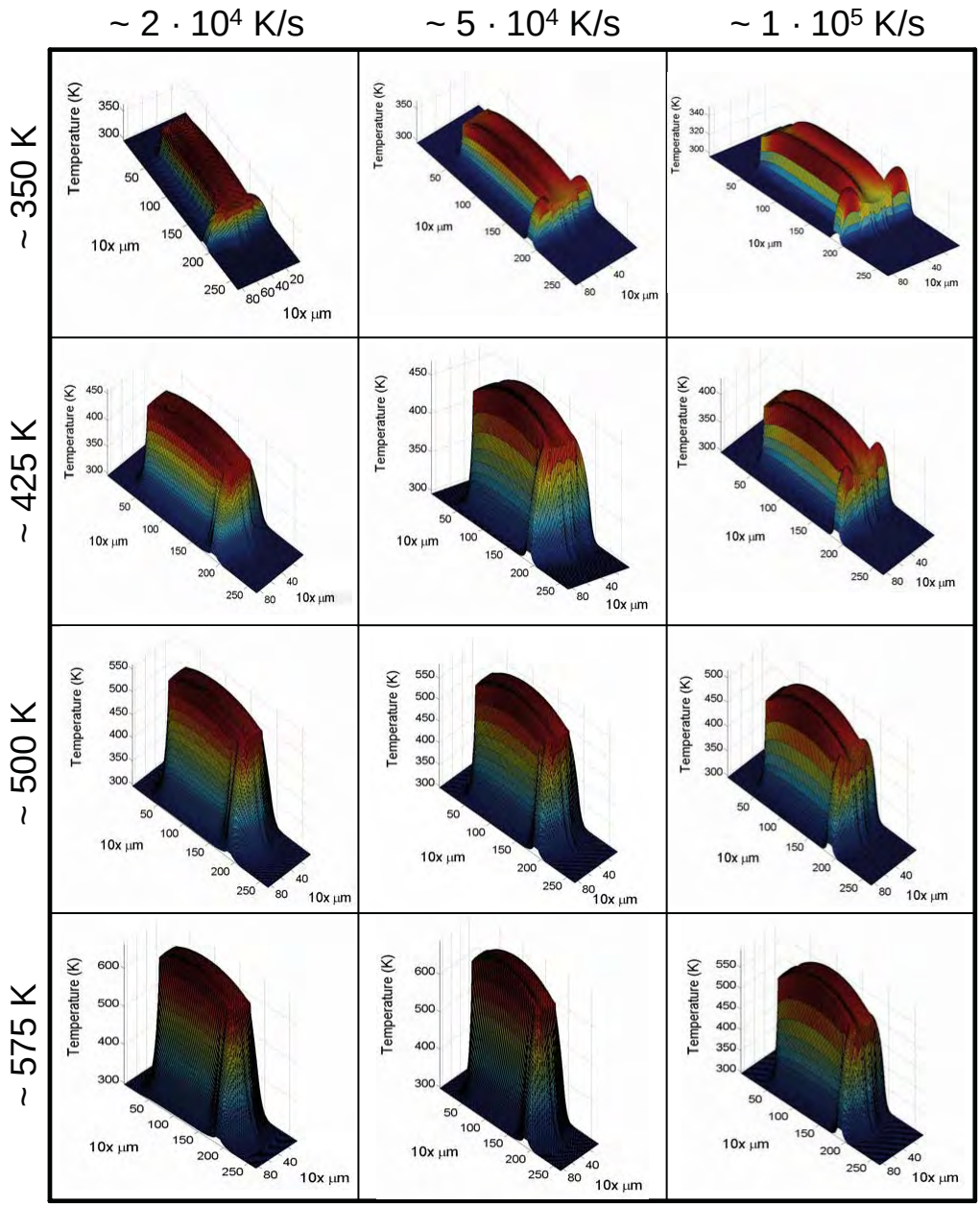

Figure 2.16: Transient temperature maps of a membrane with 150nm Ag.

2.3.2.2 Serpentine-type heater.

With the aim to improve the difficulties found in the U-shape heaters, we designed the serpentine-type heater. It essentially conserves the proportions in the membrane of the U-shape in order to preserve the mechanical stability, but it is designed to introduce the power almost isotropically to increase the sensed area. One of the conclusions of the modelling for the U-shape design is that at high heating rates only the sample deposited beneath the heater is sensed properly. This sensing area can vary with the heating rate and a thorough calibration should be performed to overtake this problem. The serpentine-type is thought to maintain a constant sensing area in the centre of the cell, solving this problem.

As was explained in the introduction of this section, an isotropic release of the heating power in the calorimetric cells tends to produce parabolic profiles, like in the strip heater. The thermal modeling of a strip design shows that this effect is amplified by the platinum wires that connect the heater with the contact pads placed in the frame. To circumvent this problem, we have redesigned the heater with the aim to improve the temperature profiles both in the longitudinal and the transversal direction of the heater. We have divided the single strip, that releases the heat isotropically, in three parallel strips. The two strips in the borders (marked as b in figure 2.17) are slightly narrower than the centre one (marked as c in figure 2.17). The current flowing through the three strips is the same, but the power released per unit area is proportional to the current density. In the centre strip, the widest, the current density will be smaller and therefore it will release less power that in the borders correcting the parabolic tendency.

In the longitudinal direction, the direction parallel to the longest edge of the membrane, the main problem is to reduce the heat lost from the calorimetric cell to the Si frame through the platinum wires that connects the heater with the contact pads. We have included an extra section in the heater (marked as a in figure 2.17) that tends to heat the surroundings. Therefore the heat released to the frame remains constant though the major contribution is from the outer elements. By doing so the thermal profile in the longitudinal direction is widely corrected, although still remains slightly parabolic. As can be appreciated in figure 2.19, and also in the section 2.3.3 the differences of temperatures in the sensing area are low enough to allow nanocalorimetric measurements.

The width was optimized by thermal modeling, taking also into account the impedances in the final circuits. In this last step, the heater thickness is critically linked with the resistivity of the material and the width of the strip is the only free variable to be properly tuned. The heaters typically have a resistance of 25Ω, measured in the four probe config-

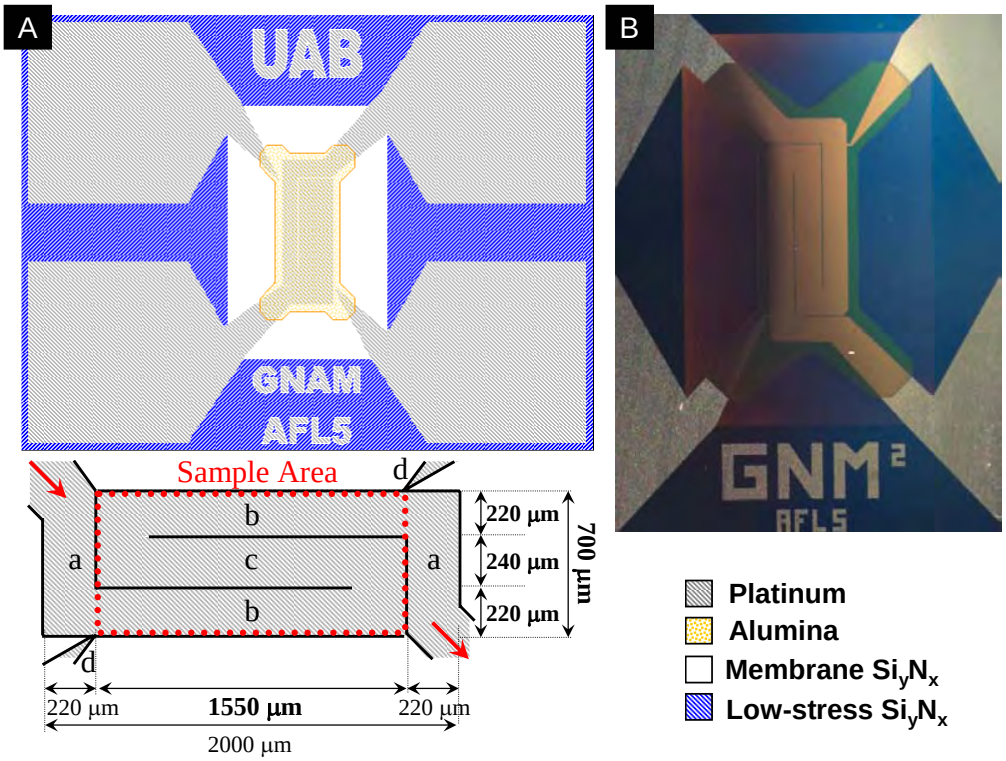

Figure 2.17: Serpentine-type heater layout.
(A) Schematics of the heater design. In the zoom can be appreciated the layout measures. The letters (from a to d) refer to the different heater zones to be identified from the main text explanation. (B) Plain view photograph of the nanocalorimeter membrane, where can be appreciated the platinum elements and the alumina capping this elements.

uration[4].

The serpentine-type heater conserves the good mechanical stability of the U-shape design while increasing the sensing area by having a more uniform temperature profile at fast heating rate experiments.

Temperature modeling (Serpentine-type heater). With the same difference-finite model used with the U-shape design, the thermal behavior of the serpentine-type heater was analyzed for the different heating rates used in the experiments. In this case, we used a mesh of 142x90 volume elements to define the 2D plane view of the total membrane, which gave us a plane resolution of 25x25 μm^2. The thermal conductivity of the Si_xN_y

[4]The two voltage probes are marked as d in figure 2.17.

membrane, was assumed to be equal to the obtained in the fitting of the previous modeling for the U-shape. The rest of the constant parameters were also assumed from the literature data, and are resumed in table 2.1.

The results of the modeling show the improvement of the temperature profiles and the increase of the sensing area. The thermal profile in the sensing area, remains almost constant for the different heating rates. As an example figure 2.18 shows the map distribution temperatures in the membrane at high temperatures during a fast heating rate of 10^5K/s. The sample area is delimited to the area where the temperature profile is almost flat, although the calorimetric cell also includes the surrounding. This fact provides a better estimation of the amount of mass measured independently of the heating rate as opposed to the U-shape heater, where the sample area was dependent on the heating rate.

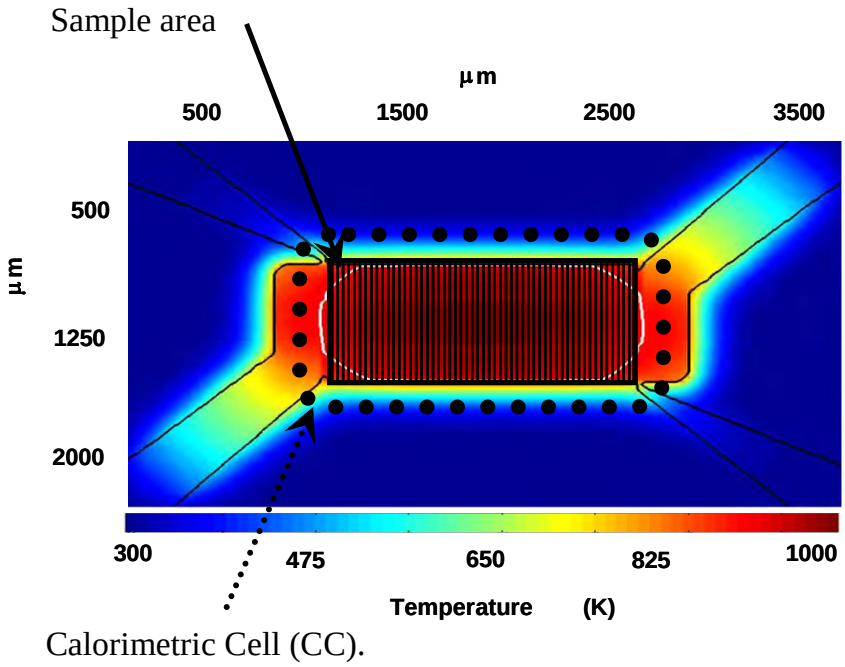

Figure 2.18: Serpentine-type heater modeling.
Temperature modeling for the serpentine-type design. Map of temperatures when it has been heated at 10^5 K/s. The stripped area marks where the sample is located. The dotted line marks the calorimetric cell.

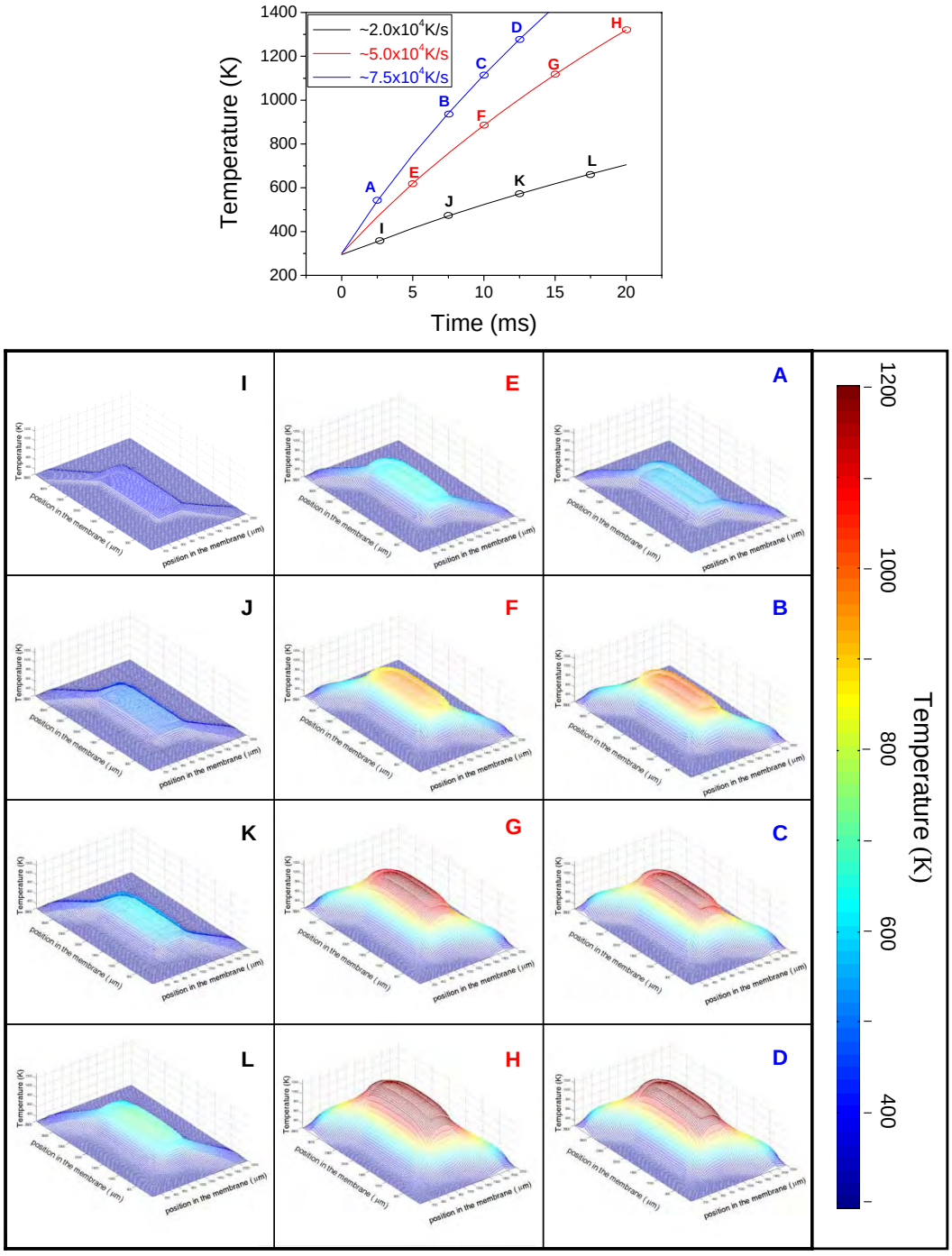

Figure 2.19: Serpentine-type heater modeling at different heating rates. The plot show the temperature vs. time modeled response of a serpentine-type nanocalorimeter for different heating rates. The 3D temperature maps correspond to the snapshots at the different points in the curves.

A precise knowledge of the temperature profiles is necessary in the temperature calibration process as we will see in section 2.3.3. In the serpentine-type design, the dependence of the temperature profile with the heating rate is clearly smaller compared with the U-shape design. Figure 2.19 show the simulated response of the serpentine-type when it is forced to attain different heating rates. In the temperature snapshots it is possible to appreciate while within the slightly parabolic tendency the temperatures in the membrane are quite flat. In next subsection we will see how this temperature difference can be estimated from the full-width-at-half-medium of the melting peaks of a well known standard material like Aluminum.

The temperature profile has been checked with an infrared camera at atmospheric pressure and steady state. Several IR images were collected when the heater was fed with different injected currents, figure 2.20. Unfortunatelly, the refresh time of the CCD was too slow to permit the images acquisition during the transient heating. Nevertheless, from this experiment we can know the contribution to emissivity of infrared spectra (0.05-0.07), and get a qualitative image of the temperature maps in the membrane (since calibration of the camera did not permitted a fully quantitative analysis). The homogeneity of temperature distribution in the calorimetric cell for different average temperatures (measured from the electrical resistance) is evidenced.

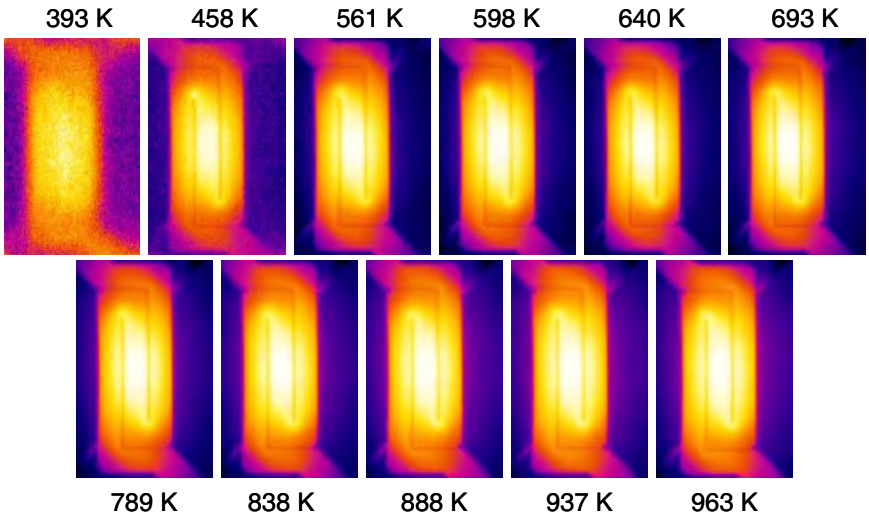

Figure 2.20: Infra-red pictures of the serpentine-type heater, at different steady state temperatures in air.

2.3.3 Temperature Calibration.

The average temperature in the calorimetric cell is measured through the temperature dependence of the metallic heaters resistance. In metals the electrical resistance is related with the interaction between electrons and phonons, and the rise of temperature implies an increase of interactions and therefore an increase of resistance. Pt was selected due to its linear response, however at high temperatures (over 900 K) a second order dependence becomes important. Its dependence can be described by:

$$R(T) = R_0 \left(1 + \alpha \cdot (T - T_0) + \beta \cdot (T - T_0)^2\right) \tag{2.5}$$

where α and β are the first and second order temperature coefficients of resistance (TCRs). Typically in Pt bulk material, the values of the TCRs are around $4{\cdot}10^{-3}\,K^{-1}$, and $7{\cdot}10^{-7}\,K^{-2}$, respectively. The values for Pt thin films grown by e-beam physical vapor deposition are typically smaller than the bulk, and the thinner the film the higher is the discrepancy. In fact that means that the calibration of the resistance versus temperature is needed for each metal deposition. Different strategies were followed to calibrate the temperature dependence of electrical resistance of the nanocalorimeter, and several problems where find out.

The shunting effect. First, the resistance of the heater against the temperature was calibrated in a custom-built hotplate, inside the HV chamber. The temperature of the hotplate was measured with a Pt100 resistor. To limit the influence of the connexion wires, the measurement is performed in four-point mode [45]. Using this setup the thermal lag between microreactor and the Pt100 sensor is negligible. When the complete nanocalorimeter, included the Si frame, is heated the different thermal expansions of membrane and Si frame introduce a mechanical stress that entail the breaking of the membrane. The maximum temperature achievable before the membrane breaks is around 875 K. Figure 2.21 shows the TCR characteristic of the Pt resistor from room temperature to 625 K. The shunting of current through the Si frame appears clearly at high temperatures, introducing a non linear term in the calibration [24] and preventing a possible calibration at high temperature with this method. At these temperatures Si becomes more conductive, and some current flows through it. The 50nm SiO_2 layer beneath the Si_xN_y membrane reduces the shunting effects. Of course, during calorimetric measurements, the Si frame remains at room temperature and shunting is not an issue.

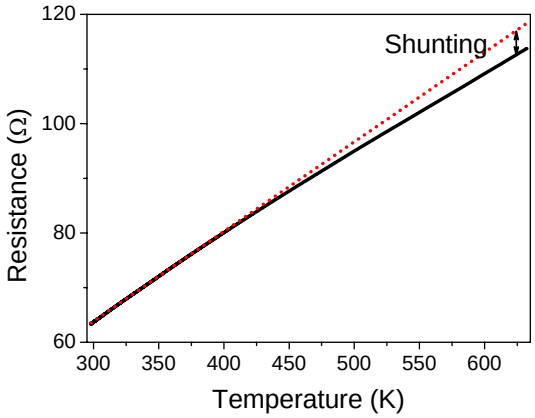

Figure 2.21: R(T) calibrations for a 150nm Al_2O_3/100nm Pt/10nm Ti nanocalorimeter with U-shape geometry. The figure shows the heater resistance evolution with temperature. At high temperatures the shunting phenomena degrades the linear behaviour of this dependence. However α extracted from regressions at lower temperatures matches with the values obtained from the onset pick of Indium calibrations.

Thermoelectrical stabilization. Typically, the nanocalorimeters are annealed in Ar atmosphere at 975 K for 2 hours. This process is carried out in order to stabilize the metals, by sintering the granular microstructure and promoting the possible intermetallic formation. This process results in a nanocalorimeter highly stable at temperatures below the annealing temperature. Annealing for long times above 975 K degrades the heaters due to the presence of oxigen traces in the furnace atmosphere. Ultra high vacuum is needed to stabilize at higher temperatures to prevent Pt degradation by agglomeration. Nevertheless, in a second stabilization process the nanocalorimeters are burned-in inside the HV-chamber using similar electrical pulses to those that are employed during the calorimetric measurements. In this step, the calorimetric cell should be heated up around one hundred degrees above the temperatures used later on in the calorimetric experiments[5]. Around one thousand measurements are typically needed to stabilize the heater, ensuring a complete repetitive measurement. Figure 2.22 (a) shows the stabilization of the voltage signal after a series of 1000 measurements in a 'fresh' nanocalorimeter.

Comparing the calibration curves (R(T)), figure 2.22 (b), obtained for a serpentine-type nanocalorimeter before and after a burn-in process at 1025 K, it is possible to see that the R(T) slightly changes. The α TCR increase from $2.33{\cdot}10^{-3}K^{-1}$to $2.42{\cdot}10^{-3}K^{-1}$at 299 K. This increase may be due to the change in the microstructure of platinum produced by a

[5]Of course in the limits of the operation ranges, around 1250K, the burn-in is performed but just to the maximum temperature, in order to preserve integrity of the microdevices.

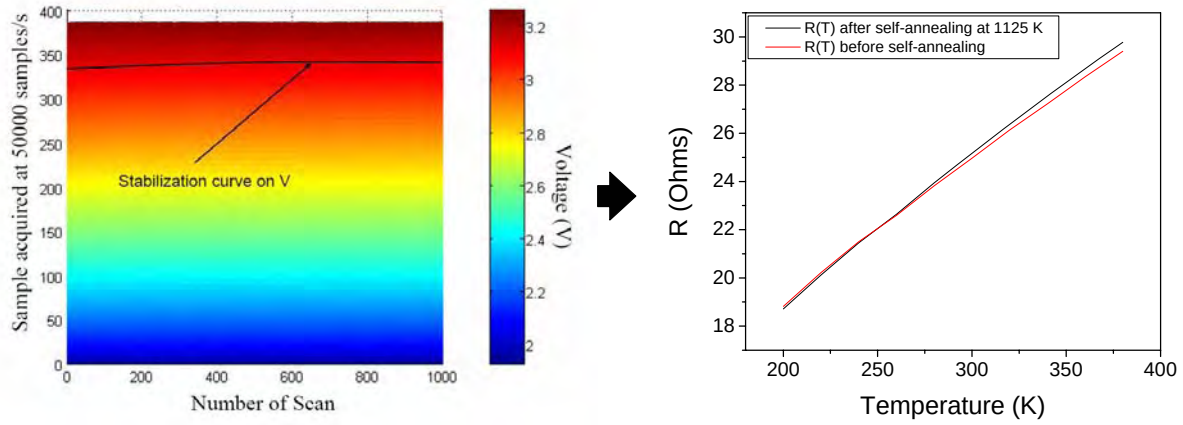

Figure 2.22: (a) Thermal stabilization monitored in voltage measurement during series of scans. (b) The resistance of a serpentine-type nanocalorimeter was calibrated with temperature in a criostate that enables the control of the temperature of the nanocalorimeter holder from 4 to 400 K. In the range between 200 and 400 K the TCR characteristics of Pt is very linear. The both calibrations curves corresponds to the same nanocalorimeter previous and after a burn-in annealing at 1025 K.

sintering process. In any case, it indicates the necessity to recalibrate the nanocalorimeters after a high temperature measurement.

Calibration procedure. At low temperatures it is possible to calibrate the TCR dependence using a thermal bath, but at high temperatures it becomes difficult and it is necessary to use additional strategies. We select several microchips of the wafer and proceed as follows: First, the microchips are thermally stabilized using the burn in process explained above. Secondly, we calibrate every microchip in an independent vacuum furnace were the entire chip is uniformly heated, including the silicon frame, from temperatures of 200 to 375 K. From these measurements we determine the temperature coefficient of resistance (TCR) of the metallic heater/sensor, which is typically measured as highly linear in this range with α average values around 2.3 $\cdot 10^{-3}$- 2.4$\cdot 10^{-3} K^{-1}$. Like commercial calorimeters, we deposit thick samples (over 40 nm) of standard materials, In and Al, and measure the melting onset. From their values we estimate the non-linear components associated to a given associated α. β parameters of the order of $10^{-7}\,K^{-2}$ are typically found. Finally for an specific nanocalorimetric experiment we use a heater/sensor with an α that matches the TCR of a fully calibrated microchip and assume they exhibit the same behavior. Using

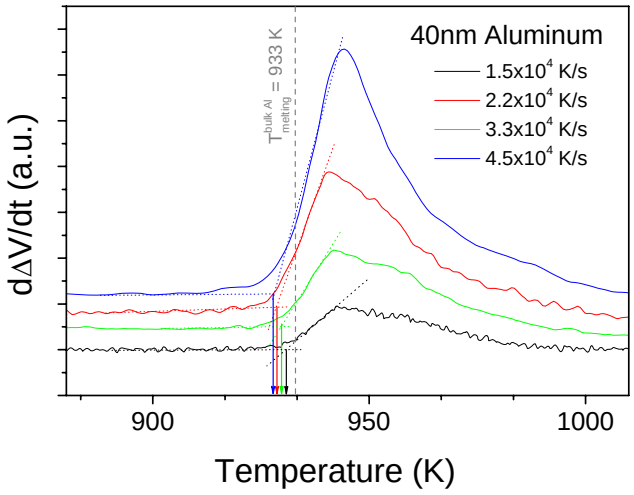

Figure 2.23: Heating rate dependence of the temperature calibration.
Shows melting peaks in the $\frac{d\Delta V}{dt}$ signal as function of temperature for a 40nm Al layer at different heating rates. The color arrow marks the onset temperature for each peak, revealing the dependence of the temperature calibration with the heating rate. Curves are vertically shifted for clarity.

this procedure we estimate a temperature error below 20K at temperatures in the vicinity of 1100 K.

Dependence of calibration with heating rate. Figure 2.23 shows the melting of a 40 nm Al film at different heating rates. The anisotropy of the melting peak observed for the slower rates originates from significant thermal nonuniformities. As the rate increases the melting peak shape improves which confirms that the serpentine geometry of the heater is more suited at fast heating rates. The FWHM of 23 K at 1100 K shows the overall goodness of the design at fast rates. The other significant information that can be extracted from this figure is the small change of the onset of melting, about 3 K, induced by different heating rates ranging from 10^4 to $5{\cdot}10^{-4}K^{-1}$. This variation is due to small nonuniformities in the sample region. Therefore, calibrations should be performed at similar rates than the experiment to minimize these error contributions. It is expected, however, that at higher temperatures heat losses through radiation will reduce the temperature differences, since the regions with higher temperatures will have stronger losses than the regions with lower temperatures. This point is confirmed by thermal modeling.

2.4 Sample Loading .

Most of the materials used in this work have been grown in the Laboratori de Capes Primes at the Universitat Autónoma de Barcelona using the e-beam evaporator facility. To limit and locate the area of deposition in evaporated samples a Si microfabricated shadow mask has been designed, figure 2.24. Under high vacuum ($\sim 10^{-6} mbar$) inside the e-beam evaporator chamber the mean free path of the evaporated atoms is around 50 m[46], 100 times bigger than the distance between material source and the deposition area. The shadow mask is placed perpendicular to the beam, and as can be observed in figure 2.24, extremely close to the membrane (distance around 100 μm) where to deposit the sample. These two facts ensure that the deviation angles will be small and the definition of the deposited area will be good. Trials with other physical vapor deposition systems like sputtering, either in DC or AC, have shown limited results and a large shadowing effect due to the lower mean free path of the atoms.

A detailed scheme of the Si shadow mask can be seen in figure 2.24. Two different mask sizes have been fabricated to evaporate the thermal plates and the samples, on the backside of the membrane. The sample area is selected to be in a quasi-isothermal area over the silicon dioxide of the backside, beneath the heater elements. Limiting the sample inside the calorimetric cell, in the active area, the thermal link between the calorimetric cell and the Si frame is not corrupted.

Other type of samples have been placed in the calorimeter by spin coating or mechanically placing the microsample in the membrane. In case of polymeric dissolutions (not shown here), like PEO in water, or nanocrystal solutions in organic solvents, like CdSe quantum dots in pyridine (not shown here), the sample location can be achieved through spin cast [47]. A drop is leaved in the membrane with a micropipette, and the calorimeter is spinned. Depending on the viscosity and the spin velocity the thickness of the layer can be controlled. Solid samples like high density polyethylene (HDPE) film are located over the thermal layer (1240x350 μm^2), with the aid of a hair and micro-manipulator tweezers as will be shown in chapter 5.

Mass estimation in e-beam evaporated samples. In the case of the serpentine-type nanocalorimeter, as previously mentioned, the active area is constant and does not depend on heating rates, contrary to the U-shape design. Therefore, in experiments with the serpentine-type nanocalorimeters, where the microfabricated shadow mask is used to delimit the sample deposition area of the evaporated species, the mass can be estimated

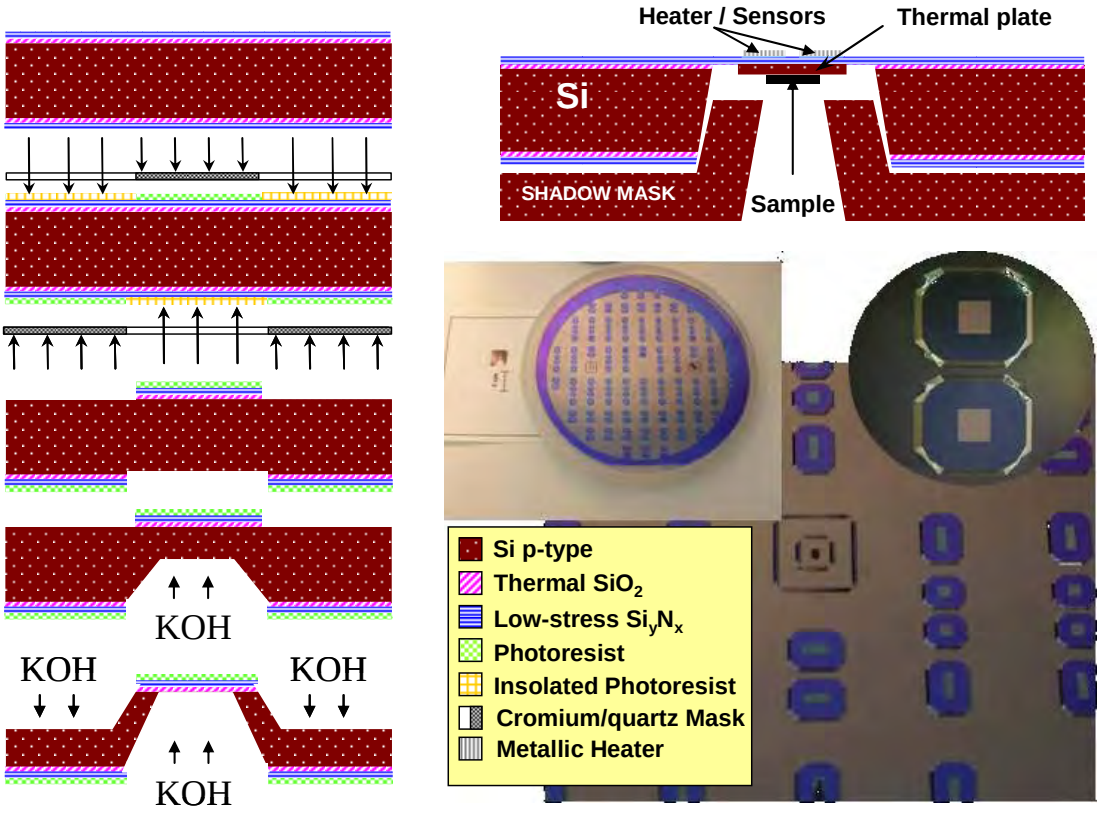

Figure 2.24: Shadow mask schematics.

previous to the sample deposition. The mask opens a deposition area of 0.9 mm^2, however shadowing effects in the boundaries produce umbra and penumbra areas limiting the amount of material that reaches the membrane. To calibrate this effect on the amount of final sample the e-beam deposition rates are previously calibrated for each material by measuring the nominal thickness with SEM cross-sections or profilometry. Therefore, in a given deposition if we consider the nominal sample thickness and the deposited area we can conclude a first value for the sample loaded in the calorimetric cell, considering the bulk density of the evaporated material (deposition area x nominal thickness x bulk density). However, depending on the deposited material and the growth conditions, it is well known that densities of e-beam evaporated thin films can differ from bulk values. The uncertainty in deposition area and mass distribution due to shadowing effects, and reduction on material density can introduce some errors in the mass estimation. Comparing nominal values with sample mass experimentally obtained from heat capacity values at a given temperature (considering the corresponding specific heat capacity), it is found a close to constant behavior where the real mass value (the experimental) is around the 73±3% of the previously estimated nominal mass value. This was proven to be similar for the different materials presented in this thesis (SiO_2, Ge, In and Ni) and for different thicknesses, preserving always the scaling factor within the error.

Chapter 3

Vacuum Experimental Setup.

In this chapter, we present the various experimental setups that have been used to carry out the nanocalorimetric experiments. Ex-situ measurements were typically realized in a HV chamber equipped with an inner minichamber that connects electrically the calorimeters whereas in-situ measurements were performed directly inside the electron beam evaporation system. The external instrumentation is specific for every type of measurement and therefore will be fully described in chapters 4 and 5.

Quasi-adiabatic calorimetric measurements require a high vacuum environment whereas power compensation can be performed either in vacuum or in a non-reactive atmosphere. The high surface-to-volume ratio in thin films enhances its reactivity, and therefore it is essential to control the environment to prevent non desired reactions, like oxidation. Moreover, in ultra sensitive quasi-adiabatic experiments, the adhesion to the nanocalorimeter membrane of any contaminant (like hydrocarbons) can be reflected as a spurious noise (desorption) in the heat capacity signal, and should be prevented. By these reasons, some of the experiments presented in this thesis were performed in-situ, what means inside the same chamber where the samples were grown without breaking the vacuum environment. This procedure requires an special setup that is also describe in this chapter.

3.1 Vacuum Chamber for Ex-situ Calorimetry.

The vacuum system consists on a high vacuum (HV) chamber, the vacuum gauges and the vacuum pump system (see figure 3.1 on the following page). The HV chamber was designed as a stainless steel cylinder with a kwik flange (KF) lid on the top, several conflate flange (CF) ports, in the lateral wall and in the bottom, and four liquid/gas feedthroughs,

in the lateral wall. In the lateral CF ports, there are three electrical ten pin feedthroughs and the vacuum gauges. The system has one PDR9000 controller unit which controls the two vacuum gauges, the 907 convection enhanced Pirani and the 903 inverted magnetron transducer [1]. With this dual system the pressure can be measured from $1.3 \cdot 10^3$ to $3.9 \cdot 10^{-10}$ mbar. The pumping system consist on a rotary vane pump model 2005C1, linearly connected to an Alcatel ATH 30 Series turbomolecular pump, which is coupled to the vacuum chamber[2].

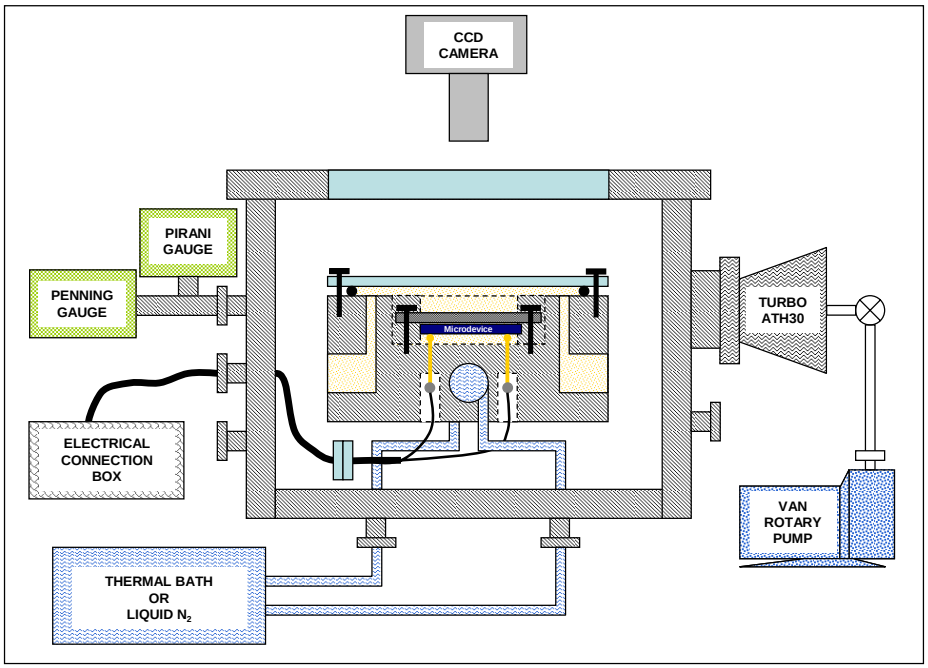

Figure 3.1: UHV chamber schematics.

A pressure of 10^{-7} mbar is easily reached in a couple of hours after opening the chamber, and with an appropriate baking the system gets down to 10^{-8} mbar [48]. Below 10^{-6}mbar convection losses are negligible. To checkout that this assertion was true, we use an IPID controller (see chapter 5) to control the calorimeter in the power compensation mode, in order to measure the power needed to reach a temperature of 353 K in the nanocalorimeter at different pressures, see figure 3.2. As both the thermal profile and the temperature are

[1]The gauge system is from MKS instruments.
[2]The pumping system is from Alcatel.

constant in the nanocalorimeter membrane the radiation and the conduction losses remain unchanged at different pressures, and the differential of power is due to convection losses.

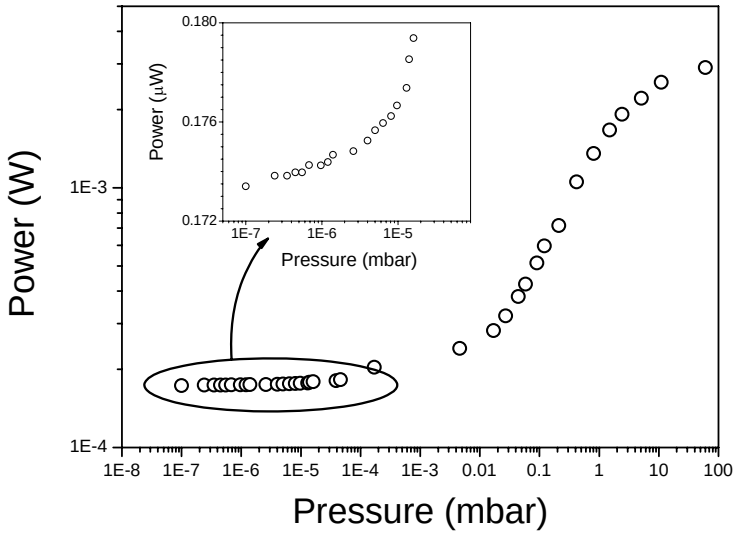

Figure 3.2: Input power as a function of pressure. Power is introduced through the metallic heater to the nanocalorimeter to keep the temperature profile at a constant value of 353K. Below 10^{-3} mbar convection decreases drastically tending to an offset value of the input power. This value is needed to compensate heat losses by conduction through the membrane and radiation at 353 K, since both of them only depend on the temperature profile in the membrane.

3.2 Inner Chamber and pogopin probes.

Inside the HV chamber we placed one small chamber, named hereafter the pogopin minichamber. It is a custom made holder that was specially designed to electrically contact the heater/sensor pads and to locally control the atmosphere surrounding the microdevices independently of the main chamber. The minichamber is made of Aluminum, and after the machining has gone through an anodizing process to electrically insulate it. (see figure 3.3)

It has an internal liquid pipeline that allows control of its temperature through a thermal bath. The temperature of the inner chamber is fixed to a constant value (currently 293 K), with a precision of 0.1 K imposed by a thermal bath controller. Using liquid nitrogen it is possible to cool it down to 77 K. The real temperature is measured through a PT100

Figure 3.3: Inner chamber front detail.

attached to the aluminum block. The good thermal link between this block and the Si frame, enforce the Si frame to remain at the same temperature during the calorimetric measurements, what becomes essential in calorimetric experiments at low heating rates (power compensated mode) where the amount of heat transfer may be enough to heat the Si frame.

The nanocalorimeters are placed as schematically shown in figure 3.4. The electrical connections to the on-chip bond pads are made using gold coated pogopins[3], that are glued with epoxy to the aluminum block.

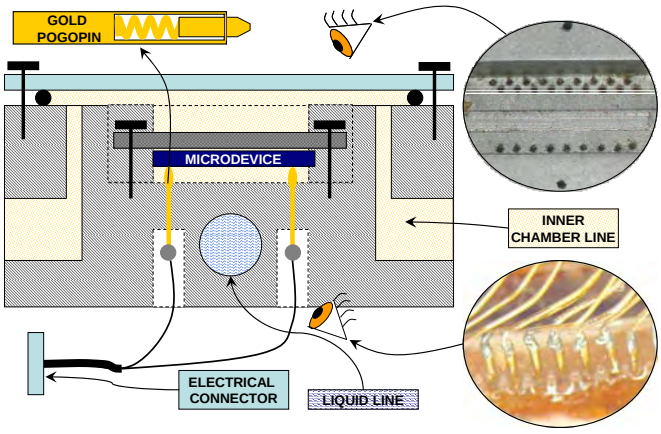

Figure 3.4: Schematics of the Inner chamber showing a cross section view. Two details of the gold pogonpins show the connection socket from top and bottom .

[3]The gold pogo pins are point probes, with an internal spring , that allow to connect electrically the Pt pads on the nanocalorimeter. (see fig.3.3)

3.3 Setup for In-situ Nanocalorimetry.

To avoid unwanted surface effects due to exposure of the samples to ambient atmosphere we prepared a setup inside the e-beam physical vapor deposition chamber of the 'Laboratori de Capes Primes' at UAB. The pressure in the chamber reaches values below 10^{-6}mbar reducing the impingement flux of gas contaminants during experiments[4]. A similar pogopin socket to the one used in the ex-situ setup permits to place the calorimeters and electrically connect them inside the e-beam chamber. A window is open in the socket to expose the bottom of both membranes. It is placed at 90º and around 0,5 m over the material source to permit the correct operation of the shadow masks that limits the deposition area. With a set of moving masks it is possible to selectively deposit materials on each calorimeter, during vacuum. Figure 3.5 show a photograph and a scheme of the in-situ setup.

In this system up to 6 different elements or compound can be sequentially deposited without breaking vacuum by e-beam (4 targets) or thermal (2 targets) evaporations. The nanocalorimetric experiments can be performed just after or even during growth of a thin film.

[4] 15 minutes is the monolayer formation time (from gas contaminants impingement) on surfaces at room temperature and pressures around 10^{-6}mbar [46].

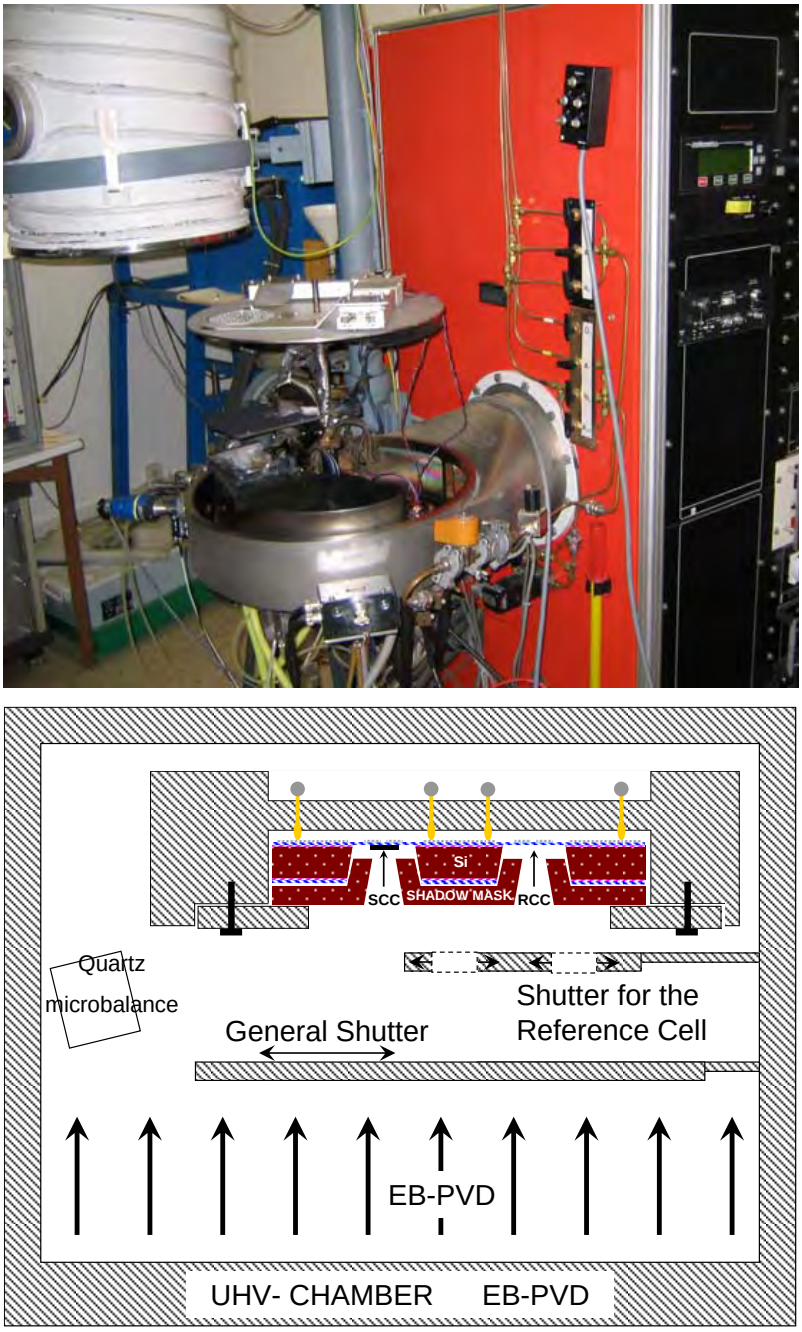

Figure 3.5: Photograph and Scheme of the in-situ measurements setup.

Chapter 4

Quasi-Adiabatic Nanocalorimetry

The main difficulty to perform calorimetric measurements in nanogram samples relies into the small amount of energy involved in their phase transitions. To increase sensitivity in the calorimeter, the heat capacity of the calorimetric cell (the addenda) is minimized to make it comparable to the heat capacity of the analyzed sample that will undergo the phase transition. Otherwise, the calorimetric signal of interest is masked in the noise of the addenda signal. In fact, the absolute accuracy of any measurement of heat capacity is limited by the fraction of the total heat capacity which is not due to the sample [5]. From yesteryear, the strategy of decreasing the addenda contribution coming from the thermometers, heaters and sample holder has driven all advances to measure lower and lower sample amounts. In the beginning the advances were modest. As an example of the first achievements, in 1963 Morin and Maita were able to measure samples of 100 mg [49]. It was not up to the final of the seventies that a new impetus in the miniaturization permitted Early et al. to measure sample of hundreds of micrograms in 1981 [50].

However it has been in the last 15 years when the advances in Si microfabrication have represented a revolution in the scaling down of devices. Membrane technology has paved the way to construct very light calorimeters like the one presented by D.W.Denlinger et al. [12] in 1994. Using a suspended membrane as a low thermal mass mechanical support, the addenda of the device was $4 \cdot 10^{-6}$ J/K at room temperature and $2 \cdot 10^{-9}$ J/K at 4.3 K, approximately two orders of magnitude lower than any pre-existing calorimeter at that time. Using AC techniques, the device was capable of measuring the heat capacity of samples of few micrograms (thin films).

However, although AC calorimetry has been shown to be well suited to measure the

heat capacities with high sensitivity[1], it can not be used to obtain accurate values for the enthalpies or kinetic parameters in phase transitions. To access this type of information it is necessary to use scanning methods. At this point, the reduced amount of energy that is involved in phase transitions of nanogram samples emerges again. The heat flow resolution needed to heat nano-sample at the typical rates of conventional calorimetry (around 10 K/min) extremely accurate current/voltage sources and sensing (resolution better than 1 nW). It is necessary to increase the heating rates to yield a measureable heat flow. The necessity to subject a sample to high heating rates introduces some restrictions in the types of samples. The first is referred to the thermal link between sample and calorimetric cell, that has to be maximized to prevent thermal lags. And the second limitation is related to the size of the sample since thick and poor conducting films may show large thermal gradients within the sample volume.

Quasi-adiabatic scanning calorimetry or pulsed-heating calorimetry at fast heating rates (500K/s) was initially developed by Hager [51]. The method was based on heating a sample, winded up into a metal sheet, that was used as a holder, heater and sensor. By applying a pulse of current the metal sheet and the sample inside rise their temperatures due to Joule heating. The temperature was measured using the sheet as a resistive thermometer. Allen's group in 1995 [52], improved this method for thin films using a membrane-based microdevice as heating pulse calorimeter. With this configuration, and working under ultra high vacuum, heating rates up to 10^5 K/s or even 10^6 K/s can be reached, opening the possibility to probe the heat capacities of ultra-thin films and directly measuring latent heats of melting with monolayer sensitivity (1 J/m^2). The possibility to perform differential measurements increased the resolution of the technique, reaching sensitivities up to 30 pJ/K. With this technique, called thin film differential scanning calorimetry (TDSC), the mass limit for their calorimeter was around $\sim$1 ng, which corresponds to thin films with an effective thickness below 1Å[15]. Several papers dealing with instrumentation and the methodology to obtain heat capacity have been published by the Illinois group [24, 53, 30]

A later contribution to thin film calorimetry has been performed by C. Schick's group [54]. Using a membrane-based microdevice equipped with thermopiles, initially commercialized by Xensor as a pressure gauge, in pulse heating mode with saw tooth pulses, they perform non-adiabatic calorimetry at high heating and cooling rates of the order of 10^3-10^5K/s under an innert gas atmosphere at reduced pressure. This way they have studied the thermodynamics involved in far from equilibrium transitions (like superheating and su-

[1]Recently, O.Bourgeois at Grenoble has reached resolutions of 10^{-18}J/K, using AC calorimeters and working at very low temperatures.

percooling), like melting and reorganization of semicrystalline polymers during fast heating scans [54, 16, 17, 20].

In spite of the latest advances summarized above, thin film nanocalorimetry is still in its infancy in the sense that further developments are still possible and that a large amount of systems still remain to be explored at the nanoscale. Moreover, non significant contributions have been reported in high temperature calorimetry (over 800K). The difficulty to built up a membrane-based nanocalorimeter with sufficient thermoelectrical and thermomechanical stability to allow repetitive and reproducible calorimetric measurements is one of the main obstacles. In adittion, high temperatures generally mean larger heat losses since radiations increase dramatically and the data treatment is prone to larger errors.

In this chapter we present our contribution to the high-temperature nanocalorimetric measurements putting forward how to achieve accurate heat loss correction to obtain the true heat capacity of the sample. We focus on three materials, although other systems have been tentatively explored and are under further development. The first example, melting transition of In thin films, is a case study performed to understand the principle and potentiality of the technique. This system was previously studied by Allen et al. [55], and it helped us to improve the design of the heaters. As a second example, we present the measurements of the heat capacity in ultrathin films of Ni in the temperature range from 350 to 800 K. The different heat capacity corrections will be applied to this data permiting to analize the continuous ferromagnetic to paramagnetic transition. The third and more complete study involves the nanocalorimetric high-temperature characterization of ultra thin films of a-Ge sandwiched between SiO_2 layers. This study was also accompanied by a more complete analysis of the formation of Ge nanocrystals in samples of different thickness. These results will be detailed in Appendix B.

4.1 Principle of operation.

The microdevice, as we described it in chapter 2, consist on a free-standing rectangular (2.5x3.5 mm^2) membrane of 180 nm of amorphous Si_xN_y supported by a Si frame. This membrane serves as mechanical support to place the metallic heater/sensor and the sample to be investigated. On top of the membrane, a metallic thin film is patterned to form the heater. This configuration leads to a heat capacity addenda around hundreds of nanoJoules per Kelvin. Introducing a constant pulse of current through the metallic heater, the calorimetric cell (heater+membrane+sample) is heated by Joule effect. Under ultra high vacuum and input currents around $\sim mA$, high heating rates can be reached ($\sim 10^6$ K/s), and the system behaves close to adiabacy, since the typical cooling rates are around ($\sim 10^3$ K/s)[2]. Only the center of the membrane (sensing area or calorimetric cell) is heated while the contacts pads in the frame remain at room temperature since the $500\mu m$ thick Si acts as a massive heat drain, due to its high heat capacity in comparison with the membrane. With the typical current densities applied to the nanocalorimeter (in the order of $\sim 10^5$ A/cm^2) the Ohms law can be applied. Therefore, by measuring the voltage on the sensing pads (four point mode) of the heater, the resistance change in the sensing area can be obtained as V(t)/I(t). With a proper calibration of the R(T) function for the metallic heater, the temperature (T(t)) in the calorimetric cell can be obtained from its resistance. The power introduced to the calorimetric cell (V(t)·I(t)) can be also monitored as a function of time. Then the measurement is reduced to the observation of the temperature rise as a function of time during the introduction of the electric power. However, not all the power introduced in the calorimetric cell is consumed either by an increase in its temperature or by a phase transition present in a sample (energy that contributes directly to the enthalpy). A certain fraction of the heat released can be lost through conduction, convection and/or radiation, and these losses should be quantified and included in the calculation to get the heat capacity of the sample. In general, we consider:

$$dH = C_P(T) \cdot dT, \tag{4.1}$$

[2]Silicon nitride is a poor thermal conductor. Therefore, it provides sufficient insulation between the center of the membrane and the silicon frame ($\sim$ 1 mm of distance) to attain small cooling rates. As the membrane is very thin, no significant temperature gradient is present between the heater (on top of the membrane) and the sample (on the bottom of the membrane). A value of 0.02 K at heating rates of 10^5K/s was extrated from modeling, but can also be obtained from a back-of-the-envelope calculation considering the thermal diffusion length of silicon nitride ($\sqrt{D \cdot t}$) to be around $1\mu m$ in $10\mu s$.

$$C_P^{True}\left(T\left(t\right)\right) = C_P^{T}\left(T\left(t\right)\right) = \frac{P_{heater}\left(T\left(t\right)\right)}{\beta\left(T\left(t\right)\right)} - \frac{P_{losses}\left(T\left(t\right)\right)}{\beta\left(T\left(t\right)\right)}; \tag{4.2}$$

where H is the enthalpy, C_P is the heat capacity, P_{heater} is the power introduced by the heater into the calorimetric cell, P_{losses} is the power lost from the calorimetric cell to the surroundings and $\beta\left(T\left(t\right)\right) = \frac{dT}{dt}\left(T\left(t\right)\right)$ is the heating rate in the calorimetric cell.

Under vacuum conditions and heating up to temperatures below around 500 K, both convection and radiation losses can be neglected in front of the conduction component. The conductive losses are limited since the main thermal link between the calorimetric cell and the Si frame is through the 180 nm thick Si_xN_y membrane (thermal conductivity, around 2.5 W/mK). In this case, the P_{losses} term is small and can be neglected with respect to the P_{heater} term if high heating rates (of the order of $\sim 10^5$K/s) are applied. Assuming this consideration holds true the calorimeter behaves quasi-adiabatically, and the heat capacity of the calorimetric cell can be estimated directly from the input power:

$$C_P^{Adiabatic}\left(T\left(t\right)\right) = C_P^{A}\left(T\left(t\right)\right) = \frac{P_{heater}\left(T\left(t\right)\right)}{\beta\left(T\left(t\right)\right)}; \tag{4.3}$$

However, as has been already shown by Allen et al. [24] the technique can become extremely sensitive if two identical calorimeters, one containing the sample (S) and the other as reference (R), are used and the measurements are performed in differential mode. We actually perform it by passing the same current pulse, and measuring the voltages, $V_R(t)$ *and* $V_S(t)$, in both heaters individually and also the differential voltage, $\triangle V = V_S - V_R$. Under several simplifying assumptions that will be explained in detail in section 4.1.2, it is possible to consider the heat capacity difference between both calorimetric cells as proportional to the $d\triangle V/dt$, improving the signal-to-noise ratio. This expression needs for some corrections already proposed by Allen's group to obtain the true value of the heat capacity of the sample. At higher temperatures we include an extra correction to account for power losses.

4.1.1 Instrumentation setup.

Figure 4.1 shows a schematic representation of the experimental setup. The microdevices are placed into the custom-build pogopin probe inside the UHV chamber and the electrical contacts are extracted through electrical feedthroughs with shielded wires to a connection

box[3]. A high precision pulsed current source (Keithley 2425) is used to create the electrical pulses that will feed the two heaters connected in series. The typical current pulses are around 5-50 mA, with an electronic noise below 50 nA. The current source has a transient behavior during the first $500\mu s$, and it prevents to extract information at this moment. The pulse width determine the scanning temperatures, and are typically in the range of 2-30 ms. The limitation of the source does not permit to control the width below the milisecond range. The voltage drop in the calorimetric cells, the sample voltage and reference voltage, is treated with a custom-made electronic circuit (signal conditioner and amplifier), which returns the two initial voltages and its difference amplified. Using a 16 bits Fast Acquisition board NI PXI 6123 of National Instruments the three raw data signals are acquired as a function of time, in differential mode at 500 Ksamples/s per channel[4]. The random noise of the signal (below 500 mV) can be reduced by a simple box averaging of ten points, that also limits the raw data to 50 Ksamples per second. This procedure limits the temperature resolution to 1K at $5{\cdot}10^4$ K/s[5], however this is a good agreement between the resolution expected from temperature profiles in the sensing area and the noise rejection from the data averaging. A NI PXI-8187 controler module with Labview (an instrumentation PC program) is used to synchronize the current source outputs and the AD card acquisitions. The Labview controls the Keithley source via GPIB protocol, programing the intensity and length (in ms) of each current pulse, and initiates the acquisition just before the pulse, gathering the raw experimental data in a file. The program permits also to perform series of pulses, controlling the times between them. Typical cooling times are around 0.2-0.5 s, which fix the maximum number of calorimetric scans per second[6]. Hardware limitations impose the operational heating rates between 20 and $250{\cdot}10^3$ K/s. Higher heating rates can

[3]This box is electromagnetically insulated by using a metallic frame with a high magnetic permitivity and BNC connectors are typically used to minimize electrical noises.

[4]This data acquisition card uses an analogic-to-digital converter (ADC) per channel, improving noise features, acquisition rates and enabling real differential measurements respect to previous version of cards used in the initial experiments (NI PCI-6063 E card). NI PCI-6063 E card uses a single ADC combined with multiplexor to measure in different channels. This configuration is not recommended since real differential measurements are not possible (only pseudodifferential) and the multiplexor may also introduce extra noises. Moreover, the acquisition rate of the ADC is shared between the different channels limiting acquisition rates at 50 Ksamples/s per channel, when using 4 channels.

[5]In fact, for a single scan the resolution on temperature can be considered directly as the difference on temperatures for two consecutive reading with the AD card:

$$resolution\ T = \frac{1}{ADC\ frequency} \cdot \frac{dT}{dt}$$

[6]It will be the main limitation for Real-time measurements.

be obtained, but the transient in the current source and, the limitation in the acquisition frequency per channel, prevents measurements with good temperature resolution.

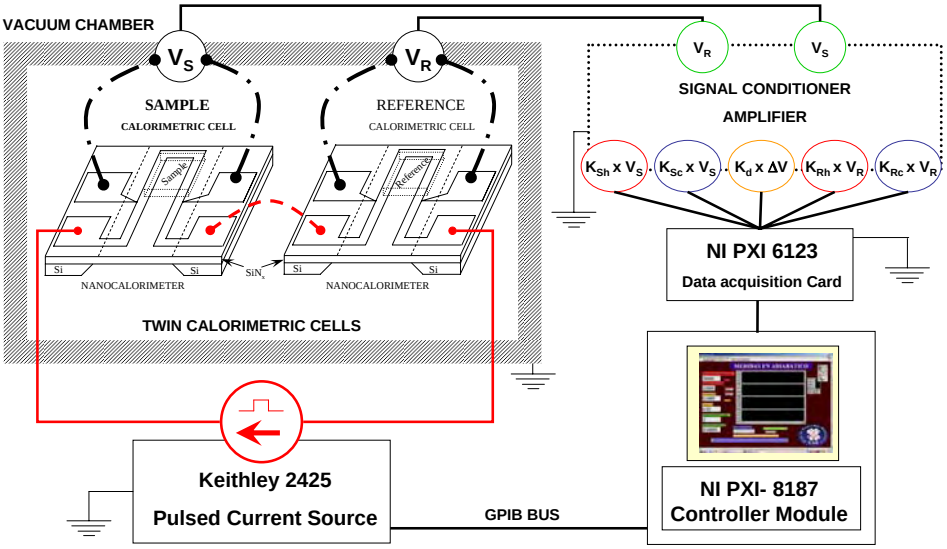

Figure 4.1: Experimental setup.

The differential configuration design shows an increase in the sensitivity, since common noises in both cells are removed. Nevertheless, several noise considerations are critical to reach a high resolution calorimetric measurement. As a basic consideration, it is necessary a proper grounding, to a common ground, and shielding all electrical signals, otherwise, unacceptable EMI-noise can be added to the data signal [45]. Several electrical noises have been detected during the experiments. With Fourier spectral analysis two main components of noise were identified: one at 50 Hz associated to the general electrical power supply and a second one of 700 Hz associated to the power supply of the turbo molecular pump. Other equipments in the laboratory can cause other components of noise, in fact, all power supplies are inherently noise sources. But all these noises are considerable reduced if measurements are performed at night, where most of the electronic equipment at the university is switched off and the electrical net is more stable. Other noises like the intrinsic noise of the pulsed source, the thermal noise in metal conductors (Johnson noise), transient noises due to uncoupled impedance in electrical contacts, are treated both with proper analogical and digital filters. Another point to be considered is that performing the experiments in-situ in high vacuum reduces the presence of spurious signals which may be related with adsorption and desorption of contaminants in poorer vacuum environments.

Figure 4.2, shows the schematic view of the electrical circuit used to treat the voltage signals. The first block is a pre-amplifier which keeps the signal inside the input range of the AD card [56]. This stage is designed using the INA 114[7], a precision instrumental amplifier with a regulated gain (from 1X to 10000X). The low input bias current of 2 nA (max.) guarantees small current drifts from the microdevice circuit. The high common-mode rejection (CMR) of 115 dB (minimum) permits the reduction of common noises (most source noises). This first pre-amplifier acts as a buffer block that takes the voltage drop in each calorimetric cell, and return these voltages (1X) referred to a common ground, with an offset lower than 50 μV. The second block takes the two voltages (V_S and V_R) and returns them and the difference amplified ($K_{Sh}{\cdot}V_S$, $K_{Sc}{\cdot}V_S$, $K_{Rh}{\cdot}V_R$, $K_{Rc}{\cdot}V_R$ and $K_d{\cdot}(V_S - V_R)$). The two original voltage signals are amplified per low gain factors K_{Sh} and K_{Rh}, in the range of 1x to 3x, to be followed during heating when high currents are applied. During coolings, only polarizing low currents feed the heaters and higher amplification gains are needed, K_{Sc} and K_{Rc} use to range between 30X and 50X. This stage was designed using the INA 110[8], a Fast-settling FET-Input instrumentation amplifier with a high CMR, and a tunable offset. The signal is also filtered for high frequencies since the typical gain-bandwidth (GBW), of INA 110, is 100 kHz at gains of 100X. An anti-aliasing filter, cleans the three signals just before they are measured with the AD card. The anti-aliasing filter is designed as a low-pass RC filter[9][56]. The cut-off frequency is reduced to 10 kHz since typical time scales for thermal processes in the calorimetric cell are around a hundred of microseconds [24, 57]. The amplification gain for the output, $\triangle V$, is limited by its amplitude, since the final signal should not exceed the range of AD card. Typical gain values for K_d range from 30X to 500X, depending on the initial differences. In practice, nanocalorimeters that are spatially located in the same region of the wafer are selected to guarantee similarity and maximize the K_d gain.

[7]Burr-Brown, INA 114 precision instrumentation amplifier data-sheet. http://www.burr-brown.com/

[8]Burr-Brown, INA 110 Fast-settling FET-Input instrumentation amplifier data-sheet. http://www.burr-brown.com/

[9]Acquiring data at a f frequency, no information can be extracted from frequencies higher than f/2 (Nyquist theorem).

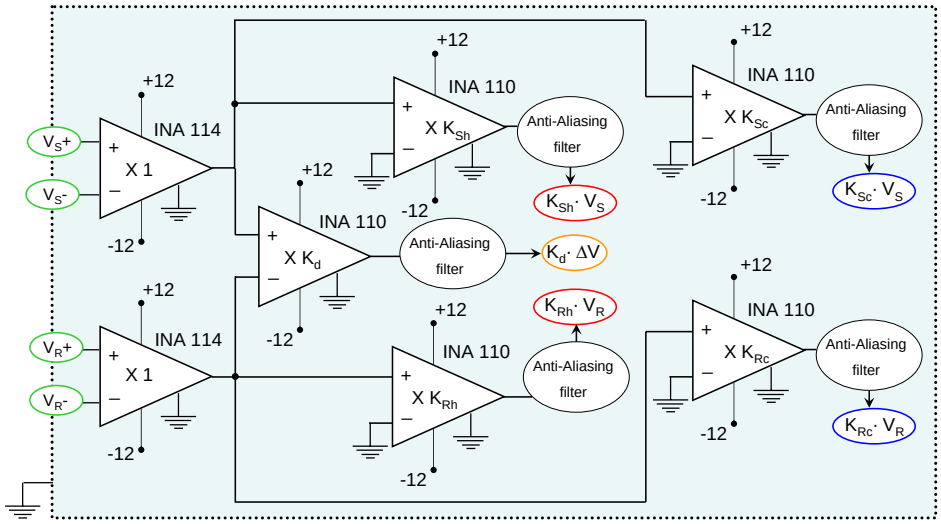

Figure 4.2: Amplifier and signal-conditioner.

4.1.2 Heat Capacity Analysis.

In this section we demonstrate how the heat capacity values can be extracted from raw voltage data [24]. Two main methods, the nondifferential and the differential mode, described by Allen's group are discussed and adapted to our nanocalorimeters. Both modes assume quasi-adiabatic conditions, that can be achieved when in equation 4.2, P_{losses} term is much smaller than P_{heater}. To satisfy this condition, the nanocalorimeters should work under several restrictions: (i) in ultra high vacuum, where the convection component of P_{losses} can be neglected, (ii) at low temperatures in order to prevent a large contribution of radiation losses and (iii) working at high heating rates (over $3{\cdot}10^4\,K/s$) compared with typical cooling rates of the calorimetric cell (around $5{\cdot}10^3\,K/s$ if condition (i) and (ii) are followed). In fact, cooling rate gives a direct information of P_{losses} magnitude, and preserving a large $\beta_{heating}$ to $\beta_{cooling}$ ratio, the main requirement $P_{heater} \gg P_{losses}$ prevails. At high temperatures (over 500 K) the radiation losses break down the close to adiabatic conditions since P_{losses} increase, and some extra correction have to be added. The numerical methods and corrections used are explained using experimental data and schemes to clarify every term. In order to keep a correct notation a superscript 'A' will correspond to all expressions where losses contributions have not been considered. In both methods we use a reference cell. In nondifferential measurements it is useful to reduce some common noises. In addition, permit to evaluate the contribution to the heat capacity addenda in the reference cell (contribution to baseline) when a extra buffer or capping layers are introduced to protect the sample as in some particular cases in the present work.

Nondifferential analysis. The heat capacity expression for each single calorimetric cell can be expressed as equation 4.3, where the input power is due to the Joule heat (V·I), and is expressed as:

$$C^A_{P_{S,0}}\left(T_{S,0}\left(t_0\right)\right) = \frac{V_{S,0}\left(t_0\right)\cdot I}{\beta_{S,0}\left(t_0\right)}. \tag{4.4}$$

$$C^A_{P_{R,0}}\left(T_{R,0}\left(t_0\right)\right) = \frac{V_{R,0}\left(t_0\right)\cdot I}{\beta_{R,0}\left(t_0\right)}. \tag{4.5}$$

where $C^A_{P_{S,0}}$ and $C^A_{P_{R,0}}$ are the heat capacities for the empty sample and reference calorimetric cell, respectively. The subscript 0 refers to the empty calorimetric cells and, S and R refer to the sample (SCC) and reference (RCC) calorimetric cells, respectively. With these two measurements, it is possible to express the initial difference of heat capacity between

both calorimetric cells just before introducing any sample, substracting expressions 4.4 and 4.5 in temperature domain, as:

$$\Delta C_{P_0}^{A}\left(T_{S,0}\right) = C_{P_{S,0}}^{A}\left(T_{S,0}\right) - C_{P_{R,0}}^{A}\left(T_{R,0}\right). \tag{4.6}$$

Once the sample is placed in the SCC, the Cp value measured with equation 4.3 includes the sample contribution, giving:

$$C_{P_{S,1}}^{A}\left(T_{S,1}\left(t_1\right)\right) = \frac{V_{S,1}\left(t_1\right)\cdot I}{\beta_{S,1}\left(t_0\right)}. \tag{4.7}$$

$$C_{P_{R,1}}^{A}\left(T_{R,1}\left(t_1\right)\right) = \frac{V_{R,1}\left(t_1\right)\cdot I}{\beta_{R,1}\left(t_1\right)}. \tag{4.8}$$

where subscript 1 refers to the measurements when the sample is placed in the SCC. The difference between heat capacities after the sample deposition, can be expressed as:

$$\Delta C_{P_1}^{A}\left(T_{S,1}\right) = C_{P_{S,1}}^{A}\left(T_{S,1}\right) - C_{P_{R,1}}^{A}\left(T_{R,1}\right). \tag{4.9}$$

The heat capacity of the sample with the nondifferential method can be evaluated as the increase of the difference in heat capacities before and after the sample deposition.

$$C_{P}^{A,\,sample}\left(T_S\left(t\right)\right) = \Delta C_{P_1}^{A}\left(T_{S,1}\right) - \Delta C_{P_0}^{A}\left(T_{S,0}\right) \tag{4.10}$$

Figure 4.3, shows the raw experimental data (a-e) for a single measurement on a 40 nm thin film of indium, the final result of heat capacity $C_{P}^{A,\,sample}\left(T_S\left(t\right)\right)$, and all data involved in the measurement.

This method is really powerful when the sample heat capacity is comparable to the addenda; however, for ultra-thin films further improvements in sensibility are needed. Equation 4.10, gives the heat capacity of the sample using a nondifferential method considering that the system behaves as an adiabatic system. Nevertheless, using equation 4.3, contains the derivative of the temperature as a function of time, β, and it is known that the differentiation of a noisy function increases dramatically the noise, degrading the signal several orders of magnitude. Although, as we explained in last subsection 4.1.1, noise has been electronically reduced with passive filters and some residual noise is still present. Moreover, added to that noise, in every acquisition process the quantification errors and missing codes inherent to AD converters can introduce extra noises [53], and should be treated with numerical filters. To reduce noise, β should be properly smoothed by averag-

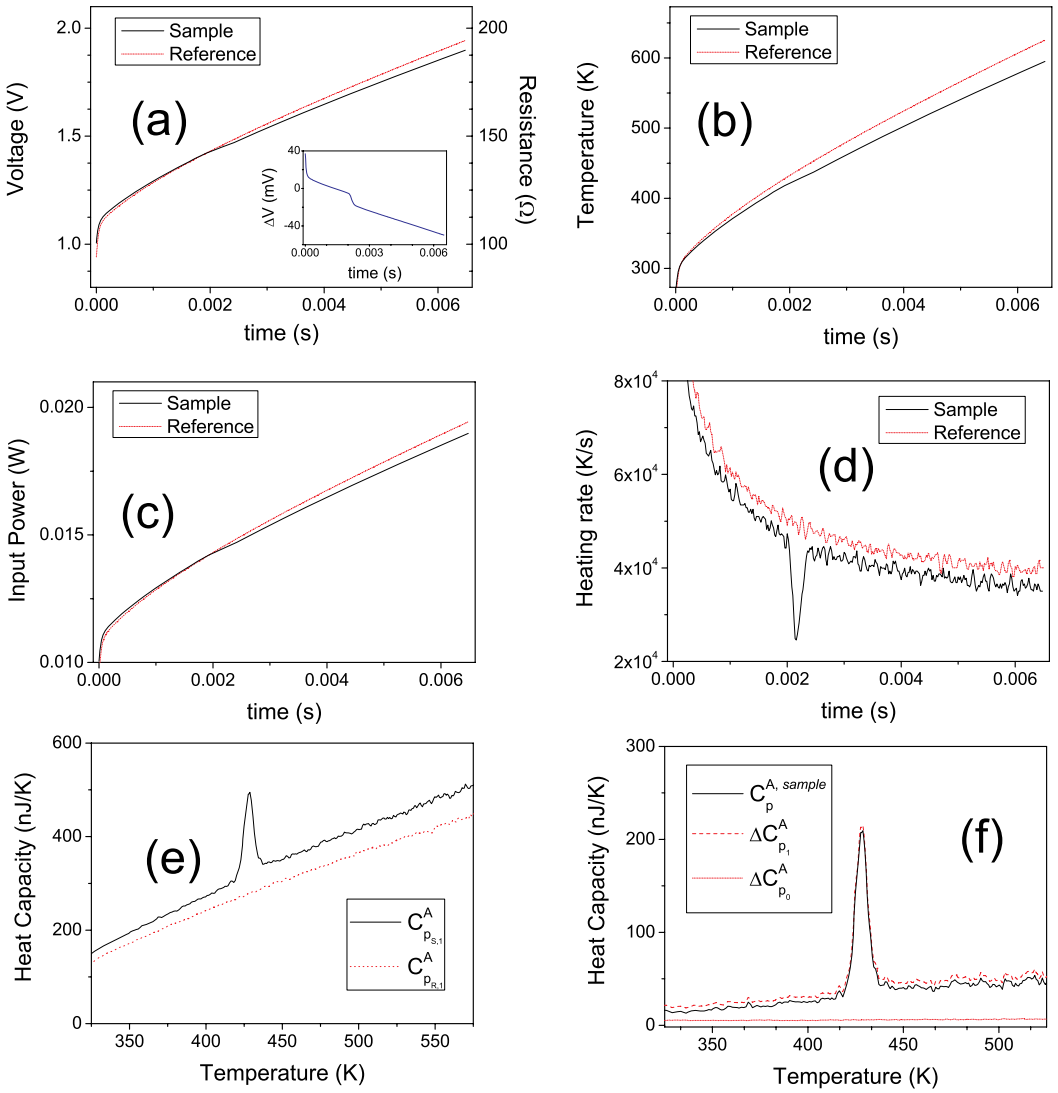

Figure 4.3: Nondifferential measurements.
Raw experimental data of a single measurement on a 40 nm thin film of indium. (a) Shows the raise of two voltages in sample and reference heaters when the input step of current applied, as a function of time. As the current is constant the resistance can directly be obtained from the voltages. (b) Temperature vs. time. (c) Input power vs. time. (d) Heating rates vs. time extracted with the numerical differentiation of T(t). It is clearly the main source of noise. (e) shows the $C^A_{P_{S,1}}$ and $C^A_{P_{R,1}}$. (f) Shows the heat capacity of the sample $C_P^{A,\,sample}$, and both initial differences between cells, before $\Delta C^A_{P_0}\,(T_{S,0})$ and after sample deposition$\Delta C^A_{P_1}\,(T_{S,1})$.

ing in time domain. As mentioned before, a box averaging process is perform after the raw data acquisition. Selecting boxes of 10 to 100 points, only signal frequencies over 50 to 5 kHz will be rejected since the acquisition is performed at 500 kHz. Most random noise, is eliminated in these smoothing process in time domain, but some spurious signals can survive in a single measurement (eg. desorption of molecules from the membrane, missing codes in the AD,...). If we analyze a reversible transformation in the sample, it is possible to reduce the global noise and increase drastically the SNR, only by averaging consecutive scans, since the noise reduction evolves as N^2. The first series of scans should be excluded from the averaging process and should be carefully analyzed in each case. During these first scans the sample is annealed and some accommodation effects may disturb the real signal. For example, in Indium thin films, after the five first measurements, the scan data are identical within the measurement error and can be averaged. In this case, averaging the data in temperature domain improves the filtering by removing non common noises. This step is performed using cubic splines from MATLAB, in order to shift data from time to temperature domain. All these noise considerations and numerical method are also applied in differential mode.

Differential analysis. Working with twin nanocalorimeters, equation 4.6, is approximately zero (see figure 4.3.f), if both RCC and SCC have the same total addenda, i.e $C^A_{P_S}(T) = C^A_{P_R}(T) = C^A_P(T)$, and if the difference between T_R and T_S is small enough at each time t, during the calorimetric scan, to consider $C^A_{P_S}(T_S) = C^A_{P_R}(T_R)$. Only near these conditions, it is possible to rewrite the difference in heat capacity between the two calorimetric cells, introducing the differential measurement of $\triangle V(t) = (V_S(t) - V_R(t))$, as previously shown by Allen et al. [24]. The heat capacity difference between calorimetric cells, i.e. equation 4.6, can be written in a general formula, independently of the sample presence, as the difference between the two calorimetric cells by directly measuring V_R and V_S, as:

$$\triangle C^A_P(T_S(t)) = \frac{V_S(t)\cdot I}{\beta_S(t)} - \frac{V_R(t)\cdot I}{\beta_R(t)}. \tag{4.11}$$

which can be rewritten as:

$$\triangle C^A_P(T_S(t)) = \frac{V_R(t)\cdot I}{\beta_R(t)} \cdot \left\{ \left(\frac{V_S(t)}{V_R(t)} \cdot \frac{1}{\beta_S(t)/\beta_R(t)} \right) - 1 \right\}. \tag{4.12}$$

Where the time derivatives are still the main sources of noise. In the first term, with

β_R in the denominator, the noise can be drastically reduced since it refers to the reference calorimetric cell (no sample). Therefore, after the previous thermal stabilization process, β_R can be obtained free of noise by a statistic measurements or by fitting it with a low order polynomial regression as it is a monotonic function. Inside the brackets, the term $\beta_S(t)/\beta_R(t)$ is the most noisy, but it can be replaced in terms of $\triangle V(t)$, using its derivative in time:

$$\frac{d\triangle V}{dt} = \beta_S(t)\cdot\frac{dV_S}{dT}|_t - \beta_R(t)\cdot\frac{dV_R}{dT}|_t. \tag{4.13}$$

$$\beta_S(t)/\beta_R(t) = \frac{d\triangle V/dt}{\beta_R(t)\cdot(dV_S/dT)|_t} + \frac{(dV_R/dT)|_t}{(dV_S/dT)|_t}. \tag{4.14}$$

Assuming that $T_S(R) = T_R(R)$, and that both resistances are fed by the same current I, equation 4.14, can be rewritten as:

$$\beta_S(t)/\beta_R(t) = \frac{d\triangle V/dt}{\beta_R(t)\cdot I\cdot(dR/dT)|_t} + 1. \tag{4.15}$$

As the signal of $\triangle V(t)$ is small and its temporal differentiation too, equation 4.15, can be approximated as:

$$\frac{1}{\beta_S(t)/\beta_R(t)} \approx 1 - \frac{d\triangle V/dt}{\beta_R(t)\cdot I\cdot(dR/dT)|_t}. \tag{4.16}$$

Considering in equation 4.12 that $\frac{V_S(t)}{V_R(t)} \approx 1$, and introducing equation 4.16, we obtain an expression of the difference of heat capacity between the two calorimetric cells in terms of the differential voltage [24],

$$\triangle C_P^{A,X}(T_S(t)) = -\frac{V_R(t)}{\beta_R^2(t)\cdot(dR/dT)|_t}\cdot\frac{d\triangle V}{dt}. \tag{4.17}$$

where the superscript X denotes that differential approximations have been already performed.

In this formula, as we have described above, the terms $V_R(t)$ and $\beta_R^2(t)$ are free of noise, $(dR/dT)|_t$ is the TCR coeficient and $\frac{d\triangle V}{dt}$ contains all the calorimetric information. It is necessary to emphasize that $\triangle V(t)$ is a relatively free of noise differential signal where common noises (in time domain) are completely rejected. The differential signal, can be widely amplified, the limit of amplification is related to the initial difference between the two calorimetric cells.

Here again, like in non-differential measurements, computing the averaging on temperature domain, if it is possible, reduces the noise more efficiently. Rarely, the original assumption of identical calorimetric cells is accomplished, and initial differences between heat capacity addendas and between the resistances exist. Therefore, the first correction in order to consider the heat capacity of the sample, is to substrat the initial differences between calorimetric cells, which is called the baseline correction. The heat capacity of the sample can be expressed as:

$$C_P^{A,X\,sample}\left(T_S\right) = \Delta C_{P_1}^{A,X}\left(T_{S,1}\right) - \Delta C_{P_0}^{A,X}\left(T_{S,0}\right) \tag{4.18}$$

In this last expression, we introduce an extra error related with the change of heating rates between the experiment with the empty SCC and the SCC with sample. The $C_P^{A,X\,sample}$ is evaluated in Ts domain, however to obtain $\Delta C_{P_1}^{A,X}$ and $\Delta C_{P_0}^{A,X}$, we evaluated them with the differential expression 4.17, where we subtract to the heat capacity of the sample cell at a given T_S the heat capacity of the reference cell at the T_R that corresponds to the same time. For the reference calorimetric cell, the heating rate of the RCC is equal before and after sample deposition in the SCC. However the SCC reduces its heating rate when the sample is present. Therefore, the corresponding $T_{R,1}$ is higher than $T_{R,0}$ for a given T_S, since β_R remain invariant and $\beta_{S,1}$ is smaller than $\beta_{S,0}$. As the final subtraction is perform in T_S domain, when $C_P^{A,X\,sample}\left(T_S\right)$ is evaluated we overestimate a term, that can be corrected by:

$$Corr\beta\left(T_S\right) = C_{P_{R,1}}^{A}\left(T_{S,1}\right) - C_{P_{R,0}}^{A}\left(T_{S,0}\right) \tag{4.19}$$

where $C_{P_{R,1}}^{A}\left(T_{S,1}\right)$ corresponds to the single heat capacity of the reference calorimetric cell evaluated at $T_{S,1}$, and $C_{P_{R,0}}^{A}\left(T_{S,0}\right)$ is the single heat capacity of the reference calorimetric cell evaluated at $T_{S,0}$. This data can be easily obtained from nondifferential signals acquired during calorimetric scans, and the relation between T_R and T_S can be extracted for each scan. Nevertheless, these two signals ($C_{P_{R,1}}^{A}$and $C_{P_{R,0}}^{A}$) are noisy since are obtained from nondifferential expressions. Typically, a liniar fitting is applied to remove noise before the subtraction of this correction to the $C_P^{A,X\,sample}\left(T_S\right)$, linear fitting is denoted by lf superscript.

$$Corr\beta^{lf}\left(T_S\right) = A + B \times T_S \tag{4.20}$$

Therefore, the heat capacity of the sample can be corrected in a first step by the

expression:

$$C_{P,\,corr\beta}^{A,X\ sample}\left(T_S\right) = C_P^{A,X\ sample}\left(T_S\right) - Corr\beta^{lf}\left(T_S\right) \tag{4.21}$$

A scheme of the correction for the change of heating rates of SCC is presented in figure 4.4, in order to clarify the former discussion.

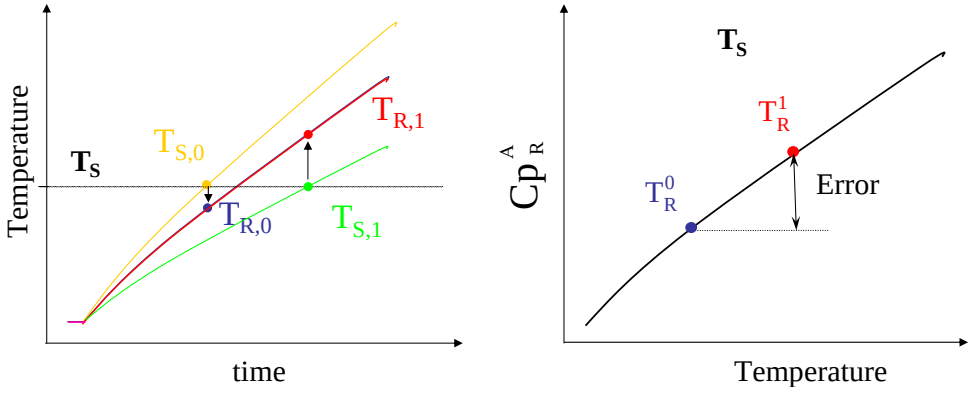

Figure 4.4: Scheme of the $Corr\beta$.
In the left figure all temperature versus time signals are represented. As shown the heating rate of the SCC decreases (from yellow to green curve) and the heating rate of the RCC remains constant (blue and red curve). Evaluating the $C_P^{A,\,sample}$ at a given T_S, the corresponding T_R is different from the idle to the experiment with sample. It promotes an error in the $C_P^{A,\,sample}$, since $C_{P_{R,1}}^{A}\left(T_{R,1}\right) - C_{P_{R,0}}^{A}\left(T_{R,0}\right)$ is not zero, and ideally should be cancelled.

When the sample heat capacity is large the β_S change drastically, and the correction can become larger than the original signal. This fact introduces some restrictions on the amount of mass that it is possible to analyze in differential mode. Typically, samples bellow 50 nm thick can be routinely analyzed by this procedure. As an example, we show in figure 4.5 the raw experimental data for a 5 nm In thin film, after an average of 500 scans and smoothing the signal with a box of 10 points. Raw data was acquired at 50 KHz and a resolution around 20 pJ/K was reached. The result extracted from the differential method, using equation 4.21, is compared with the nondifferential approximation, confirming the improvement in the signal-to-noise ratio. Figure 4.5 (a) shows the noise reduction in the heating rate curve, after the numerical method has been used to reduced the noisy effect of the derivative. Figure 4.5 (d) shows the final results for the heat capacity of a 5 nm thin film obtained with both methods: differential $C_P^{A,X\ sample}$and nondifferential $C_P^{A,\,sample}$. Similar absolute heat capacity values are obtained with both methods as it can be clearly

seen in the inset of figure 4.5 (d), after correction 4.19 , is applied in the differential method, $C_{P,corr\beta}^{A,X\ sample}$.

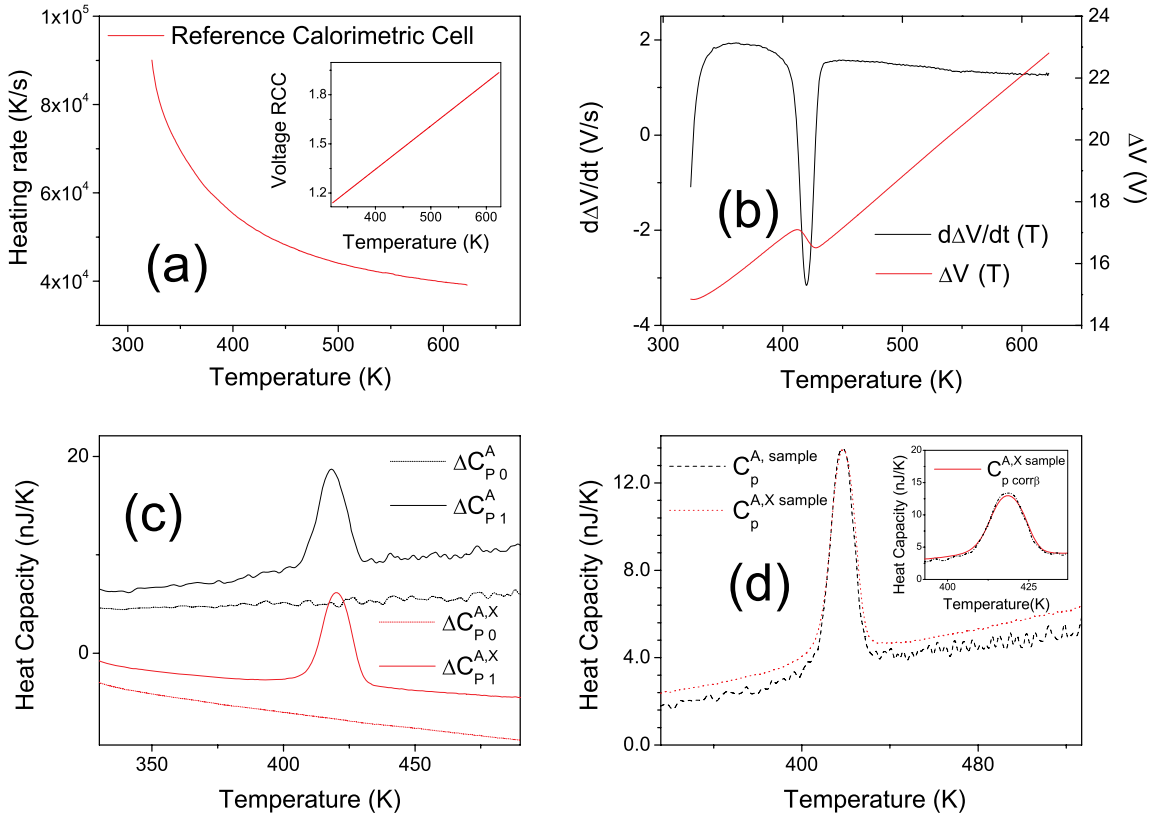

Figure 4.5: Differential measurements.
The raw experimental data used in the differential measurements for a 5 nm In thin film, after the numerical treatments. (a) Shows the heating rates vs temperature free of noise after polynomial fitting. The inset represents the voltage drop in the RCC as function of time. (b) The $\triangle V$ and its time derivate $\frac{d\triangle V}{dt}$ are represented as a function of temperature. (c) In red is plotted both the $\Delta C_{P_0}^{A,X}$ previous to sample deposition and $\Delta C_{P_1}^{A,X}$ once the SCC contains the sample. The difference between the heat capacities of the CC is also calculated with the non-differential mode and plotted in black for both before and after the sample deposition. (d) shows the final results for the heat capacity of 5 nm thin film obtained with both methods: the differential and nondifferential. The inset shows how the correction 4.19, $C_{P,corr\beta}^{A,X\ sample}$, produces identical values in both the differential analysis and the nondifferential, but with a much more better SNR in the first case.

Heat loss corrections. In the expressions for heat capacity presented above (nondifferential and differential mode) adiabatic conditions are assumed. However, at high temperature the nanocalorimeters are far from ideal behaviour and power losses become relevant to the heat capacity evaluation. The corrections to be performed depend on a proper estimation of the real P_{losses} term for every calorimetric cell in all the scans. First, we identify this term in the differential equation that describes the nanocalorimeters.

$$C_p(T) \cdot \frac{dT}{dt} = P_{heater}(t) - K_{th} \cdot (T - T_{frame}) - e \cdot \left(T^4 - T_{Room}^4\right) - h \cdot (T - T_{Room}) \quad (4.22)$$

where C_p is the heat capacity of the calorimetric cell, T is the average temperature in the calorimetric cell, P_{heater} is the power introduced by the heater in the calorimetric cell, T_{frame} is the temperature of the silicon frame, T_{Room} is the room temperature and K_{th}, e and h are the parameters that describe radiation and convection losses, respectively. From the general expression, it is possible to identify P_{losses} as:

$$P_{losses}\,(T) = K_{th} \cdot (T - T_{frame}) - e \cdot \left(T^4 - T_{Room}^4\right) - h \cdot (T - T_{Room}) \quad (4.23)$$

In a first approximation, we tried to use this model with lumped parameters to simulate the behavior of the nanocalorimeter when is fed by a constant current pulse, fitting the parameters (K_{th}, e, h) with experimental data. Several previous conditions were imposed over each parameter to simplify the fitting and keep its physical meaning: (i) h was fixed to zero, since under vacuum conditions convection losses can be neglected in comparison with the other terms, (ii) we used e as a radiation constant (that over 500K turns to be the most important channel for heat losses) and finally, (iii) the thermal conductance was chosen with a linear dependence with temperature. However, it was not possible to fit the experimental data for different heating rates with the same parameters. The main conclusion extracted from this test is the highly dependent behaviour of the K_{th} term with heating rates. In reality, the thermal conductivity can not be only understood as a heat transfer promoted by the differences in temperatures between the centre of the membrane (the calorimetric cell) and the Si frame. The thermal profiles in the rest of the membrane play an important role, since the conductive losses of the calorimetric cell depend on the surrounding temperatures of the calorimetric cell boundaries. This dependence explains the diversity of conductive parameters needed to fit the data for the different heating rates, but also informs about the hysteresis of K_{th} from heating to cooling. This behavior is related to

the variation of the temperature map, which depend on the previous temperature history. This hysteresis prevents an accurate evaluation of P_{losses} directly from the cooling behaviour of the nanocalorimeters. On the contrary, the parameter e only depends on the temperature of the calorimetric cell independently of the heating rate applied (since different heating rates do not change significantly the thermal profiles inside the calorimetric cells).

This limitation reduces the possibility to calculate the P_{losses}, to obtain it from the raw data during heating. However, while from previous results it is clear that the P_{losses} term slightly depends on heating rate, when we look at the equation 4.2, its variation can be neglected compared to the high change of P_{heater} needed to increase the heating rate. Consequently, the contribution of P_{losses} to the heat capacity measured with equation 4.3, decreases when the heating rate increases. Therefore, an estimation of P_{losses} can be obtained by comparing the heat capacity measured at different heating rates in a single nanocalorimeter. Figure 4.6, shows the heat capacity measurements for a single serpentine-type nanocalorimeter, for different injection currents promoting different heating rates. The smaller is the current the smaller is the heating rate, and therefore the ratio between P_{losses}/P_{heater} becomes larger (in equation 4.2) and, as can be appreciated in the experimental curves, the measured heat capacity has a larger contribution from heat losses. In the limit of an infinite heating rate, the P_{heater} should also grow to infinite while P_{losses} will remain finite. Then, if for a given temperature we plot the heat capacity values of the calorimetric cell measured at different heating rates as a function of the inverse of the heating rate, the points will be aligned and the heat capacity for an infinite heating rate Cp^{∞}(it means without losses) can be extracted from a linear regression, see figure 4.6. With this approximation the $P^{\beta}_{losses}(T)$ term can be calculated for each heating rate β and for each temperature, as the $\left(Cp^{\beta}(T) - Cp^{\infty}(T)\right) \cdot \beta(T)$.

This methodology, applied for each calorimetric cell before and after sample deposition, produces four noisy $P^{\beta}_{losses}(T)$ functions. To eliminate the noise, these functions can be fitted with a polynomial (denoted by superscript pf), with the following appearance:

$$P^{\beta pf}_{losses}(T) = A + B \cdot (T - T_{frame}) + C \cdot \left(T^4 - T^4_{Room}\right) \tag{4.24}$$

The term A ideally should be zero. However, we have evidenced that the linear fitting procedure introduces some errors in P_{losses} and the curves are slightly shifted to positive values at low temperature. In this temperature range the dependence of P_{losses} with conduction (K_{th}) become more relevant since at the beginning of the heating process the transients temperature maps are sharpening when increasing the heating rates and it may

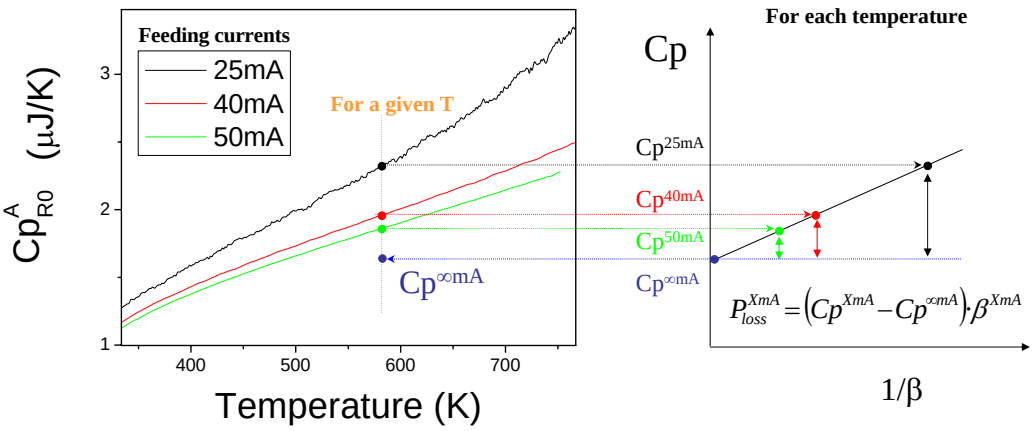

Figure 4.6: Estimation of P^{β}_{losses} from the behaviour of single calorimetric cells at different heating rates.

introduces some non-linearity in obtaining Cp^{∞} that can be appreciated as a shift. This error tends to zero at high temperatures when emissivity dominates. In order to consider the final losses we always impose A equal. At low temperatures, the value of $P^{\beta pf}_{losses}$ is very small and the heating rates β are the largest in the scan. In the final correction of heat capacity, the P_{losses} term is weighted by the β, and therefore, the error is minimized.

Figure 4.7 shows the four polynomial functions $\left(P^{\beta pf}_{losses}(T)\right)$ extracted from a specific experiment, where we analyze the heat capacity of a 9nm Ni thin film. It is possible to observe how the $P^{\beta pf}_{losses}$ for the sample calorimetric cell increases showing that thermal losses increase, however the reference calorimetric cell remains equal.

In order to obtain the global heat loss correction expression, it is necessary to compute all contributions of $P^{\beta pf}_{losses}/\beta$ in the T_S domain:

$$CorrP = -\frac{P^{\beta pf}_{losses,S,1}}{\beta_{S,1}}(T_S) + \frac{P^{\beta pf}_{losses,R,1}}{\beta_{R,1}}(T_S) + \frac{P^{\beta pf}_{losses,S,1}}{\beta_{S,1}}(T_S) - \frac{P^{\beta pf}_{losses,R,1}}{\beta_{R,1}}(T_S)\,; \qquad (4.25)$$

When this expression is calculated we obtain, again, a noisy correction since some noise is introduced in the $P^{\beta pf}_{losses,R}$ terms when they are expressed as function of T_S, using the $T_S(T_R)$ relation, and, of course, when are divided by the heating rate data. This correction should be applied either in the nondifferential and in the differential method in order to subtract the losses contributions. As an example, figure 4.8 (a) shows the main

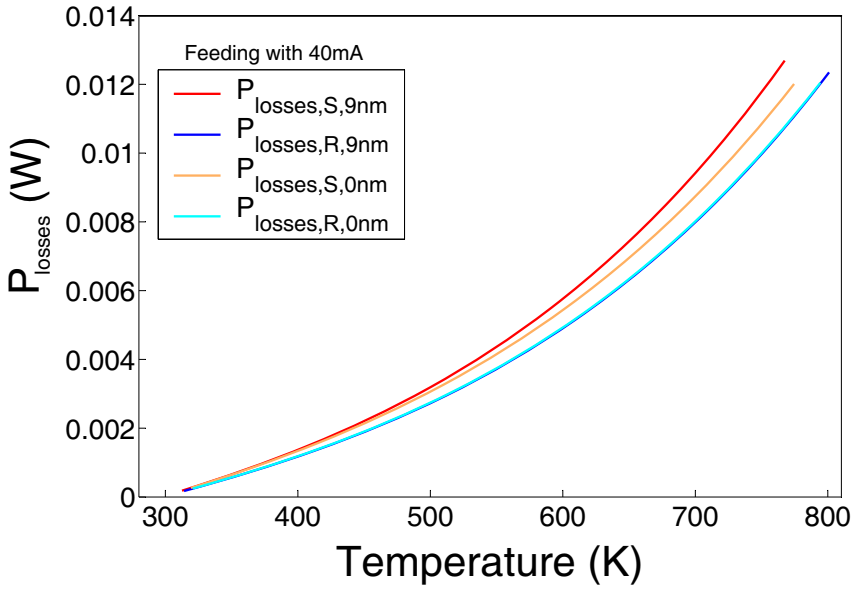

Figure 4.7: Calculated P^{β}_{losses} in the nanocalorimetric measurements with 9nm Ni.

curves in the heat capacity analysis of a 9nm Ni thin film deposited on a meander-shape nanocalorimeter and figure 4.8 (b) shows the final result for the real heat capacity once a polynomial fit of $CorrP + Corr\beta$ has been subtracted to $\Delta C^{A,X}_{P_1}(T_{S,1}) - \Delta C^{A,X}_{P_0}(T_{S,0})$.

$$C^{A,X\,sample}_{P,\,real}(T_S) = \Delta C^{A,X}_{P_1}(T_S) - \Delta C^{A,X}_{P_0}(T_S) - CorrP^{pf}(T_S) - Corr\beta^{lf}(T_S)\,; \quad (4.26)$$

The methodology outlined above is applied to reversible transformations with a monotonic behavior of the different parameters. Irreversible reactions should be analyzed differently.

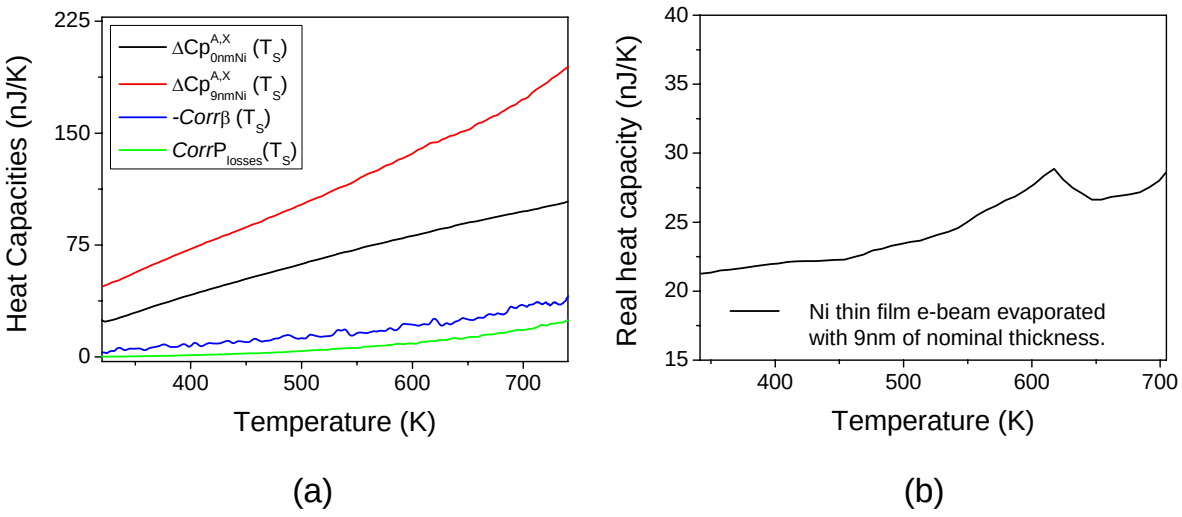

Figure 4.8: (a) Example of experimental curves and corrections for a nanocalorimetric measurement on a 9 nm Ni thin film. At higher temperatures the correction for power losses may become the main source of corrections. (b) Resulting real heat capacity after correction for the 9 nm thin film.

4.2 Case study: In ultra-thin films.

Measurements on ultra-thin layers of Indium with different thicknesses are presented. Indium has been widely used in investigations of melting in small particles by different groups [55, 58], and it is a good test to check the potentialities of the nanocalorimeters and to learn about the measurements and data analysis procedure. The small sample mass involved in these experiment combined with the low heat of fusion of indium, is a hard test that will show the capabilities of the nanocalorimeters. As Indium has a low affinity with the SiO_2 film that covers the bottom of the membrane, during the first calorimetric scans the deposited In film dewets to forms a discontinuous film that consist on nanoislands. The average size of the nanoparticles increases almost linearly with the equivalent indium thicknesses [59]. For low enough thickness, it is expected to appreciate the depression in both the melting point and the latent heat of fusion, according with established theories [60, 61, 62, 63, 64]

4.2.1 Experiment and results

The calorimetric experiments are carried out inside the UHV chamber of the e-beam evaporator of the Laboratori de Capes Primes at UAB, at a pressure below 10^{-6} mbar, see experimetal for in-situ measurements in figure 3.5. A previous experiment showed up the necessity to perform in-situ measurements when ultra thin film samples of indium are analyzed, since surface oxidation (around 3nm [59]) may occur during the transfer to the ex-situ HV chamber. A couple of twin U-shape nanocalorimeters with a metallic heater made of 75 nm of Pt with 10 nm Ti as adhesion layer are employed. Previous to the experiments, an in-situ self-annealing is performed with a series of ten thousand heating ramps until 775 K, around 100 K over the maximum temperature in the scanning measurements, with same current values than in the experiments. This procedure guarantees the thermal stability, and cleans the membrane surface from organic contamination. For the experiments two pair of nanocalorimeters were prepared. The first with a thermal layer made of 150 nm of Ag, using 10 nm of Ti as adhesion layer and capping it with 20 nm of SiO_2 to avoid formation of In-Ag intermetallic phases during calorimetric scans. The second with a bare membrane, with the SiO_2 layer. The parallel experiment gives the possibility to check and compare, the sensitivity, the accuracy and the resolution for both cases. In each one a previous characterization of the empty nanocalorimeter (after the stabilization), that consist on a series of 2000 calorimetric scans, at heating rates around $\sim 5 \cdot 10^4$ K/s was

performed. To reach those heating rates, current pulses of 10 mA and 14 mA were input to the nanocalorimeter with the bare membrane microdevice and with the thermal layer, respectively. From these measurements we calculated the initial heat capacity difference (the baseline) between calorimetric cells, previous to the sample deposition.

In both experiments a sequence of In films are deposited onto the backside of the membrane of the sample calorimetric cell. Using a microfabricated shadow mask the sample is only deposited over the sensing area. The evaporation rate of Indium is fixed to 0.02 nm/s, controlling the power of the e-beam evaporator. The nominal thickness of the layers is calculated by comparison with an in-situ quartz microbalance which has been previously calibrated for the experimental conditions. After each deposition series of calorimetric scans are performed, and the next deposition is added to the previous sample material.

The thicknesses of indium analyzed were 2, 4, 8, 16, 24, 32, 40, 50, 60, 80, 100, 150, 200 and 400Å. Up to 16Å, averaging of 1000 consecutive scans was performed, for higher thicknesses 500 were enough to minimize noise. Those measurements produce a high quantity of data, that was treated with the numerical method explained above, using MATLAB. Figure 4.9 (a) and (b), show the heat capacity curves as a function of temperature, obtained from the calorimetric measurements in both experiments. These curves have been calculated using the differential expression, i.e $\Delta C_P^{A,X}(T)$, considering the baseline correction, the initial difference of heat capacities between both calorimeteric cells calculated with the same expression. As it will be shown below the difference in the shape of melting peak between figures 4.9 (a) and (b), is related to the temperature profiles in the nanocalorimeters, without and with thermal plate.

4.2.2 Discussion.

The shape of the calorimetric traces is remarkably different in both cases. Whereas Indium on the bare membrane shows one peak with a narrow full-width-at-half-maximum (FWHM), the sample growth on the thermal plate shows a large FWHM and several consecutive peaks that cannot be resolved. In fact, the FWHM of the indium sample on the bare membrane is dominated by the size distribution of the population of indium nanoislands, each one with a different melting temperature. The enthalpy of the melting transition and the heat capacity values at low temperatures, both proportional to the sample mass involved in the measurements, are also remarkably different for both set of curves.

In order to understand the shape of the heat capacity curves and to confirm that is linked to the thermal profile we modified the thermal modelling program described in

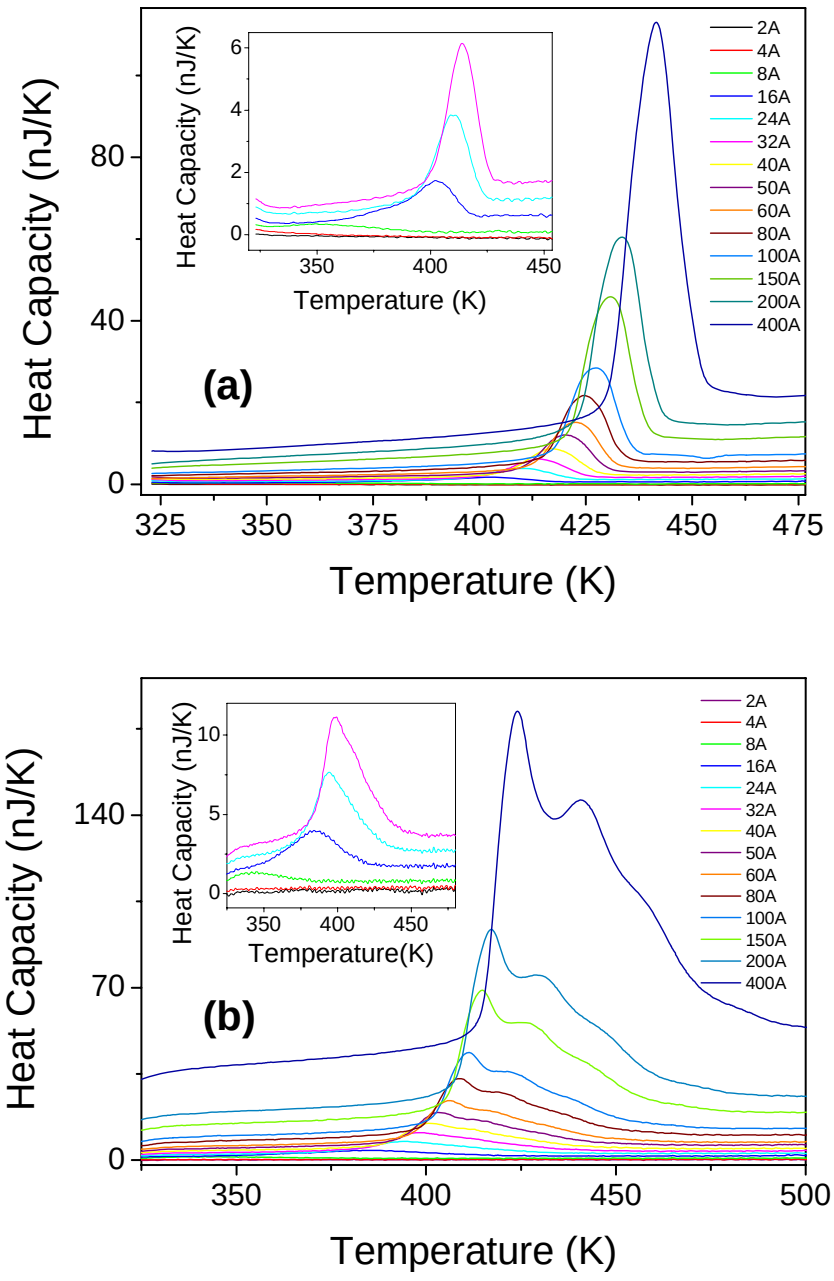

Figure 4.9: Heat capacity .vs. temperature curves for all the deposition thicknesses of indium. (a) Over the bare membrane and (b) over the membrane with a Ag thermal layer of 150 nm. The inset shows a zoom view of the smaller thicknesses in each case.

chapter 2, to reproduce the heat capacity data, by incorporating in the mesh an Indium film on the backside of the membrane. The In film will experience a first order transition at a given temperature. To model this type of transition (melting) we fix the temperature of each sample volume in the mesh, until the total energy required to promote the solid-to-liquid transition is attained. At this stage, the volume is liberated and rises its temperature again. With this simplified approach we prove the tight relationship between temperature profiles, the area of analysis and the shape of the calorimetric traces.

Figure 4.10 (a) shows the modeled heat capacity data (addenda+sample) for a single nanocalorimeter with a sample of 10 nm of Indium. The three surface colour-plots in the figure correspond to the frame caption of the surface for sequential average temperatures showing a contrast difference between melted and unmelted In regions. In green color is painted the area where indium is melted. At $5 \cdot 10^4$ K/s the simulated sequence reveals that with the empty nanocalorimeter, melting occurs only beneath the heater metalization. Under this assumption the temperature differences on the sensed area (only below the heater) is very small, and the heat capacity curves represents the true value of the material which is beneath the heater. This result explains the narrow FWHM of the experimental melting peaks.

The same type of figure, but including a thermal layer is shown in figure 4.10 (b). The addition of the thermal layer (150nm Ag) improves the thermal homogeneity, but the frames show that although all the indium (10nm thick) in the sensing area melts, due to temperature non uniformities the FWHM of the peak is larger and the shape is not representative of the melting of a pure substance. In fact, from the surface plots we can infer the main difficulty arises due to the thermal gradients that exist in the longitudinal direction.

These results demonstrate that at fast heating rate the addition of a thermal layer degrades the calorimetric data for the U-shape design. However, the thermal layer will become essential to perform power compensated with variable speed calorimetry, in order to leave the thermal resistance of the calorimetric cells unvariable. Also from this result we get valuable information about the sensing area, for the calorimeter without plate, which enables part of the further analysis for In samples shown in this section. This result has been basic on the redesign of the heater geometry, improved in the serpentine-type design.

Analysis of experimetal Cp curves for the nanocalorimeter without thermal layer. The indium mass can be estimated from the heat capacity values at 333K, dividing

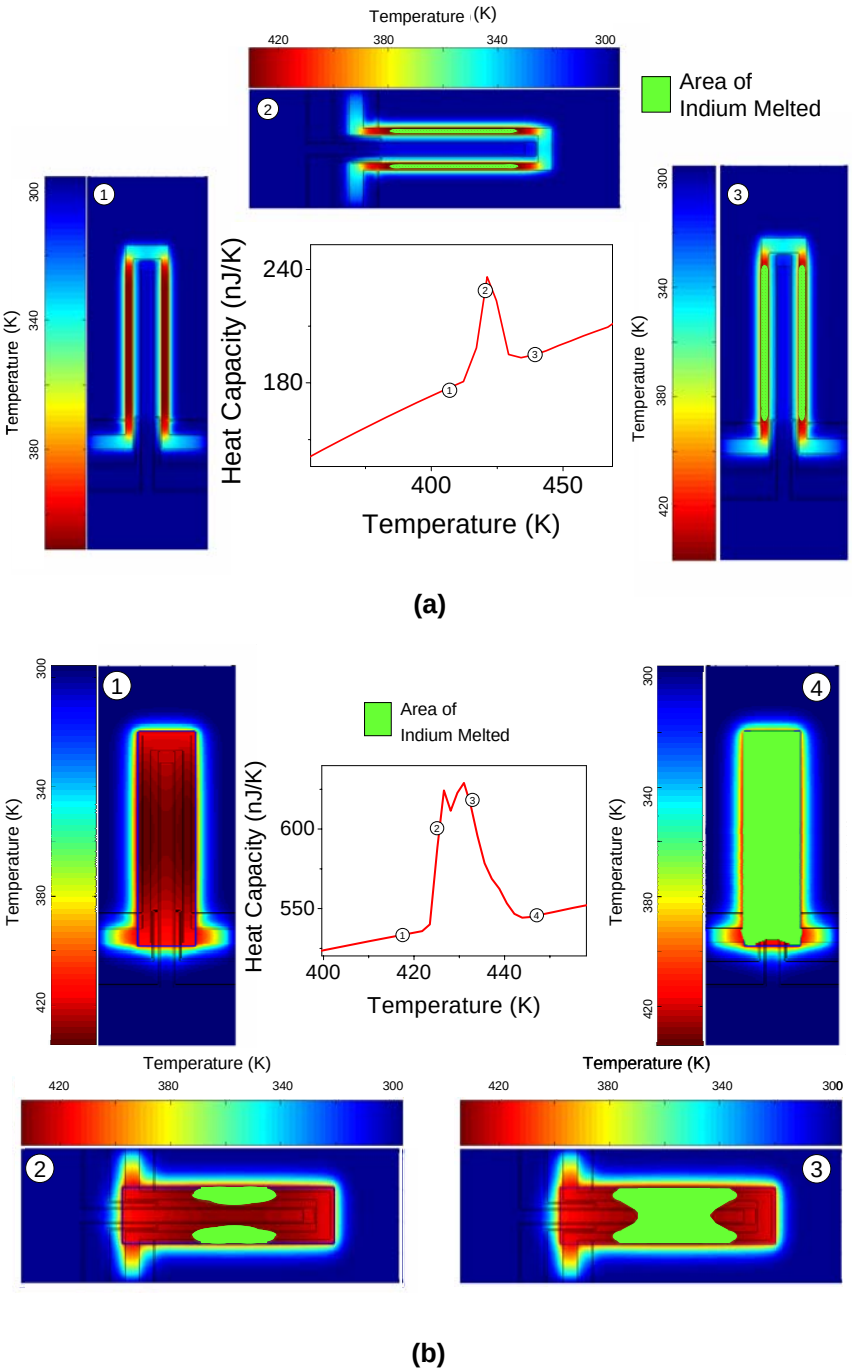

Figure 4.10: Modelled curve for the calorimetric measurement of 10 nm In in a bare membrane (a) and with a 150 nm of Ag as a thermal layer (b). The frames show the profile of temperatures over the membrane and the area of indium melted marked in green.

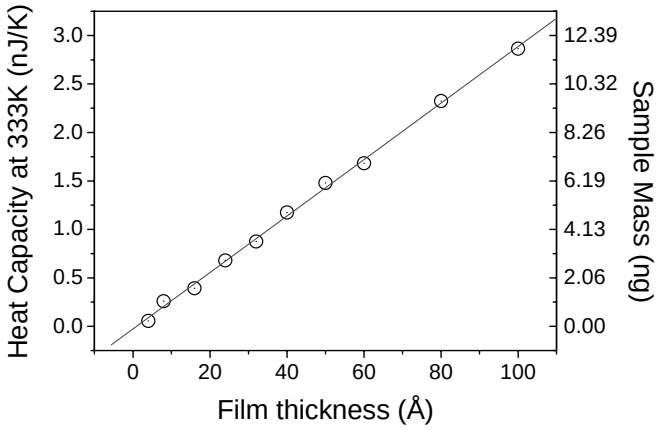

Figure 4.11: Heat capacity at 333 K and Sample mass vs film thickness measured with quartz microbalance.

by the specific heat at this temperature. The values obtained confirm that the sensed area is only beneath the Pt heater in the nanocalorimeter without plate and the complete plate area in the nanocalorimeter with the thermal layer. The thickness obtained from the crystal quartz monitor in the evaporation setup has been used to estimate the sensing area, obtaining a good agreement in both cases. Since the effective temperature profile in the sensing area is better in the microdevices without thermal plate, we focus our analysis in this experiment. The calculated sensing area is (0.161±0.006) mm^2, and it is not dependent on the sample thickness, with a variation smaller than 3%. Comparing this area with the value of the area beneath the heater, 0.155 mm^2, we conclude that the information extracted from the modelling is accurate. A key point, which corroborates that the sensing area is constant is the linear dependence of the heat capacity with the thickness, see figure 4.11. The combination of high heating rates with the bad wetting behavior of liquid indium over the membrane, prevents the lateral growth of the sensing area produced by the contribution of sample to the heat conduction. Figure 4.11, also shows how the nanocalorimeter can be used as a nanobalance, to measure ultra small masses. For example, in case of 16Å indium deposition, the mass involved in the analysis is around 1.6 ng [10]. The information extracted from the calorimetric curves in figure 4.9, is compiled in table 4.1.

Figure 4.12 shows the heat capacity curves presented in figure 4.9, normalized by the

[10]Dividing the heat capacity value at 333 K, 0.393 nJ/K, by the specific heat capacity at that temperature [39]

$Thickness$ (Å)	$Cp\,at\,333K$ (nJ/K)	m (ng)	$T^{m}_{onset\ peak}$ (K)	$\triangle H$ (nJ)	$FWHM$ (K)	H_m (J/g)
4	0.056	0.2	-	-	-	-
8	0.258	1.1	-	-	-	-
16	0.393	1.6	380.4	35	22.8	21.6
24	0.680	2.8	394.0	55	16.6	19.4
32	0.875	3.6	401.0	76	14.4	21.0
40	1.174	4.8	405.3	102	13.6	21.0
50	1.478	6.1	412.4	136	12.8	22.3
60	1.681	6.9	415.6	168	12.6	24.2
80	2.324	9.6	417.5	229	11.8	23.9
100	2.865	11.8	421.0	338	12.2	28.5
150	4.535	18.7	424.2	477	11.8	25.5

Table 4.1: Characteristic magnitudes extracted from calorimetric measurements of indium different thicknesses, presented in figure 4.9.

mass. The shift of the peaks as the thickness decreases shows the dependence of melting temperature with the nanoparticle size. As the indium deposition forms a discontinuous film made of nanocristals, each nanocristal size contributes to a specific melting temperature. Complementary TEM analysis may enable to associate the shape of the peaks with the size distribution of nanocrystals [59]. The dispersion in the size distribution of the nanocristals is directly related with the FWHM of the calorimetric peaks. The broadening of the peak as the film thickness decreases shows that the size dispersion increases.

Figure 4.13 shows the evolution of the melting peak as a function of the deposited film thickness. The melting temperature was obtained by extrapolation of the baseline and the slope of the melting peak. The temperature resulting from crossing of these two lines is defined as the onset for melting. These results are in agreement with the values obtained by M. Zhang et al. [59]. This phenomenum can be understood by a classical thermodynamic description of the melting behaviour of nanoparticles, which takes account of the surface/interface energy to evaluate the total free energy of the system. This approach leads to a $\triangle T(r) = T^{bulk}_{melting} - T_{melting}(r)$ dependence as r^{-1}. The inset of figure 4.13 shows the FWHM of the melting peaks as a function of deposited thickness, showing not only the small dispersion for nanocrystal size above 2 nm, but also the small temperature gradient in the sensing area of the nanocalorimeter (without thermal plate).

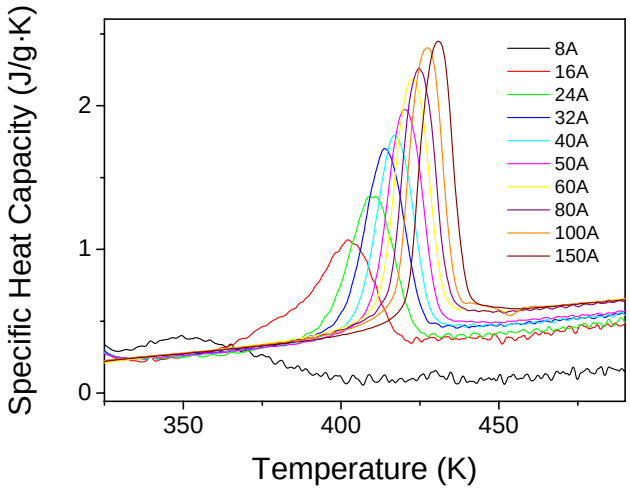

Figure 4.12: Specific heat capacity vs temperature, for the series of indium depositions in the microdevice without thermal plate.

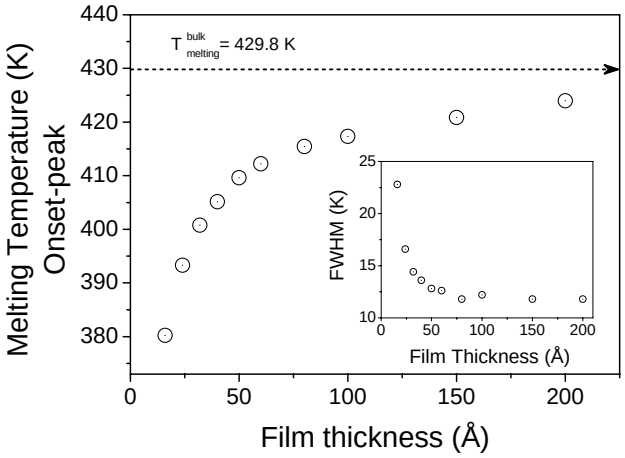

Figure 4.13: Melting temperature as function of equivalent thickness of indium deposition. To determinate the melting temperature the onset peak criteria is assumed. The inset shows the full width at half maximum (FWHM) of the melting peaks.

The value of the heat of fusion can also be extracted from the calorimetric curves, as the area under the melting peak in the Cp(T) curve $\left(H = \int Cp(T) \cdot dT\right)$. Figure 4.14 (a), shows the heat of fusion for the different apparent film thickness. The grey line shows the expected value assuming bulk parameters. While the correspondence is very good

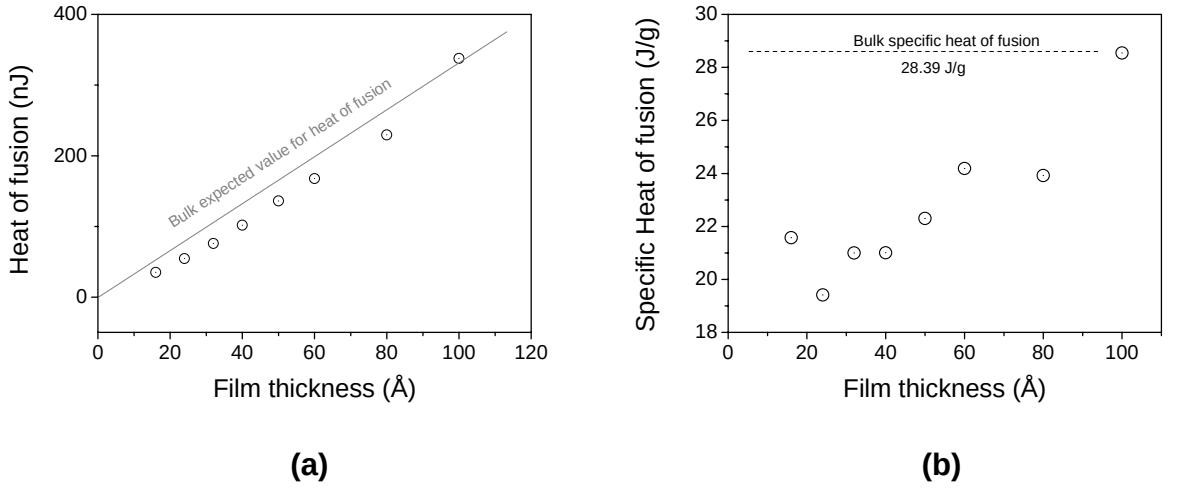

Figure 4.14: Heat of fusion (the integral on temperature of the heat capacity peak) and Specific heat of fusion as a function of the equivalent thickness of indium deposition measured by the quartz crystal.

for 10 nm sample it shows a reduction for the smallest films. Figure 4.14 (b), represents the heat of fusion by unit mass as a function of film thickness. The decrease of melting enthalpy with thickness is clear and it is also mainly related to a size effect, although other sources like the contribution of adatoms, may play a significant role at low thicknesses in the divergence between the measured mass and the energy below the melting peak.

4.3 Real-time measurements on In.

Adiabatic nanocalorimetry can be used to monitor thin film growth in real-time [65]. Following the same procedure detailed in last section, the indium thin film growth over the membrane can be followed in real-time by the calorimetric measurements. As we have already explained two consecutive calorimetric scans can be performed with time delays of 500 ms, the relaxation time needed to return to room temperature. With an evaporation rate fixed at 0.02 nm/s is possible to scan each 0.01 nm increments. As a result the technique generates a 3 dimensional data, shown in figure 4.15 (a), which shows the quasi-continuous growth changes during the evaporation, as a function of temperature and the thickness measured by the quartz crystal. The depression on the melting temperature is clearly appreciated with the 2D colour plot, see figure 4.15 (b).

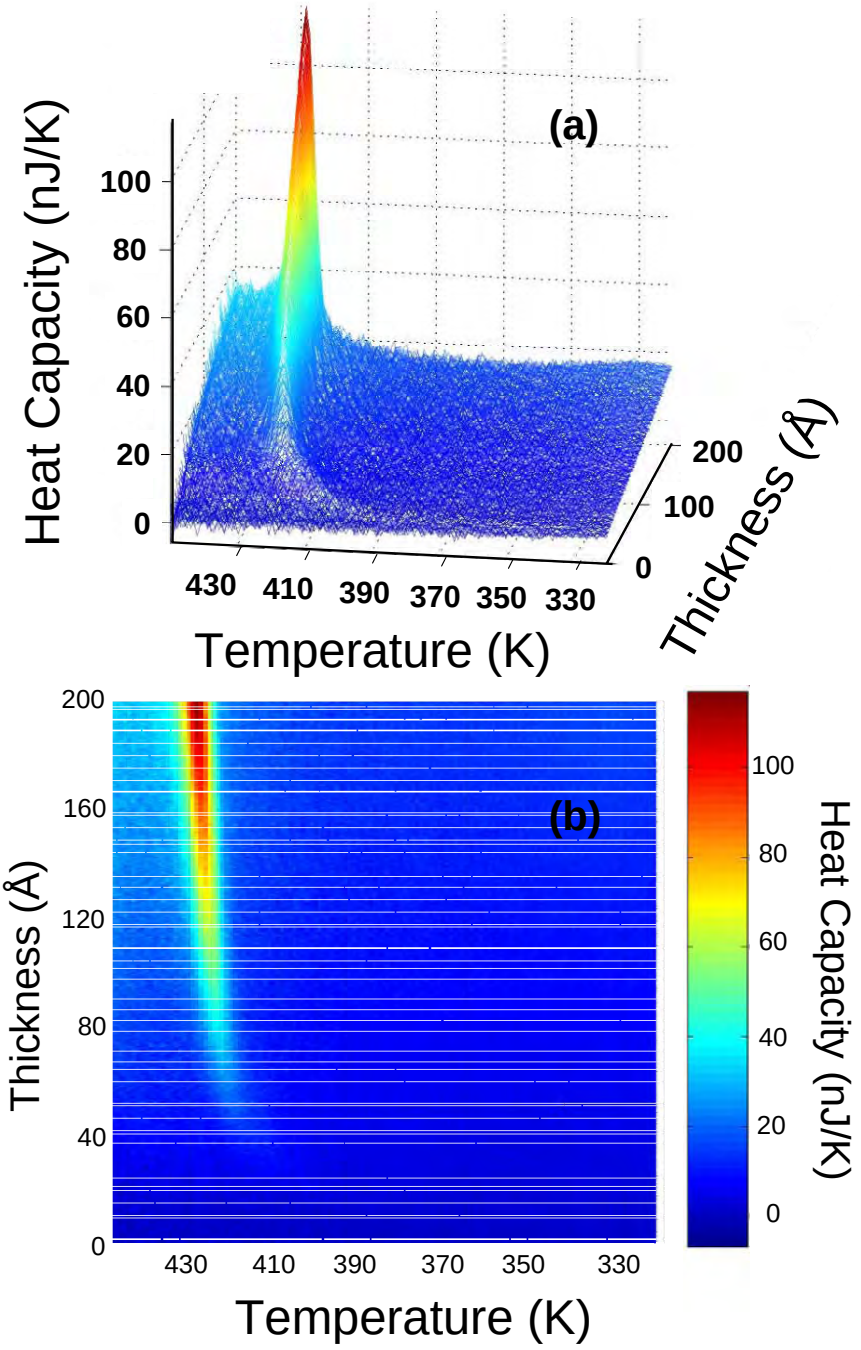

Figure 4.15: (a) 3D real-time heat capacity measurements during indium deposition as function of temperature and equivalent thickness of Indium. (b) 2D colour plot.

4.4 Analysis of Curie Transition in ultrathin films of Ni.

Thermal processes such as sublimation, vaporization and melting are called first order phase transitions because the first order derivates of the Gibbs energy function, the entropy S=-$(\partial G/\partial T)_P$ and the volume V=$(\partial G/\partial P)_T$ experience finite variations during the change. Other phase transition, named second-order or lately continuous, show a discontinuity in the second order derivates of the Gibbs free energy (such as heat capacity,..) whereas the first derivative remain continuous. When Ehrenfest introduced the criteria for the classification of the phase transitions it was thought that there were a large number of second order transitions. However, experimental measurements [66, 67] over different systems have shown that at temperatures close to a phase transition the heat capacity tends to non finite values in many cases. In fact, only superconductivity transition at zero magnetic field has been found to exhibit a pure second order transition.

Transformations such as order-disorder in alloys, ferroelectricity in some crystals, superfluidity in He or ferromagnetic to paramagnetic transitions at the Curie point in ferromagnetic materials are some examples of a type of second-order phase transitions known as lambda transitions. In the bulk the specific heat is a powerful tool to investigate phase transitions because it exhibits large variations near critical points. The theory predicts a power-law temperature dependence near the transition points. For the Curie transition in ferromagnets the specific heat is of the logarithmic type near Tc. The specific heat behaves symmetrically below and above the transition temperature, however the high-T branch is typically shifted down.

It is well known that the magnetic phase transition temperature in a magnetic thin film decreases as the film thickness D decreases according to [68]

$$\frac{T_{c0} - T_c(D)}{T_c(D)} = \left(\frac{D}{D_0}\right)^{\lambda}$$

where D_o is the characteristic length at which the magnetic phase transition disappear and λ is the shift exponent which characterizes the sensitivity of the transition temperature to the decrease in film thickness.

A crossover from power law to linear behavior is observed in the ultrathin film thickness limit, for a number of magnetic thin film systems [69, 70, 71]. However, the dimensionality has an important effect on the depression of the Curie transition and the above relation has been shown to be inappropriate for materials with lower dimensionality (nanoparticles or wires). A recent study of the shift of Tc with nanomemer diameter in Ni nanowires

shows a similar power law compared to ultrathin films, however, the authors observed that the rapid drop in Tc occurred at higher thicknesses than that of the Ni thin films [72]. They attributed this behavior to the S/V increase because spins at the surface have fewer spin interactions than those in the interior and the number of nearest magnetic interaction neighbors decreases. The magnetic exchange has also been shown to decrease [73]. In fact, the investigation of second-order transitions like the ferromagnetic-to-paramagnetic phase transition in clusters or even nanoparticle systems is still scarce[74].

Recently Jiang et al [75] have proposed a unified model for the Tc function that can be applied to low dimensionality systems. The model is based on thermodynamics and similarity arguments with other phase transitions and predicts an exponential dependence of the Curie temperature with well defined bulk parameters

$$\frac{T_c}{T_{co}} = exp\left[\frac{-2 \cdot \triangle Cp}{3 \cdot R \cdot ((D/D_o) - 1)}\right] \tag{4.27}$$

Where $\triangle Cp$ denotes the specific heat difference between bulk ferromagnetic phase and bulk paramagnetic phase at the bulk transition temperature. D is the nanoparticle diameter and $2D_o$ represents the critical size where the Curie transition is still present. When the film thickness is below 30 h (h, interlayer distance 2.492 Å in Ni [76]) the film is considered to be discontinuous (island-like configuration) and the magnetic domains also show an island-like pattern.

In this section we want to assess the performance of membrane-based nanocalorimetry in the analysis of lambda-type phase transitions in nanoscale materials. We chose Ni because it is a ferromagnetic material that experiences a ferromagnetic to paramagnetic phase transition at a temperature of 627 K[77], high enough to apply heat loss corrections but low enough to permit reproducible scans. Furthermore, the small change in specific heat at the Curie transition in combination with the small mass of the samples represents a good test on the capabilities of the technique.

4.4.1 Experimental.

A pair of identical nanocalorimeters with alumina-capped serpentine-type heaters are mounted inside the UHV e-beam chamber as described in chapter 3. The nanocalorimeters are isothermally annealed at temperatures over 800K to clean the Si_xN_y membrane. Nevertheless some carbon traces may remain from pyrolysis of hydrocarbons. To prevent any reaction of the Ni film with carbon traces we used a SiO_2 buffer layer, which is well known

to be a barrier diffusion layer of Ni up to temperatures around 1200K [78]. The 10 nm SiO_2 layer is deposited on both calorimetric cells at room temperature using the shadow mask. The material is e-beam evaporated from pure SiO_2 pellets under an oxygen rich atmosphere at 10^{-3} mbar. The oxygen presence prevents sub-stoichiometry in oxygen contents that can appear in SiO_2 if it is evaporated under high vacuum. The 10 nm thickness is chosen to ensure layer continuity. After the SiO_2 growth, the pressure is reduced again to 10^{-7} mbar. Series of hundreds of quasi-adiabatic scans up to temperatures around 800 K are carried out in order to obtain a previous characterization of the calorimetric cells and the initial discrepancy in heat capacity between them. In order to apply power loss corrections, the calorimetric scans are performed at different heating rates by injecting pulses with different current values (25, 40 and 50 mA). Subsequently, with the aid of the moving shutter the Ni sample is selectively grown in one of the nanocalorimeters, the other one is used as reference. Ni is evaporated from pure pellets in a high vacuum environment and the substrate is maintained at room temperature. The deposition rate is controlled, and fixed at 0.25 nm/s, by measuring the mass deposited in a quartz crystal monitor. During the evaporation the working pressure increases up to values around $5{\cdot}10^{-6}$ mbar. Previous to the deposition on the nanocalorimeters, the deposition rates and the microstructure are analyzed in Ni films grown onto thermally oxidized Si substrates. By using cross-section SEM the thickness of a thick Ni film (50 nm) is measured and the crystal quartz monitor is calibrated accordingly. X-ray diffraction analysis shows the polycrystalline nature of the Ni film, and the large full-width-at-half-maximum evidences the nanocrystalline nature of the grains.

Three sequential nominal thicknesses of Ni are analyzed by nanocalorimetry (3, 6 and 9 nm). In parallel, a set of moving shutters is used to deposit identical Ni thicknesses (3, 6 and 9 nm) and SiO_2 buffer layer onto 30 nm silicon nitride membranes used as grids for TEM analysis purposes. After each deposition, several scans at different heating rates (25, 40 and 50 mA) are realized to obtain the calorimetric data. The maximum temperature during the scans is fixed at 800 K to prevent any morphological change of the Ni surface [78].

4.4.2 Results

Figure 4.16 shows bright-field TEM photograps of the Ni films at the three nominal thicknesses evaluated in calorimetry. An island-like morphology which originates from a 3D Volmer-Weber growth is clearly identified in the thinnest sample (fig. 4.16 (a)) The film

is composed of quasi-spherical grains forming a meandering structure. Darker points in the TEM images correspond to thicker grains. Figure 4.16 (e) shows a detailed view of a nanoparticle of the 3nm film where the lattice planes correspond to the (111) crystalline planes of cubic Ni. The ED pattern shows the presence of a diffused halo associated to the amorphous structure of the grids and a more intense ring at 4.916 nm^{-1} that corresponds to the {111} family of planes for cubic Ni with planar distance of 0.2034 nm. To determine the average Ni nanoparticle sizes, the lateral diameter is evaluated from TEM images and the height is assumed from the nominal thicknesses of the thin films. The nanocrystals are roughly spherical with average diameters of 4, 6 and 8 nm for the thin films with 3, 6 and 9 nm of nominal thickness, respectively.

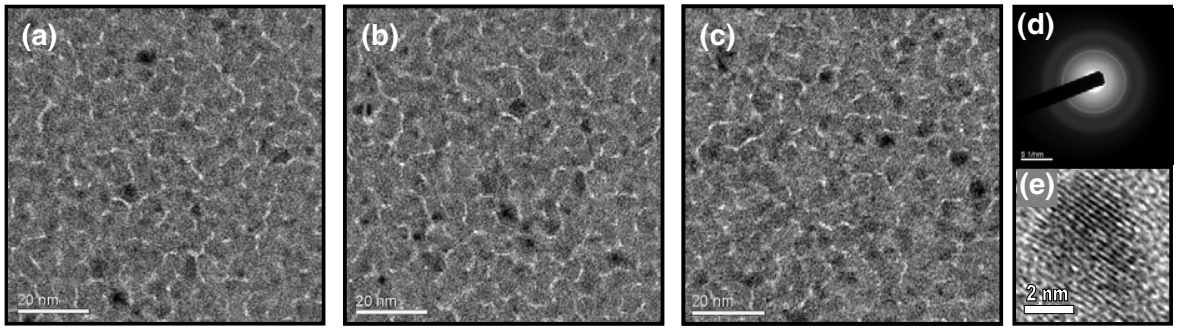

Figure 4.16: Planar view TEM pictures of Ni films of different nominal thickness. (a) 3nm; (b) 6nm; (c) 9nm; (e) shows a detail of a nanoparticle in the 3nm film. (d) ED pattern of the 3nm Ni film.

The heat capacity of the Ni thin films is determined from the raw data after applying the various correction steps detailed in section 4.1.2. Figure 4.17 shows the heat capacity data for the three Ni thicknesses evaluated at a heating rate of $4.2{\cdot}10^4$ K/s. Using a precalibration procedure (see section2.4) which empirically considers shadowing effects and the lower density of thin films compared to bulk materials, the mass of Ni evaporated in each calorimetric cell is estimated to be 16.2, 32.2 and 48.1 ng for the films with nominal thicknesses of 3, 6 and 9 nm, respectively. These values agree within 3% with the values obtained if the measured heat capacity is divided by the bulk specific heat at a given temperature m=$Cp(350K)/Cp_{esp}(350K)$. Some uncertainty remains here because of the tendency of small systems to present an increase in specific heat. According to Liu et al. [79] for Ni the enhancement in Cp in going from the polycrystalline material to the nanocrystalline state (40 nm diameter particles) is around 2-4% in the range 100-370 K, although this value may depend on the size of the particles.

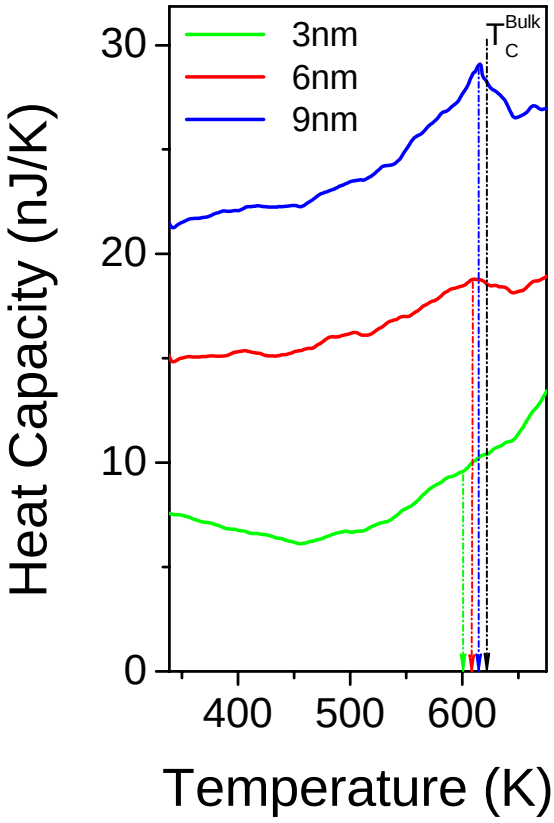

Figure 4.17: Heat capacity vs. temperature for Ni films of different thickness.

The heat capacity curves show a peak at a temperature close to the Curie temperature of Ni. The rounded appearance of the maximum in Cp is a characteristic feature of the measurements and should be related to the small size of the particles. The smallest particles show a more pronounced effect. The temperature of the transition, taken as the maximum in the heat capacity data, decreases with size reduction. Figure 4.19 (a) shows the normalized Curie temperature measured in the calorimetric trace as a function of the mean nanocrystal diameter for each film thickness. The corresponding values are written in table II, although the Curie temperature assignment for the thinnest film is susceptible of considerable uncertainty. The reduction with the size of the nanoparticle has been tentatively fitted with equation 4.27 using a D_o of 0.35 nm (dashed line in Figure 4.19 (a)). The fitting parameter D_o is slightly smaller than the value obtained from epitaxial Ni films grown on top of a Cu substrate which is 0.458 nm [69].

The specific heat of a ferromagnetic nanoparticle is composed of different contributions. The main one comes from lattice vibrations which approaches the classical Dulong and Petit

Material Constant	Value
Curie Temperature (T_C)	627 K
Density (r)	8.9 g/cm^3
Atomic Weight (MM)	58.69 g/mol
Specific heat at 350 K (Cp_e^{350K})	0.459 J/g·K
Specific DCp at the Curie point	0.0862 J/g·K

Table I: Material properties of bulk Ni.

Nominal thickness (nm)	Calculated mass from thickness (ng)	Experimental Cp (nJ/K) at 350K	Estimated mass from Cp at 350 K (ng)	DCp/mass (J/gK)	Tc (K)	Mean NC Diameter (nm)
3	48.1	21.6	46.9	0.0767	616	4
6	32.2	15.0	32.8	0.0732	611	6
9	16.2	7.46	16.3	0.0616	603	8

Table II: Characteristic magnitudes extracted from the calorimetric experiments.

value in the high-T limit. We compute this term under the Debye approximation[80]:

$$C_{V,latt} = 9 \cdot N \cdot k_B \cdot \left(\frac{T}{\theta_D}\right)^3 \cdot \int_0^{x_D} \frac{x^4 \cdot e^x}{(e^x - 1)^2} \cdot dx$$

where N is the number of atoms, k_B is the Boltzmann constant, θ_D is the Debye temperature (for Ni, 375 K[81]) and $x_D = \frac{\theta_D}{T}$. Another contribution is the electronic specific heat which originates from the valence electrons. The temperature dependence of the electron specific heat is taken from [82] as $C_e = A_e \cdot T_e$, where T_e is the electron temperature and A_e a constant with value 1065 $J \cdot m^{-3} \cdot K^{-2}$ for Ni.

The last contribution to the specific heat arises from phase transitions in the region of interest. In this case the magnetic phase transition occurring at the Curie temperature provides the excess specific heat. The experimental specific heat curves can be interpreted in this general frame. The magnetic contribution is obtained subtracting the different contributions to the total specific heat (Fig 4.18 (b)). Figure 4.18 (a) shows the lattice and electron contributions, the experimentally measured specific heat for the 6 and 9 nm samples and the magnetic contribution obtained by subtraction (Fig 4.18 (b)).

Interestingly, if we compare the specific heat reduction of the ferromagnetic to paramagnetic transition at the Curie temperature with the surface-to-volume (S/V) ratio, it appears to exists a clear correlation. In a 8nm diameter Ni nanoparticle 13% of the atoms are at the surface whereas in a 4 nm nanoparticle this number increases to 26%. Consid-

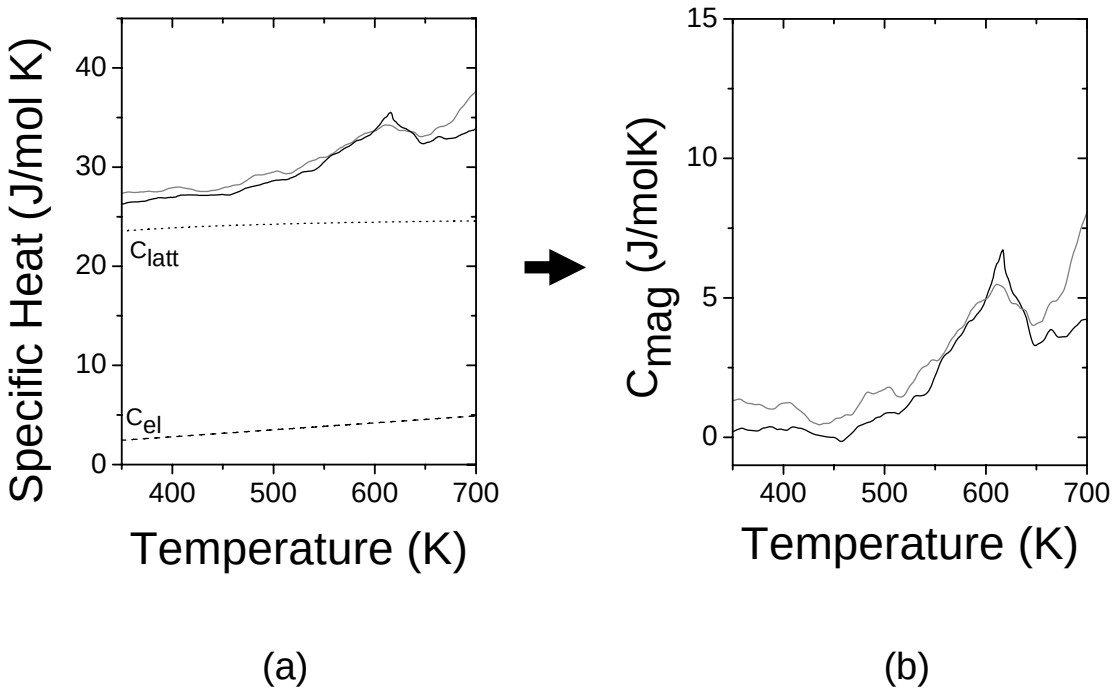

Figure 4.18: (a) Experimental specific heat for the 6 and 9 nm and lattice and electronic contribution to the specific heat of Ni. (b) Magnetic specific heat of 6 and 9 nm Ni films.

ering the uncertainty in the measurements this is strikingly similar to the ratio of specific heat with respect to the bulk value (see figure 4.19 (b) and values in table II). Therefore, although further measurements at several film thicknesses (nanoparticle diameter) should be carried out it seems that there is experimental evidence of a quenching of the magnetic moments of the surface atoms. In fact previous studies with Ni clusters 3 nm in diameter have shown that the value of the saturation magnetization is 0.4 μ_B/atom which is significantly lower than the bulk value of 0.6 μ_B/atom[83].

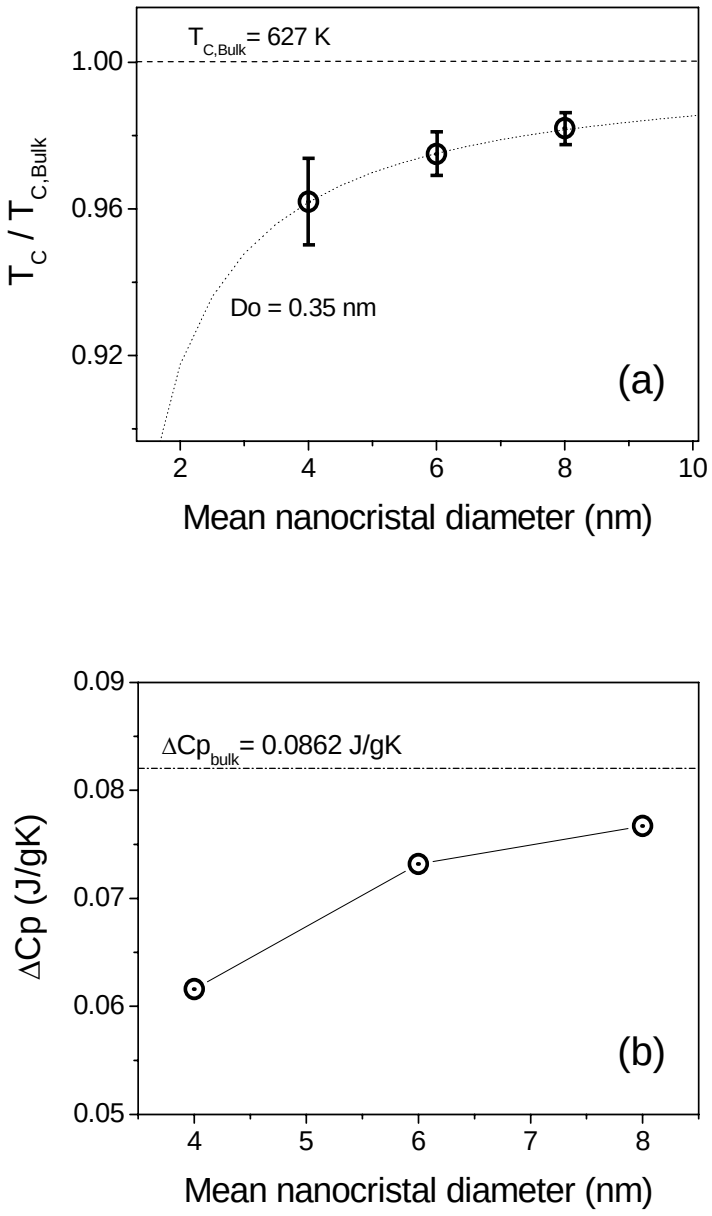

Figure 4.19: (a) Normalized Curie temperature as a function of the nanocrystal diameter. (b) Variation of the specific heat at the Curie transition temperature with nanocrystal diameter. The longitudinal dashed line is the reference value for Ni bulk.

4.5 Study of thermal transitions in ultrathin films of a-Ge and nc-Ge embedded in SiO_2.

Ge nanocrystals embedded in SiO_2 have attracted a strong interest in the scientific community due to their potential application in the development of optoelectronic devices, because of its light-emitting properties, and in high-speed and low-power logic and non-volatile memory devices [84, 85]. A promising way to synthesize Ge nanocrystals within a SiO_2 matrix film is by high temperature annealing of SiO_2/a-Ge/SiO_2 trilayer structures [86]. During the annealing treatment, typically carried out by rapid thermal annealing or laser processing [86, 87], phase transitions such as melting, crystallization and solidification of the amorphous or nanocrystalline phases are often found [88]. Therefore, the ability to obtain a suitable distribution of nanocrystals with a specific size relies on a deep knowledge of the kinetics and thermodynamics involved in the nucleation and growth process. Regarding crystallization of ultra-thin films of amorphous Ge very few studies can be found in the literature. It has been appreciated a decrease of the crystallization temperature when a-Ge is sandwiched between metals [89] where surface induced crystallization prevails. However, in Ge/SiO_2 superlattices it has been observed an increase in the crystallization temperature with thinner Ge layers, and this is supported by the inhibition of a-Ge nucleation in the SiO_2 interface [90]. Considering these results Zacharias et al. propose a model based on interface energies, the thickness of the a-Ge layer, the melting point of the system, and the crystallization temperature of the thick amorphous film [87]. Previous studies have shown that nucleation of the crystalline phase is prevented in a-Ge films thinner than 2.5 nm, since the critical nuclei size estimate is around 2 nm. Moreover, the presence of SiO_2 at both interfaces prevents the heterogeneous nucleation of the crystalline phase at distances lower than 0.5-1 nm.

Due to their dimensions Ge nanocrystals may also show distinct properties compared to bulk Ge. Past studies have corroborated that freestanding nanocrystalline Ge experiences melting depression [91, 92]. However, a recent TEM analysis of Ge nanoparticles embedded in a SiO_2 matrix shows the existence of a large hysteresis around the bulk melting temperature[93]. The authors interpret it from the modified surface free energy between the silicon dioxide matrix and the Ge particle.

The melting depression [60] associated to size-dependent phenomena has been described in many systems [94, 62, 63, 61]. Several models have been proposed to describe how a nanoparticle melts. In general they predict an inverse dependence of the melting tempera-

ture with the radius of the particle and $\triangle T(r)$ is proportional to α/r. The various models differ in the parameter α which involves the interfacial energies between the solid phase and the surroundings and the solid and liquid densities. The Homogeneous Melting Model (HMM) is the most used and assumes that at a given temperature the particle melts at once. In this model the parameter α is $\alpha_{HMM} = \sigma_{SV} - \sigma_{LV} \left(\rho_S/\rho_L\right)^{2/3}$ [59]. The melting models are based on thermodynamic arguments and do not include possible kinetic effects related to rapid heating. On the other hand, superheating is a scarce phenomenon that can be found in nanoparticles embedded in a material of a higher melting point but supercooling is routinely observed in most materials. For superheating to occur above the equilibrium melting temperature at low to moderate heating rates it is often necessary to have lattice matching at the interface between the particle and the matrix. When nanoparticles are embedded randomly in a high-T_m matrix a depression of melting temperature is also typically observed in analogy to the behavior of freestanding nanoparticles [95], although the particular melting temperature depends on the nature of the particle/matrix interface.

A proper technique to characterize these properties during and after the synthesis process is calorimetry. However, very few data regarding crystallization and melting behavior of Ge thin films [86, 87] or nanocrystals [84] can be found in the literature, mainly motivated by the lack of sensitivity of conventional scanning calorimeters (DSC) on measuring small samples. As has been explained in this chapter, quasi-adiabatic nanocalorimetry overcomes most of the sensitivity limitations, however other groups working in the field have focused their investigation in temperature ranges below than those required to analyze phase transitions in Ge.

Another aspect that deserves further comments is that as crystallization is kinetically limited and its temperature increases as the a-Ge thickness decreases ultrafast quasi-adiabatic nanocalorimetry opens the possibility to study the amorphous-to-liquid transition in very thin films of germanium. It is clear that this transition will only occur in very rapid heating experiments; otherwise the amorphous will crystallize as observed in furnace heating measurements. Interestingly, the transition from the amorphous to the liquid phase is first order in Germanium since it involves a change in bonding from the covalent four-fold coordinated in amorphous phase to twelve-fold coordinated bonds in the metallic liquid. The a-Ge melting is currently achieved in laser processing of a-Ge layers, but thermodynamic data available regarding this process is limited to theoretical calculations [96, 97]. From experimental values of the crystallization enthalpy and Gibbs

free-energy calculations, a depression on the melting temperature of the amorphous phase (T_{al}) is predicted to be around the 80% of the crystal melting temperature (T_{cl}). This behavior is a consequence of the higher free energy of the amorphous state. The T_{al} value has been corroborated by optical experiments where the melting temperature is obtained by monitoring the evolution of reflectivity and transmission of a-Ge during flash laser annealing [98].

In this section we present nanocalorimetric measurements at fast heating rates, $5{\cdot}10^4$ K/s, on trilayer structures formed by 1-3 nm a-Ge layers sandwiched between 10 nm SiO_2 thin films grown by EB-PVD. In the first scan, melting of the as-deposited film and solidification results on Ge nanocrystals embedded within a 20 nm SiO_2 film. The high sensitivity of the technique is well suited to probe melting (both amorphous and crystal phase) and solidification transitions during heating and cooling cycles in the temperature range from room T to 1200K. The upper temperature limit in these measurements is imposed by thermomechanical instabilities which arise at higher temperatures and produce the rupture of the membrane. With the current source used in these experiments (Kth2425) the time-control of the pulse-width is not accurate enough to prevent temperature overruns above 1200K at the different heating rates. Therefore, not enough curves could be measured to apply heat corrections and to get a quantitative estimation of the heat capacity and the energies involved in the different phase transitions. Therefore, in this section the calorimetric traces are presented either as apparent heat capacity or as $d\Delta V/dt$. From them the transition temperatures and qualitative information on the various physical processes can be inferred. Complementary information on the crystallization of a-Ge layers of thicknesses from 2 to 50 nm is presented in appendix B.

4.5.1 Experimental

Sample deposition of the SiO_2/a-Ge/SiO_2 and nanocalorimetric scans. A pair of twin serpentine-type nanocalorimeters is mounted inside an UHV e-beam evaporation chamber as already presented in chapter 3. In high vacuum (10^{-7}mbar), and previous to any sample deposition a series of scans up to temperatures around 800K are performed in both calorimetric cells (CC) to clean the membrane surface. With the set of moving masks we select in which nanocalorimeter to deposit the sample. The silicon microfabricated shadow mask is attached to the bottom of the Silicon frame limiting the sample growth to the sensing area of the CC.

In a first step, the moving masks are placed as to deposit on both CC a buffer SiO_2

layer with a nominal thickness of 10 nm. The deposition conditions for SiO_2 are the same than those detailed in subsection 4.4.1. Following the general procedure described in this chapter, 500 calorimetric scans are carried out from room temperature up to 1200 K, showing a monotonic rise in temperature. These curves serve as the baseline for subsequent analysis. Afterwards in a second step, the moving masks are placed to permit deposition only in the SCC, and layers of a-Ge between 1-3nm nominal thickness are deposited onto it. The material is evaporated at a pressure around $5{\cdot}10^{-6}$ mbar from pure Ge pellets. To minimize surface mobility of the Ge adatoms during growth and therefore promote an amorphous Ge structure, the CCS cell is maintained at room temperature and the growth rate is fixed to 0.1 nm/s. Furthermore, SiO_2 is a well known inhibitor of the heterogeneous nucleation of Ge at the interface and previous work presented in appendix B has shown that under these conditions the as-deposited Ge is fully amorphous,.

The moving mask is opened again and an identical capping SiO_2 layer of 10 nm thickness is deposited in both CC. The final structure of the sample in the CCS is a trilayer of two 10 nm SiO_2 sandwiching a 1-3nm a-Ge layer. With all these elements, in-situ calorimetric measurements are carried out. The nanocalorimeters are fed with a constant current pulse of 40 mA and width of some ms, followed by a continuous current of 1 mA to monitor the cooling process as shown in figure 4.20. The ΔV signal is measured after amplification by a factor of 210.

Complementary characterization tools are used to gain further insigth into the structural and morphological evolution of the films after the thermal treatments.

Raman spectroscopy. Raman spectroscopy was carried out in backscattering geometry with a high resolution LabRam HR800 spectrometer, using the 514.5 nm line of an Ar-ion laser for excitation. The beam was focused onto the sample, in the nanocalorimeter membrane, with a spot size of about 1 μm and a laser power of 2 mW.

AFM characterization. Surface morphology of samples was tested by AFM working in tapping mode with a Molecular Imaging PicoSPM. To access the samples, the nanocalorimeter membranes were adhered to a silicon piece using a double side adhesive tape.

TEM characterization. An special custom build sample holder was designed and fabricated to mount the nanocalorimeter in a Jeol JEM-2021 Transmision electron microscope. From the top of the silicon nitride membrane, both the heater and the membrane

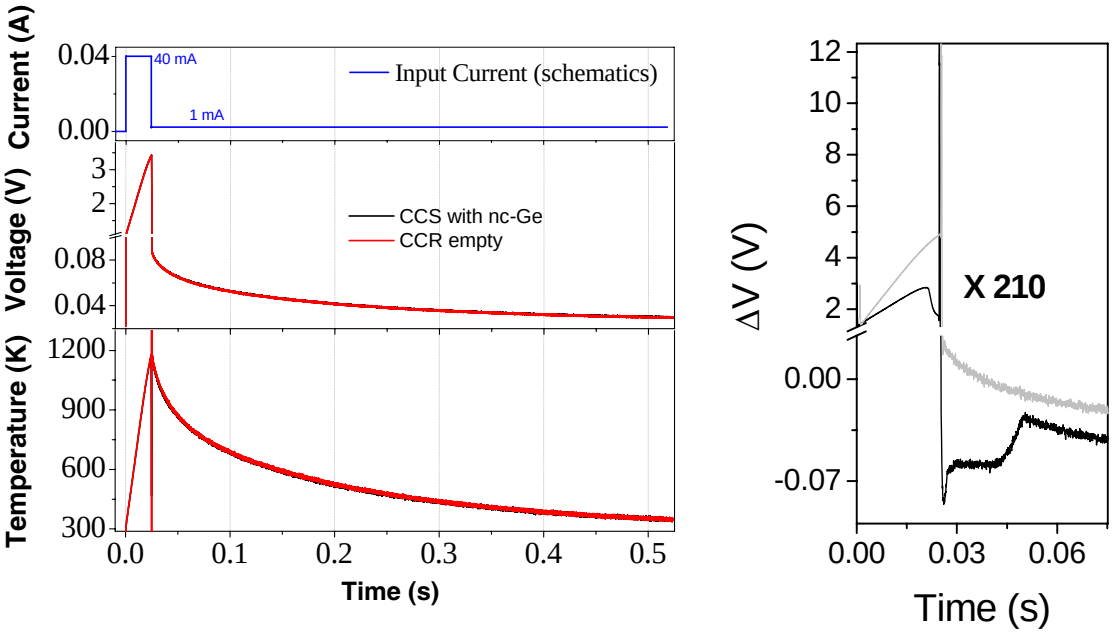

Figure 4.20: Experimental data as a function of time corresponding to voltage and temperature signal in experiments where cooling is also acquired. The differential voltage between sample and reference calorimetric cells as a function of time is shown in the right figure. The gray curve represents the data obtained before growth of the 3nm Ge layer. The black curve corresponds to the temperature increase after formation of nanocrystals. The slope changes are related to melting and solidification of Ge nanoparticles.

were chemically etched to reduce the thickness and improve electron transparency, thus enabling a direct sample observation. This way bright-field micrographs in plane-view (TEM), selected area electron diffraction (SAED), and EDX nanoanalysis were performed.

4.5.2 Results and discussion

The structure of the as-deposited Ge thin film is fully amorphous according to plane-view transmission electron microscopy (TEM) images and Selected Area Electron Diffraction (SAED) patterns. The continuity of the as-deposited film is confirmed by means of EDX nanoanalysis with a spot size of 5 nm.

Figure 4.20 shows the raw data obtained in differential mode during a typical heating ramp on a Ge sample. The grey curve represents the ΔV signal after amplification by 210 of the initial difference between the empty calorimetric cells which is taken as the baseline for measurements with sample. The presence of the sample (black line) induces some differences due to the increase of the heat capacity and the existence of phase transitions. The slope change at 21-23 ms in the amplified ΔV signal upon heating is related to an endothermic transformation, whereas the second change in slope at 45-50 ms is due to an exothermic reaction during the cooling process.

Figure 4.21 shows three calorimetric traces obtained on a 3nm a-Ge layer upon heating to 1200 K. It is important to highlight that these curves correspond to single scans from which the averaged baseline contribution is subtracted. The first scan shows some irreversible features: A broad peak on the low temperature region (see inset), a small endothermic peak centred at 900 K and a large endothermic peak with two overlapping contributions with the onset at 980K. After the second scan a reversible reaction at slightly higher temperatures is shown to be highly reproducible and no variations are observed between the second and the fifteen scan. The elevated increase in heat capacity at the higher end may be due to uncorrected heat losses, or incomplete melting (see below)

In order to identify the nature of the reactions involved in these scans, several samples 3nm thick of a-Ge sandwiched between 10nm of SiO_2 are grown on top of other nanocalorimeters. Figure 4.22 shows a systematic study of the sample structure performed by micro-Raman spectroscopy after rapid heating, $5{\cdot}10^4$ K/s, within the nanocalorimeter up to different temperatures. The micro-Raman spectrum of the as-deposited sample shows a broad peak centred near 270 cm^{-1} which corresponds to a-Ge [99]. After heating to 803 K, the Raman spectrum remains as for a-Ge, however, the low frequency shoulder at 220 cm^{-1} disappears. Comparing this result with the apparent heat capacity data, we can

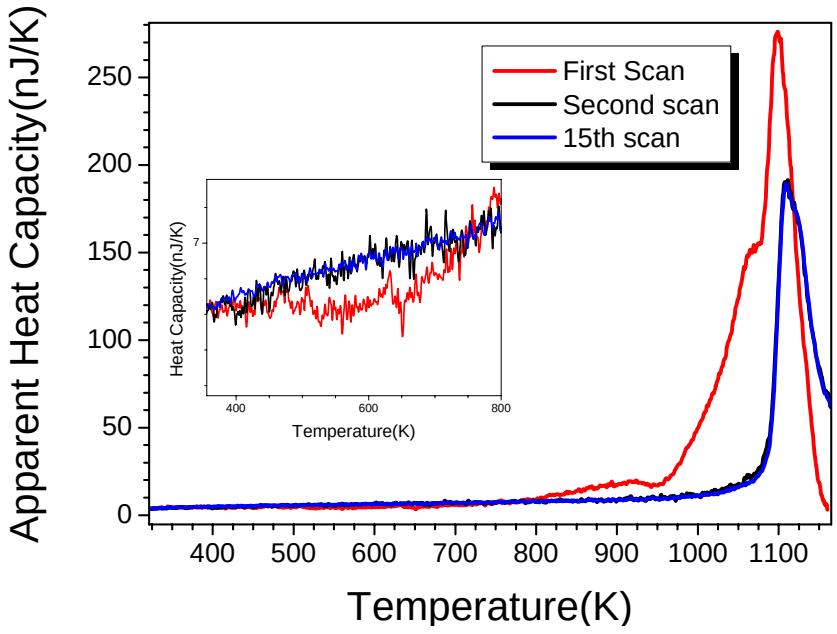

Figure 4.21: Apparent heat capacity vs. temperature for the 3nm a-Ge thin film sandwiched between two films of 10nm thick SiO_2.

associate this change with the small broad exothermic peak of the a-Ge which corresponds to an irreversible structure relaxation of the a-Ge, characteristic of non-equilibrium amorphous phases [100]. After the rapid heating to 955 K the Ge layer remains amorphous. No changes were observed in the Raman spectra which imply that the small shoulder endothermic feature centered at 900 K may correspond to a reversible transformation in the amorphous phase[101], perhaps the melting of one of the multiple configuration of the a-Ge. It has been reported that a-Ge prepared under high deposition rates shows multiple amorphous configurations with a large dependence on the deposition conditions.

Heating to 1013 K, slightly above the onset of the endothermic calorimetric peak of the first scan, induces some changes in the structure of the film and the micro-Raman indicates now a partially nanocrystalline/amorphous structure. During cooling, due to the lower cooling rate, the previously small melted fraction transforms into nanocrystalline Ge and non-melted material remains amorphous. The Raman spectrum exhibits a sharp peak at 296 cm^{-1} associated to the optical Raman mode of crystallized Ge on top of the broad band of a-Ge. The shift of the Ge peak frequency with respect to the value for bulk c-Ge (301 cm^{-1}), might be due to confinement effects in the Ge nanocrystals. By inspection of

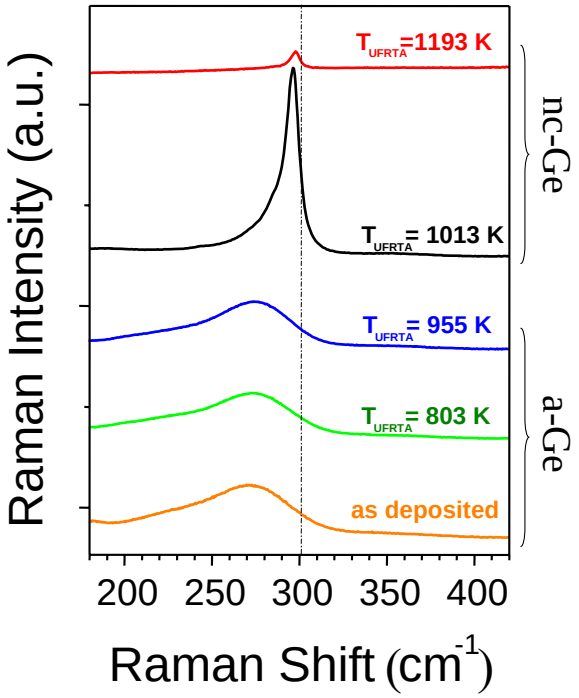

Figure 4.22: Raman spectra of a SiO_2/a-Ge/SiO_2 trilayer after rapid heating to different temperatures. The structure of the Ge phonon mode is representative of the crystalline state of the Ge layer. The spectra are vertically shifted for clarity. The vertical line corresponds to phonons frequency for bulk crystalline Ge.

the phonon dispersion in Ge we infer that a shift of $\sim 5\ cm^{-1}$ corresponds to an average nanocrystal size of at most 10 nm. The absence of a Si- Ge phonon mode reflects no interdiffusion and mixing in spite of the high temperatures.

Heating to higher temperatures, 1193 K, results in complete melting of the as-deposited Ge layer. The micro-Raman spectrum after cooling back shows only the contribution from crystalline Ge which is again formed upon solidification of the melt. Comparing the two last spectra, we observe a clear reduction in the intensity of the fully crystallized Ge peak as well as a shift towards the bulk frequency, indicating a smaller confinement in the last one. The peak intensity is resonantly enhanced in the nanocrystals due to E_1-like electronic transitions close to the exciting laser energy. In bulk Ge the enhancement occurs at lower energy, ~ 2.2 eV which is consistent with the loss of resonance in the highest heated sample. AFM imaging of the sample after a first complete scan to 1200 K shows the formation of nanoislands with an average height around 10 nm.

The above findings support the idea that the large endothermic peak of the first calorimetric scan is due to an amorphous-to-liquid transition because crystallization is hindered upon heating by the fast heating rates and the small thickness of the layer, However the double peak structure of the 1st scan observed in all the capped Ge films in the 1-3 nm range suggest a more complex process and will be further discussed below.

The other two calorimetric traces in figure 4.21 correspond to the second and the fifteen consecutive scans. The endothermic feature is representative of the melting of nanocrystalline Ge, formed after the previous melting/crystallization scans. The onset for melting of a nanocrystalline Ge layer with a nominal thickness of 3nm Ge is 1090 K. After 15 identical and consecutive scans up to 1170 K the signal was unchanged and therefore we assume the existence of a stable distribution of nanoparticles. To determine the range of particles size that corresponds to the calorimetric scan, ex-situ AFM is realized after the calorimetric experiment and compared with AFM images of samples before any treatment. The background is removed by image threshold and subsequently the images are analyzed to determine the projected area of each particle. As the calorimetric signal of melting is proportional to the volume, the size distribution is multiplied by the volume of every particle for each radius. Figure 4.23 shows the existence of a bimodal volume distribution of nanocrystals. The smaller distribution covers particle sizes between 5 and 15 nm of radii with an average value around 10 nm and a FWHM of 2 nm and the second distribution is centered in particle radii around 26 nm with a FWHM of 7nm. TEM images, in figure 4.24, confirmed the presence of nanocrystalline Ge with a diamond like structure.

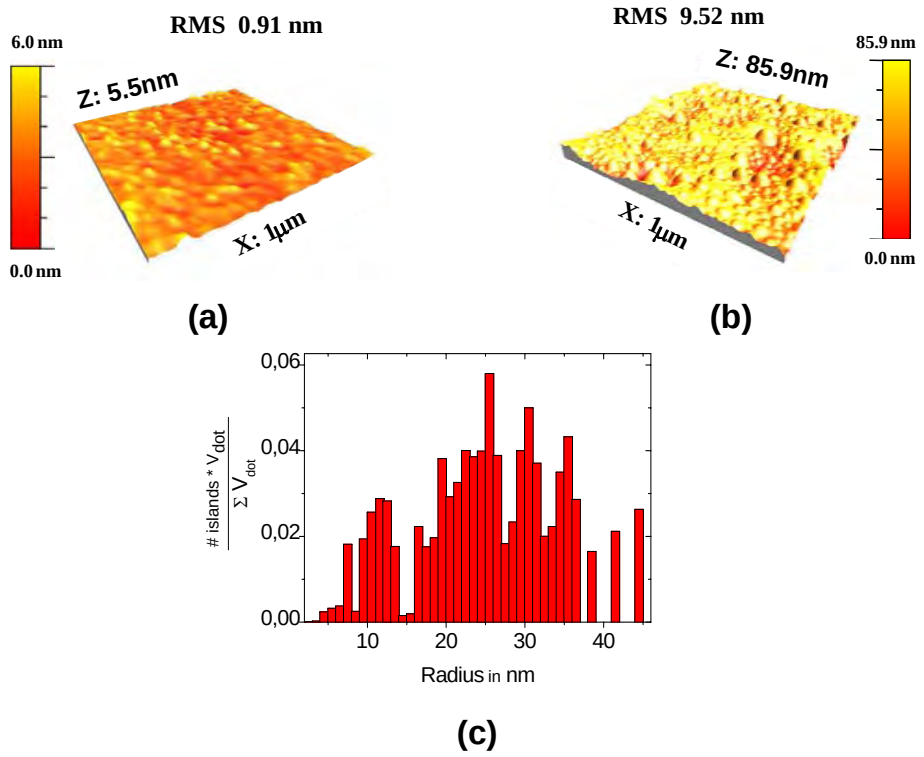

Figure 4.23: (a) AFM image obtained in tapping mode before heat treatment and (b) after heating to 1200K. (c) Volume distribution of the nanoparticles after heating to 1200K.

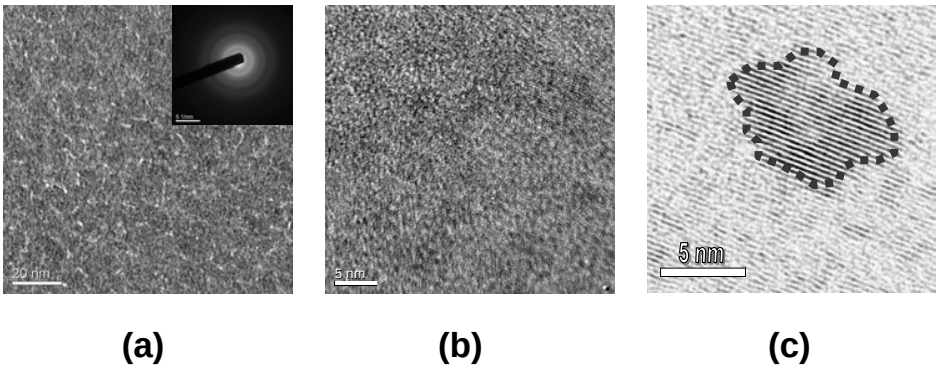

Figure 4.24: TEM micrographs of the 3 nm Ge sample.
(a) TEM micrograph showing the amorphous structure of the 3 nm thin film of Ge as deposited. The inset shows the SAED pattern where the different difused halos corroborates the amorphous structure of the different layer that compose the analyzed sample (Si_yN_x, SiO_2, a-Ge and SiO_2) (b) TEM micrograph of an identical sample shown in a, after thermal treatment at 975 K. It is possible to observe the nanocrystals formed (c) Detail of image b after digital filtering, showing the diamond-like crystalline structure of Ge nanocrystals.

Melting of Ge nanoparticles. Further insight into the melting process of the Ge nanocrystals can be gained analyzing the calorimetric traces after heating to different temperatures. The different curves in figure 4.25 show the derivative of the differential voltage with time, $d\Delta V/dt$, obtained during heating with pulses of different widths. This signal provides information of the phase transitions occurring in the sample. The derivative process is typically very noisy and as the typical time scales of the thermal phase transformation in the sample are in the millisecond range box averaging can be applied. Initially, a box of 10 points is used in the original ΔV signal and after differentiation a box of 5 points in the $d\Delta V/dt$ signal. The black line shows the characteristic $d\Delta V/dt$ signal, when the SCC is empty. The endothermic peak of the bottom curve of figure 4.25, negative $d\Delta V/dt$ signal, corresponds to the melting of the smaller distribution mode of Ge nanoparticles. The onset of the peak at 1090K marks a clear depression of 125 K below the expected value for bulk Ge. The FWHM of the peak is around 30 K and it is related to both the size distribution of nanoparticles, and the temperature differences in the calorimetric cells which has been experimentally measured to be around 23 K. The other curves probing the structure up to lower temperatures, correspond to incomplete melting, i.e. only those nanoparticles below a given radii are melted. Contrary to recent experimental evidence of superheating above the bulk melting temperature in Ge nanocrystals embedded in a SiO_2 matrix [93] we do observe a depression of the melting temperature with respect to the bulk material. Although both particles are Ge nanocrystals embedded in SiO_2 the preparation method differs greatly and may explain the different behavior. In our case, the nanocrystals are embedded within a thin film of SiO_2 which does not introduce compressive stresses in the Ge nanocrystals as we have already probed by micro-Raman analysis [19]. In the case of the work of Xu et al. [93] pressure build up at the nanoparticles may play a non-negligible role in the observed anomalous superheating.

The observed melting temperature has been compared with predictions from the HMM model using parameters extracted from the literature, latent heat of fusion, L=510 J/g [100], surface energy for the liquid Ge-SiO2 matrix, σ_{LM} =0.15 J/m^2[102], and for the solid Ge-SiO_2 matrix, σ_{SM}=0.7-0-9 J/m^2 [93]. Figure 4.26 shows the results obtained as a function of r^{-1} for the two values of the solid nanoparticle-matrix surface energy. The experimentally measured temperatures are represented by the vertical bar and the nanoparticle sizes measured by AFM by the horizontal bar. Our data falls within the limit range predicted by the HMM model, excluding at least in principle the presence of superheating with respect to the equilibrium melting temperature for every size. Nevertheless,

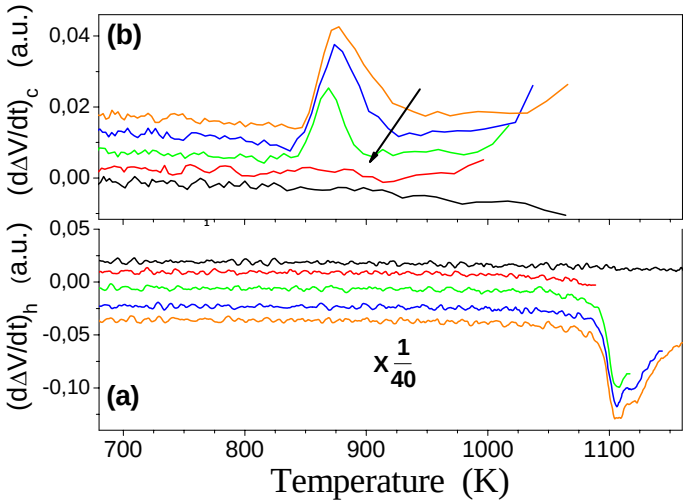

Figure 4.25: The derivative of the differential voltage with time as a function of temperature. (a) measurements during heating: Pulses of different duration are injected to probe a different population of nanocrystals. (b) measurements during cooling of the different heat treatments shown in (a). The continuous line in both graphs is obtained from the empty cells. The arrow marks the temperature variation of the onset of solidification. The curves are vertically shifted for clarity.

the uncertainty in some of the parameters entering the model renders difficult an unambiguous interpretation about the melting process. Superheating of the nanocrystals due to melting kinetics during the rapid heating of our experiments ($5{\cdot}10^4$ K/s) also appears to be insignificant in these nanoparticles. An approximation of the sizes melted can be assumed directly confronting the melting peak and the size distribution of the nanoparticles. Within the HMM model we estimate the maximum nanoparticle size that is melted in each scan. Heating up to 1170 K (bottom curve) nanoparticles from 5 to 15 nm are melted, whereas for the next two curves in figure 4.25 (a) the maximum sizes melted are 9 and 12 nm, respectively

Solidification and size dependent supercooling of Ge nanoparticles. The upper curve of figure 4.25 (b) shows the exothermic peak present in $\mathrm{d}\Delta V/\mathrm{dt}$ upon cooling. The peak corresponds to the solidification of the melted nanoparticles due to previous heating up to 1170 K. The signal to noise ratio of the ΔV data during cooling is 40 times smaller than during heating. Given this fact an extra box averaging of 20 points was performed with special care as to avoid manipulation artifacts. The cooling rate at the point of solidification was near 8000 K/s. From figure 4.25 (b) a dependence of the solidification temperature

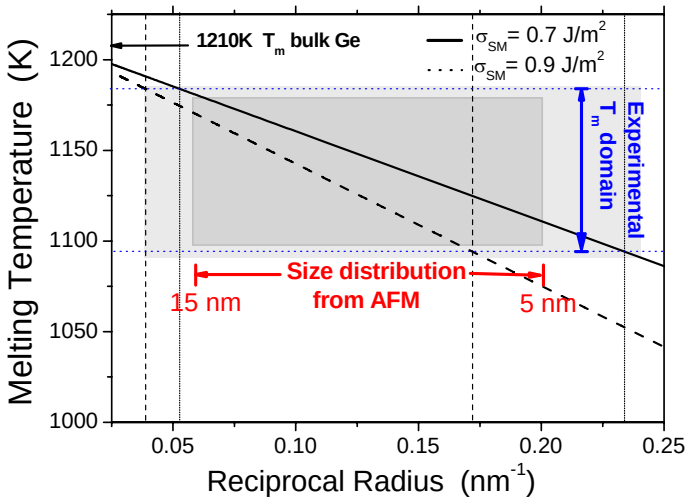

Figure 4.26: Melting temperature as a function of the reciprocal radius deduced from the HMM model for the two values of the solid Ge-SiO_2 matrix surface energy. The dashed and dotted vertical lines indicates the radius range for the experimentally observed melting temperatures through the HMM model for both values of surface energy.

with the previous heating is observed. By inspection of the solidification curves, obtained after partial melting to different nanocrystal sizes, we demonstrate the occurrence of size-dependent supercooling in the Ge nanoparticles. The onset of solidification appears at 895, 920 and 935 K for samples heated to 1120, 1140 and 1170 K, respectively. For a given nanocrystal size a hysteresis of around 220-230 K with respect to the melting temperature is observed. The size dependent supercooling can be understood from the temperature dependence of the critical size necessary for solidification. Since the critical radius depends on the supersaturation, the lower the temperature the smaller the critical grain size. Using different current pulses we probe the melting of a reduced population of nanocrystals, the shorter the pulse the lower the temperature reached and therefore only the smaller nanocrystals undergo the solid-to-liquid transition. Solidification of a given liquid particle can only occur if the critical grain size is below the radius of the particle and the solid grain can fit within the liquid. Therefore, for the smaller particles a lower temperature is needed for solidification.

Melting of the ultrathin a-Ge layer. We discuss now on the appearance of a double peak in the first calorimetric scan. It is worthy to note that this behaviour has been observed in multiple samples and its appearance for a given thickness is independent of the

shape of the heater, either U-shape or serpentine-type, which reveals it is something intrinsic to the melting process. We suggest the observed phenomenon bears some resemblances to melting/recrystallization in polymer films and in the following we argue in favour of this analogy.

Comparing the traces of the first calorimetric scan with the traces of subsequent scans (Figure 4.21), it is tempting to attribute the second contribution to the large endothermic peak of the first scan to the melting of a nanocrystalline phase. Upon heating for the first time the ultra-thin amorphous structure may melt at temperatures below those required to melt the crystalline phase as predicted by Turnbull et al.[96, 97]. If we take the onset of melting as the intersection of the slope of the peak at the maximum with the baseline a value of 980 K is determined. Interestingly, this value is in agreement with the melting of a bulk amorphous sample (970 K). However, the shape of the peak suggest a continuous transition initiated at lower temperatures which could be related to size effects in the amorphous structure.

Melting of the amorphous solid layer will create an ultrathin liquid metallic layer. Generally speaking, it is well known that metallic films, evaporated on glass are in a metastable state and dewet upon annealing in both solid and liquid forms. Dewetting in thin flms is driven by surface tension and intermolecular interactions with the solid substrate. Therefore, we expect a dewetting of the Ge layer as soon as surface mobility is high enough. In the liquid form this dewetting process must be extremely fast, although the presence of an upper SiO_2 layer must introduce some constraints to this process. The wetting angle of a Ge melt on a fused silica substrate in vacuum has been measured by Kaiser et al. [103]. The value of 120^o shows the non-wetting behavior of the liquid on the oxide surface. This value is in agreement with our observations in a-Ge samples annealed by Rapid Thermal Annealing at 1175K (see appendix B for details).

The AFM scan of figure 4.23 (b) provides more information on the dewetting mechanism. A specific feature of the AFM image is the absence of a characteristic length scale in the films after annealing which suggest dewetting is not dominated by spinodal instabilities but by homogeneous/heterogeneous nucleation. The random spatial distribution of the nanoislands is consistent with a stochastic nucleation process on the surface of the SiO_2 layer.

Therefore, during heating the metastable disordered phase melts, dewetts forming liquid droplets which subsequently solidify into nanocrystalline Ge since at these temperatures the stable phase is the crystalline. Upon further heating the nanocrystals melt at their

corresponding temperature analogously to what is observed in subsequent scans. This scenario needs further confirmation and additional nanocalorimetric measurements at different heating rates including in-situ complementary optical tools are envisaged in a near future.

Chapter 5

Power compensated Calorimeter for thin film samples.

In this chapter, we present the development of active-control systems to use the membrane-based nanocalorimeters as in power compensation mode [104]. Many modern materials currently used in nanotechnology or microelectronics industry are implemented in thin film form or in very small quantities of mass per sample area. To analyze these samples it is necessary to overcome current limitations in terms of sample amount, energy resolution and heating rates imposed by conventional calorimeters (typically limited to samples of few mg, energies tens of μJ and heating rates below 5 K/s). This has been the driving force to develop new calorimetric tools. In previous chapters we have shown that by using membrane-based microchips with pulse heating methods non active-control heating rates above 10^4 K/s can be achieved in high vacuum permitting to analyze ultrathin films. A variant of this method has been proposed and developed by Schick's group [16, 54]. It consists on applying a predefined saw-tooth shape pulse in low pressure helium atmosphere to achieve nearly constant scanning rates in the range from 10^2 to 10^5 K/s both during heating and cooling. In these methods, the scanning rate fundamentally depends on the current injected through the heater (power introduced in the calorimetric cell), on the thermal losses and on the addenda (heat capacity of the calorimetric cell plus the sample loaded), but since no active control is used the scanning rate may change during a phase transition if the energy involved is comparable to the addenda ($1\mu J/K$). Many materials are used in non-equilibrium states (crystallization or diffusion controlled processes...), and for quantitative thermal analysis a constant heating rate is preferable. Besides, the quantitative determination of the enthalpy involved in kinetically limited phenomena like

dehydrogenation of metallic hydrides and formation of metallic siliciures require slower heating rates than those achieved in pulse-heating mode. With the goal to analyze such processes in submicrogram samples, we have developed temperature controllers to attain scanning rates from 0.05 to ∼1000 K/s. In a first approach we started with an analog controller but due to the difficulties arising during the development we focused our attention in more flexible solutions with digital controllers.

To realize slow heating rates, a controller was implemented with a windows-based application using Labview®(from National Instruments) that controls via GPIB a Keithley sourcemeter (Kth2425) (which gives a high resolution and low noise analog I/O). The control algorithm selected to attain constant ramps with the nanocalorimeter was an IPID (proportional double integral differential control) [105]. It guarantees temperature errors below 0.05 K in all the dynamic range which spans from 0.05 to 10 K/s. The higher rate is limited by the minimum control loop time (160 ms), imposed by GPIB communication protocol. At low heating rates the energy involved in a phase transition is released in a larger time and the main limitation to measure it relies in the power resolution of the hardware employed to feed the calorimeter. This fact introduces some constraints on the amount of sample mass measurable. With a Keithley sourcemeter 2425, power resolutions around 100 nW are easily achieved, permitting analysis of submicrogram samples. The special design of this implementation provides the grounds for the scalability of this type of calorimeter to a multi-cell calorimetric system. Using multichannels DAC and ADC cards, a large number of calorimetric cells can work in parallel, and therefore a high-throughput and fast-screening technique can be obtained. This high-throughput screening technique is under development in our group for the simultaneous characterization of libraries of metal hydrides for hydrogen storage and other applications.

To overcome limitations on the higher scanning rates, a PI (proportional integral) controller algorithm was implemented using a field programmable gate array (FPGA). We selected the NI PXI 7831R card from National Instruments which includes a 1M gates inside with reconfigurable I/O, 16 bits ADC and DAC integrated onboard. FPGA gives better performances than microprocessor-based controller, basically since it permits parallel calculations and fast analog I/O reducing the control loop time up to 20 μs. In addition, FPGA warrants the real-time control avoiding the influence of errors on time of windows-based programs. This improvement in the control loop time increase the stability and higher heating rates, up to 1000 K/s, can be achieved. Figure 5.1, shows how the full dynamic range is covered with the three methods, and the power resolution achieved in

each mode, from very low heating rates, 0.05 K/s, up to ultra-fast heating rates, $5{\cdot}10^5$K/s. To attain constant scanning rates over 1000 K/s, it is necessary to reduce the control loop time, and up to our knowledge nowadays it will be only possible with analog controllers which can reduce the control loop time working at MHz [106].

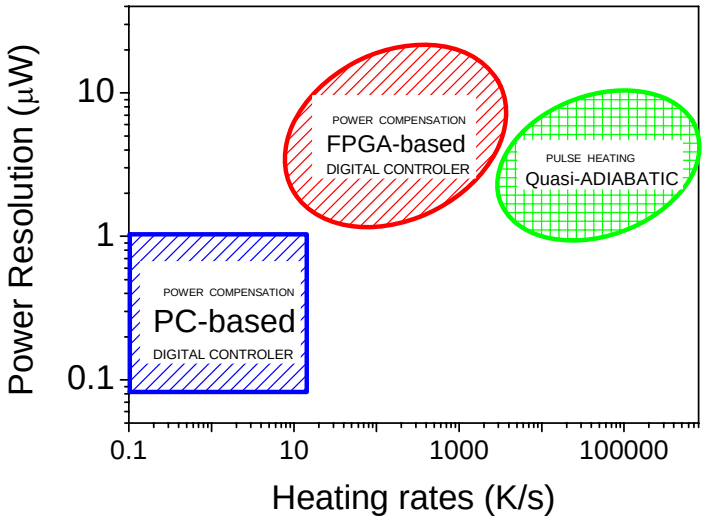

Figure 5.1: Operative mode and dynamic ranges of the nanocalorimeter.
The figure shows the regions that delimits the domains in power resolution and applicable heating rate for the different operative modes.

To attain fast scanning rates, the sample should be small at least in one direction (thin film). For low thermal conductive materials, a considerable thermal gradient may appear across the sample. Therefore, the limit in heating rate will be imposed by the maximum gradient of temperatures permitted inside the sample (which should be equal or smaller than the temperature resolution required in the calorimetric measurement). For example, in vacuum for a $10\mu m$ of high density polyethilene (HDPE) a temperature gradient of 1K across the sample is expected for a heating rate around 1250 K/s. The thermal link between sample and calorimetric cell can impose extra limitations since a non ideal thermal contact can introduce non controlled thermal lags between them.

Along this chapter we will present a simple mathematical model for the nanocalorimeter, and we will survey how it fits the experimental responses. The mathematical model describes the dynamic response of the controlled variable[1] to a change in the manipulated

[1]Temperature (resistance).

variable[2], and it is used in the selection of the controller architecture and its tuning. The experimental implementation of the controllers will be explained in detail for both cases. Several case studies of known phase transitions will be analyzed to show the potentiality of the technique.

[2]Current is the input variable (Power).

5.1 Mathematical model and control algorithms.

From the point of view of control theory, in the design or architecture selection of a controller, it is necessary to understand the dynamics of the system to be controlled, that means to know the behavior of the output response when the input signal changes. This dynamic behavior can be described by a mathematical model in terms of the differential equations extracted from the physical laws governing the system. Therefore, we need a model for the thermal response of the calorimeter, which provides the value of temperature evolution of the calorimetric cell when the heater is fed with a given current. We reduce from the Fourier equations for the heat transfer a simple zero order model based on lumped parameters, thermal resistances and thermal capacitances [107, 18]. With this simplification we obtain the transfer function[3] of the calorimeter, which becomes essential to select the type of controller (control-action) to attain the desired scanning ramps responses. In this section, we present the mathematical model of the nanocalorimeters and the selected control structure based on a combination of a feedforward and a feedback controller. The final control algorithm is described for each implementation (windows-based IPID and FPGA-based PI), however for simplicity considerations the details of the controller design and tuning are explained in appendix C.

5.1.1 Mathematical model of the calorimeters. Transfer function.

One general approximation to a calorimeter is to consider it as a vessel that contains the sample. This vessel will have thermal links with the surroundings. To describe it mathematically, we can take into account the power source and different heat loss contributions, and build the differential equations based on lumped parameters. Figure 5.2 shows a diagram of the model. The most general approximation is described in equation 5.1, where we include the power introduced by the heaters P_{IN} and the three types of heat losses (conduction K_{cd}, radiation ε and convection h_{cv}). We write the heat capacity of the vessel (or calorimetric cell (CC)) as Cp_{CC} and the heat capacity of the sample as Cp_{sample}, and its temperature as T. We assume that T is uniform [4] over the whole vessel (or CC) and sample. In the membrane-based calorimeter the thermal contact between sample and membrane can be considered infinite, therefore the thermal resistance between them is neglected (Ro=0 in figure 5.2). Using a thermal bath, the surroundings (Si frame) remain

[3]The transfer function relates the response of the system to a change in the input variable.

[4]This condition is achieved in the membrane based devices with a proper selection of a thermal plate.

at a constant temperature, T_o, and act as a permanent heat drain.

$$(Cp_{CC} + Cp_{Sample}) \cdot \frac{dT(t)}{dt} + (K_{cd} + h_{cv}) \cdot [T(t) - T_o] + \varepsilon \cdot \left[T^4(t) - T_o^4\right] = P_{IN} \quad (5.1)$$

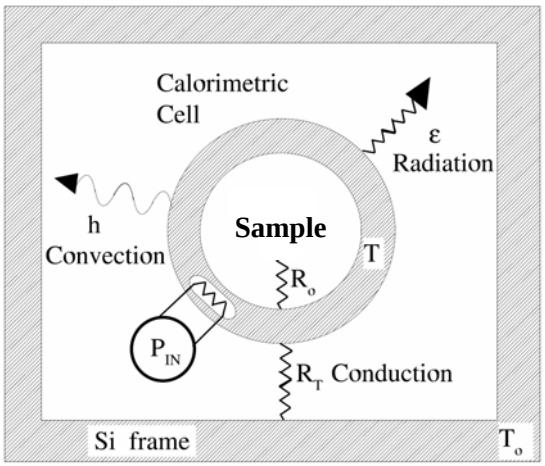

Figure 5.2: Schematics of the lumped parameters model.

To simplify eq. 5.1, the conduction and convection terms can be added in an effective heat transfer coefficient $1/R_T^{eff\,1}$. In high vacuum the $R_T^{eff\,1}$ coefficient will be maximum since only conduction contributes to heat losses, and as soon as the working pressure increases over values around 10^{-3} mbar, the value of $R_T^{eff\,1}$ decreases, being convection through the gas the dominant source of heat losses. Besides, the P_{IN} can be expressed as the power released by an electrical resistance by Joule effect. These two simplifications can be introduced in the general expression 5.1 resulting in,

$$(Cp_{CC} + Cp_{Sample}) \cdot \frac{dT(t)}{dt} + \frac{1}{R_T^{eff\,1}} \cdot [T(t) - T_o] + \varepsilon \cdot \left[T^4(t) - T_o^4\right] = R(T) \cdot I^2 \quad (5.2)$$

From this expression, figure 5.3 shows the schematic model implemented in Simulink of Matlab.

Figure 5.4 shows the agreement between equation 5.2 and experimental data. Through the choice of suitable parameters the model fits perfectly the experimental data.

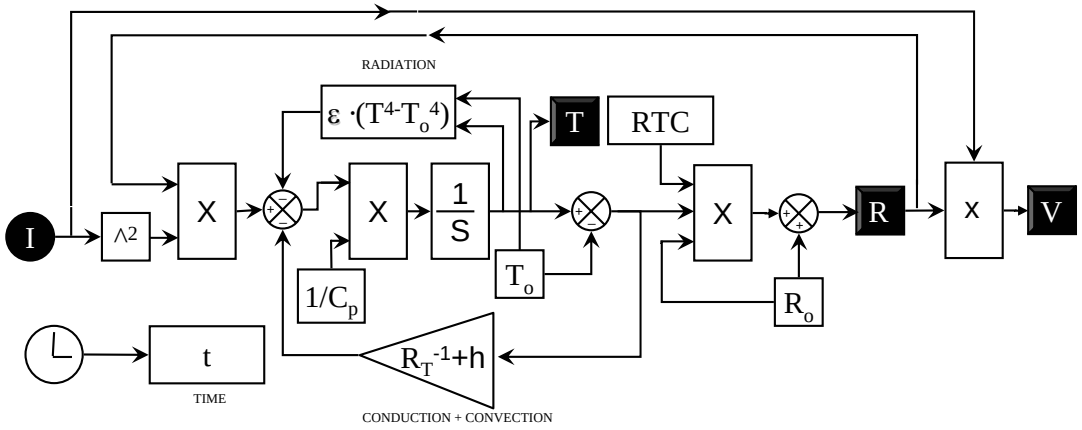

Figure 5.3: Flow chart of the model implemented in Simulink. The input variable is the current I and the output variables are the voltage V, the resistance R and the Temperature.

The measurements analyzed in this work are performed below 500 K. Only above this temperature the contribution from radiation losses becomes important. Therefore, we simplify the model extracting the non linearity that introduces the presence of radiation. The fitting of the experimental data will be not as good, but on the other hand we can assume the system as a first order, see chapter 3 in [107], taking the temperature as a controlled variable and the power as a manipulated variable. First order systems have been widely studied in control theory (RC electrical circuits). Setting aside a possible transformation in the sample, and not considering the emissivity, equation 5.2 can be further reduced to equation 5.3, with a new effective thermal resistance R_T^{eff}.

$$(Cp_{CC} + Cp_{Sample}) \cdot \frac{dT\,(t)}{dt} + \frac{1}{R_T^{eff}} \cdot [T\,(t) - T_o] = R\,(T) \cdot I^2 \tag{5.3}$$

In order to develop a digital controller[5], it is strictly necessary to know the transient response of the calorimeter. The main parameter is the time constant τ. τ is defined as the time that the calorimeter takes to reach a 63.2% of the final temperature value when the input is a current step, and it can be also defined in terms of the heat capacity and effective thermal resistance as:

$$\tau = (Cp_{CC} + Cp_{Sample}) \cdot R_T^{eff} = Cp \cdot R_T^{eff} \tag{5.4}$$

[5]A digital controller acts with discrete actions on time. Each action is separated by the necessary time to perform the controller calculations and the instrumental communications.

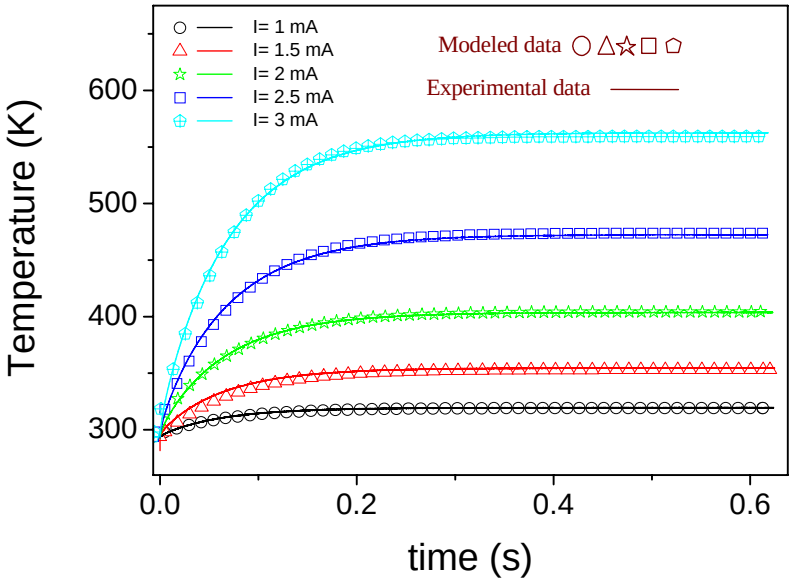

Figure 5.4: Experimental and modeled data for the transient response for a step input signal. We can see the transient evolution of the temperature when the calorimeter is feed by 5 different current values, in continuous line. The prediction of the model is plotted in dots.

Therefore, in the membrane-based calorimeter, the transient response τ depends heavily on the characteristics of the membrane and on the working environment pressure. The thinner is the membrane the smaller is the heat capacity addenda and the better thermally insulated (increase of R_T^{eff}) is the calorimetric cell. That means that the dependence of τ with membrane thickness is weak. However, other considerations concerning energy sensitivity impose the choice of membranes as thin as possible. With the expansion of the membrane area with respect to the heater size the losses are reduced with the corresponding increment in both tau and thermal resistance. In both nanocalorimeters designs, U-shape and serpentine-type, the ratio between heated area and total membrane area is the same and a typical value for τ is around 50-150 ms working in high vacuum. Rising the nanocalorimeter environment pressure with an ambient gas (He, Ar, N) the heat transfer by convection increases, disminishing the thermal resistance $R_T^{eff}$and therefore the τ. Working at pressures of few mbar τ typically decreases to values of few ms. As can be deduced from an analysis of stability the shorter is τ the easier is to tune the controller and the range of stability increases.

In general, we can propose an expression for the transfer function of the calorimeter based on equation 5.3, in terms of its Laplace Transform, as:

$$G(s) = \frac{T(s)}{P_{IN}(s)} = \frac{R_T^{eff}}{R_T^{eff} \cdot Cp \cdot s + 1} = \frac{R_T^{eff}}{\tau \cdot s + 1} \tag{5.5}$$

5.2 Controller Design.

The basic idea is to design an active controller to actuate over the input current in order to control the temperature evolution of the membrane-based calorimeters. The temperature response should follow ramp type set-points, correcting the perturbations produced by the phase transitions in the sample. A typical solid-to-liquid transition can be considered as a sharp endothermic transformation, and a valid controller should correct the temperature perturbations by increasing the input power [6]. The viability of a controller can be tested by the error on temperature during the ramp and by the drift during the transformation. The maximum error limits the power resolution and scanning rates achievable for each controller. To minimize the temperature errors, higher order (number of integrators) controllers are preferable, however stability requirements do not permit them. Of course the selection of the controller algorithm depends not only on the set points (ramps), but also on the hardware used to implement it. As explained in the introduction, two digital controllers have been designed to cover scanning rates from 0.05 to 1000 K/s. Although hardware implementations are clearly different and a detailed analysis for each controller algorithm will be presented in sections 5.2.1 and 5.2.2. In appendix C.1 some general considerations that have been taken into account in the design of the feedback controller algorithm are presented.

General Structure for the Digital Temperature Controller. Figure 5.5 presents the global structure for all the controllers presented in this thesis. A feedfoward controller (open-loop controller) based on the thermal models for the nanocalorimeters, equation 5.3, have been included in parallel to the feedback controller.

From a thorough previous characterization of the lumped parameters in an idle experiment, approximated scanning ramps can be performed by only applying the feedforward model as an open-loop controller, relieving the feedback controller actions. This strategy

[6] An important point is that a real transformation will be characterized by consumption or released of power with a triangular shape.

is specially suited when the sample heat capacity small compared to the heat capacity of the calorimetric cell. In this case, the role of the feedback controller is to refine the control action correcting perturbations introduced by the sample loading. When a sample undergoes a phase transition some energy is released or adsorbed in a characteristic time that mainly depends on the kinetics, at the same moment the feedback actions should correct the perturbation that this energy will induce in the temperature of the calorimetric cell.

For slow heating rates (below 10 K/s), we use the windows-based controller. In some cases time limitations imposed by the communication between the computer and the source-meter via GPIB protocol (160 ms) are larger than typical values for τ. In these case, it is possible to neglect the transient behavior, because in every refresh the calorimeter reaches the steady state and the model can be rewritten as $P_{IN} = (T(t) - T_0)/R_T^{eff}$. At high heating rates (over 10 K/s), with FPGA the control loop refresh is around 20μs, and in this case it is necessary to consider the full expression 5.3 to implement the feedforward taking into account the transient response.

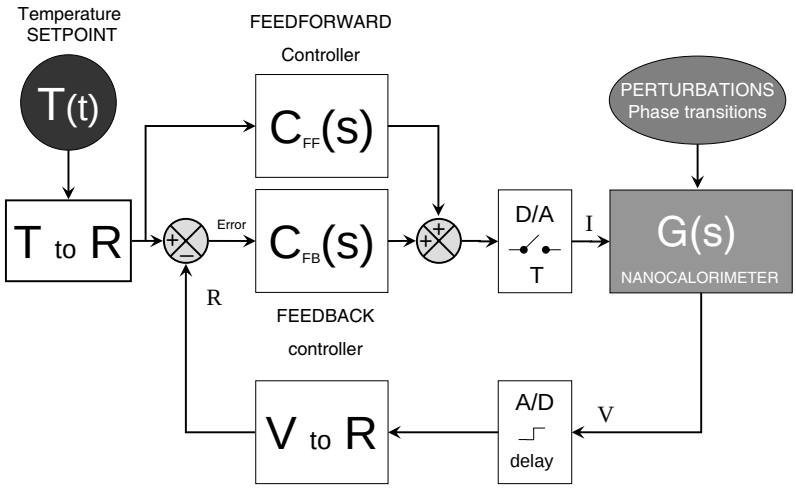

Figure 5.5: General block diagram for the temperature controllers.

5.2.1 IPID controller for slow heating rates.

Based on arguments discussed on appendix C.1 we selected an IPID feedback controller to perform power compensated calorimetric measurements at heating rates below 10 K/s. A double integrator sluggish the transient response and limits the range of scanning rates.

The presence of the parallel feedforward minimizes wind-up problems that this type of controllers show in front of step inputs. As will be shown in section 5.3 the hardware implementation with a sourcemeter (Keithley 2425) permits to generate control actions and acquire the system response with reduced noise. This fact allows inclusion of a differential action which improves the transient response. The algorithm for the IPID feedback controller action is described by:

$$C_{IPID}(t) = \int \left(K_I \int \varepsilon(t) \cdot dt + K_P \cdot \varepsilon(t) + K_d \cdot \frac{d\varepsilon(t)}{dt} \right) \cdot dt \tag{5.6}$$

It can be expressed in terms of its Laplace Transform,

$$C_{IPID}(s) = \frac{K_d \cdot s^2 + K_P \cdot s + K_I}{s^2} \tag{5.7}$$

The viability of the algorithm was demonstrated by modeling the response of the completed system (controller plus nanocalorimeter model, figure 5.3) using Simulink® Mathworks for a temperature ramp where an endothermic transition (triangular shape) was included during the ramp as a perturbation. Figure 5.6 shows the response of the IPID. The controller is tuned following the procedure explained in appendix C.2. With simulink several algorithms have been tested and IPID provides the best performances.

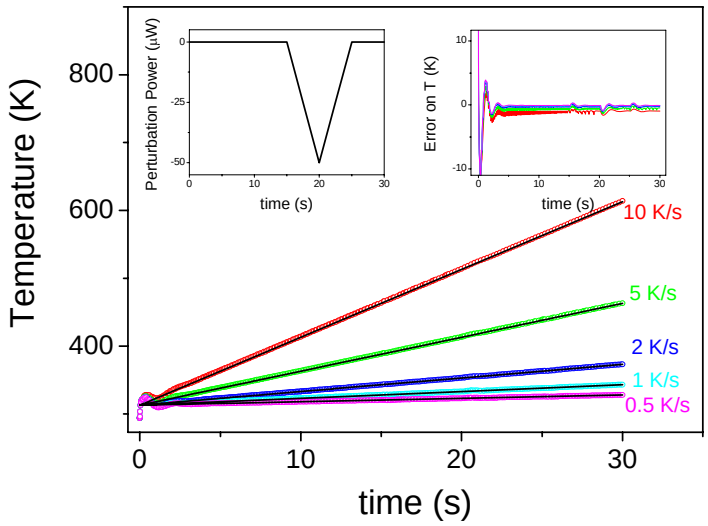

Figure 5.6: Temperature vs. time showing the response of the membrane-based calorimeter under an IPID control action.

5.2.2 PI controller for fast heating rates.

To attain fast scanning ramps we selected a PI feedback controller. With a single integrator, the static error does not cancel and tends to a constant value that will depend on the controller gains. With an underdamped tuning of the controller the response of the system will be faster and the error in steady state smaller but overshoots and settling times can be large. An experimental compromise between the allowable temperature error tolerance and the maximum overshoot and settling time should be taken during controller tuning. The proportional action introduces an extra degree of freedom that permits to increase the stability range of the single integrator based controller. The implementation of the fast controller is carried out with fast ADC and DAC integrated in the FPGA board. Unfortunately the intrinsic noise of the action and measured signals does not permit to include a differential control action. The algorithm for the PI feedback controller action is described by:

$$C_{PI}(t) = K_I \int \varepsilon(t) \cdot dt + K_P \cdot \varepsilon(t) \tag{5.8}$$

It can be expressed in terms of its Laplace Transform,

$$C_{PI}(s) = \frac{K_P \cdot s + K_I}{s} \tag{5.9}$$

5.3 IPID-based scanning calorimeter[7].

5.3.1 IPID controller implementation

The IPID controller algorithm was implemented in a Labview windows-based application that controls via GPIB protocol a sourcemeter (keithley 2425 [8]) with a high resolution and low noise I/O. Typically the minimum control loop times are imposed to values over 160 ms, by the limitations in GPIB communication. The application permits to program different ramps, by giving the initial and final temperatures (in the range from 300 to 900 K) and heating rates (from 0.05 to 10 K/s). From these parameters the array of setpoint temperatures that correspond to the desired temperature at each time is generated. At each control loop the application is based on the scheme showed in figure 5.7. From the input temperature the error on resistance is calculated. The addition of the feedback controller and the feedforward controller gives the value of the power to introduce in the calorimeter. The Labview application communicates the output current to the source and reads the measured resistance of the calorimetric cell. The resultant temperature is measured from this resistance value and the loop begins again. The application stores all the data involved in the process in each control loop to be processed after. With an empty calorimeter, the temperature difference between the setpoint and the measured temperature is below 10 mK independently of the heating rate.

5.3.2 Tests over thin films.

The combination of the membrane-based calorimeter and the IPID controller results in a highly sensitive calorimeter able to detect phase transitions at heating rates between 0.05 and 10 K/s, in submicrogram samples. Its use and dynamic sensitivity will be demonstrated by analyzing two well known processes, the melting behavior of indium and of a high density polyethylene film (HDPE).

The selected nanocalorimeters to make these tests are the U-shape design with a deposition of 75nm of Pt forming up the heater over a 180 nm thick low-stress membrane of Si_xN_y. After the membrane reduction process, 100 nm of Ag are deposited on the backside of the membrane using a shadow mask. The presence of this thermal layer ensures a

[7]Part of this chapter appears in [105].

[8]The Keithley 2425 is a pulsed source-meter able to perform current pulses with a programming resolution of 500 nA and 50 nA of noise (peak-to-peak), in the range of operation of the calorimeter. Simultaneously is able to measure the voltage drop in the resistance with an accuracy of $100\mu V$ in the range of 20V.

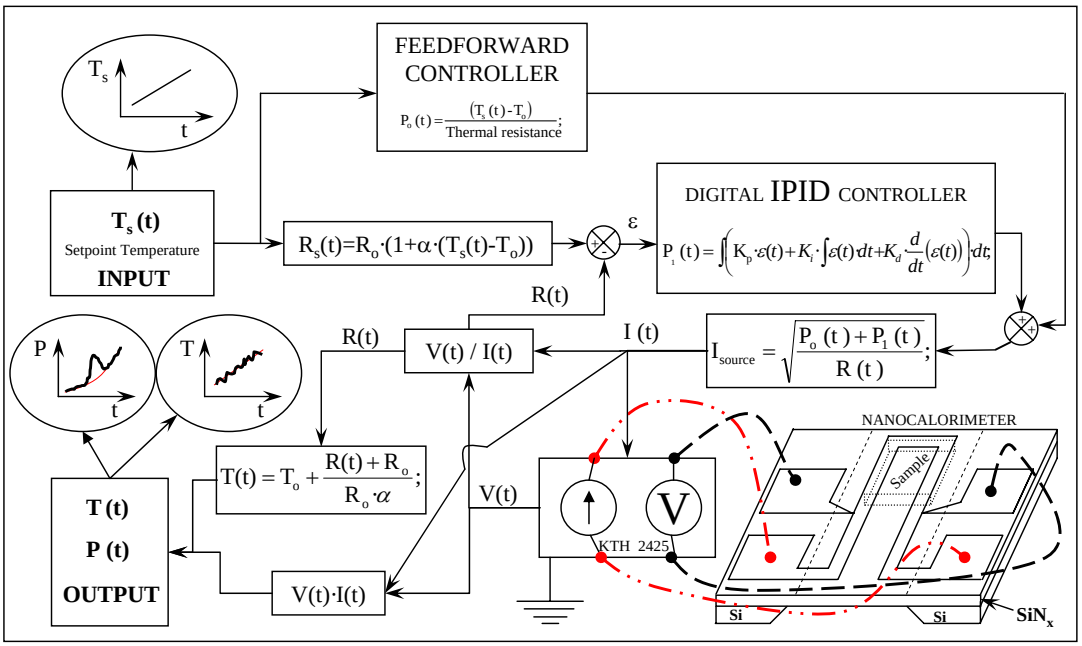

Figure 5.7: The IPID controller structure.

constant value for the thermal resistance with and without sample. Before use, the devices are thermally stabilized by a two step process. First, annealing in Ar at temperatures around 975 K and, subsequently, with fast heating ramps in HV performed with series of 10000 electrical pulses in the heater, reaching 475 K over the transition to be studied. Temperature calibration was carried out by independent 4-point probe measurements, obtaining values around 0.0024 K^{-1} for the TCR. The heat capacity of the addenda of the calorimetric cell is determined in quasi-adiabatic conditions, see chapter 4. The exact value is strongly dependent on the reduction of the membrane and the thickness of the heating plate, but typical values around 120 nJ/K are experimentally determined at room temperature.

The calorimetric measurements are performed inside the specially high vacuum chamber, described in chapter 3. The experiments are typically carried out in the 10^{-7}mbar range to minimize convection heat losses and surface modification of the thin films during heating. The microdevice is placed in the innerchamber and temperature of the Si frame is maintained within 0.1 K of the block temperature (T=283 K) during the experiment, with the aid of an external thermal bath. In a typical calorimetric experiment, the Pt resistor serves both as a heater and as a thermometer and the temperature of the calorimetric cell,

the center of the membrane, can be monitored by the variation of heater resistance with temperature.

The lumped model, see equation 5.1, suffice for a thin film sample since the improved thermal contact between sample and heater makes it feasible to assume that the sample and heater temperatures (T_S and T_H) remain equal during a scan, independently of the specific transformation occurring on the sample side. Assuming an insulating film is located onto the thermal layer, the temperature difference across the thickness of the sample can be expressed as :

$$\triangle T = \left(\frac{\rho c h^2}{\lambda}\right) \cdot \left(\frac{dT}{dt}\right) \tag{5.10}$$

For a 50 μm thick polyethylene film (see below), using ρ=0.95 g/cm^3, c=1.5 $J \cdot (g \cdot K)^{-1}$ and λ=0.20 $W \cdot (m \cdot K)^{-1}$, gives a temperature difference of 0.2 K at a heating rate of 10 K/s, the maximum used in this work. The close proximity between sample and heater and the high vacuum conditions, which gives h_{cv}=0 (no convection), of our setup are necessary for the device to work as if the sample is inside a feedback loop similar to that established by Randzio [18]. Under those conditions, the input power is close to the measured power if the temperature difference between setpoint and sample is maintained low. The heat transfer coefficient, R_T^{eff}, is determined previously at steady-state, with measures of the resultant temperatures for a staircase of current, for a range of experimental conditions. Between room temperature and 500 K, R_T^{eff} has a slight non linear temperature dependence and a polynomial fit is used to interpolate its value. The presence of a thick sample could change the R_T^{eff}value and further corrections to equation 5.3 would then be necessary, preventing consecutive differential measurements. The presence of the thermal plate decreases this dependence on the sample, fixing the heat transfer coefficient[9].

[9]In fact, with thermal resistance measurements is possible to get the thermal conductivity of thin films [108].

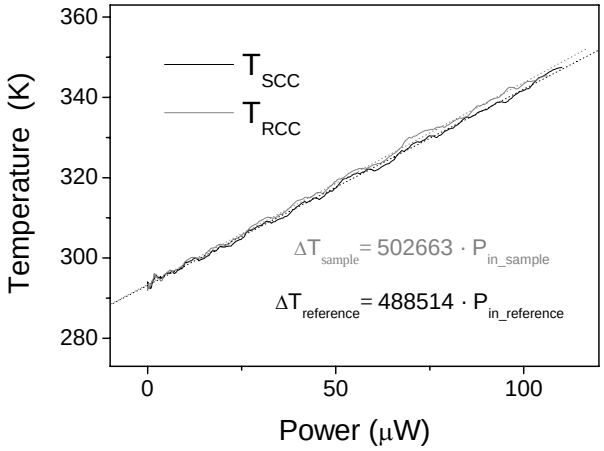

Figure 5.8: Temperatures vs. Power.
Measurement of the thermal resistance in a twin system of calorimetric cells. A typical value of R_T^{eff}, $5 \cdot 10^5\, W/K$, is extracted with a linear fitting of the experimental data. To obtain these curves the calorimeter is fed with a constant current and the voltage is measured at the steady state.

Typical experimental parameters are: heating rates between 0.1-10 K/s, temperature range from room temperature to 500 K, Pt resistance 100-120 Ω , average heat transfer coefficient R_T^{eff} $\sim 5 \cdot 10^{-6}\ W/K$, and power input 0-1.5 mW. The repeatability of the power output to the microdevice from consecutive measurements is below 100 nW and the limit of detection of thermal power was around 200 nW, twice the peak-to-peak electrical noise in the electronics. In experiments, the heat absorbed (or released) by the sample is measured with respect to a reference calorimeter to compensate for minimal temperature changes in the calorimetric block.

Results & Discussion The apparatus is particularly well adapted to measure the latent heat of first-order phase transitions occurring in thin film samples. To check the performances of the calorimeter, we have selected standard samples in thin film form of indium and high density polyethylene (HDPE). HPDE is chosen as a reference material since it is well known and provides a severe test for the microdevices in terms of both its relatively low thermal conductivity and poor wettability with the Ag layer. The crystallinity of the polyethylene thin film (thickness, 10 μm) is 60 % at room temperature.

Figure 5.9 shows the calorimetric measurement at different heating rates on the HDPE film after baseline subtraction. The baseline is taken as the empty calorimeter for each heating rate, since the thermal resistance (heat transfer coefficient, R_T^{eff}) between heater

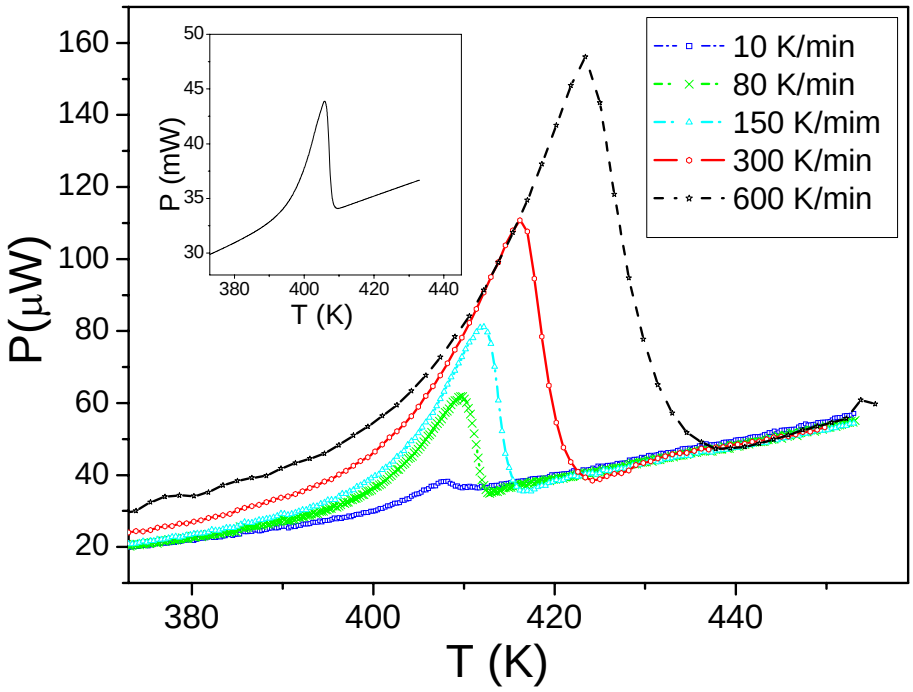

Figure 5.9: Calorimetric measurements on HDPE.
Continuous heating thermogram at different heating rates of the melting endotherm of a 10 μm thick high density polyethylene film. The inset shows the peak of 2.85 mg of HPDE measured by a Perkin Elmer DSC7 at 10 K/s .

and surroundings does not change appreciable upon location of the sample on the center of the membrane. For comparison, the inset shows the signal obtained from a Perkin Elmer DSC7 at a heating rate of 10 K/min for a sample of mass 2.84 mg. This measurement yielded an onset temperature for melting, T_{on}=394 K and a heat of fusion of 165 ± 10 J/g. The sample is placed with the aid of a hair and a micromanipulator on the Ag thermal layer (surface 1240x350μm^2), just beneath the heater and temperatures sensors. Initially, the area of the film was 470x350 μm^2 and its thickness 10 μm, with a density of 0.95 g/cm^3. Prior to acquiring the data shown in figure 5.9, the sample is held isothermally at 398 K, slightly above the onset for melting, to melt completely the film and improve the contact, i.e., the heat transfer between sample and Pt heater. A film, which do not properly wets the Ag surface upon melting, decreased its contact surface by about a fifth with a corresponding thickness increase. This phenomenon posed an important constraint to the calorimetric cell and the behavior of the calorimeter. Different heating rates from 10^{-3} to 10 K/s

were explored to analyze their influence on the thermal profile. As polyethylene is a poor thermal conductor, and it is extremely thick compared to the heater/membrane/thermal layer stack, the thermal lag would be dominated by the sample for large heating rates if the thermal contact between sample and calorimetric cell is not properly realized. This effect could be responsible for the displacement of the peak temperature as the heating rate increases from 0.17 to 10 K/s. However, as expected, the peak onset is relatively unaffected by variations in heating rate or thermal conductance, with a value of T_{on}=396 ± 0.5 K within the range 0.17-5 K/s.

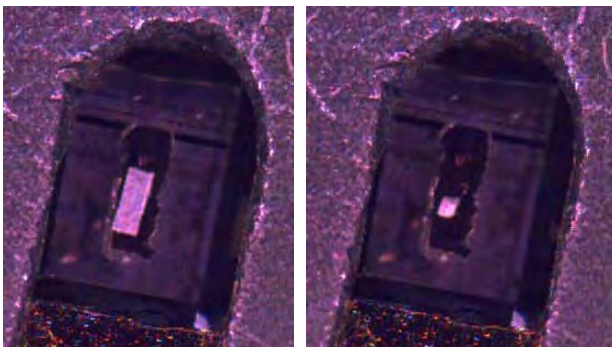

Figure 5.10: HDPE sample photographies.
On the left image the as-placed HDPE film over the Ag thermal plate. On the right the HDPE film after the preheating, showing that the polymer does not wet properly on the Ag surface.

A value of 250 ± 15 μJ for the enthalpy of melting of the HDPE film is determined at heating rates below 0.3 K/s. Although the exact mass of the sample is not known, an estimate based on the initial sample dimensions, 470 x 350 x 10 μm^3 yields a value of 1.56 μg, which provides a ΔH of 160 ± 10 J/g, in agreement to the measured value with the DSC7. At higher heating rates (80-600 K/min), the enthalpy decreases with increasing heating rate with an average value of 120 ± 20 J/g. The lower value of the heat of fusion at the higher heating rates can be attributed to both the increased thermal lag between sample and heater and the increased temperature difference between the set point temperature and the sample temperature during the transformation. At high rates the digital controller is no longer able to compensate exactly for the difference in temperature. Correcting the measured power by this last effect yields an average enthalpy value of ∼145 J/g, within 15% of the expected value. For comparison, the signal obtained from a 500 nm In thin film (m=1.55 μg) at a heating rate of 1 K/s is shown in figure 5.11 . The measured heat of fusion is 44 ± 2 μJ, which taking into account the estimated mass of the sample

corresponds to 28.0 ± 1.0 J/g, in good agreement with the accepted value of 28.4 J/g. The full-width-at-half-maximum of the peak is only 6 K which confirms the satisfactory steady state thermal profile at such heating rates. With the current electronic system, the dynamic sensitivity (minimum amount of heat that can be detected) at a scanning rate of 1 K/s would be around 2 μJ, which for the HDPE samples studied in this work correspond roughly to 10 ng.

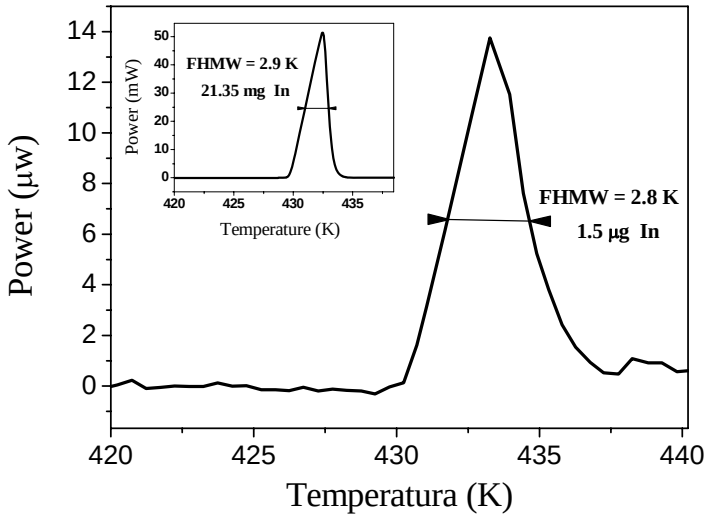

Figure 5.11: Calorimetric measurements on 500nm In film .
Calorimetric trace under power-compensated mode of the melting of a 500 nm thick In film at a scanning rate of 1 K/s. . The inset shows the signal obtained from a 21.3 mg In sample using a Perkin Elmer DSC7.

In order to test the impulse response of the system either in isothermal or scanning mode to a fast exothermic event, the empty calorimeter is exposed to light pulses of several seconds in duration. Figure 5.12 shows the power increase due to light exposure of the calorimetric cell during isothermal (a) or constant heating rate (1 K/s) experiments (b). The off-on and on-off light transitions show the short response time, τ= 200ms, of the calorimeters and the slightly damped response of the IPID controller, even in the case of a larger instantaneous heat flow, as shown in the continuous heating rate figure. The small time constant of the devices eliminates the need for deconvolution of the irradiant heating data with the impulse response, and provides a high definition of the heat transitions.

In exothermic events, the total heat absorbed by the sample is not in agreement with the total heat measured by the IPID controller, because these measurements were performed in high vacuum, and the time constant is too large to allow for a temperature recovery to

the setpoint temperature at each step. Working under an inert gas flow should allow for quantitative measurements in exothermic transitions.

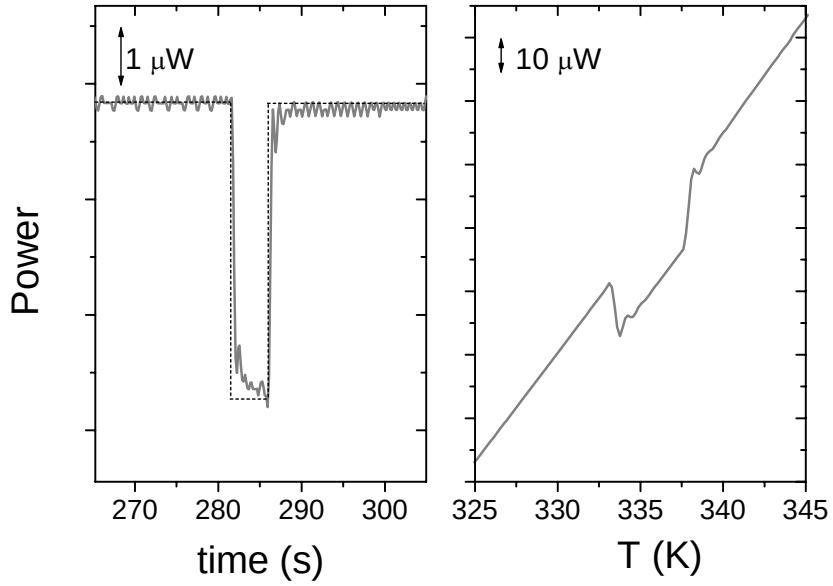

Figure 5.12: Calorimetric measurements of a fast exothermic event .
Isothermal (a) and continuous heating rate at 1 K/s (b) thermal power from exposure to light radiation pulses. The dashed line represents the input light pulse.

5.4 FPGA-based Non-adiabatic Fast-DSC.

Rapid thermal processing has become an indispensable tool in the manufacture of integrated circuits, replacing conventional annealing approaches [109]. It is used to thermally promote ordering of implanted samples (i.e., Si doped) [110], or to produce new intermediate phases (i.e., NiSi [111]) at heating rates that typically span 10 to 100 K/s. Recently, it has also been used to form ultra-shallow junctions in complementary metal-oxide semiconductor transistors with 10-nm-scale gate lengths [112]. In situ mapping of the kinetics and thermodynamics of the transformation remains a difficult task with conventional tools, in spite of the need to understand the phase sequence and formation at the established heating rates in nanoscale materials. The challenge is to achieve fast heating rates ($\sim 10-10^3\,K/s$) under controlled conditions and to measure the heat released or absorbed by small samples during a phase transition.

With the use of membrane-based nanocalorimeters, the sensibility limit is highly enhanced; however, improvements in the controllers are also necessary to attain linear scans at fast rates. The already presented windows-based controller (section 5.3) is limited to operate at scanning rates below 10 K/s due to GPIB communication of the computer with the sourcemeter. This limitation can be resolved by using dedicated hardware like analog controllers that can increase the control frequency up to 10MHz. The implementation of analog controllers, however, has some drawback in terms of design stiffness. Several years ago, we realized first trials to develop analog control circuits with operational amplifiers defining the proportional, integral and derivative constants through the resistances in the circuit. The tuning of this type of controllers is hard and the stability ranges are short, limiting the temperature range achievable in a single scan. Moreover, the need to introduce an extra sensor or noisy analog dividers to obtain the resistance, when working with a single heater/sensor element, complicated the task. Nevertheless, Mezliakov has recently published the implementation of an analog controller, showing its viability to attain fast (up to 10^5 K/s) ramps with empty calorimeters [106]. In our case, the difficulties found in the initial test with analog controllers led us to think in digital solutions to work in intermediate heating rates. Digital controllers present several advantages in front of analog versions, such as more flexibility, greater facility of implementation, better accuracy and better robustness (sensitivity to parameter variations) .

During last years several instrumentation companies have presented in the market new hardware solutions that fit to our necessities. To overcome speed limitations imposed by Windows-based systems and GPIB communications [105], we use a Field Programmable

Gate Array (FPGA)-based controller. FPGAs are arrays of interconnected logic gates that permit programming of a large number of operations in parallel, improving the features of classical microprocessors limited to sequential computation. The National Instruments 7831 R card, which includes an FPGA with 1-M gates inside and the ADC and DAC integrated onboard, is selected as dedicated hardware with the controller algorithm embedded inside. The control loop time, which includes sensing, digital calculation, and control actuation is reduced to 20 μs, around three orders of magnitude faster than in GPIB-based controllers. FPGA allows real-time control with an internal clock at 40 MHz, avoiding the errors that Windows-based programs can introduce in time. Below, we describe the implementation of an essentially nonadiabatic fast differential scanning calorimeter using the FPGA and a custom-built circuitry to control the heating ramps of a twin system of nanocalorimeters working in parallel.

5.4.1 Implementation.

Figure 5.13 shows the block diagram of the control loop structure proposed to implement the nanocalorimetric setup. It is divided into several blocks. The first is devoted to the digital calculations performed within the FPGA (setpoint generation, digital multipliers, and dividers on both temperature controllers). Another block contains the necessary circuitry (current driver, current and voltage sensing with instrumentation amplifiers), and the final block includes the acquisition and storage of raw data. As the FPGA is loaded with the controller algorithm, the acquisition and storage of all the signals involved in the calorimetric measurements are performed with the NI PXI 6123 card, which permits acquisitions up to 500 kHz per channel. This strategy releases memory and also accelerates the control loop in FPGA, since the communication between the FPGA card and the computer is limited to the starting trigger. The acquisition frequency is varied in each experiment to obtain a single value every 10 mK. Box-averaging procedures are employed during the data treatment, preserving a temperature resolution below 0.5 K. Both cards, NI 7831R (with FPGA) and acquisition card NI PXI 6123, are mounted in an NI PXI-8187 computer rack with a Windows-based LabVIEW installed inside. A host program permits introduction a priori of the parameters that define the FPGA controller action and also synchronization of the triggers for the initialization of the FPGA control action and the raw data acquisition.

The programming of the FPGA is performed with the LabVIEW FPGA module. It permits defining the various tasks (digital operations, analog inputs and outputs) in a

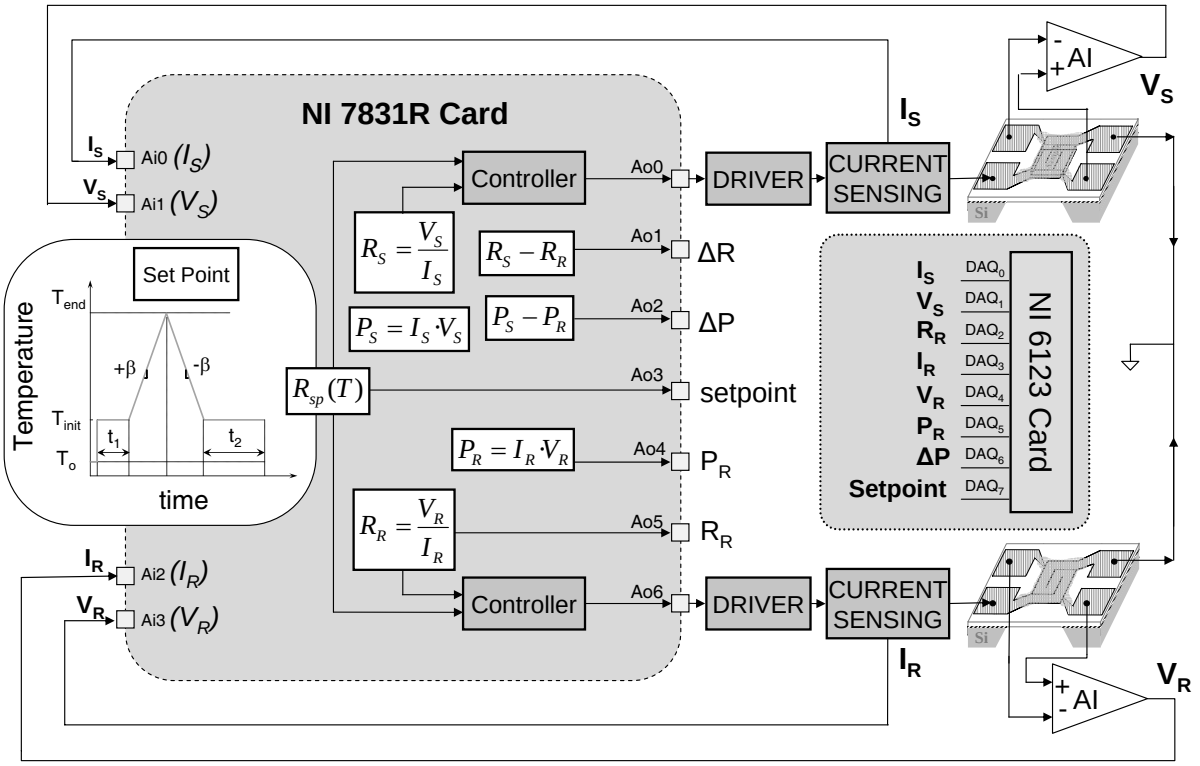

Figure 5.13: General block diagram of the instrumental setup.

high-level graphical programming language and afterwards compilation of it in the FPGA to use the NI 7831R card as a dedicated hardware. During programming, it is necessary to take into account that the FPGA is limited to work with integer variables with a maximum resolution of 32 bits for internal computation and 16 bits for the I/O variables. To increase the resolution, internal variables are spread through scaling factors, and all of the I/O variables are extended to cover the maximum range of converters (+10V $\Longleftrightarrow$ +32768).

5.4.1.1 Setpoint generation and controller implementation in FPGA.

The various FPGA tasks repeated in each control loop are as follows:

i) Setpoint generation; The FPGA is programmed to generate in each control loop an internal variable that is proportional to the temperature at a given time. Figure 5.13 shows the triangular-shaped temperature profile selected to perform calorimetry. It is defined in terms of five parameters: time that the temperature remains at the initial temperature

(t_1); initial temperature (T_{init}); final temperature (T_{end}); scanning rate (β); and time that temperature remains at T_{init} after the scan (t_2). This definition of temperature setpoints facilitates the generation of temperature ramps to analyze samples in scanning mode (heating and cooling) when $T_{init} < T_{end}$, but also to carry out measurements in isothermal mode if the temperature parameters are defined as $T_{init} = T_{end}$. The physical measure of temperature is obtained through the temperature dependence of the Pt heater/sensor electrical resistance in the calorimetric cell. To simplify the number of operations inside the FPGA, the internal setpoint is calculated as the resistance value for each temperature.

ii) Calculation of resistances (process variables); The signals (in voltage) proportional to the current injected in the calorimeters ($I_S \, and \, I_R$) and the voltage drops in each calorimetric cell ($V_S \, and \, V_R$) are sensed with the analog inputs of the NI 7831R and converted to 16-bit variables. The resistances, which are process variables, are obtained from an internal digital division between V_i and I_i. To improve the resolution of the integer division, the voltages are multiplied by a constant factor that accommodates the internal values of the process variable with the resistance setpoint values to make its comparison possible. We use two analog outputs of the NI 7831R to generate the voltages proportional to the process variables R_S and R_R. Both values are acquired and stored together.

iii) Controller algorithm implementation; Two identical controllers have been implemented to calculate the control actions needed to attain the setpoint with the process variable resistances ($R_S = R_{setpoint} = R_R$). The algorithm structure is summarized in the scheme presented in Figure 5.14. Some external parameters (K_P, K_I, R_o, R_T, C_P) are introduced to define and properly tune both control actions. The addition of control actions in power is transformed into a control action in current, considering that the power in the resistive heater is released by the Joule effect $\left(I = \sqrt{\frac{P}{R_{PV}}}\right)$.

iv) Power calculation; In calorimetry, one of the main variables is the power released to reach a temperature. The FPGA is used as a digital multiplier to generate a signal proportional to the power. The subtraction of both power signals, $\triangle P = P_S - P_R$, is performed internally (with 32-bit variables to improve resolution) and generated with the NI 7831 R analog output.

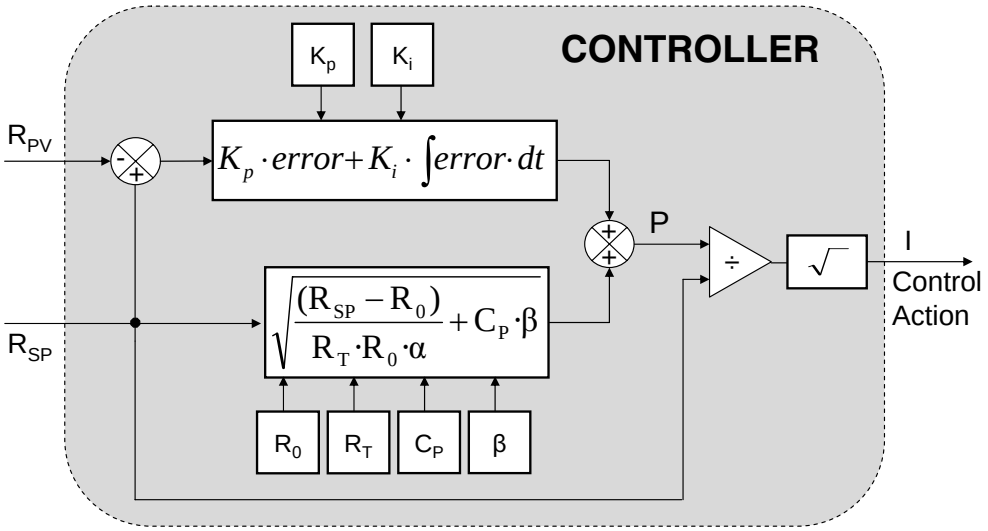

Figure 5.14: Block diagram of the controller algorithm.

5.4.1.2 Current driver, current and voltage sense stage.

The control actions from the FPGA embedded controller are output as a voltage signal. The NI 7831 R does not have sufficient output power to feed the nanocalorimeters (typically limited to a few milliamps). Therefore, we have implemented a voltage-to-current converter that is used as a current driver. Figure 5.15 shows the circuit of the voltage-to-current converter, which includes the commercial converter XTR110 from Burr-Brown. Using a resistance of 25Ω as R_{ext}, the output current reaches 40 mA when the input voltage is at maximum (+10 V). The converter is linear, which (taking into account the resolution of the ADC (16 bits) between ±10V) permits estimation of the minimum current step related to the increment of an LSB around $\sim 1.2\,\mu A$. Current resolution can be improved with reduction of the range of currents, increasing the R_{ext}.

Although the current driver has a quasi-linear behavior, a precise estimation requires a direct measurement of this variable. Figure 5.15 also shows the circuit that measures the current introduced into the nanocalorimeter. The instrumentation amplifier is the INA 114 from Burn-Brown. This is an amplifier with a high common-mode rejection of 115 dB (minimum) which guarantees low noise signal, a low output offset (max. $50\,\mu V$), and mainly a low input bias current (max. 2 nA) that ensures a very small current drift out of the calorimeter circuit during measuring. The maximum output current supplied by the

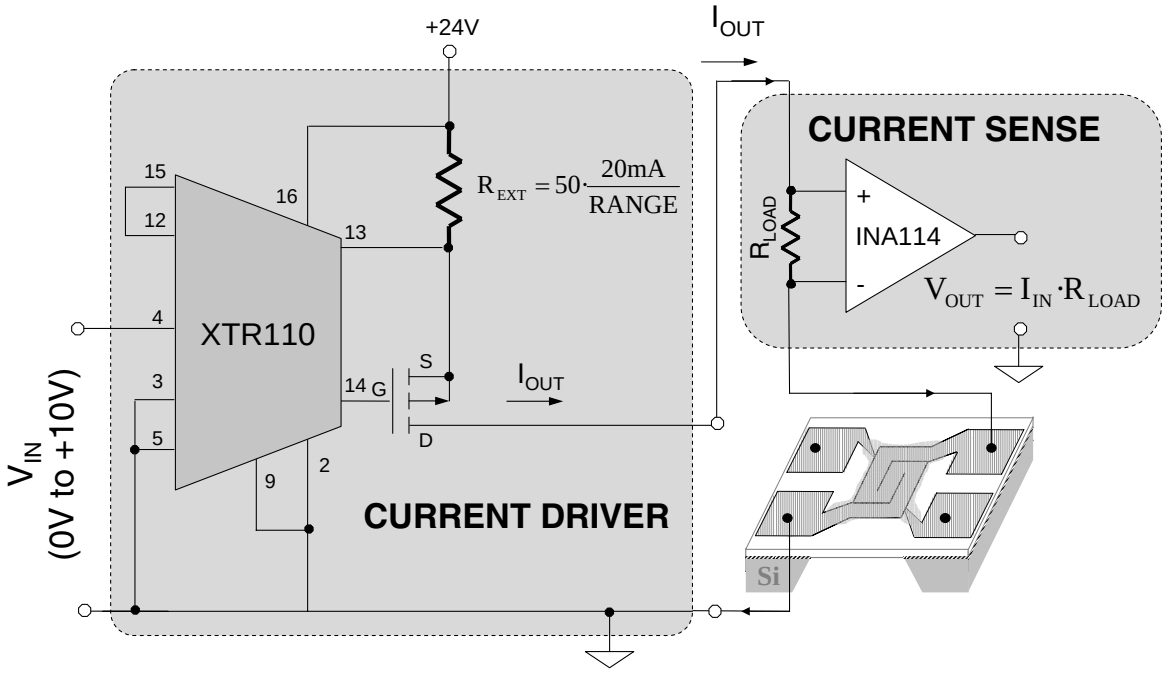

Figure 5.15: Block diagram of the current driver and current sensing circuit.

current driver is limited by the total impedance loaded on it. With increasing R_{load}, the impedance (R_{load}+R_{heater}) may limit the maximum output current values. The choice of an R_{load} of 250Ω permits measurement of the entire current range up to 40 mA. Values over 250Ω limit the maximum current below 40 mA when the nanocalorimeter resistance reaches values on the order of 100Ω which corresponds to temperatures around 1200 K. To improve resolution in small currents sensing it is possible to change the amplifier gain.

5.4.2 Analysis of measurement possibilities.

The combination of the FPGA based controller and a twin membrane-based calorimeter results on a high speed power compensation calorimeter. In figure 5.16 we analyze in detail the power curves as function of time. The schematic inset in figure 5.16 shows the characteristic power cycle with temperature for a calorimeter with sample (continuous line) and without sample (dashed line). The final power curve in time can be described through equation 5.15. Working in a differential configuration with two identical calorimetric cells the difference in power $\triangle P = P_S - P_R$ is equal to $Cp_{Sample} \cdot \frac{dT(t)}{dt}$ due to the presence of the sample in one cell.

This expression is valid if we consider that in both cells the heat capacity of the calorimetric cells and the power losses are equal. Both conditions are achievable through a proper selection of the empty calorimetric cells. However, if the measurement is performed on a highly thermal conductive sample the conductive losses through the membrane may change between the reference cell (empty) and the sample cell. To prevent this possibility it is often useful to incorporate a thermal layer beneath the calorimetric cell, which not only improves the thermal profiles but also equals the thermal losses of both cells. Moreover, working in gas ambient, the largest contribution to heat loss is convection through the gas which minimizes the changes in R_T^{eff} when sample is located in the cell. Therefore, with a previous selection of suitable calorimeters and either the incorporation of a thermal layer or working with gas at reduced or ambient pressure we can consider that the calorimetric information of the sample is contained in the $\triangle P$ signal. Nevertheless, in real experiments the initial difference (before sample location in CCS) between the cells can be calculated as a correcting baseline $\triangle P_o$ that reduces the possible errors introduced by this simplification, obtaining the power employed to heat the sample as:

$$Cp_{Sample} \cdot \frac{dT\,(t)}{dt} = \triangle P - \triangle P_o \tag{5.11}$$

Necessity to work under ambient gas. With the aim of measure the calorimetric transformation during cooling, it is necessary to increase the thermal losses of the nanocalorimeter. The Pt heater is only able to behave as a heat source of power, and the limit in cooling is fixed by the power released from the calorimetric cell by losses. The power losses of the calorimeter depends on the cell temperature and on the surrounding temperatures (T_o): T of Si frame and of ambient gas, if it is present. As can be appreciated in the scheme presented in figure 5.16, if the initial temperatures of the scan are very close to this T_o, the power needed to attain the ramp at the end of the scan (continuous dark blue curve) becomes negative, and this condition can not be reproduced. This undesired effect can be solved by increasing the power losses by introducing an inert gas (Ar, He) that acts as a cooling medium. Increasing the power losses enforces to widespread the feeding current range which can results on a decrease of the resolution, but also solves similar problems that can be appreciated in samples with large masses or high energetic transformations. If the sample mass is high the characteristic transient cooling times of the calorimetric cell becomes larger with a subsequent reduction of the speed response of the calorimeter. Therefore it is advisable to increase the losses through convection to minimize

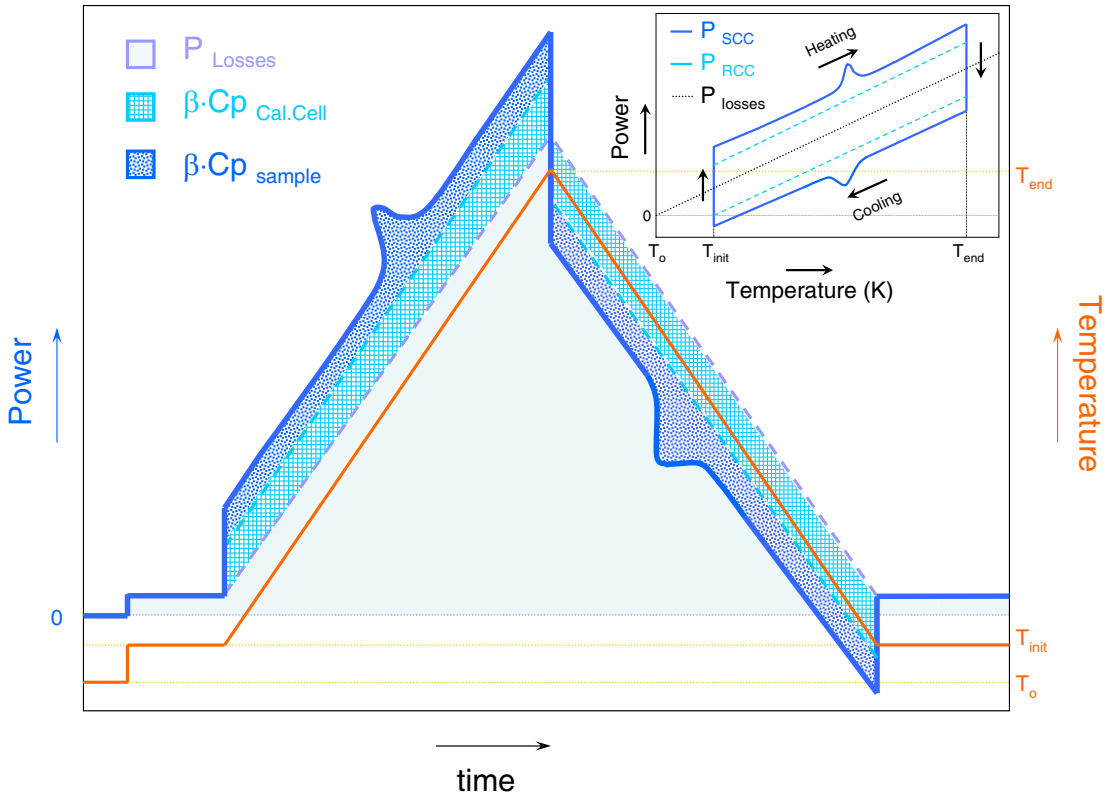

Figure 5.16: Schematics of power curves.

this effect. A similar problem is found when high energetic transformations require power dissipation. This is the case of many first order transitions in vacuum, i.e. if the energy released is large enough the controller may not act as a power sink (negative power) being limited if the power losses baseline are not larger than the power released by the transformation. Following the above mentioned arguments we realized most of the measurements in the presence of a gas. While it is not the main issue of this thesis working at atmospheric pressures opens the possibility to analyze biological samples which is impossible in vacuum conditions due to water evaporation even at room temperature.

Non-active control mode. Working only with the feedforward controller, a predefined current pulsed with a saw tooth profile will produce scanning ramps at the desired rates. This methodology has been demonstrated by Schick's group [54]. The feedforward parameters can be adjusted in an idle experiment to attain a given heating/cooling rate by a trial and error procedure. With this method the limit in power and temperature resolution,

similarly to the adiabatic method is mainly determined by the noise associated to the current generated and to the voltage drop measured in the calorimetric cells. Typically both signals are sensed in voltage with maximum noises always below 2 mV (6-7 LSB) [10], which in the case of current sensing with a resistance R_{load} of 250Ω results on a peak-to-peak noise of $\pm 10\,\mu A$.

In slow rate scanning ramps, where feeding currents are small and the signal to noise ratio is worst, the resistance calculation in FPGA generates a voltage with an associated a noise around 6 mV. This noise corresponds to a noise in resistance of 0.02Ω, a ∼0.1% of the room temperature resistance 26-27Ω. At higher temperatures and for higher heating rates the applied currents are also higher and therefore the associated noise to the resistance decrease. Therefore the noise in temperature is around 0.1% of the temperature values, which depending on the heating and data acquisition rates allow the use of box averaging procedures to improve the signal-to-noise ratio. Concerning the power, the widespread analysis of noises in the original voltage signals represents a final noise below 0.2% of power value for currents around 5mA decreasing up to noises below 0.05% of power value for currents over 20mA.

Active control mode. Using the combination of the feedfoward and the feedback controllers to correct the power perturbations that occur during a phase transitions, the linear ramp can be mantained during the complete temperature scan. The active control prevents the increase/decrease of the temperature by adjusting the power introduced in each control loop. On the other hand as a main drawback the noise levels in temperature and power degrade due to the control action. The level of noise highly depends on the tuning of the controller. An underdamped tuning will fast decrease the transient errors on temperature by introducing oscillations that can be considered as a noise, while and overdamped tuning sluggish the correction of temperature errors preserving a better noise. A compromise between both situations is highly preferred. Therefore, we focus the work presented in this thesis in active control operation mode, since it can result on better performances to analyze different types of samples at typical conditions of Rapid Thermal Processing. A detailed analysis is presented in the next section with several experimental measurements on thin film samples.

[10] Acquiring at rates of 50 Khz

5.4.3 Case study: In thin films.

The melting transition in In thin films is chosen to analyze the capabilities of the proposed controller. A pair of twin meander-shape nanocalorimeters with a resistance difference below 0.5% (26 Ω at 293 K) is mounted inside an ultra-high vacuum e-beam evaporation chamber. The calorimeters are placed into a custom-built probe with gold pogopins that electrically connect both devices. Several shutters permit selection of the nanocalorimeter to be deposited. A shadow mask defined by photolithography and etching is attached to the bottom of the silicon frame, limiting sample growth to the sensing area of the calorimetric cell. With all these elements, in situ calorimetric measurements are carried out. Details of the experimental setup have already been presented elsewhere, see chapter 3.

To reduce the time response of the calorimeters, all experiments presented in this section are carried out in the range 1-10^3mbar. To prevent the complexity that radiation losses may introduce into the analysis of the calorimetric traces, initial tests are mainly realized at low temperatures. The empty calorimeters are heated several times at different scanning rates following a common setpoint. Measurements show that the sensitivity in differential power ($\triangle P_0$) is around 5 μW (or 5 nJ/K at 10^3 K/s), and the temperature error (T_R and T_R versus $T_{setpoint}$) remains below 0.1 K for ramps at 50 K/s and below 2 K for ramps up to 10^3 K/s. Considering the limitations on power resolution, we chose to analyze the first-order solid-to-liquid transition of an In film with a nominal thickness of 100 nm in order to test the controller with a small perturbation.

Indium is a well established standard in calorimetry, with a melting transition at 429.75 K and a specific heat of fusion of 28.39 J/g [77]. The In sample is e-beam evaporated onto the active area of the membrane using a shadow mask. The mass deposited (evaluated according to procedure describe in section 2.4) is estimated around 470 ± 50 ng.

Results and Discussion. Figure 5.17 (a) shows the raw data of the temperature time profiles for the nanocalorimeter loaded with the In sample operating at 1 atm Ar pressure. The controller forces both calorimeters to follow the predefined setpoint and temperature time profile, and generates the differential power between cells in real time, shown in figure 5.17 (b). Because the melting transition is reversible, no baseline subtraction of the second scan can be performed. Therefore, we realized identical experiments previous to the sample deposition in order to evaluate the drift of the differential power ΔP_0 and determine ΔP-ΔP_0, which should be proportional to the power absorbed/released by the sample during heating/cooling.

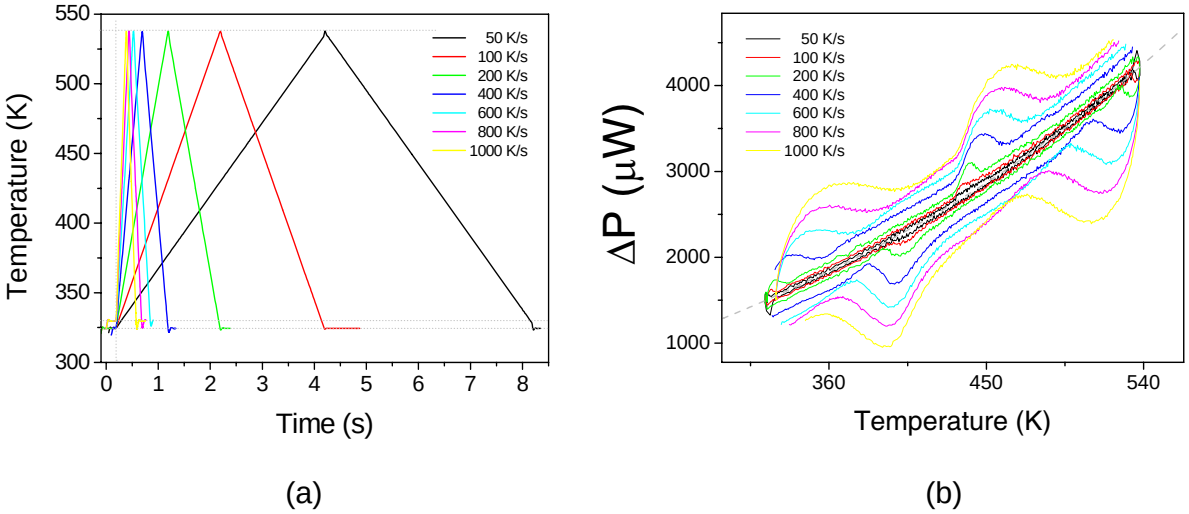

Figure 5.17:
(a) Temperature time profiles of the calorimeter loaded with 100nm In for several predefined setpoints. Scanning rates ranges from 50 to 1000 K/s. (b) ΔP signals as function of temperatures for the calorimetric scans. The dashed line shows the average ΔP_0 drift obtained from a previous idle experiment.

Figure 5.18 shows ΔP-ΔP_0 signal as a function of temperature. The first bump in the heating and cooling traces is related to the time the controller needs to ensure a suitable control action. The melting transition during heating appears as an endothermic peak (down arrow), whereas the solidification during cooling produces an exothermic peak for all the heating rates (up arrow). Because the solidification process very often presents undercooling, we focus the analysis on the melting peak in which kinetic effects are less important because of the easy of nucleation of the liquid phase. A quick analysis of the calorimetric traces in figure 5.18 shows a dramatic enlargement of the melting peak as the heating rate increases. Below 200 K/s, the FWHM of the peak is narrow and constant; however, at higher rates, the onset of the peak remains constant but the end moves toward high temperatures, reaching an FWHM of 100 K at 1000 K/s. The peak variation could be explained by an association with temperature non-uniformities in the active area of the calorimetric cell. However, previous analysis showed the maximum temperature difference expected at these low temperatures and heating rates remains below 20 K [34]. On the other hand, we have shown that the temperature variation across the sensing area diminishes at higher heating rates, see subsection 2.3.3 [34, 113].

More information can be extracted from the analysis of the temperature errors and

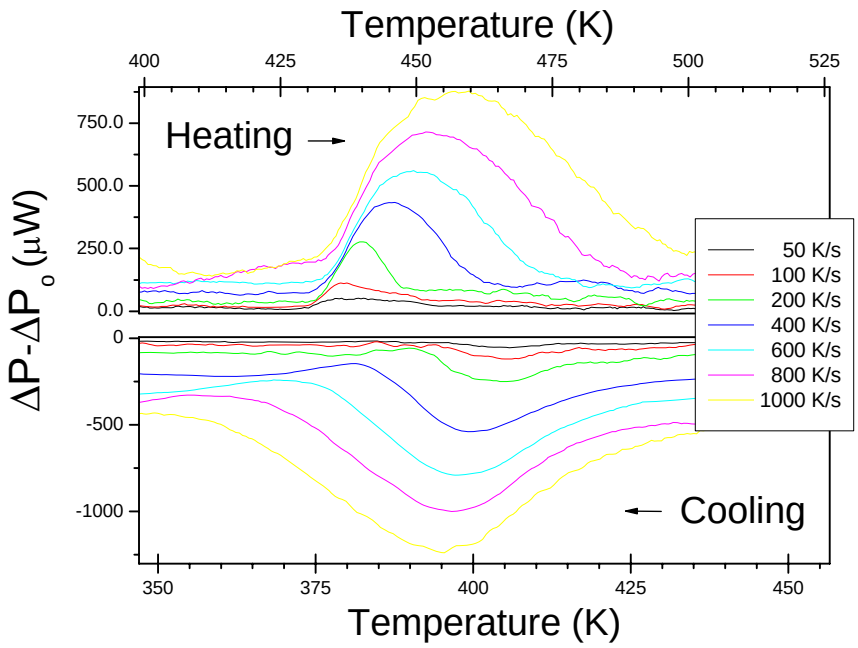

Figure 5.18: ΔP-ΔP_0 signal of 100 nm as a function of time at heating rates spanning 50 to 1000 K/s.

heating rate signals for the nanocalorimeter loaded with sample in comparison with the predefined setpoint. Figure 5.19 shows the controller cannot guarantee a constant error during the phase transition. This fact becomes especially relevant at heating rates above 200 K/s; at this point, the temperature variation is larger, producing a significant change in the scanning rate. The temperature errors are not common in both cells because the reference calorimeter still exhibits the monotonic behavior imposed by the setpoint.

This temperature variation introduces the need to correct for power losses because one of the main contributions to the non-differential power signals of the nanocalorimeters working in a gas cooling medium is the convection through the gas, which depends on temperature. Therefore, during the transformation, the differences in temperature between the sample and the reference cell introduce a term in the ΔP that comes from the non-cancellation of the power losses in both cells.

This effect can be verified by reducing the Ar gas pressure during the experiment, which in fact means decreasing the power losses. As the time constant of the nanocalorimeters gets larger the maximum heating rates where the controller can be properly tuned is reduced to around 300K/s. Figure 5.20 shows that at low pressures the FWHM of the melting peak remains rather constant.

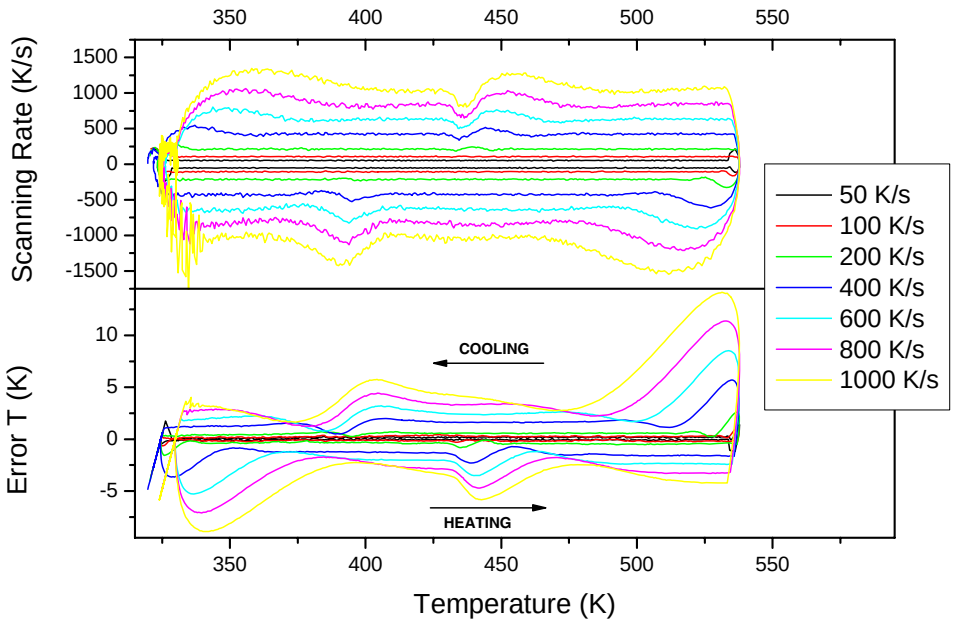

Figure 5.19: Heating rate (upper curve) and temperature error signal (bottom curve) as function of time for the calorimeter loaded with sample at heating/cooling rates from 50 to 1000 K/s.

Analysis of the calorimetric traces at rates below 200K/s. At 1 bar and heating rates below 200 K/s, the maximum temperature error is 0.25 K, which induces power differences below 5 μW (the signal-to-noise ratio of the controller). Under these conditions, the ΔP-ΔP_0 signal can be assumed as $Cp_{sample} \cdot \frac{dT}{dt}$ within the error. Figure 5.21 shows a zoom of the ΔP-ΔP_0 signals during heating: the endothermic peak associated with the melting transition appears at 430 K with an FWHM of 10 K. The enthalpy of the transformation is readily obtained by integrating the area inside the peak with temperature and scaling by the heating rate $\left(\Delta H = \frac{1}{\beta} \cdot \int ((\Delta P - \Delta P_0) - baseline) \cdot dt\right)$. A constant value of 13 $\pm$ 1 μJ is obtained independent of the heating rate. This value closely agrees with the expected 13.4 $\pm$ 1.5 μJ, considering the mass of the In sample is 470 $\pm$ 50 ng.

Analysis of scans at rates over 200K. To analyze the phase transition in the scans obtained above 200 K/s, it is necessary to consider a correction for the different contribution of power losses. To account for power loss we proceed similarly to the analysis in section 4.1.2. During the experiment, both the current injected and the voltage drop in the calorimetric cell are measured through proportional signals in voltage. An example

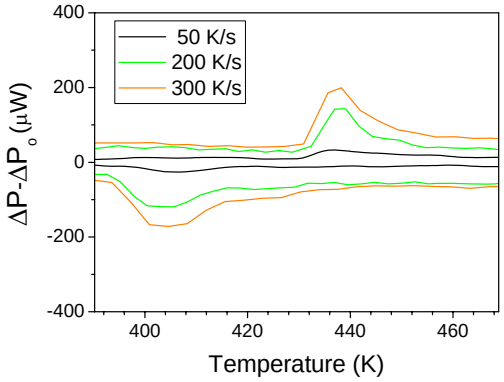

Figure 5.20: ΔP-ΔP_0 curves as function of temperature when a 100nm In sample is loaded onto the sample nanocalorimeter with the Ar atmosphere pressure fixed to 4 mbar.

of the raw data acquired in one scan is shown in figure 5.22 (a). From it we calculate, as shown previously in pulsed-heating experiments, the non-differential heat capacity $Cp = V \cdot I \cdot \left(\frac{1}{R_0 \cdot \alpha}\frac{d(V/I)}{dt}\right)^{-1}$.

Figure 5.22 (b) shows the apparent heat capacity for the sample calorimetric cells when it is loaded with 100 nm In thin films for four scanning rates at 400, 600, 800, and 1000 K/s. Power losses linearly depend on cell temperature, and the contributions to the apparent heat capacity are larger as the heating is rate slower. Figure 5.22 (c), shows the plot of the apparent heat capacities for the calorimetric cell at different temperatures before and after the melting peak as a function of the inverse of the heating rate. As can be appreciated for each temperature, the apparent heat capacity values obtained for the different heating rates are arranged along a line. A linear fitting of these data can be used to predict the $Cp_{apparent}$ value for an infinite heating rate $\left(\frac{1}{\beta} = 0\right)$ which gives directly the real heat capacity Cp_{real} at a given temperature. If the Cp_{real} at several temperatures is known, the power losses for those selected temperatures can be obtained as $P_{losses}(T) = (Cp_{apparent}(T) - Cp_{real}(T)) \cdot \beta(T)$ and plotted as a function of temperature, see figure 5.22 (d). The dependence of Plosses with temperature is obtained by a low order polynomial fitting. Afterwards, we recalculate the real heat capacity from the curves presented in figure 5.22 by using the relation $Cp_{real}(T) = Cp_{apparent}(T) - P_{losses}(T)/\beta(T)$.

Figure 5.23 (a) shows the real heat capacity signal as a function of temperature obtained from applying the loss corrections to the original apparent heat capacity curves. All the curves converge into a common one, which shows the goodness of the correction. Figure 5.23 (b) shows the common curve for sample heat capacity, after subtraction of the

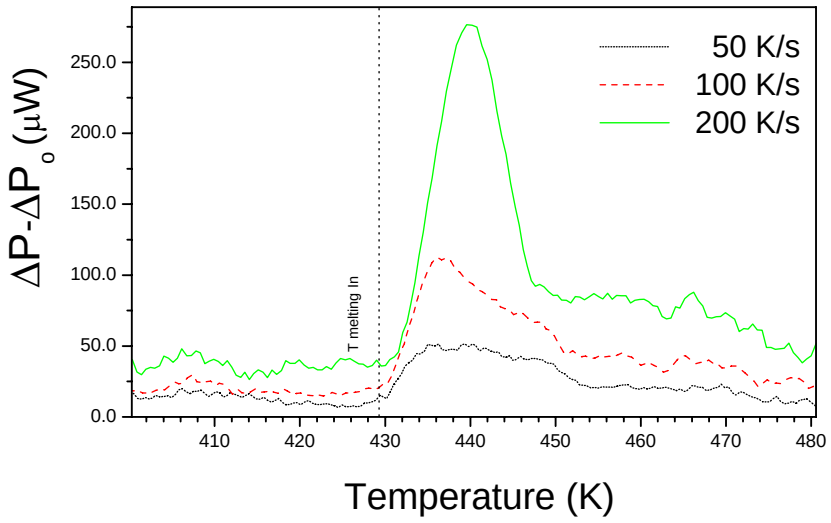

Figure 5.21: ΔP-ΔP_0 curves as function of temperature at low heating rate for 100nm In sample loaded onto the sample nanocalorimeter with the Ar atmosphere pressure fixed at 1 bar. The vertical line marks the bulk melting temperature of indium.

initial difference in heat capacities (baseline correction). Integrating the melting peak, we obtain a transformation enthalpy of 11.4 $\pm$ 1 μJ, which is slightly smaller that the value obtained from slower heating rates. We believe that this second value is more accurate because possible differences in power losses introduced by the sample presence are taken into account and for this reason the enthalpy value is reduced. The results achieved so far demonstrate that the dynamic sensitivity (minimum amount of heat that can de detected) of the instrument is below 1 μJ, which for the In sample analyzed here, corresponds to roughly 50 ng.

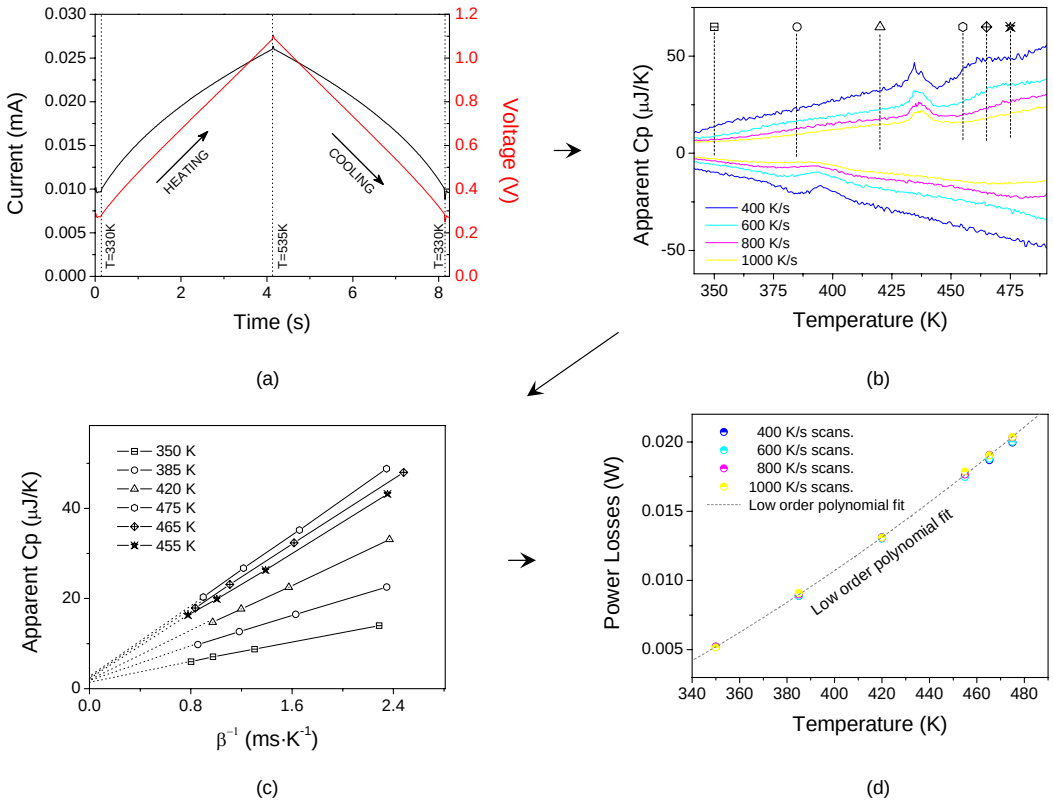

Figure 5.22:
(a) Typical voltage and current raw data signals acquired in a calorimetric experiment (b) Apparent heat capacity of the 100nm In sample at 4 different heating rates (400, 600, 800 and 1000 K/s) (c) Linear regressions of the apparent heat capacities measured at different β at a given temperature. The extrapolation to $\beta^{-1} = 0$ permits to obtain the Cp_{real}. (d) Plot of P_{losses}values as a function of the respectives temperatures and low order polynomial fitting to obtain $P_{losses}(T)$.

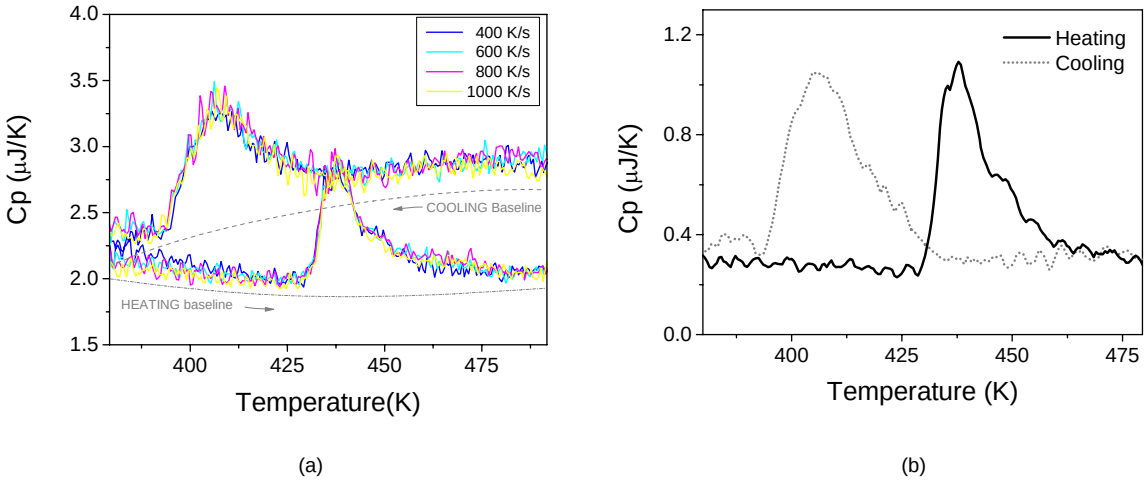

Figure 5.23:
(a) Real heat capacities of the calorimetric cells after power losses correction for experiments performed at different heating rates. The dashed lines are the initial difference between cells before sample deposition. Note the curves at different heating rates converge to a common one. (b) Sample heat capacity during heating (continuous line) and cooling (dotted line).

Chapter 6

Conclusions.

The research work presented herein involves the development of membrane-based calorimeters that are capable of measuring the heat released or absorbed during a phase transformation in thin films from temperatures up to 1200 K.

The main conclusions can be summarized as follows:

- We have used standard semiconductor processing techniques to fabricate the microdevices. The 180 nm silicon nitride membrane has been used as a mechanical support to the thin film heaters/sensors and to the sample, preserving a low heat capacity addenda (below μJ) to enhance sensitivity. The design of the membrane has been optimized to preserve the mechanical stability for temperatures below 1250 K. Heating and sensing is typically performed using a metallic thin film of Pt(100nm)/Ti(10nm) covered by 150 nm of Al_2O_3 which prevents degradation. This configuration provided reproducible measurements at high temperatures. Thermal modeling of the microdevices has been used as a tool to improve the designs. The final design for adiabatic measurements is a serpentine-type heater that provided good temperature profiles at ultra-fast heating rates. The combination of materials properties and geometry design is the key point for reproducible nanocalorimetric measurements.

Two modes of operation have been successfully implemented: quasi-adiabatic nanocalorimetry (chapter 4) and power compensated scanning nanocalorimetry (chapter 5).

Quasi-adiabatic nanocalorimetry The quasi-adiabatic calorimetry permits to study phase transitions in samples of ng. Typically the scanning rates range from 10^4 to 10^5 K/s, to preserve quasi-adiabatic conditions. We have established a methodology to correct for power losses. This procedure was used to obtain the heat capacity of Ni thin films.

Different types of thin film samples have been analyzed:

- The sensitivity of the U-shape membrane-based nanocalorimeter was tested with ultrathin In films. A resolution of 20 pJ/K has been achieved which permits to measure samples of few pg. During the first calorimetric scan In sample dewetts forming quasi-spherical droplets over the membrane with a size distribution that depends on the original nominal thickness of the In thin film. The nanocalorimetric traces revealed the size dependent behavior of the melting temperature and the enthalpy. This study also supported the need to improve the heater design to perform quasi-adiabatic calorimetry.

- We have shown the idoneity of quasi-adiabatic nanocalorimetry to analyze Curie transitions by measuring the heat capacity of ultra-thin films of Ni with nominal thicknesses in the 3 to 9 nm range. The calorimetric traces showed a change in heat capacity at the curie transition. The depression in the Curie transition temperature as the thickness decreases is in good agreement with established models for low dimensional systems. We have also observed a decrease in the change of the specific heat at the curie temperature. This behavior needs further measurements and analysis.

- We have performed nanocalorimetric measurements on 1-3 nm a-Ge sandwiched between 10nm SiO_2 layers. In the first scan, the calorimetric curve shows the structure relaxation of the amorphous Ge and the amorphous-to-liquid melting transition with an onset temperature of 980 K. During cooling to room temperature solidification results in the nanocrystallization of the sample and in the second and subsequent scans the calorimetric curve shows the crystalline-to-liquid transition of the nc-Ge structure during heating and solidification upon cooling.

- It has been observed the size dependent melting and size dependent supercooling of the population of Ge nanocrystals with an average radii of 10 nm embedded within a 20 nm SiO_2 film. The incoherent interface between Ge and the SiO_2 matrix inhibits the existence of a large superheating. However, the onset temperature of solidification exhibits a significant supercooling that depends on the previously melted size of the nanocrystals. For smaller nanocrystals a lower solidification temperature is observed in agreement with expectations from thermodynamic estimations of the critical grain size.

Power compensation calorimetry

- We have developed scanning temperature controllers to use the microdevices at constant heating rates from 0.01 to 1000 K/s in power compensated mode. We have analysed several transformations of samples in the microgram range, opening the possibility to study kinetically limited processes not suited to ultra-fast heating.

- At lower rates (below 10 K/s), with a windows-based IPID controller operating via GPIB with a keithley 2425 sourcemeter, power resolutions up to 100 nW are achieved. To show the feasibility of the technique several thin film samples in the microgram range (High-Density Polyethylene and Indium) have been tested.

- Higher scanning rates (up to 1000 K/s) have been attained with an FPGA-based controller. This development facilitates the analysis of phase transformations under similar conditions that those used in rapid thermal processing. With a 1 μJ energy sensitivity, this is to our knowledge one of the most sensitive scanning calorimeters working in power-compensation mode. The present development paves the way for exploring phase transitions in thin films or microgram inorganic samples at heating rates much higher than conventional systems, and may also be used to address a high number of soft-matter issues and biological systems.

6.1 Perspectives.

If any, this research work has the merit to open a vast field of opportunities for future research at the nanoscale. The development of the nanocalorimetric tools, either at ultra-fast or moderate heating rates, provides our group with a unique characterization tool to explore thermal properties at the nanoscale level. In this sense the Nanomaterials and Microsystems Group at UAB is already exploring several systems in which the reduced dimensions play a key role in the physical properties.

There are still many opportunities to improve the existing characterization tools. New devices based on SOI substrates to produce single-crystalline Si free-standing membranes are being developed to span the range of applications with a special care devoted to their high temperature stability and sensitivity. Sensors consisting of arrays of nanocalorimeters will allow multiple sensing and detection paving the way for fast screening of new compounds. In this sense high-throughput nanoscreening has a tremendous potential to reveal

unique structure-property relationships and to identify new materials. With the incorporation of nanofabrication tools into the processing new nanocalorimeters with better spatial resolution and higher sensitivity will be developed.

Appendix A

Power Compensated DSC and Adiabatic Calorimeters.

Calorimetry is the measurement of the heat, released or absorbed, by a material during a chemical reaction or a physical transition. The exchanges of heat tend to produce a temperature change in the material. For a correct understanding of a calorimetric measurement knowledge of thermodynamics is necessary. The first law of thermodynamics establishes that in absence of other forms of energy exchange, the change in the internal energy, $\triangle U$, of a given system is equal to the heat supplied by the surrounding minus the mechanical, magnetic and chemical work performed by the system:

$$\triangle U = Q - p \cdot \triangle V + M \cdot \triangle H + \mu \cdot \triangle N$$

The measures of the specific heat can be performed under two conditions, volume or pressure constant. First, under constant volume, the specific heat directly relates to the change of internal energy, $\triangle U = Q = m \cdot C_v \cdot \triangle T$, since no work will be done as $p \cdot \triangle V = 0$. Second, under constant pressure, the value for the specific heat capacity is slightly direct since an additional energy contributes to perform the mechanical work, $p \cdot \triangle V$. The addition of these contributions to the internal energy at a constant preassure is the enthalpy (H), the specific heat capacity is :

$$C_P = \left(\frac{dH}{dT}\right)_P$$

Measurements of heat capacity allows access to the normally highly theoretical quantities of entropy $S = S_o + \int_0^T \frac{C_V(T)}{T} \cdot dT$ and internal energy $U = U_o + \int_0^T C_V(T) \cdot dT$.

For a given temperature and pressure, the equilibrium phase of any substance is defined as the phase which minimizes its Gibbs free energy (G), which i defined as a function of the entropy (S) and inner energy (U), as G=U-TS+PV. Lowering the temperature reduces the effect of the TS term, allowing the ordered states to arise in a substance when it is cooled [114].

In general, the properties in matter change slowly with external parameters (e.g. temperature and pressure), and these regions with continuous properties are called phases. But, sometimes the properties can change almost discontinuously with the external parameters in the phase boundaries. Figure A.1, shows the Gibbs and its derivative as a function of temperature for a typical material that undergoes 2 first-order phase transitions. The type of transitions have always associated heat effects and volume changes, (e.g. melting transitions). Ehrenfest in 1933 classified the phase transitions according to the lowest-order derivative of the thermodynamic potential which changes discontinuously at the transition. A second-order transition is not accompanied by a heat effect and volume change; instead at the temperature of the second-order transition only a change in the slope of the enthalpy function (abrupt change in heat capacity) can be observed (e.g. conductor-superconductor transitions).

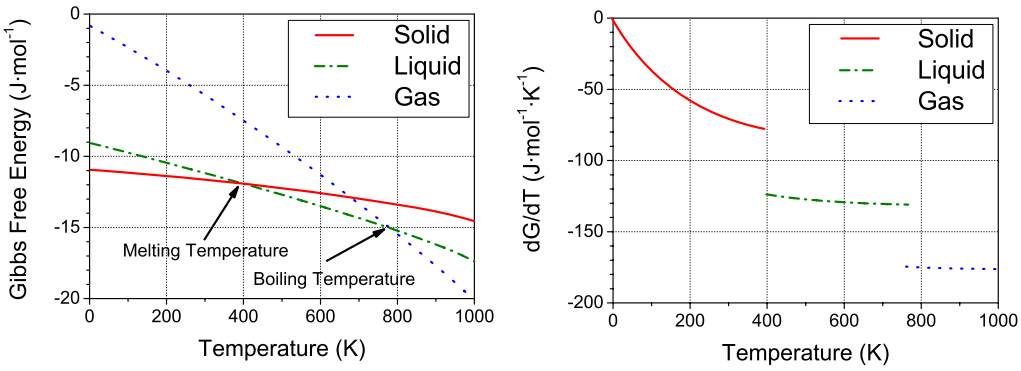

Figure A.1: First order transitions.

Measuring the low temperature specific heat reveals a great deal of information about the lattice and electronic properties of a material. One can expect to have the heat capacity as a function of temperatures, $C_P = \gamma \cdot T + \alpha \cdot T^3$, where γ is related to the electronic contribution and α is related to the lattice contribution to the heat capacity. In 1911,

Nernst and Lindemann measured the heat capacity at low temperatures of Cu and KCl. This measurement showed that the Einstein's model of lattice vibrations was incorrect at low temperatures leading to the calculations of Debye in 1912, which is still in use [5].

Calorimeters

The calorimeters are devices able to measure the amount of heat introduced into a sample, or extracted from it, as a function of temperature. These caloric measurements have been used in several areas of research, since the middle of the 18th century (Lavoisire and Laplace made the ice calorimeter in 1780). A great variety of calorimeters serve to measure heat flows and heat capacities, in different fields of application [115] like: characterization of materials, comparison (relative) measurements (quality control, identification of substances or mixtures), stability investigations, evaluation of phase diagrams, purity determinations, kinetic investigations, safety research... A calorimeter can also be classified according to several characteristics: heat measurement method, surrounding, initiation of measured effect and operation mode (classification proposed by Hansen [116]). A large varity of calorimeters are presented by Höhne et al. [115], as examples; however we will only briefly summarized the two operative modes related to the present work: adiabatic scanning calorimeter and power compensated DSC.

Adiabatic Scanning calorimeter

In adiabatic scanning calorimeters, see figure A.2, electrical heating power is supplied to a sample in order to follow a preset temperature program [115]. Experimentally, as in adiabatic nanocalorimetry, is the electrical heating power for the sample the preset and is the resulting heating the measured variable. The complexity of this type of calorimeter is large, because in order to minimize the heat losses the temperature of the surroundings should be adapted to the sample temperature (adiabacy). This type of calorimeter allows the mesure of heat capacities with high accuracy. From the adiabatic condition it is easy to get the heat capacity value, since all the power introduced is transformed in inner energy, leaving the equality dH(t)=Cp(t)dT(t). The experimental measure gives the power introduced (dH/dt) and the heating rate (dT/dt) as functions of time. Then,

$$C_P(T) = \frac{P_S}{\left(\frac{dT}{dt}\right)_S} - \frac{P_R}{\left(\frac{dT}{dt}\right)_R}$$

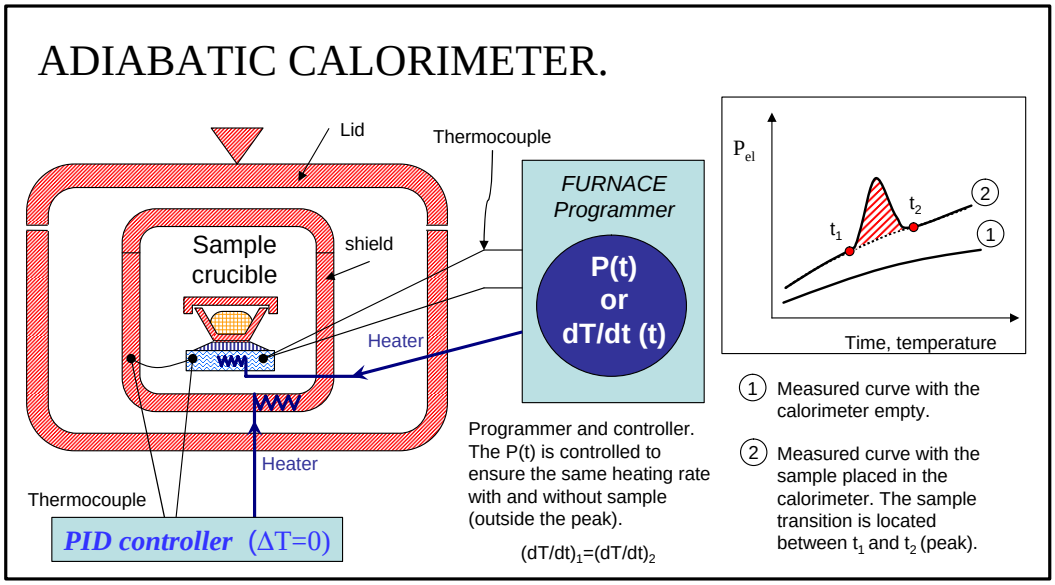

Figure A.2: Schematics of an Adiabatic Calorimeter.

Power Compensation Differential Scanning calorimeter

Differential scanning calorimetry (DSC) is a widely-used method in calorimetry. Several companies offer commercial calorimeters based on the DSC method, allowing the calorimetric measurements of samples in the mg range over a large range of temperature, with high resolution in power. The DSC method is based in a differential twin system of calorimetric cells, one used as reference and the other as sample container. The heat is measured in a differential way during a stroll on temperatures. This differential signal can be strongly amplified, and it is the essential characteristic of this equipment.

The DSC method operates in a dynamic mode allowing different types of heating ramps or isothermal treatments. It can function as a heat-flow or power-compensated calorimeter. In power compensated differential scanning calorimeters (PCDSC) the heat to be measured is (almost totally) compensated by an electrical energy, increasing or decreasing with a controller the joule effect of a resistance in the holder. Most of commercial PCDSC are instruments that work in isoperibol mode of operation[1]. The measuring system consists on two twin microfurnaces made of a platinum-iridium alloy, containing an electrical heater

[1]Isoperipol is the term to denote that a calorimeter has a uniform surrounding.

and a temperature sensor. Both furnaces are positioned in an aluminium block at constant temperature.

The heating-up is performed supplying the heating power with a control circuit [104] to the two microfurnaces in order to follow a preset temperature ramp. The difference on temperatures should be zero until any asymmetry occurs. A second controller tries to compensate the reaction heat flow rate with a second controller. The heat flow into the sample can be assigned with a linear dependence (calibration) to the measured signal $\triangle T$, since to extra power is introduced throuh a proportional controller to reduce the difference of temperatures to zero. At high temperatures, the encapsulation of the sample assure the repetitibility on the measurements, maintaining the radiation losses constant.

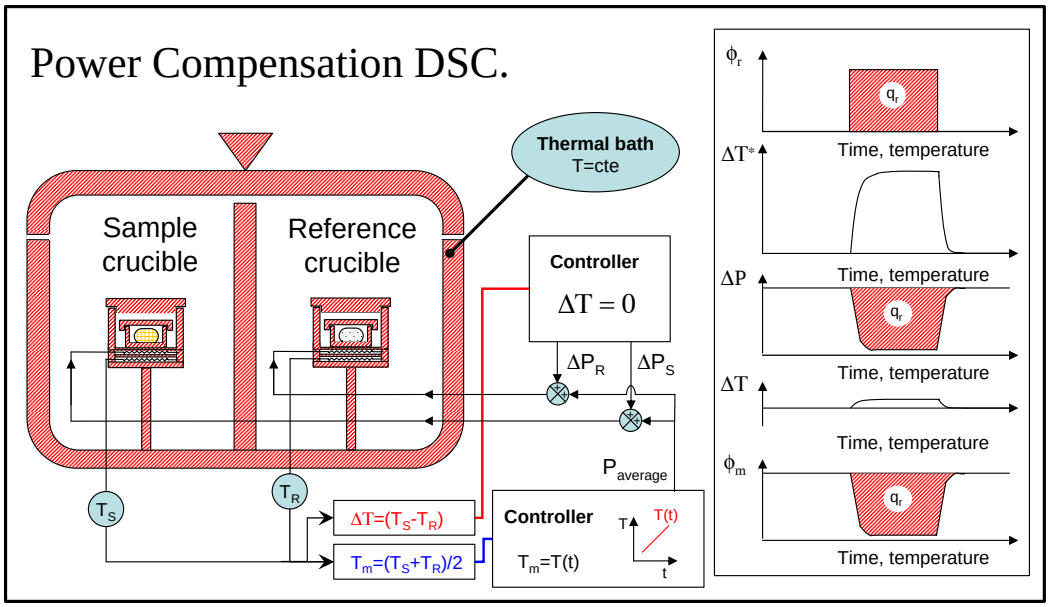

Figure A.3: Schematics of a Power Compensation DSC.
ϕ_r is the heat flow released by an exothermic reaction (q_r is the heat released), and $\triangle T^*$ is the increase of temperature in the furnace if no compensation is applied (as in heat flow DSC). $\triangle P$ is the negative compensation power to contrarest the exothermic transformation in the sample, $\triangle T$ is the error in temperatures that the controller can not compensate during the transformation. $\phi_m$is the output signal. (ϕ_m=K$\cdot\triangle T$, where K is extracted after a calibration made with previous measurements in standard materials at a given heating rates)

Appendix B

Study of crystallization of a-Ge thin films.

Semiconductor nanostructures exhibit unique properties based on quantum confinement. A promising and effective way to create embedded nanocrystals consist in submitting ultra-thin films of amorphous germanium (a-Ge) embedded in SiO_2 layers to high temperature annealing. Several methods have been developed to prepare nc-Ge embedded in a SiO_2 matrix, PECVD [117, 118], PLD [119], sputtering [84, 120, 121, 122, 123], e-beam evaporation [124] and direct oxidation of germanium embedded in silicon [125]. Nevertheless, the controlled fabrication process of uniformly distributed number and size distribution of the dots is still a step to overcome. In case of obtaining nc-Ge from thermal treatments of the amorphous phase, thermal transitions involved in the nanocrystallization are still an issue. As was mention, it is known that decreasing the thickness of the a-Ge layer increases its crystallization temperature. Besides, it is well known that the crystallization temperatures of amorphous Ge (a-Ge) can be drastically reduced when in contact with certain elements such as carbon [126], aluminum [127] and mainly silicon [128], due to heterogeneous nucleation at the interfaces. In this appendix we report on the preparation of nc-Ge starting from amorphous germanium thin films embedded into SiO_2 thin layers that are submitted to thermal annealing processes. The SiO_2 layer grown between the Si substrate and the Ge layer avoids formation of SiGe upon heating. We examine the effect of the reduced thickness (2 to 50nm) on the crystallization temperature of the a-Ge thin layers. We present here combined micro-Raman, SEM and TEM characterization performed on SiO_2/a-Ge/SiO_2 trilayers with different a-Ge thickness after several thermal treatments. Preliminar real-time micro-Raman measurements during the heat treatment is also shown

though its complete discussion is beyond the scope of this work.

Experimental. The amorphous germanium and SiO_2 films were prepared in a Leybold UNIVEX 450 e-beam evaporation set-up. Several germanium thicknesses were deposited on a 100nm thick SiO_2 buffer layer thermally grown on a silicon wafer surface. The bilayers were then coated by a 20nm thick SiO_2 to form the studied trilayers. The evaporation parameters were optimized individually to stabilize the growth rate of the different materials. Using a quartz microbalance located inside the deposition chamber the growth rates were previously determined in 0.1 nm/s at P= 10^{-6} mbar and 0.2 nm/s at P=$2{\cdot}10^{-4}$ mbar for Ge and SiO_2, respectively. In a single experimental run and using a set of moving masks, six different germanium thicknesses were deposited onto the four inches SiO_2/Si wafer. The fully amorphous nature of the as-deposited samples, from few nm to 50 nm, was confirmed by plane-view transmission electron microscopy (TEM) images and Selected Area Electron Diffraction (SAED) patterns as shown in figure B.1 (a). On the other hand, EDX nano-analysis maps along the surface showed a continuous germanium composition confirming that even the 2 nm thick germanium layers were totally continuous without forming separated islands.

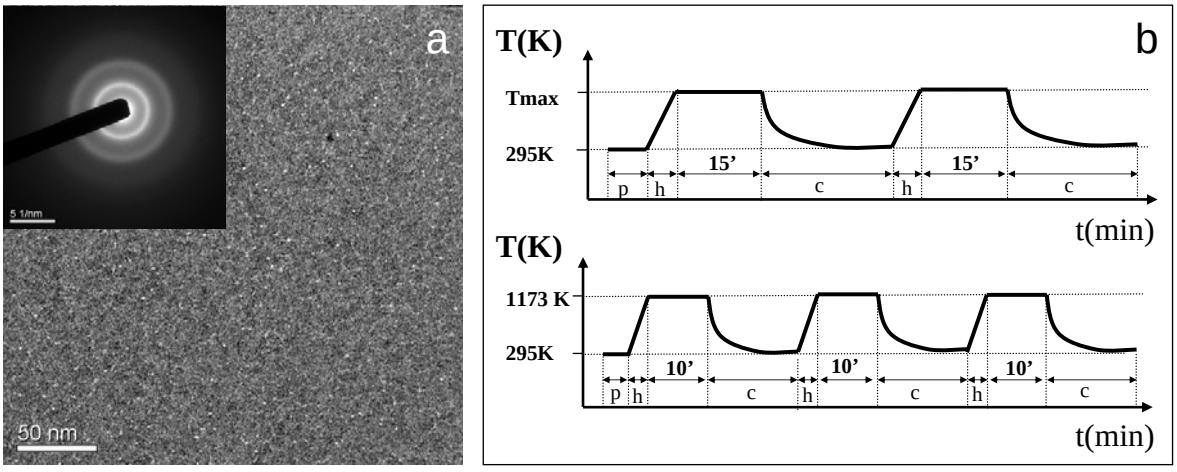

Figure B.1: (a) TEM +ED; (b) Annealing description where p = 15 min correspond to the time elapsed to stabilized the high vacuum pressure, h correspond to the heating rate that take 80s that correspond to 315K/min for 723K maximum temperature; 356K/min for 773K; 435K/min for 873K; 504K/min for 973K and 656K/min at 1173K. c is the cooling period around 20 minutes before starting the second heating cycle.

The amorphous germanium films embedded into amorphous SiO_2 layers were then submitted to different thermal treatment under high vacuum conditions. The thermal

treatment processes were performed in Jetstar Jipelec system adapted to high vacuum pressure. Prior to heating, several argon purges were done at ambient temperature to ensure the highest vacuum possible in the reaction chamber. Then with ultra-fast heating the set point temperature were reached after 80 seconds and maintained during 15 minutes for treatment between 673 and 973 K; at 1173 K the plateaus were limited to 10 minutes. This procedure was performed two or three consecutive times after a cooling process to ambient temperature to achieve 30 minutes of thermal heating for all the germanium thicknesses as schematize in figure B.1 (b).

The Raman spectroscopy was carried out at room temperature with the 514.5 nm line of an Ar-ion laser for excitation. The beam was focused onto the sample with a spot size of about 1 μm and a laser power of 4 mW. Contributions from second-order processes were suppressed using the scattering geometry z(xy)z, where x, y, and z are the [100], [010] and [001], respectively. Raman spectroscopy was used to determine crystallinity of the samples as well as to give an estimation of average grain size. TEM /HREM were also used to characterize the encapsulated germanium after thermal treatment by cross section observations. Atomic Force Microscopy (AFM), profilometry and SEM were employed to investigate the surface morphology of the as-prepared and annealed samples. Real-time Raman spectroscopy during heat treatment was carried out using a furnace/holder of a Perkin Elmer DSC-7 adapted in a vacuum mini-chamber. With the help of a PC-based controller (similar to the presented in section 5.3), scanning ramps of 3 K/s were performed in a controlled atmosphere of Ar of few mbar. Raman spectra were recorded every 5 seconds to follow the sample crystallinity evolution.

Results and Discussion

Influence of aGe thickness and annealing temperature The amorphous germanium with varying thickness, from 2 to 50 nm, was deposited and annealed to six different temperatures: 673, 723, 773, 873, 973 and 1173 K. In order to analyze the effect of the initial a-Ge thickness on the crystallization, we use the standard characterization techniques such as AFM, SEM, TEM and mainly micro-Raman to characterize the 36 matrix members. The effect of the thickness was observed by comparing the matrix rows where the treatment temperature is constant while the influence of the temperature is determined comparing the columns where thickness is constant. As can be seen in figure B.2 (a), the Raman spectra within a row clearly changes from the amorphous state for 2 nm thick germanium to the 50nm thick, treated at 973K in this particular example. Similar spectra

and behavior were observed for thermal treatment below this temperature, varying only the thickness threshold where signal corresponding to crystallized phase started to appears. From this type of analysis we determine that reducing the films thickness directly induce a reduction of the phase transition temperature in the germanium. As observed in figure B.3, a closer examination of the surface morphology performed by AFM on the rows did not show a clear correlation with the crystalline phase formation at least for those treated at or below 973K.

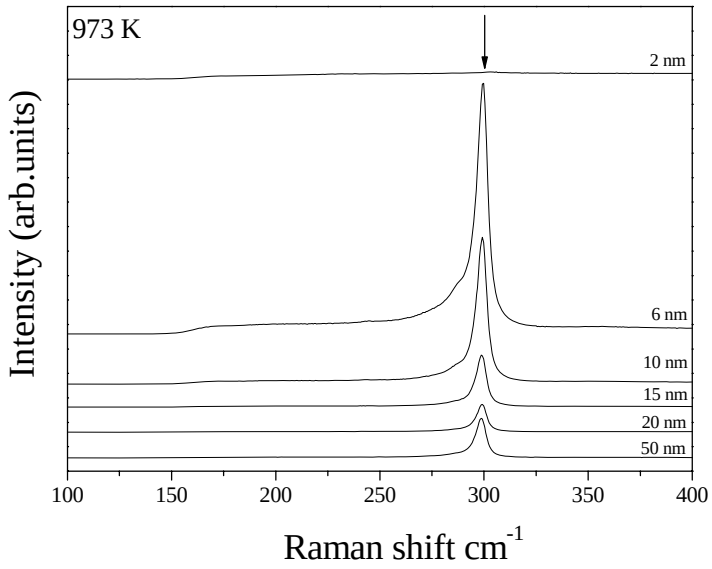

Figure B.2: Raman spectra of the samples treated at 973K as a function of thickness

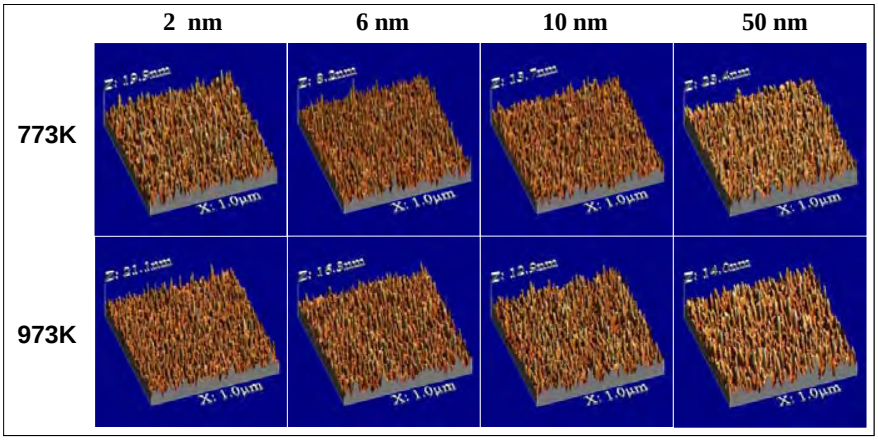

Figure B.3: AFM surface morphology of the samples treated at 773K and 973K.

The influence of the annealing temperature on the germanium crystallization was also determined by Raman spectroscopy. In figure B.4, for a fixed thickness, 10nm in the example, we determine the temperature at which the signal from the crystalline phase appears. We can clearly differentiate the spectra of the amorphous germanium measured at 673 K with the spectra at 723K which is a combination of amorphous phase with the appearance of a crystalline phase, as shown in the inset where a deconvolution of the measured spectra is done. For higher temperatures the spectra is mainly formed by the crystalline contribution peak that narrows with temperature although an accurate fitting points out the detection of amorphous traces at least for temperatures that do not exceed 973K.

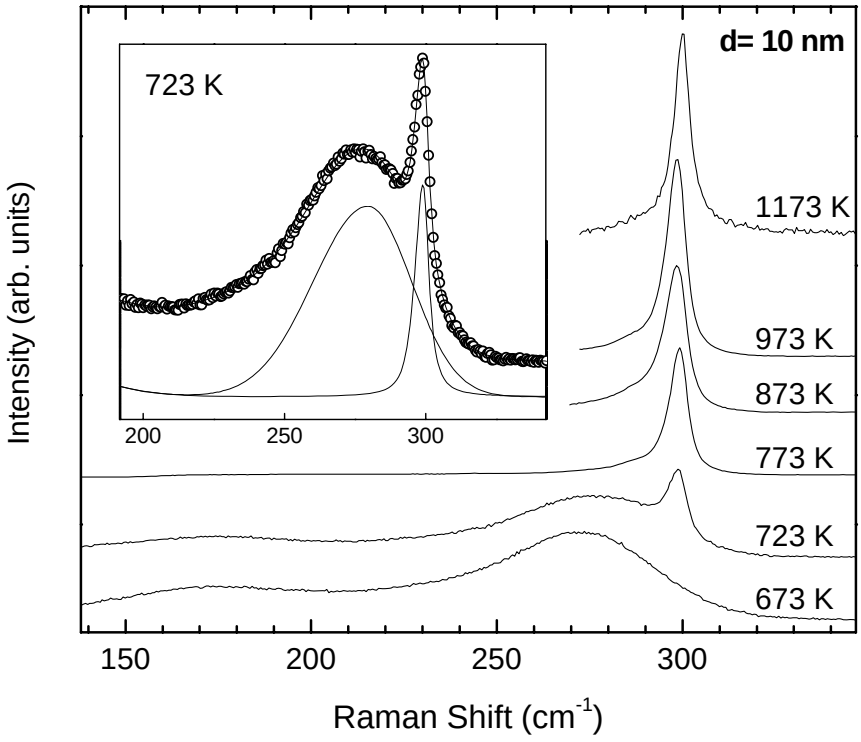

Figure B.4: Raman spectra for a 10nm thick germanium samples treated at different temperatures.

In the particular case of 10 nm thick samples, the Raman study was also complemented by transmission electron microscopy through cross-sectional analysis of the trilayers, figure B.5. From the TEM images we can clearly see that the germanium layer is continuous and mainly formed by nanocrystals of germanium confirming the Raman conclusions. In

the inset we can see quasi-spherical nanocrystals of germanium with a diameter almost equal to the initial layer thickness. For samples treated at 973 K, as shown by Raman, the germanium layer is still continuous and almost totally crystalline; inset shows a detail of a columnar growth with nc ranging from 7 to 10 nm approximately, although grain boundaries can be easily confused with twinning. In some images facetted germanium crystals were observed. Samples treated at 1173K showed a particular behavior that will be specially discussed below. In that case the germanium is totally crystalline as confirmed by XRD, but the germanium is formed by a discontinuity of larger Ge islands coated by a continuous silica top layer. We have to mention that TEM cross-section micrographs also allowed us to confirm the initial germanium and SiO_2 top layers thickness.

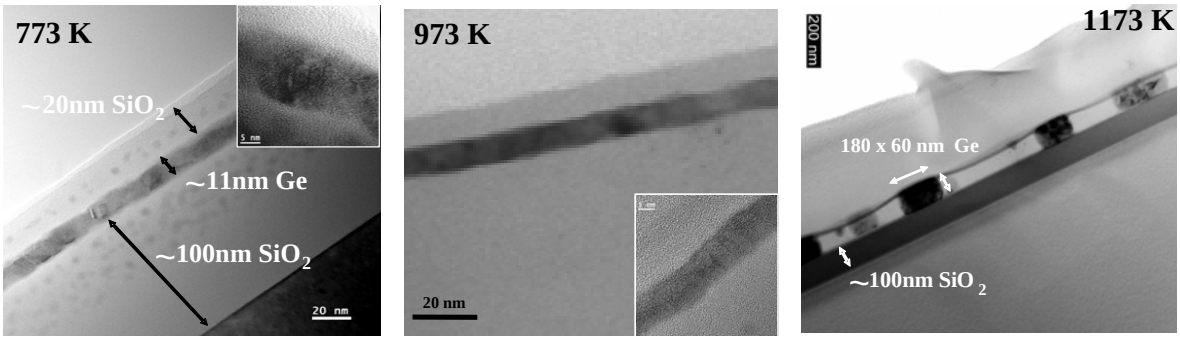

Figure B.5: TEM cross-section of 10nm samples treated at 773, 973 and 1173 K. Inlets correspond to a larger magnification of the nanocrystals formed.

The complete matrix phase determination as a function of thicknesses and treatment temperature determined by Raman is shown in figure B.6. The first observation is that samples treated at 673K, maintain the amorphous structure independently of their thickness. Also, all the 2 nm samples maintain an amorphous structure even those submitted at thermal treatment as high as 1173K. This is a bit surprising based on the nanocalorimetric measurements presented in section 4.5. We believe as shown by ellipsometry that the real thickness of this layer is below 1 nm. On the contrary, only samples thicker than 2 nm and treated at 1173K, were totally crystallized. Although the division curve is not clear, globally we can define an imaginary curve separating amorphous samples from almost totally crystallized samples representing the transition phase line. Above this border line, samples are mainly formed by crystalline germanium with some traces of amorphous phase. It is clear from this study that reducing the amorphous germanium thickness will increase considerably the amorphous to crystal transformation temperature. This phenomenon has

been used to study the amorphous-to-liquidus phase transition using nanocalorimetry [19].

	2nm	6nm	10nm	15nm	20nm	50nm
673 K	A	A	A	A	A	A
723K	A	A + c	A + c	C + a	C + a	C + a
773K	A	A + c	C + a	C + a	C + a	C + a
873K	A	C + a	C + a	C + a	C + a	C + a
973K	A	C + a	C + a	C + a	C + a	C + a
1173K	A	C	C	C	C	C

Figure B.6: Complete matrix phase determination as a function of thicknesses and treatment temperature determined by Raman.

Furthermore, by examining the Raman lines, we have estimated an average size for the crystallized portion of the germanium layer, see figure B.7, and despite the large existing scattering we can observe that the mean crystal diameter is uniform and almost constant with values between 9 and 11 nm until the temperature is maintained below or equal to 973K while for higher temperature, 1173K, the crystal size increases until diameters larger than 15nm. Comparing those results with the TEM observation we notice that for 973K and lower, the main crystal size determined by Raman can be associated with the diameter of the column crystal detected by TEM. In the case of 1173K samples, the islands observed in TEM are much larger than expected from the Raman results. This contradictory result can be related with the hypothesis that islands present a large density of defects that in the Raman spectroscopy can be interpreted as grain boundaries.

High temperature dewetting Figure B.5 pointed out that annealing at 1173K produces large crystal growth due to dewetting of the Ge layer from the SiO_2. The TEM cross-sectional images in figure B.8 for the 6 nm a-Ge sample shows the formation of islands still embedded into the silica layer. As can be seen in the image inset, the SiO_2 top layer forms a kind of suspended bridge between Germanium pellets. When we increase the thickness up to 10nm the islands have grown enough to produce the total detachment of the SiO_2 top layer giving rise to a suspended silica membrane covering the germanium islands. From these cross-section micrographs we estimate that the crystal size distribution

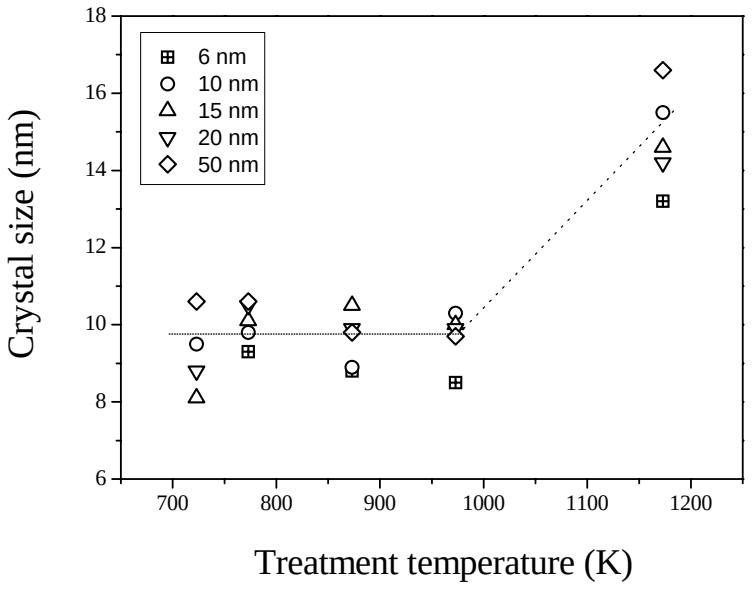

Figure B.7: Crystal size average as a function of treatment temperature determined by Raman spectroscopy.

was not homogeneous as different diameters of the germanium pellets were obtained. The resulting shape of the nanocrystals originating from the 10 nm layer is of the barrel type, very different to free nanocrystals often found in the literature which are nearly spherical. This difference may be explained by the hydrostatic pressure exerted by the top silica layer. It is also worthy to mention, the large height of the islands (around 60nm). From local transversal images we estimate the germanium volume per area confirming initial germanium volume conservation.

To confirm the island size distributions we also perform profilometry and SEM/EDX analysis as shown in figures B.9, respectively. The islands formation for those samples is even detected by SEM surface morphology analysis. EDX analysis confirmed that white islands correspond to the germanium and that the density and size increases with increasing temperature. It is worth noting that for 10 nm samples or thinner the samples showed a low roughness with waves around 30nm height that correspond to the ripple of the suspended SiO_2 top layer as already detected by TEM cross-sections. For samples thicker or equal to 20nm we observed in the SEM images fractures of the SiO_2 top layer that are larger for the thicker films.

From detailed observation of the samples by SEM and TEM we estimate the island size distribution. In 6nm films we detect a bimodal crystal distribution with 70 and 140nm

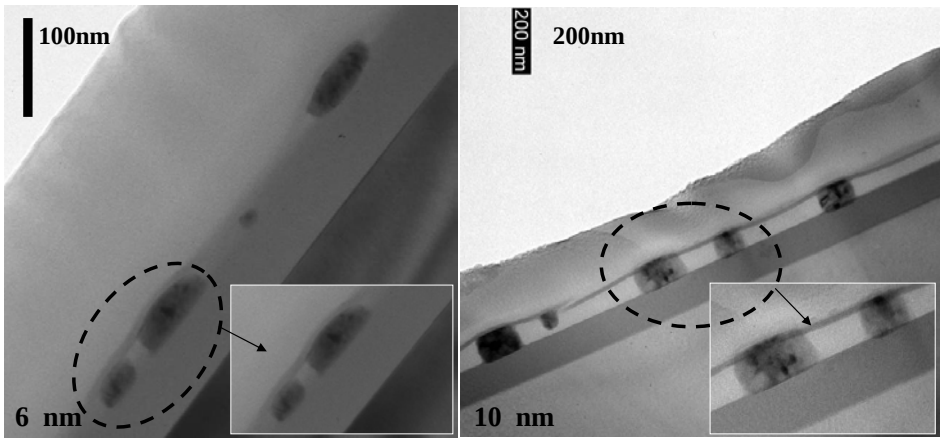

Figure B.8: TEM cross-section micrograph of 6nm and 10nm samples treated at 1173K, inset shows detail of the microstructure where dewetting of the germanium crystals is observed.

diameters, while for 10nm samples, we observe a trimodal distribution with mainly 35, 70 and 130 nm large diameters. Profilometry performed in the extreme case, 50 nm thick, give rise to a surface formed by 600 to 800 nm high islands with variable diameters as large as 3 microns. It thus seems that for such thick layers the formed islands are high enough to break the top layer as confirmed by SEM surface images. For films thinner or equal to 10nm the tension produced in the suspended top layer by the germanium islands grown up to 60 nm can withstand the stress and therefore no cracks develop in the top layer surface.

Real-time temperature scanning micro-Raman analysis. Figure B.10 shows the micro-Raman spectra acquired for samples of 6, 10 and 50 nm during a thermal treatment that consist on a ramp at 3 K/s from room temperature up to nearly 973K. As can be appreciated the spectra evolves from the typical amorphous broad peak (centered at 280 cm^{-1}) to the sharp peak characteristic of the crystalline phase (centered at 301 cm^{-1}). The higher is the sample temperature the smaller is the Raman intensity in both cases (amorphous and crystalline) as can be expected due to a higher phonon vibration amplitude. Rising in temperature, the transition amorphous to crystalline occurs abruptly (time lower than 5s). The exact temperature is measured from the shift of the Si Raman line at 522 cm^{-1}. The dw/dT has been reported in the literature as -0.0215 cm^{-1}/K [129]. Unfortunately, for the 50 nm thick Ge sample the Si phonon is not visible and temperature cannot be directly followed, though we assume that the heating ramp is similar to the preceding cases.

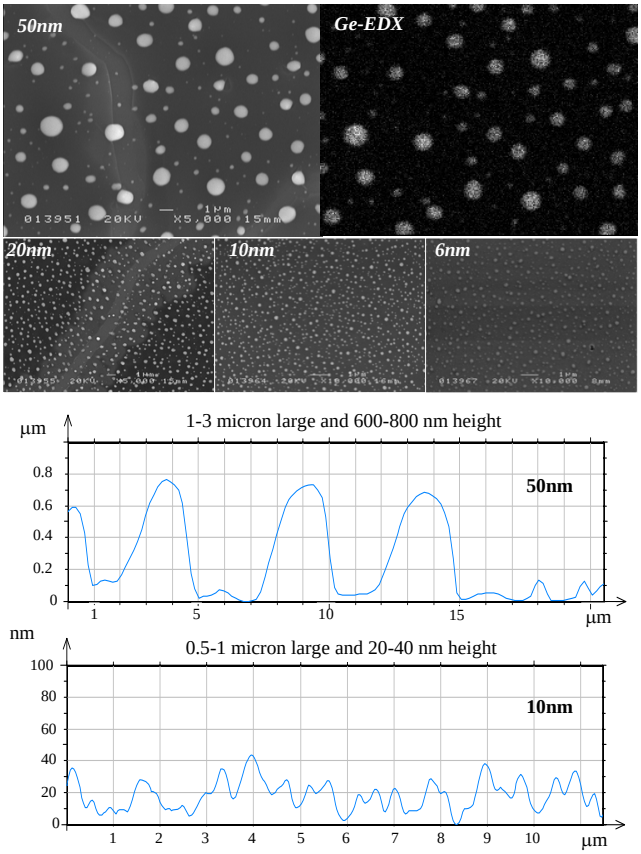

Figure B.9: SEM micrographs of 6, 10, 20 and 50nm samples treated at 1173K with an EDX germanium map distribution of the 50nm sample. Surface roughness profiles of the 10nm and 50 nm samples treated at 1173K.

Figure B.11, shows the Raman shift for samples of 6 and 10nm, and the Raman intensity for a frequency of 291 cm^{-1} as function of time. In the intensity evolution of this frequency it is possible to appreciate the step corresponding to the exact instant of the phase transition as an step. The transformation into a crystal occurs at 930K and 920K for samples of 6nm and 10nm, respectively. This temperature is very close to the value obtained in nanocalorimetric measurements for the melting of the amorphous phase, but it is not clear from those measurements if the liquid phase is involved in this very rapid crystallization. Further measurements combining in-situ Raman and nanocalorimetry are under way to clarify the influence of the heating rate on the thickness on the nanocrystallization process.

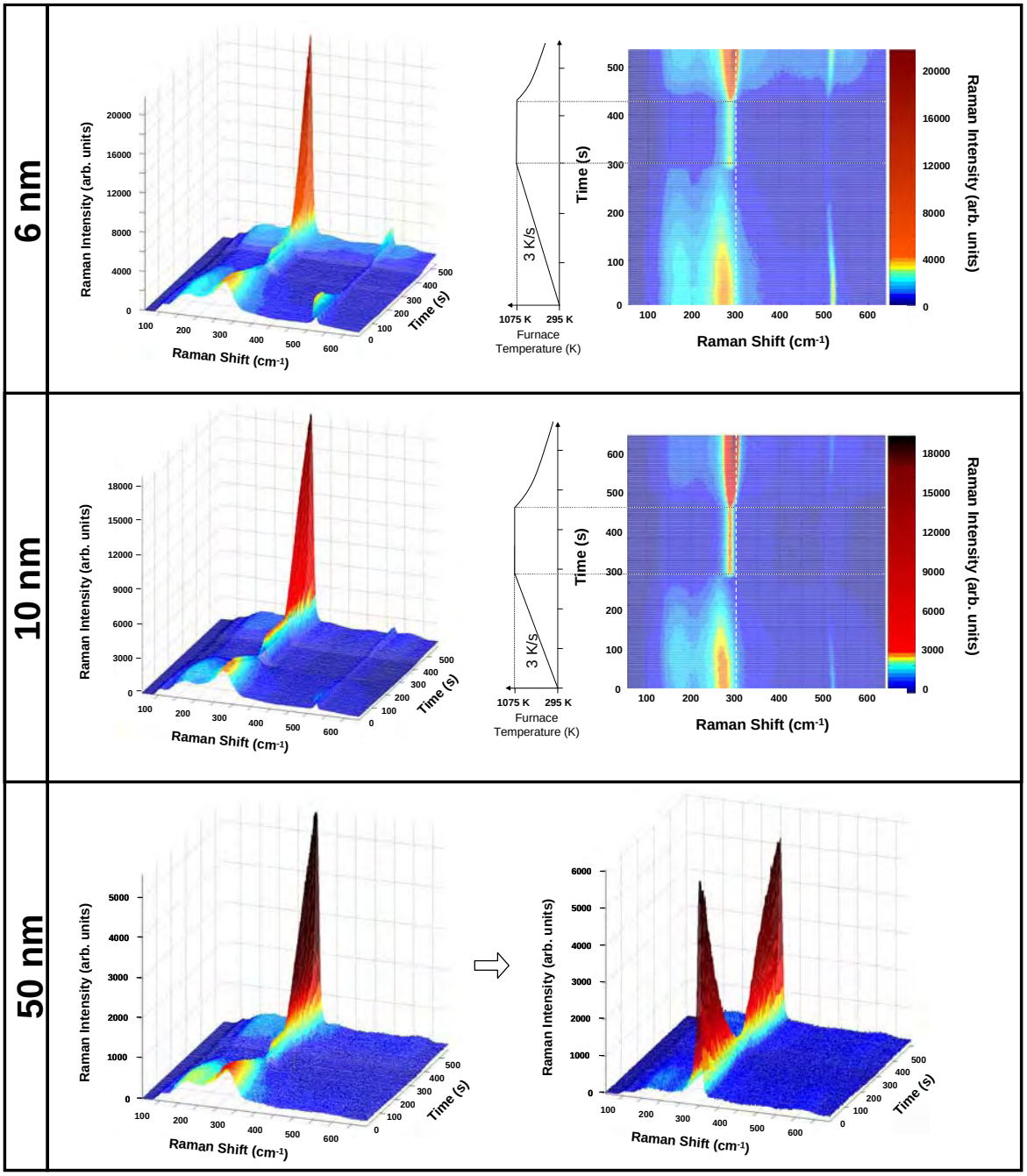

Figure B.10: Real-time Raman spectroscopy during thermal treatment for samples of 6, 10 and 50nm.

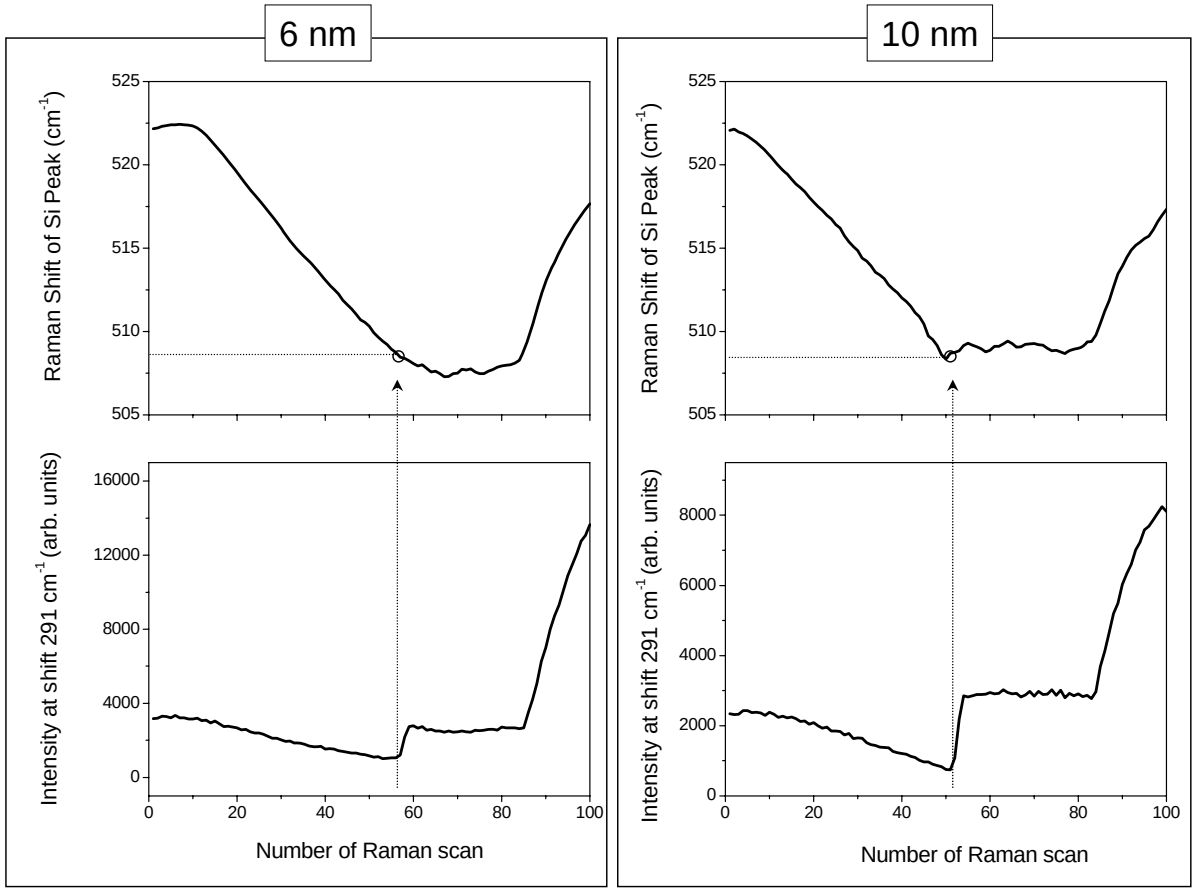

Figure B.11: Raman shift evolution of the Si peak and Raman intensity at 291 cm^{-1}(a frequency between a-Ge and c-Ge) for the complete series of scans during the thermal treatment. The transition amorphous-to-crystalline appears as an step in the Raman intensity. From the movement in Raman shift of the Si peak the temperature is extrapolated.

Appendix C

Feedback controller selection and tuning.

C.1 Feedback controller.

The role of the feedback controller is to process the error signal[1] and generate a response with the objective to reduce it and reach the maximum precision. Engineering of control is not the aim of this thesis, however a brief introduction on several basic concepts can make easier the comprehension of the taken decisions. The controllers presented are digital, which means that both actuation and sensing are discrete on time. In order to select the feedback structures, we simplify the control loop removing the feedforward to simulate the worst experimental case where all control charge relapse in the feedback. Under this assumption, the global transfer function (T(s)) can be calculated as follows:

$$T(s) = \frac{C(s) \cdot G(s)}{1 + C(s) \cdot G(s)} \tag{C.1}$$

where C(s) and G(s) are the expressions in terms of the laplace transform of the transfer functions for feedback controller and nanocalorimeter, respectively.

To proof the viability of any controller algorithm (C(s))[2], it is useful to check the resulting static error and transient behavior of T(s) for different standard inputs (step, ramp, parabola...). In general, in calorimetry we will perform temperature scanning ramps, where the temperature error should be as small as possible while always preserving a non-

[1] Difference between process a setpoint temperatures.

[2] Controller algorithms are combinations of the different control actions described in this section: proportional, integral or derivative.

oscillatory transient response[3]. Both conditions are difficult to attain, since overdamped controllers may prevent oscillations but the response speed to fast perturbations also decreases. On the other hand, underdamped controllers may follow fast perturbations but can exhibit oscillations. Of course, the solution is to design controllers with an appropriate combination of different control actions, with enough freedom to achieve a critical damping during tuning, a compromise between both conditions simultaneously.

The types of control actions. To design the controller algorithm (C(s)) a different combinations of control actions can be considered. We distinguish between three types of control actions: the proportional (P), the integral (I) and the derivative (D). Here we discuse the controller combinations:

1. Controller P. The proportional control action generates an output control signal proportional to the 'present' error. The higher is the proportional gain the higher is the control signal generated for a same error (Action=Kp·error). In general an increase of the proportional gain permits to reduce the error in the steady state. But, the nanocalorimeter behaves as a first order system without any pure integrator (1/s) and the proportional control action alone can not eliminate this static error even for the simplest input signal (the step). In fact, the static error of T(s) for a step input signal (1/s) conserves a an offset of $\frac{1}{1+Kp}$, that worsens in the case of ramp setpoint where error tends to infinite.

2. Controller I. The integral action is evaluated as the integral of the error signal on time (Action=Ki·$\int$error·dt), therefore it depends on the previous history of the error signal. A controller based on a single integrator permits to eliminate the steady state error in T(s) for step inputs and to obtain a finite error in front of a constant ramp, which depends on Ki gain ($1/K_i$). However the integral action may sluggish the dynamic response in front of fast perturbances and may introduce oscillations degrading the stability of the controller.

3. Controller PI. A design with a combined control action (PI) permits a more versatil responses of the system (from oscillatory to overdamped). The integral contribution still serves to eliminate or reduce (depending on input signal) the stationary error,

[3]In calorimetry, it is necessary to prevent the oscillations in order to be able to compute properly the transformation enthalpy.

while the inclusion of the proportional action permits to improve the transient response without increase the instabilities risks. In front of a ramp type setpoint with a PI the system response conserves an offset in steady state that can be reduced by increasing the controller gain.

4. Derivative D and PID controllers. The derivative control action generates a control action proportional to the temporal derivate of the error signal (Action=Kd·$\frac{d\,error}{dt}$). It can not be used alone since for constant error the output action is zero. The addition of derivative action to the PI combination increase its sensibility[4], improving the transient response and enlarging the relative stability. As derivative control action predicts further actions from the dynamic characteristics (increase or decrease) of the error signal, it prevents the growth of error signals, so that it is also called anticipative action. Nevertheless, the derivative action is highly disturbed by the signal noise and in some cases it is better to eliminate it to preserve the system stability.

5. IPID controller. When the ramp setpoint is slow enough compared with the characteristical times of the calorimeter an extra integrator can be added to the PID structure. This is specially suited for digital controllers, with a very low noise in the process signal. The double integrator highly sluggish the response of the controller, limiting the upper dynamic range of applicability. On the contrary a double integrator permits to obtain a zero static error for ramp type setpoints.

General analysis of static errors. In general the global transfer function in closed-loop T(s) (including the feedback controller and nanocalorimeter) can be expressed factorizing the numerator and denominator as:

$$T(s) = \frac{K \cdot (\tau_{z1} \cdot s + 1) \cdot (\tau_{z2} \cdot s + 1) \cdot ... \cdot (\tau_{zi} \cdot s + 1)}{s^n \cdot (\tau_{p1} \cdot s + 1) \cdot (\tau_{p3} \cdot s + 1) \cdot ... \cdot (\tau_{pj} \cdot s + 1)} \tag{C.2}$$

where τ_{zi}, τ_{pj} and n, are the i zeros, the j poles and n is the system order, respectively. Analyzing the static error in closed-loop for different input signals and system orders we obtain the following table:

[4]PID controllers are the most common in Industry.

System order (n)	step setpoint $\left(\frac{1}{s}\right)$ *velocity*=0 *acceleration*=0	ramp setpoint $\left(\frac{1}{s^2}\right)$ *velocity*≠0 *acceleration*=0	parabola setpoint$\left(\frac{1}{s^3}\right)$ *velocity*≠0 *acceleration*≠0
0	$\frac{1}{1+K}$	∞	∞
1	0	$\frac{1}{K}$	∞
2	0	0	$\frac{1}{K}$

Table C.1: Steady state error for different input signals and system orders.

To attain ramps with zero static error the controller structure should include a double integrator. However, difficulties in stability and mainly the sluggish dynamics of this type of controllers limit the applications to slow heating ramps. For very fast heating processes, a compromise between acceptable transient-response and acceptable steady-state error advises to use only an integrator.

Dynamic Response and Stability Dynamics and stability of any system can be understood from the root locus of the global transfer function. In order to explain it we describe in detail the behavior of a second order system and extend it to higher orders. A typical second order system can be represented by equation:

$$T(s) = \frac{\omega_n}{s^2 + 2 \cdot \xi \cdot \omega_n \cdot s + \omega_n^2} \tag{C.3}$$

where ξ is the damping ratio parameter, and ω_n is the undamped natural frequency of the system. The poles of a second order system are determined by the expression:

$$s_{1,2} = -\xi \cdot \omega_n \pm \sqrt{\xi^2 - 1} \tag{C.4}$$

The dynamic behavior of this system can then be described in terms of ξ and ω_n. The response of the second order system to a unit-step input is summarized in figure C.1 (a), for different ξ values and ω_n=1. Figure C.1 (b) shows the poles locus. If ξ=0, the poles are in the imaginary axis, the response to a unit-step does not die and it exhibits a sinusoidal oscillation undamped response with a ω_n frequency. When $0<\xi<1$, the poles are complex conjugates and lie in the left half S plane.

The system is called to be underdamped, since it exhibits an oscillatory transient response that is vanished on time converging to the setpoint value. The oscillation decreases as ξ values are closed to 1. If ξ=1, the system has two identical negatives poles in the real axis $-\xi \cdot \omega_n$. This case is called critically damped and the system does not exhibit

oscillations and the error quickly approaches zero, showing the faster response without oscillations. ξ>1 corresponds to the overdamped case where both poles are real and located in the left half of the S plane. The system response is similar to that of a first order system since it does not exhibit oscillations, but the zero error is only reached at infinite time.

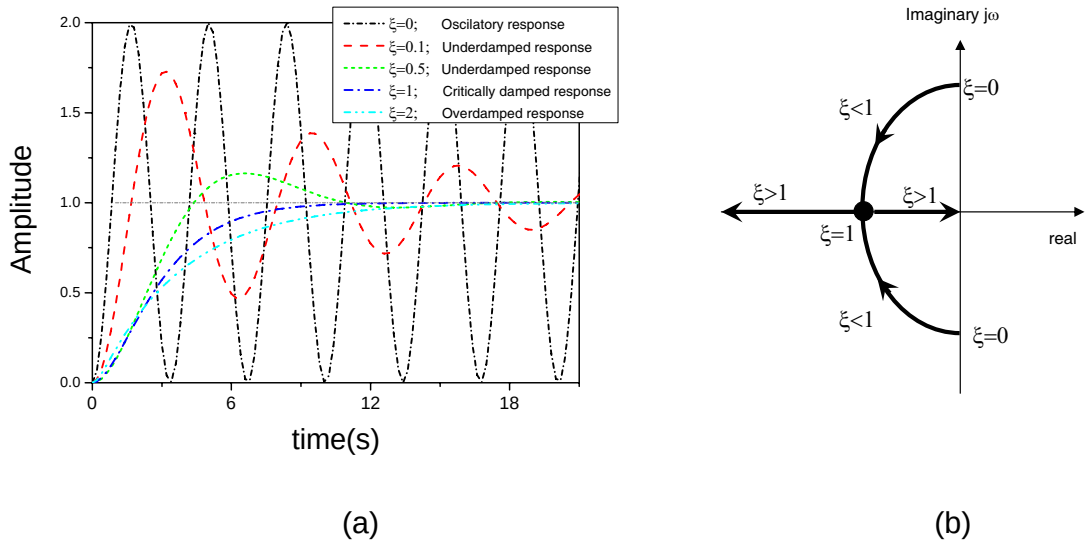

Figure C.1: (a) Response of a 2nd order system in front of an input step depending on ξ values. (b) Root locus for different values of ξ.

The poles locus determine the dynamic evolution of the system. Poles with an imaginary component introduce oscillations in the response, however while real component is negative the transient evolution of the poles tend to converge within the setpoint. Figure C.2, shows how the response of a second order system in front of an input step (for ξ= 0.1 and ω_n=0) is enveloped by two exponential decays that can be defined in terms of ξ and ω_n, that determine the position of the poles. The influence of all poles to the system response have an associated envelop function and while the real component of this pole is negative this enveloped is described by an exponential decay, and the system response converges. Higher order systems can introduce extra number of poles, however the analysis can be similar since for different poles its influence decay at different speeds, leaving one as the dominant of the transient response. The dominance of the poles increases when decreases its module. Poles away from zero are responsible of fast dynamics but its influence is also quickly vanished. When one or several poles lies in the imaginary axis, the speed of the

decay of the oscillatory response is zero, and therefore it never die (like undamped case). More critical results the case of poles in the right-half of the S plane, since the envelope becomes an exponential growth that result in an infinite divergence of the response.

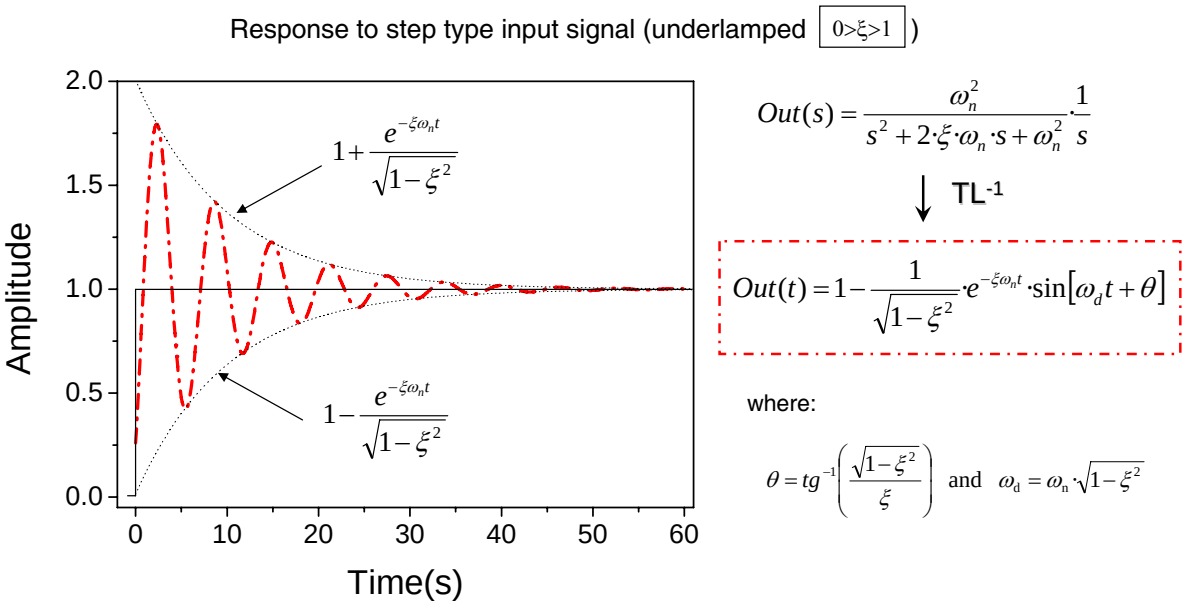

Figure C.2:
Underdamped response of a second order system. Description of the enveloping exponentials that define the system convergence to the setpoint in term of system paramenters.

The degrees of freedom that will be introduced with the controller constants (Kp, Ki and Kd) can be used to tune the system placing the poles to achieved an appropriate behavior.

C.2 Controller tuning.

Applying the equation C.1 with both transfers function of the controllers presented in subsection 5.2.1 and 5.2.2 and the transfer function for the nanocalorimeter, the global transfer function in closed loop can be expressed as follows.

IPID case:

$$T_{IPID}(s) = \frac{\frac{K_d \cdot R^{eff}}{\tau} \cdot s^2 + \frac{K_p \cdot R^{eff}}{\tau} \cdot s + \frac{K_i \cdot R^{eff}}{\tau}}{s^3 + \left(\frac{1+K_d \cdot R^{eff}}{\tau}\right) \cdot s^2 + \left(\frac{K_p \cdot R^{eff}}{\tau}\right) \cdot s + \frac{K_i \cdot R^{eff}}{\tau}} \tag{C.5}$$

PI case:

$$T_{PI}(s) = \frac{\frac{K_p \cdot R^{eff} \cdot s + K_i \cdot R^{eff}}{\tau}}{s^2 + \left(\frac{1+K_p \cdot R^{eff}}{\tau}\right) \cdot s + \frac{K_i \cdot R^{eff}}{\tau}} \tag{C.6}$$

In the IPID the complete system behaves as a high order system, and the transient response is the sum of the responses of first and second-order systems. In the PI the global system behaves as a second order. Both expressions permit to apply the poles placement criterion, placing all the closed-loop poles in the left-half S plane in order to tune the controller by an appropriate selection of parameters K_I, K_d and K_P. Focusing the attention on the denominators, it is possible to factorize them as the combination of first and second order systems, where the parameters effects become clearer:

IPID case:

$$D(s) = s^3 + a_2 \cdot s^2 + a_1 \cdot s + a_0 = \left(s^2 + 2 \cdot \zeta \cdot \omega_o \cdot s + \omega_o^2\right) \cdot (s + a) \tag{C.7}$$

PI case:

$$D(s) = s^2 + a_1 \cdot s + a_0 = \left(s^2 + 2 \cdot \zeta \cdot \omega_o \cdot s + \omega_o^2\right) \tag{C.8}$$

Equalizing these expressions with the denominator of the global transfer function, it is possible to express the K_I, K_d and K_P in terms of the standard second and first order system expression as follows

IPID case:

$$\frac{1 + K_d \cdot R_T^{eff}}{\tau} = 2 \cdot \zeta \cdot \omega_o + a; \tag{C.9}$$

$$\frac{K_P \cdot R_T^{eff}}{\tau} = \omega_o^2 + 2 \cdot \zeta \cdot \omega_o \cdot a; \tag{C.10}$$

$$\frac{K_I \cdot R_T^{eff}}{\tau} = \omega_o^2 \cdot a; \tag{C.11}$$

PI case:

$$\frac{1 + K_P \cdot R_T^{eff}}{\tau} = 2 \cdot \zeta \cdot \omega_o; \tag{C.12}$$

$$\frac{K_I \cdot R_T^{eff}}{\tau} = \omega_o^2; \tag{C.13}$$

To obtain the tuned values of K_I, K_d *and* K_P, it is only necessary to fix the values of ζ, ω_o and a with the criteria that all poles should be negative to prevent oscillations. As higher is the magnitude of the pole smaller is its dominance. Accordingly, the values of ζ, ω_o and a, are fixed a priori as 1, 4 and 20, respectively[5]. Calculating the controller parameters with these premises provides a first tuning approximation near critically damped conditions. In this bare tuning the error contribution can come from different sources: uncertainties in the calorimeter model, the non consideration of feedforward during tuning analysis and the nonconsideration of discretization essentially for slow heating ramps (extra analysis in terms of Z transform [107]).

There are several methods to experimentally refine the tuning of PID controllers, like the Ziegler-Nichols rules. These methods are widely used in control systems where the plant dynamics[6] are not precisely known, see chapter 10 in [107]. However, from an experimental point of view, the best solution was to build up a map of the controller. By analyzing the system responses when the values of K_I, K_d *and* K_P are varied around those obtained from the first tuning analysis. The influence of different parameters K_I, K_d *and* K_P, over the transient response of the controller, see figure C.3, are reviewed in the next table, describing the behavior of the controlled variable with the increment of each parameter, separately.

[5] ζ=1 fix the system to be underdamped.
$\omega_o = \frac{4}{\zeta \cdot T_S} = 4$; where T_S is the settling time ($T_S = 1s$), see chapter 5 in [**?**].
$a = 5 \cdot \omega_o \cdot \zeta$; the third pole is placed in a zone where to cancel its influence.
[6] In our case the model of the calorimeter.

	K_P	K_I	K_d
Rise Time	decrease	decrease	no change
Overshoot	increase	increase	decrease
Settling Time	no change	increase	decrease
offset	decrease	desappear	not changes

Table C.2: Tendency of IPID response for different parameter increments

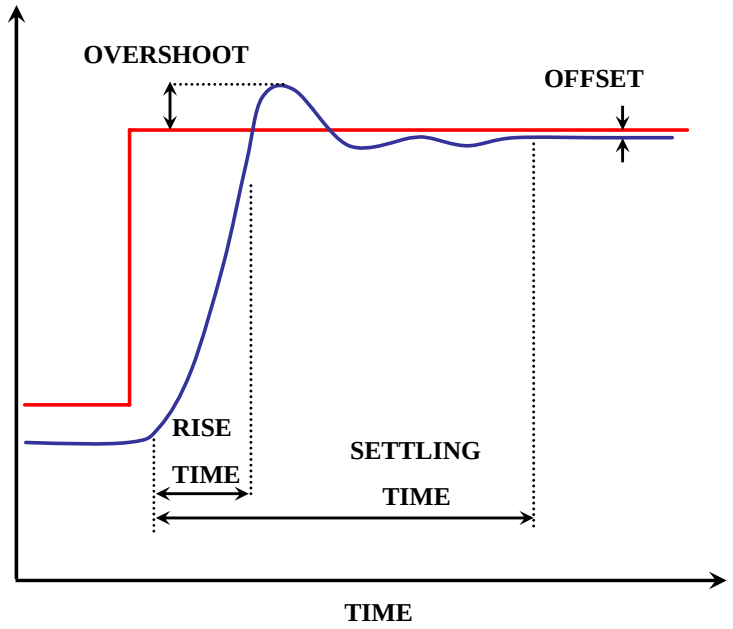

Figure C.3: Controller transient response.

Bibliography

[1] D.O.Dabbousi *et al.* Cdse-zns core-shell quantum dots: Synthesis and characterization of size series of high luminiscent nanocristallites. *J. Phys. Chem. B* **101**, 9463–9475 (1997).

[2] V.L.Colvin, A.N.Echer & P.A.Alivisatos. Melting in semiconductor nanocristals. *Science* **256**, 1425–1427 (1992).

[3] S.H.Tolbert & P.A.Alivisatos. High-pressure structural transformations in semiconductor nanocristals. *Annu. Rev. Phys. Chem.* **46**, 595–625 (1995).

[4] J.P.K.Doye & F.Calvo. Entropic effects on the size dependence of cluster structure. *Phys. Rev. Lett.* **86**, 3570 (2001).

[5] G.R.Steward. Measurement of low temperture specific heat. *Rev. Sci. Instr.* **54** (1983).

[6] F.Spaepen & C.V.Thompson. Calorimetric studies of reactions in films and multilayers. *Appl. Surf. Sci.* **38**, 1–12 (1989).

[7] M.Gonzalez-Silveira, M.T.Clavaguera-Mora, F.Pi & J.Rodriguez-Viejo. Calorimetric evidence of asymmetry in the nucleation of cumg2 in cu/mg multilayers. *Phys.Rev.B* **69**, 113411 (2004).

[8] J.Lerchner. Report on the workshop "nanocalorimetry". *Thermochim. Acta.* **337**, 231–233 (1999).

[9] K.D.Wise & K.Najafi. Microfabrication techniques for integrated sensors and microsystems. *Sciences* **254**, 1335–1341 (1991).

[10] E.Thielicke & E.Obermeier. Microactuators and their technologies. *Mechatronics* **10**, 431–455 (2000).

[11] R.Srinivasan *et al.* Micromachined reactors for catalytic partial oxidation reactions. *Aiche journal* **43**, 3059–3069 (1997).

[12] D.W.Denlinger *et al.* Thin film microcalorimeter for heat capacity measurements from 1.5k to 800k. *Rev.Sci.Instrum.* **65**, 946–959 (1994).

[13] O.Bourgeois, S.Skipetrov, F.Ong & J.Chaussy. Attojoule calorimetry of mesoscopic superconducting loops. *Phys. Rev. Lett.* **94** (2005).

[14] L.H.Allen *et al.* 1000000 c/s thin film electrical heater: ln situ resistivity measurements of al and ti/si thin films during ultra rapid thermal annealing. *Appl. Phys. Lett.*. **64**, 417–419 (1994).

[15] S.L.Lai, G.Ramanath, L.H.Allen & P.Infante. Heat capacity measurements of sn nanostructures using a thin-film differential scanning calorimeter with 0.2nj sensitivity. *Appl. Physs. Lett.* **70**, 43–45 (1997).

[16] S.A.Adamovsky, A.A.Minakov & C.Schick. Non-adiabatic thin-film (chip) nanocalorimetry. *Thermochim. Acta* **432**, 177–185 (2003).

[17] R.T.Tol, A.A.Minakov, S.A.Adamovsky, V.B.F.Mathot & C.Schick. Metastability of polymer crystallites formed at low temperature studied by ultra fast calorimetry: Polyamide 6 confined in sub-micrometer droplets vs. bulk pa6. *Polymer* **47**, 2172–2178 (2006).

[18] S.L.Randzio. Recent develop in calorimetry. *Annu. Rep. Prog. Chem. Sect. C* **94**, 433–504 (1998).

[19] A.F.Lopeandía *et al.* Nanocalorimetric high-temperature characterization of ultrathin films of a-ge. *Mater. Sci. Semicond. Process.* **9**, 806–811 (2006).

[20] A.A.Minakov, R.T.Tol, D.A.Mordvintsev & C.Schick. Melting and reorganization of the crystalline fraction and relaxation of the rigid amorphous fraction of isotactic polystyrene on fast heating (30,000k/min). *Thermochim. Acta* **442**, 25–30 (2006).

[21] K.F.Jensen. Microreaction engineering - is small better? *Chem.Eng. Sci.* **56**, 293–303 (2001).

[22] Madou, M. *Fundamentals of microfabrication. The science of miniaturation.* (CRC Press LLC, 2000).

[23] S.Marco. *Microsistemas Phd. course notes*. Universitat de Barcelona (2003).

[24] M.Y.Efremov *et al.* Thin-film differential scanning nanocalorimetry: heat capacity analysis. *Thermochimica Acta* **412**, 13–23 (2004).

[25] A.F.Lopeandía, E.Leon-Gutierrez, J.Rodríguez-Viejo & F.J.Munoz. Design issues involved in the development of a membrane-based high-temperature nanocalorimeter. *Microelectron. Eng.* .

[26] Zink, B. L., Revaz, B. & Hellman, R. S. F. Thin film microcalorimeter for heat capacity measurements in highmagnetic fields. *Rev.Sci.Instrum.* **73**, 1841–1844 (2002).

[27] J.Spannhake *et al.* High-temperature mems heater platforms: Long-term performance of metal and semiconductor heater materials. *Sensors* **6**, 405–419 (2006).

[28] M.Schmidt, R.Kusche, B.von-Issendorff & H.Haberland. Irregular variations in the melting point of size-selected atomic clusters. *Nature* **393**, 238–240 (1998).

[29] K.D.Irwin, GC.Hilton, D.A.Wollman & J.M.Martinis. X-ray detection using a superconducting transition-edge sensor microcalorimeter with electrothermal feedback. *Appl. Physs. Lett.* **69**, 1945–1947 (1996).

[30] Olson, E., M.Y.Efremov, M.Zhang, Z.Zhang & L.H.Allen. The design and operation of a mems differentialscanning nanocalorimeter for high-speed heatcapacity measurements of ultrathin films. *J. Microelectromech. Syst.* **12**, 355–364 (2003).

[31] S.L.Firebaugh, K.F.Jensen & A.Schmidt, M. Investigation of high temperature degradation of platinum thin film with an insitu resistance measurement apparatus. *J. Microelectromech. Syst.* **7**, 128–135 (1998).

[32] Wedler, G. & Alshorachi, G. The influence of thickness on the resistivity,the temperature coefficient of resistivity and the thermoelectricpower of evaporated palladium films at 77 k and 273 k. *Thin Solid Films* **74**, 1–16 (1980).

[33] D.J.Quiram, I.M.Hsing, A.J.Franz, K.F.Jensen & M.A.Schmidt. Design issues for membrane-based, gas phase microchemical systems. *Chem.Eng.Sci.* **55**, 3065–3075 (2000).

[34] A.F.Lopeandia, J.Rodriguez-Viejo, M.Chacon, M.T.Clavaguera-Mora & F.J.Munoz. Heat transfer in symmetric u-shape microreactors for thin film calorimetry. *J. Micromech. Microeng.* **16**, 965–971 (2006).

[35] J.H.Matthews & K.Fink. *Numerical Methods with Matlab* (2001), 3rd edn.

[36] C.R.Bowen & B.Derby. Finite difference modelling of self-propagating high temperature syntesis of materials. *Acta metall. mater.* **43**, 3903–3913 (1995).

[37] P.Hunter. *FEM/BEM notes*. Department of Engineering Science, The University of Auckland New Zealand.

[38] Y.S.Touloukian, R.W.Powell, C.Y.Ho & P.G.Klemens. *Thermodinamical properties of mather*, vol. 4 (Plenum, 1970).

[39] J.F.Shackelford & W.Alexander. *CRC materials science and egineering handbook* (CRC Press, cop. 2001), 3rd ed. edn.

[40] C.Mastrangelo, Y.C.Tai & R.S.Muller. Thermophysical properties of low-residual stress, silicon rich, lpcvd silicon nitride films. *Sensors and actuators B* **A21-A23**, 856–860 (1990).

[41] R.P.Manginell, D.A.Rosato, D.A.Benson & G.C.Frye-Mason. Finite element modeling of a microhotplate for microfluidic applications. *Technical Proceedings of the 1999 International Conference on Modeling and Simulation of Microsystems.* **18**, 663 – 666 (1999).

[42] I.M.Hsing, R.Srinivasan, M.P.Harold, K.F.Jensen & M.A.Schmidt. Simulation of micromachined chemical reactorsfor heterogeneous partial oxidation reactions. *Chem.Eng. Sci.* **55**, 3–13 (2000).

[43] Zhang, X. & Grigoropoulosa, C. P. Thermal conductivity and diffusivity of freestanding silicon nitridethin films. *Rev.Sci.Instrum.* (1995).

[44] J.Alvarez-Quintana & J.Rodríguez-Viejo. Extension of the 3w method to measure the thermal conductivity of thin films without a reference sample. *Sensors and actuators A* **In press** (2007).

[45] Keithley. Low level measurements handbook.

[46] M.Ohring. *Material science of thin films: Deposition and Structure* (Academic Press, 2002), 2nd edition edn.

[47] J.Rodriguez-Viejo *et al.* Microreactor for thin film calorimetry. *MAt.Res.Soc.Symp.Proc.* **741** (2003).

[48] Vacuum technology seminar (Varian Vacuum Technologies, Telstar).

[49] F.J.Morin & J.P.Maita. Specific heats of transition metal superconductors. *Phys. Rev.* **129**, 1115 (1963).

[50] S.R.Early, F.Hellman, J.Marshall & T.H.Geballe. A silicon on sapphire thermometer for small sample low temperature calorimetry. *Physica B* **107B**, 327 (1981).

[51] N.E.Hager-Jr. Thin heater calorimeter. *Thermochim. Acta* **35**, 618–624 (1964).

[52] S.L.Lai, G.Ramanath, L.H.Allen, P.Infante & Ma, Z. High speed (10^4 c/s) scanning microcalorimetry with monolayer sensitivity (j/m^2). *Appl. Physs. Lett.* **67**, 1229–1231 (1995).

[53] M.Y.Efremov *et al.* Ultrasensitive, fast, thin-film differential scanning calorimeter. *Rev. sci. instr.* **75** (2004).

[54] S.A.Adamovsky, A.A.Minakov & C.Schick. Scanning microcalorimetry at high cooling rate. *Thermochim. Acta* **403**, 55–63 (2003).

[55] M.Yu.Efremov *et al.* Discrete melting point observations for nanostructure ensembles. *Phys.Rev. Lett.* **85**, 3560–3563 (2000).

[56] P.Horowitz & W.Hill. *The art of electronics* (Cambridge University Press, 1989), 2on ed. edn.

[57] M.N.Touzelbaev & K.E.Goodson. Impact of experimental timescale and geometry onthin-film thermal property measurements. *Fourteenth Symposium on Thermophysical Properties.* **25-30** (2000).

[58] K.M.Unruh, T.E.Huber & C.A.Huber. Melting and freezing behaviour of indium metal in porous glass. *Phys. Rev. B* **48**, 9021 (1993).

[59] M.Zhang *et al.* Size-dependent melting point depression of nanostructure: Nanocalorimetric measurements. *Phys. Rev. B* **62**, 10548–10557 (2000).

[60] P.Pawlow. *Z. Phys. Chem.* **65**, 1–35,545–548 (1909).

[61] A.N.Goldstein, C.M.Echer & A.P.Alivisatos. Melting in semiconductor nanocrystals. *Science* **256**, 1425 (1992).

[62] Ph.Buffat & J-P.Borel. Size effect on the melting temperature of gold particles. *Phys. ReV. A* **13**, 2287 (1976).

[63] A.N.Goldstein. The melting of silicon nanocrystals: Submicron thin-film structures derived from nanocrystal precursors. *Appl. Phys. A* **62**, 33–37 (1996).

[64] P.R.Couchman & W.A.Jesser. Thermodynamic theory of size dependence of melting temperature in metals. *Nature* **269**, 481–483 (1977).

[65] M.Zhang, M.Yu.Efremov, E.A.Olson, Z.S.Zhang & L.H.Allen. Real-time heat capacity measurement during thin-film depositionby scanning nanocalorimetry. *Appl. Physs. Lett.* **81**, 3801–3803 (2002).

[66] M.W.Zemansky & R.H.Dittman. *Heat and Thermodinamics* (McGraw-Hill), 6th edition edn.

[67] D.L.Connelly, J.S.Loomis & D.E.Mapother. Specific heat of nickel near the curie temperature. *Phys.Rev. B* **3**, 924 (1971).

[68] T.Ogawa, H.Nagasaki & T.Sato. Size dependent magnetic phase transition in reentrant ferromagnet nimn multilayer films. *Phys. Rev. B* **65**, 024430 (2001).

[69] R.Zhang & R.F.Willis. Thickness-dependent curie temperatures of ultrathin magnetic films: Effect of the range of spin-spin interactions. *Phys. Rev. Lett.* **86**, 2665 (2001).

[70] A.V.Bune *et al.* Two-dimensional ferroelectric films. *Nature* **391**, 874 (1998).

[71] Y.Li & K.Barbeschke. Dimensional crossover in ultrathin ni(111) films on w(110). *Phys.Rev.Lett.* **68** (1992).

[72] L.Sun, P.C.Searson & C.L.Chien. Finite-size effects in nickel nanowire arrays. *Phys. Rev. B* **61**, R6463 (2000).

[73] M.E.Fisher & M.N.Barber. Scaling theory for finite-size effects in the critical region. *Phys. Rev. Lett.* **28**, 1516 (1972).

[74] D.Gerion, A.Hirt, I.M.L.Billas, A.Châtelain & W.A.deHeer. Experimental specific heat of iron, cobalt, and nickel clusters studied in a molecular beam. *Phys.Rev. B* **62** (2000).

[75] X.F.Cui, M.Zhao & Q.Jiang. Curie transition temperature of ferromagnetic low-dimensional metals. *Thin Solid Films* **472**, 328–333 (2005).

[76] X.Y.Lang, W.T.Zheng & Q.Jiang. Size and interface effects on ferromagnetic and antiferromagnetic transition temperatures. *Phys.Rev.B* **73**, 224444 (2006).

[77] *Handbook of Chemistry and Physics* (CRC, 2004), 84th edition edn.

[78] M.Liehr, H.Lefakis, F.K.LeGoues & G.W.Rubloff. Influence of thin sio2 interlayers on chemical reaction and microstructure at the nisi interface. *Phys. Rev. B* **33**, 8 (1986).

[79] L.Wang, Z.Tan, S.Meng, D.Liang & B.Liu. Low temperature heat capacity and thermal stability of nanocrystalline nickel. *Thermochim. Acta* **386**, 23–26 (2002).

[80] C.Kittel. *Introduction to the Solid State Physics* (Reverte, 1993), 3rd edition edn.

[81] N.W.Ashcroft & N.D.Mermin. *Solid State Physics* (Saunders College publising, 1976), 3rd edition edn.

[82] S.Amoruso, R.Bruzzese, X.Wang, N.N.Nedialkov & P.A.Atanasov. Femtolaser ablation of nickel in vaccum. *J.Phys.D: Appl. Phys.* **40**, 331–340 (2007).

[83] Y.Volokitin, J.Sinzig, G.Schmid, H.Bönnemann & L.J.DeJongh. Thermodynamic properties of nm-sized pd and ni particles. *Z.Phys.D* **40** (1997).

[84] A.V.Kolobov *et al.* Formation of ge nanocrystals embedded in a sio2 matrix: Transmission electron microscopy, x-ray absorption, and optical studies. *Phys.Rev.B* **67** (2003).

[85] K.Das *et al.* Charge storage and photoluminescence characteristics of silicon oxide embedded ge nanocrystal trilayer structures. *Appl.Phys.Lett.* **84** (2004).

[86] W.K.Choi *et al.* Investigation of ge nanocrystal formation in sio2-ge-sio2 sandwich structure. *Scr Mater* **44**, 1873–1877 (2001).

[87] M.Zacharias & P.Streitenberger. Crystallization of amorphous superlattices in the limit of ultrathin films with oxide interfaces. *Phys. Rev. B* **62**, 8391 – 8396 (2000).

[88] J.Solis, J.Siegel, C.N.Afonso, J.Jimenez & C.Garcia. Supercooling and structural relaxation in amorphous ge films under pulsed laser irradiation. *J. Appl. Phys.* **82**, 236 (1997).

[89] C.M.Yang & H.A.Atwater. Crystallization and diffusion in progressively annealed a-ge/siox superlattices. *APL* **68**, 24 (1996).

[90] G.V.M.Williams, A.Bittar & H.J.Trodahl. Crystallization and diffusion in progressively annealed a-ge/siox superlattices. *JAP* **67**, 4 (1990).

[91] S.H.Yang & R.J.Berry. Molecular dynamics simulation of germanium nanoparticles. *Mat. Res. Soc. Proc.* **769**, 201 (2003).

[92] H.W.Chiu, C.N.Chervin & S.M.Kauzlarich. Phase changes in ge nanoparticles. *Chem. Mater.* **17**, 4858 (2005).

[93] Q.Xu *et al.* Large melting-point hysteresis of ge nanocrystals embedded in sio2. *Phys. Rev. Lett.* **97**, 155701 (2006).

[94] M.Takagi. Electron-diffraction study of liquid-solid transition of thin metal films. *J. Phys. Soc. Jpn* **9**, 359–363 (1954).

[95] K.Lu & Z.H.Jin. Melting and superheating of low-dimensional materials. *Curr. Opin. Sol. State Mat. Sci.* **5**, 39 (2001).

[96] F.Spaepen & D.Turnbull. Kinetics of motion of crystal-melt interfaces. *AIP Conf. Proc.* **50**, 73 (1979).

[97] B.G.Bagley & H.S.Chen. A calculation of the thermodynamic first order amorphous semiconductor to metallic liquid transition temperature. *AIP Conf. Proc.* **50**, 97 (1979).

[98] J.Solis & C.N.Afonso. Reflectivity and transmission of amorphous thin films at the melting temperature. *J. Appl. Phys.* **72**, 2125–2130 (1992).

[99] S.Kumar & H.J.Trodahl. Folded phonon spectra of progressively annealed amorphous si/ge superlattices. *J. Appl. Phys.* **70**, 508–510 (1991).

[100] E.P.Donovan, F.Spaepen, D.Turnbull, J.M.Poate & D.C.Jacobson. Calorimetric studies of crystallization and relaxation of amorphous si and ge prepared by ion implantation. *J. appl. phys.* **57**, 1795–1804 (1984).

[101] J.C.C.Fan & C.H.Anderson. Transition temperatures and heat of crystallization of amorphous ge, si and gesix alloys determined by scanning calorimetry. *J. Appl. Phys.* **52**, 4003–4006 (1981).

[102] A.Karmous, I.Berbezier & A.Ronda. Formation and ordering of ge nanocrystals on sio2. *Phys. Rev. B* **73**, 075323 (2006).

[103] N.Kaiser, A.Cröll, F.R.Szofran, S.D.Cobb & K.W.Benz. Wetting angle and surface tension of germanium melts on different substrate materials. *J. Cryst. Growth* **231**, 448–457 (2001).

[104] M.J.O'Neill. The analysis of temperature-controlled scanning calorimeter. *Analytical Chemistry* **36**, 1238–1245 (1964).

[105] A.F.Lopeandia *et al.* A sensitive power compensated scanning calorimeter for analysis of phase transitions in small samples. *Rev.Sci.Instrum.* **76** (2005).

[106] M.Merzlyakov. Method of rapid (100000 k/s) controlled cooling and heating of thin films. *Thermochim. Acta* **442**, 52–60 (2006).

[107] Ogata, K. *Modern control engineering.* (Prentice Hall, 2002).

[108] S.Govorkov, W.Ruderman, Horn, M., R.B.Goodman & M.Rothschild. A new method for measuring thermal conductivity of thin films. *Rev. Sci. Instrum. 68 (10), October 1997* **68**, 3828–3834 (1997).

[109] A.T.Fiory. Rapid thermal processing for silicon nanoelectronics applications. *JOM* **57**, 21–26 (2005).

[110] X.A.Cao *et al.* Ultrahigh si+ implant activation efficiency in gan using a high-temperature rapid thermal process system. *Appl. Phys. Lett.* **73**, 229 (1998).

[111] Y.Hu & S.P.Tay. Spectroscopic ellipsometry investigation of nickel silicide formation by rapid thermal process. *J. Vac. Sci. Tech. A: Vacuum, Surfaces, and Films* **16**, 1820 (1998).

[112] D.M.Camm, J.C.Gelpey, T.Thrum, G.C.Stuart & S.McCoy. Flash-assist rtp for ultra-shallow junctions. *JOM* **58**, 32–34 (2006).

[113] A.F.Lopeandía & J.Rodríguez-Viejo. Size-dependent melting and supercooling of ge nanoparticles embedded in a sio2 thin film. *Thermochim. Acta* **In press** (2007).

[114] M.Podesta. Understanding heat capacity measurements. www.physicofmatter.com.

[115] G.Hohne, W.Hemminger & H.J.Flammersheim. *Differential Scanning Calorimetry. An introduction to Practitioners.* (springer, 2002).

[116] D.Hansen, L. Toward a standard nomenclature for calorimetry. *Thermochim. Acta.* **371**, 19–22 (2001).

[117] S.Agan, A.Celik-Aktas, J.M.Zuo, A.Dana & A.Aydinli. Synthesis and size differentiation of ge nanocrystals in amorphous sio2. *Appl.Phys. A.* **83**, 107–100 (2006).

[118] S.Foss, T.G.Finstad, A.Dana & A.Aydinli. Growth of ge nanoparticles on sio2/si interfaces during annealing of plasma enhanced chemical vapor deposited thin film. *Thin Solid Films* **515**, 6381 (2007).

[119] S.T.Ngiam, K.F.Jensen & K.D.Kolenbrander. Synthesis of ge nanocrystals embedded in a si host matrix. *JAP* **76**, 8201 (1994).

[120] W.K.Choi *et al.* Raman characterization of germanium nanocrystals in amorphous silicon oxide films synthesized by rapid thermal annealing. *JAP* **86**, 1398 (1999).

[121] V.Craciun, I.W.Boyd, A.H.Reader & D.E.W.Vandenhoudt. Low temperature synthesis of ge nanocrystals in sio2. *Appl.Phys.Lett.* **65**, 3233 (1994).

[122] K.L.Teo, S.H.Kwok, , P.Y.Yu & S.Guha. Quantum confinement of quasi-two-dimensional e1 excitons in ge nanocrystals studied by resonant raman scattering. *Phys. Rev. B* **62**, 1584–1587 (2000).

[123] E.W.H.Kan *et al.* Effect of annealing profile on defect annihilation, crystallinity and size distribution of germanium nanodots in silicon oxide matrix. *Appl. Phys. Lett.* **83**, 2058 (2003).

[124] Q.Wan, T.H.Wang, W.L.Liu & C.L.Lin. Ultra-high-density ge quantum dots on insulator prepared by high-vacuum electron-beam evaporation. *Journal of Crystal Growth* **249**, 23–27 (2003).

[125] T.Stoica & E.Sutter. Ge dots embedded in sio2 obtained by oxidation of si/ge/si nanostructures. *Nanotechnology* **17**, 4912 (2006).

[126] O.G.Schmidt, C.Lange, K.Eberl, O.Kienzle & F.Ernst. Formation of carbon-induced germanium dots. *Appl. Phys. Lett.* **71**, 2340 (1997).

[127] Z.M.Wang, J.Y.Wang, L.P.H.Jeurgens & E.J.Mittemeijer. Explosive crystallisation of amorphous germanium in ge/al layer systems; comparison with si/al layer systems. *Scripta Materialia* **55**, 987 (2006).

[128] Wang, K. L., J.L.Liu & G.Jin. Self-assembled ge quantum dots on si and their applications. *Journal of crystal growth* **1892**, 237–239 (2002).

[129] X.Huang *et al.* Temperature dependence of raman scattering in si crystals with heavy b and-or ge doping. *Mat. sci. Sem. Proc.* **9**, 257–260 (2006).